

AN INVESTIGATION OF THE VIVALDI ANTENNA

By

Venkata Krishna Tulasi Kota

A Thesis
submitted to the Faculty of Graduate Studies
in partial fulfillment of the requirements
for the degree of

Master of Science

Department of Electrical and Computer Engineering
The University of Manitoba
Winnipeg, Manitoba, Canada

Copyright © August 2009 By Venkata Krishna Tulasi Kota

**THE UNIVERSITY OF MANITOBA
FACULTY OF GRADUATE STUDIES

COPYRIGHT PERMISSION**

An Investigation of the Vivaldi Antenna

By

Venkata Krishna Tulasi Kota

A Thesis/Practicum submitted to the Faculty of Graduate Studies of The University of

Manitoba in partial fulfillment of the requirement of the degree

Of

Master of Science

Venkata Krishna Tulasi Kota©2009

Permission has been granted to the University of Manitoba Libraries to lend a copy of this thesis/practicum, to Library and Archives Canada (LAC) to lend a copy of this thesis/practicum, and to LAC's agent (UMI/ProQuest) to microfilm, sell copies and to publish an abstract of this thesis/practicum.

This reproduction or copy of this thesis has been made available by authority of the copyright owner solely for the purpose of private study and research, and may only be reproduced and copied as permitted by copyright laws or with express written authorization from the copyright owner.

ACKNOWLEDGEMENTS

I would like to acknowledge and extend my heartfelt gratitude to my research advisor, Professor L. Shafai for his supervision, guidance and constant encouragement throughout my research. His priceless knowledge and advice are most appreciated.

I would like to thank the members of my examining committee, Dr. B. Kordi and Dr. T. ElMekkawy. Special thanks to Mr. C. Smit and Mr. B. Tabachnik for their extensive help provided during required fabrication work and experimental measurements. I would also like to express my sincere appreciation to Ms. S. Girardin for her patient and kind assistance whenever it was needed during my studies at The University of Manitoba.

Finally, I wish to thank my loving family, and am extremely grateful for their endless encouragement and moral support through all my endeavors.

Abstract

An exponentially tapered slot line antenna named the Vivaldi is studied in this thesis. This antenna has ultra-wideband (UWB) characteristics and is used in applications ranging from feeds for reflectors to microwave imaging. In all these applications, knowledge of the far-field radiation characteristics and location of phase centre of the antenna are greatly required. This thesis deals with the study of two different kinds of Vivaldi antennas. A thorough parametric study of a single sided Vivaldi antenna is carried out with the help of simulation software. Through this study, a compact design is developed which exhibits a performance superior to that of the existing one with regard to radiation patterns and phase centre location.

From this compact design, a balanced antipodal Vivaldi antenna which also exhibits a commendable performance is developed and studied for a better understanding of the different types of these antennas. In order to understand the achievable bandwidth of the Vivaldi, a balanced antipodal model with a larger aperture is simulated and a study of its gain enhancement through substrate elongation and shape is made. Experimental investigations are also carried out and it is seen that the measured far-field radiation patterns and phase centre location are in close agreement with the simulated results.

TABLE OF CONTENTS

ACKNOWLEDGEMENTS	i
ABSTRACT	ii
TABLE OF CONTENTS	iii
LIST OF FIGURES	v
LIST OF TABLES	xiii
CHAPTER 1: INTRODUCTION	1
1.1 Preface	1
1.2 Literature Review	2
1.3 Structure of the Thesis	4
CHAPTER 2: BRIEF OVERVIEW OF TAPERED SLOT ANTENNAS	6
2.1 Introduction	6
2.2 Tapered Slot Antennas (TSAs)	7
2.2.1 Characteristics of TSAs	7
2.2.2 Taper Profiles	7
2.2.3 Feeding Techniques	8
2.3 The Vivaldi Antenna	9
2.3.1 Introduction	9
2.3.2 Microstrip/Stripline to Slotline Transitions	11
2.3.3 Antipodal Vivaldi Antenna	13
2.3.4 Balanced Antipodal Vivaldi Antenna	14
2.4 Phase Centre	16
2.5 Summary	17
CHAPTER 3: PARAMETRIC STUDY OF VIVALDI ANTENNA-I	18
3.1 Introduction	18
3.2 Original Model (Model 1)	18
3.2.1 Antenna Model	18
3.2.2 Antenna Performance	20
3.2.3 Study of Phase Centre	29
3.3 Extended Flare Model (Model 2)	32
3.3.1 Antenna Model	32
3.3.2 Antenna Performance	33
3.3.3 Study of Phase Centre for Model 2	41
3.4 Truncated Flare Model (Model 3)	42
3.4.1 Antenna Model	42
3.4.2 Antenna Performance	43
3.4.3 Study of Phase Centre for Model 3	52

3.5 Summary	53
CHAPTER 4: PARAMETRIC STUDY OF VIVALDI ANTENNA-II	54
4.1 Introduction	54
4.2 Fast Opening Flare Model (Model 4)	54
4.2.1 Antenna Model	54
4.2.2 Antenna Performance	55
4.2.3 Study of Phase Centre for Model 4	64
4.3 Slow Opening Flare Model (Model 5)	65
4.3.1 Antenna Model	65
4.3.2 Antenna Performance	66
4.3.3 Study of Phase Centre for Model 5	74
4.4 Width Truncated Model (Model 6)	75
4.4.1 Antenna Model	75
4.4.2 Antenna Performance	76
4.4.3 Study of Phase Centre for Model 6	86
4.5 Summary	87
CHAPTER 5: STUDY OF BALANCED ANTIPODAL VIVALDI ANTENNA	88
5.1 Introduction	88
5.2 Balanced Antipodal Vivaldi Antenna	88
5.2.1 Antenna Model 1	88
5.2.2 Antenna Performance	90
5.2.3 Study of Phase Centre for the balanced antipodal Vivaldi antenna 1	99
5.2.4 Antenna Model 2	100
5.2.5 Antenna Performance	102
5.3 Increase in Length of Substrate	110
5.3.1 Elongated Antenna Models and Performance	111
5.3.2 Study of Phase Centre for the 12.80 mm elongated substrate model	117
5.4 Shaping of Substrate	119
5.4.1 Antenna Substrate Shapes and Performance	120
5.5 Summary	129
CHAPTER 6: EXPERIMENTAL VERIFICATION	130
6.1 Introduction	130
6.2 Fabricated Antenna	130
6.3 Simulated vs. Measured Results	132
6.4 Study of Phase Centre	153
6.5 Summary	155
CHAPTER 7: CONCLUSION	156
7.1 Summary	156
7.2 Future Work	159
REFERENCES	160

LIST OF FIGURES

Fig. 2.1 Three basic taper profiles (a) Linear taper (b) Constant width taper (c) Non-linear taper	8
Fig. 2.2 Basic model of the Vivaldi antenna	9
Fig. 2.3 Microstrip to slotline transition	11
Fig. 2.4 Microstrip to slotline transition with radial stub	12
Fig. 2.5 Antipodal Vivaldi antenna	14
Fig. 2.6 Cross sectional view of the top of the antipodal Vivaldi depicting the E-field skew across the slot of the antenna	14
Fig. 2.7 Balanced antipodal Vivaldi antenna	15
Fig. 2.8 Cross sectional view of the top of the balanced antipodal Vivaldi depicting the resultant E-field across the slot of the antenna	16
Fig. 3.1 The geometry of the Vivaldi antenna (Model 1) including the microstrip feed along with the co-ordinate system: $L_s=22.86\text{mm}$, $W_s=38.10\text{mm}$, $L_c=16.51\text{mm}$, $W_m=0.81\text{mm}$, $W_a=6.35\text{mm}$, $D_s=3.30\text{mm}$ with $\epsilon_r=2.2$, $h=0.508\text{mm}$ and $\tan\delta=0.001$	19
Fig. 3.2 Simulated (a) S_{11} and (b) input impedance plot measured with respect to $75\ \Omega$ for antenna Model 1 shown in Fig. 3.1 and described by (3.1)	21
Fig. 3.3 Simulated E-plane ($\phi=90^\circ$ plane) co-pol and cross-pol patterns of Model 1 shown in Fig. 3.1 and described by (3.1)	24
Fig. 3.4 Simulated H-plane ($\phi=0^\circ$ plane) co-pol and cross-pol patterns of Model 1 shown in Fig. 3.1 and described by (3.1)	27
Fig. 3.5 (a) plot of E and H-planes' phase centre location (for a maximum tolerable phase difference $\Delta\phi=30^\circ$ and θ ranging from 0 to 60°) of Model 1 given in Fig. 3.1; (b) geometry of Model 1 indicating the portion of the antenna	30

axis where phase centre lies for both E and H planes

- Fig. 3.6 (a) plot of Average E and H-planes' phase centre location (for a maximum 31
tolerable phase difference $\Delta\phi=30^\circ$ and θ ranging from 0 to 60°) of Model
1 given in Fig. 3.1; (b) geometry of Model 1 indicating the portion of
antenna axis where these Average phase centres lie for both E and H
planes
- Fig. 3.7 The geometry of the Vivaldi antenna (Model 2) including the microstrip 32
feed along with the co-ordinate system: $L_s=22.86\text{mm}$, $W_s=38.10\text{mm}$, $L_c=$
 19.05mm , $W_m=0.81\text{mm}$, $W_a=14.73\text{mm}$, $D_s=3.30\text{mm}$, with $\epsilon_r=2.2$,
 $h=0.508\text{mm}$ and $\tan\delta=0.001$
- Fig. 3.8 Simulated (a) S_{11} and (b) input impedance plot measured with respect to 34
 $75\ \Omega$ for antenna Model 2 shown in Fig. 3.7 and described by (3.2)
- Fig. 3.9 Simulated E-plane ($\phi=90^\circ$ plane) co-pol and cross-pol patterns of Model 2 36
shown in Fig. 3.7 and described by (3.2)
- Fig.3.10 Simulated H-plane ($\phi=0^\circ$ plane) co-pol and cross-pol patterns of Model 2 40
shown in Fig. 3.7 and described by (3.2)
- Fig. 3.11 (a) plot of Average E and H-planes' phase centre location (for a 42
maximum tolerable phase difference $\Delta\phi=25^\circ$ and θ ranging from 0 to
 60°) of Model 2 given in Fig. 3.7; (b) geometry of Model 2 indicating
the portion of antenna axis where these Average phase centres lie for
both E and H planes
- Fig. 3.12 The geometry of the Vivaldi antenna (Model 3) including the microstrip 43
feed along with the co-ordinate system: $L_s=22.86\text{mm}$, $W_s=38.10\text{mm}$,
 $L_c=15.24\text{mm}$, $W_m=0.81\text{mm}$, $W_a=4.06\text{mm}$, $D_s=3.30\text{mm}$, with $\epsilon_r=2.2$,
 $h=0.508\text{mm}$ and $\tan\delta=0.001$

Fig. 3.13 Simulated (a) S_{11} and (b) input impedance plot measured with respect to 75Ω for antenna Model 3 shown in Fig. 3.12 and described by (3.3)	44
Fig. 3.14 Simulated E-plane ($\phi=90^\circ$ plane) co-pol and cross-pol patterns of Model 3 shown in Fig. 3.12 and described by (3.3)	47
Fig. 3.15 Simulated H-plane ($\phi=0^\circ$ plane) co-pol and cross-pol patterns of Model 3 shown in Fig. 3.12 and described by (3.3)	50
Fig. 3.16 (a) plot of Average E and H-planes' phase centre location (for a maximum tolerable phase difference $\Delta\phi=35^\circ$ and θ ranging from 0 to 60°) of Model 3 given in Fig. 3.12; (b) geometry of Model 3 indicating the portion of antenna axis where these Average phase centres lie for both E and H planes	52
Fig. 4.1 The geometry of the Vivaldi antenna (Model 4) including the microstrip feed along with the co-ordinate system: $L_s=22.86\text{mm}$, $W_s=38.10\text{mm}$, $L_c=16.51\text{mm}$, $W_m=0.81\text{mm}$, $W_a=13.72\text{mm}$, $D_s=3.30\text{mm}$, with $\epsilon_r=2.2$, $h=0.508\text{mm}$ and $\tan\delta=0.001$	55
Fig. 4.2 Simulated (a) S_{11} and (b) input impedance plot measured with respect to 75Ω for antenna Model 4 shown in Fig. 4.1 and described by (4.1)	56
Fig. 4.3 Simulated E-plane ($\phi=90^\circ$ plane) co-pol and cross-pol patterns of Model 4 shown in Fig. 4.1 and described by (4.1)	59
Fig. 4.4 Simulated H-plane ($\phi=0^\circ$ plane) co-pol and cross-pol patterns of Model 4 shown in Fig. 4.1 and described by (4.1)	62
Fig. 4.5 (a) plot of Average E and H-planes' phase centre location (for a maximum tolerable phase difference $\Delta\phi=30^\circ$ and θ ranging from 0 to 60°) of Model 4 given in Fig. 4.1; (b) geometry of Model 4 indicating the portion of antenna axis where these Average phase centres lie for both E and H	64

planes

- Fig. 4.6 The geometry of the Vivaldi antenna (Model 5) including the microstrip feed along with the co-ordinate system: $L_s=22.86\text{mm}$, $W_s=38.10\text{mm}$, $L_c=16.51\text{mm}$, $W_m=0.81\text{mm}$, $W_a=3.05\text{mm}$, $D_s=3.30\text{mm}$, with $\epsilon_r=2.2$, $h=0.508\text{mm}$ and $\tan\delta=0.001$ 65
- Fig. 4.7 Simulated (a) S_{11} and (b) input impedance plot measured with respect to $75\ \Omega$ for antenna Model 5 shown in Fig. 4.6 and described by (4.2) 66
- Fig. 4.8 Simulated E-plane ($\phi=90^\circ$ plane) co-pol and cross-pol patterns of Model 5 shown in Fig. 4.6 and described by (4.2) 69
- Fig. 4.9 Simulated H-plane ($\phi=0^\circ$ plane) co-pol and cross-pol patterns of Model 5 shown in Fig. 4.6 and described by (4.2) 72
- Fig. 4.10 (a) plot of Average E and H-planes' phase centre location (for a maximum tolerable phase difference $\Delta\phi=30^\circ$ and θ ranging from 0 to 60°) of Model 5 given in Fig. 4.6; (b) geometry of Model 5 indicating the portion of antenna axis where these Average phase centres lie for both E and H planes 74
- Fig. 4.11 The geometry of the Vivaldi antenna (Model 6) including the microstrip feed along with the co-ordinate system: $L_s=22.86\text{mm}$, $W_s=17.94\text{mm}$, $L_c=16.51\text{mm}$, $W_m=0.81\text{mm}$, $W_a=6.35\text{mm}$, $D_s=3.30\text{mm}$, with $\epsilon_r=2.2$, $h=0.508\text{mm}$ and $\tan\delta=0.001$ 75
- Fig. 4.12 Simulated (a) S_{11} and (b) input impedance plot measured with respect to $75\ \Omega$ for antenna Model 6 shown in Fig. 4.11 and described by (3.1) 77
- Fig. 4.13 Simulated E-plane ($\phi=90^\circ$ plane) co-pol and cross-pol patterns of Model 6 shown in Fig. 4.11 79

Fig. 4.14 Simulated surface current at 15 GHz on the copper cladding of Model 1 given in Fig. 3.1 and described by (3.1)	81
Fig. 4.15 Simulated surface current at 15 GHz on the copper cladding of Model 6 given in Fig. 4.11 and described by (3.1)	82
Fig. 4.16 Simulated H-plane ($\phi=0^\circ$ plane) co-pol and cross-pol patterns of Model 6 shown in Fig. 4.11	84
Fig. 4.17 (a) plot of Average E and H-planes' phase centre location (for a maximum tolerable phase difference $\Delta\phi=10^\circ$ and θ ranging from 0 to 60°) of Model 6 given in Fig. 4.11; (b) geometry of Model 6 indicating the portion of antenna axis where these Average phase centres lie for both E and H planes	86
Fig. 5.1 (a) Three dimensional view of balanced antipodal Vivaldi depicting the various layers (b) Front view of the antenna along with co-ordinate system: $L_s=22.86\text{mm}$, $W_s=17.94\text{mm}$, $L_c=16.51\text{mm}$, $W_a=6.35\text{mm}$ and described by (3.1) with $\epsilon_r=2.2$, height of each dielectric $h=0.508\text{mm}$ and $\tan\delta=0.001$	90
Fig. 5.2 Simulated (a) S_{11} and (b) input impedance plot measured with respect to $50\ \Omega$ for the balanced antipodal Vivaldi antenna shown in Fig. 5.1 and described by (3.1)	91
Fig. 5.3 Simulated E-plane ($\phi=90^\circ$ plane) co-pol and cross-pol patterns of the balanced antipodal Vivaldi shown in Fig. 5.1 and described by (3.1)	94
Fig. 5.4 Simulated H-plane ($\phi=0^\circ$ plane) co-pol and cross-pol patterns of the balanced antipodal Vivaldi shown in Fig. 5.1 and described by (3.1)	97
Fig. 5.5 (a) plot of Average E and H-planes' phase centre location (for a maximum tolerable phase difference $\Delta\phi=15^\circ$ and θ ranging from -30 to 30°) of the balanced antipodal Vivaldi given in Fig. 5.1; (b) geometry of the antenna	99

indicating the portion of antenna axis where Average E and H-plane phase centres lie

- Fig. 5.6 Front view of the balanced antipodal Vivaldi antenna 2 along with co-ordinate system: $L_s=75.90\text{mm}$, $W_s=55.90\text{mm}$, $W_a=43\text{mm}$ and described by (5.1), with $\epsilon_r=2.5$, height of each dielectric $h=1.50\text{ mm}$ and $\tan\delta=0.001$ 101
- Fig. 5.7 Simulated (a) S_{11} and (b) input impedance plot measured with respect to $50\ \Omega$ for the balanced antipodal Vivaldi antenna 2 shown in Fig. 5.6 and described by (5.1) 102
- Fig. 5.8 Simulated E-plane ($\phi=90^\circ$ plane) co-pol and cross-pol patterns of the balanced antipodal Vivaldi antenna 2 shown in Fig. 5.6 and described by (5.1) 105
- Fig. 5.9 Simulated H-plane ($\phi=0^\circ$ plane) co-pol and cross-pol patterns of the balanced antipodal Vivaldi antenna 2 shown in Fig. 5.6 and described by (5.1) 108
- Fig. 5.10 Front view of the balanced antipodal Vivaldi with substrate elongation of 12.80mm along with co-ordinate system: $L_s=88.70\text{mm}$, $L_c=75.90\text{mm}$, $L_e=12.80\text{mm}$, $W_s=55.90\text{mm}$, $W_a=43\text{mm}$ and described by (5.1), with $\epsilon_r=2.5$, height of each dielectric $h=1.50\text{ mm}$ and $\tan\delta=0.001$ 111
- Fig. 5.11 Front view of the balanced antipodal Vivaldi with substrate elongation of 12.80mm along with co-ordinate system: $L_s=105.90\text{mm}$, $L_c=75.90\text{mm}$, $L_e=30\text{mm}$, $W_s=55.90\text{mm}$, $W_a=43\text{mm}$ and described by (5.1), with $\epsilon_r=2.5$, height of each dielectric $h=1.50\text{ mm}$ and $\tan\delta=0.001$ 114
- Fig. 5.12 (a) plot of Average E and H-planes' phase centre location (for a maximum tolerable phase difference $\Delta\phi=35^\circ$ and θ ranging from -30 to 30°) of the balanced antipodal Vivaldi given in Fig. 5.10; (b) geometry of the antenna indicating the portion of antenna axis where Average E 118

and H-plane phase centres lie

- Fig. 5.13 Comparison of the relative sizes of (a) the balanced antipodal Vivaldi given in Fig. 5.10 and (b) the balanced antipodal Vivaldi given in Fig. 5.1 119
- Fig. 5.14 Front view of the sharp tip substrate model along with co-ordinate system: $L_s=105.90\text{mm}$, $L_c=75.90\text{mm}$, $W_s=55.90\text{mm}$, $W_a=43\text{mm}$ and $L_t=41\text{mm}$ and described by (5.1), with $\epsilon_r=2.5$, height of each dielectric $h=1.50\text{ mm}$ and $\tan\delta=0.001$ 120
- Fig. 5.15 Front view of the curved substrate model along with co-ordinate system: $L_s=105.90\text{mm}$, $L_c=75.90\text{mm}$, $W_s=55.90\text{mm}$, $W_a=43\text{mm}$ and described by (5.1), with $\epsilon_r=2.5$, height of each dielectric $h=1.50\text{ mm}$ and $\tan\delta=0.001$ 123
- Fig. 5.16 Front view of the curved sharp tip substrate model along with co-ordinate system: $L_s=105.90\text{mm}$, $L_c=75.90\text{mm}$, $W_s=55.90\text{mm}$, $W_a=43\text{mm}$ and described by (5.1), with $\epsilon_r=2.5$, height of each dielectric $h=1.50\text{ mm}$ and $\tan\delta=0.001$ 126
- Fig. 6.1 (a) Photograph of the two dielectric substrates of the fabricated antenna showing the etched stripline to flare transition on one slab and the ground plane to flare transition on the other (b) Fabricated balanced antipodal Vivaldi antenna described by (5.1) with substrate elongation of 12.80mm , $L_s=88.70\text{mm}$, $L_c=75.90\text{mm}$, $W_s=55.90\text{mm}$ 132
- Fig. 6.2 Simulated and measured S_{11} patterns with respect to $50\ \Omega$ for the balanced antipodal Vivaldi shown in Fig. 5.10 and Fig. 6.1 respectively and described by (5.1) with $\epsilon_r=2.5$, $h=1.5\text{mm}$, $\tan\delta=0.001$. Other parameters are given in Fig. 6.1 133
- Fig. 6.3 Measured input impedance plot of the antenna in Fig. 6.1 with respect to $50\ \Omega$ on a substrate with $\epsilon_r=2.5$, $h=1.5\text{mm}$, $\tan\delta=0.001$. Other parameters 135

are given in Fig. 6.1

- Fig. 6.4 Picture of the fabricated balanced antipodal Vivaldi showing the mounting Position in the anechoic chamber for measuring E-plane radiation patterns 136
- Fig. 6.5 Picture of the fabricated balanced antipodal Vivaldi showing the mounting Position in the anechoic chamber for measuring H-plane radiation patterns 136
- Fig. 6.6 Simulated and measured E-plane ($\phi=90^\circ$ plane) radiation patterns of the balanced antipodal Vivaldi given in Fig. 5.10 and Fig. 6.1 respectively with $\epsilon_r=2.5$, $h=1.5\text{mm}$, $\tan\delta=0.001$. Other parameters are given in Fig. 6.1 143
- Fig. 6.7 Simulated and measured H-plane ($\phi=0^\circ$ plane) radiation patterns of the balanced antipodal Vivaldi given in Fig. 5.10 and Fig. 6.1 respectively with $\epsilon_r=2.5$, $h=1.5\text{mm}$, $\tan\delta=0.001$. Other parameters are given in Fig. 6.1 151
- Fig. 6.8 Geometry of the balanced antipodal Vivaldi with substrate elongation of 12.80mm indicating the portion of antenna axis where the simulated ($\Delta\phi=15^\circ$) and measured ($\Delta\phi=35^\circ$) H-plane phase centre lie; $d_{1m}=74.22\text{mm}$ $d_{2m}=80.75\text{mm}$, $d_{1s}=57\text{mm}$, $d_{2s}=90\text{mm}$. Dimensions of the antenna are given in Fig. 5.10 154

LIST OF TABLES

Table 3.1 Summary of E-plane co-pol pattern characteristics of Model 1 given in Fig. 3.1 and described by (3.1)	24
Table 3.2 Summary of E-plane cross-pol pattern characteristics of Model 1 given in Fig. 3.1 and described by (3.1)	25
Table 3.3 Summary of H-plane co-pol pattern characteristics of Model 1 given in Fig. 3.1 and described by (3.1)	28
Table 3.4 Summary of H-plane cross-pol pattern characteristics of Model 1 given in Fig. 3.1 and described by (3.1)	28
Table 3.5 Summary of E-plane co-pol pattern characteristics of Model 2 given in Fig. 3.7 and described by (3.2)	37
Table 3.6 Summary of E-plane cross-pol pattern characteristics of Model 2 given in Fig. 3.7 and described by (3.2)	37
Table 3.7 Summary of H-plane co-pol pattern characteristics of Model 2 given in Fig. 3.7 and described by (3.2)	40
Table 3.8 Summary of H-plane cross-pol pattern characteristics of Model 2 given in Fig. 3.7 and described by (3.2)	41
Table 3.9 Summary of E-plane co-pol pattern characteristics of Model 3 given in Fig. 3.12 and described by (3.3)	47
Table 3.10 Summary of E-plane cross-pol pattern characteristics of Model 3 given in Fig. 3.12 and described by (3.3)	48
Table 3.11 Summary of H-plane co-pol pattern characteristics of Model 3 given in Fig. 3.12 and described by (3.3)	51

Table 3.12 Summary of H-plane cross-pol pattern characteristics of Model 3 given in Fig. 3.12 and described by (3.3)	51
Table 4.1 Summary of E-plane co-pol pattern characteristics of Model 4 given in Fig. 4.1 and described by (4.1)	59
Table 4.2 Summary of E-plane cross-pol pattern characteristics of Model 4 given in Fig. 4.1 and described by (4.1)	60
Table 4.3 Summary of H-plane co-pol pattern characteristics of Model 4 given in Fig. 4.1 and described by (4.1)	63
Table 4.4 Summary of H-plane cross-pol pattern characteristics of Model 4 given in Fig. 4.1 and described by (4.1)	63
Table 4.5 Summary of E-plane co-pol pattern characteristics of Model 5 given in Fig. 4.6 and described by (4.2)	69
Table 4.6 Summary of E-plane cross-pol pattern characteristics of Model 5 given in Fig. 4.6 and described by (4.2)	70
Table 4.7 Summary of H-plane co-pol pattern characteristics of Model 5 given in Fig. 4.6 and described by (4.2)	73
Table 4.8 Summary of H-plane cross-pol pattern characteristics of Model 5 given in Fig. 4.6 and described by (4.2)	73
Table 4.9 Summary of E-plane co-pol pattern characteristics of Model 6 given in Fig. 4.11	80
Table 4.10 Summary of E-plane cross-pol pattern characteristics of Model 6 given in Fig. 4.11	80
Table 4.11 Summary of H-plane co-pol pattern characteristics of Model 6 given in	85

Fig. 4.11

Table 4.12 Summary of H-plane cross-pol pattern characteristics of Model 6 given in Fig. 4.11	85
Table 5.1 Summary of E-plane co-pol pattern characteristics of the balanced antipodal Vivaldi given in Fig. 5.1 and described by (3.1)	94
Table 5.2 Summary of E-plane cross-pol pattern characteristics of the balanced antipodal Vivaldi given in Fig. 5.1 and described by (3.1)	95
Table 5.3 Summary of H-plane co-pol pattern characteristics of the balanced antipodal Vivaldi given in Fig. 5.1 and described by (3.1)	98
Table 5.4 Summary of H-plane cross-pol pattern characteristics of the balanced antipodal Vivaldi given in Fig. 5.1 and described by (3.1)	98
Table 5.5 Summary of E-plane co-pol pattern characteristics of the balanced antipodal Vivaldi antenna 2 given in Fig. 5.1 and described by (5.1)	105
Table 5.6 Summary of E-plane cross-pol pattern characteristics of the balanced antipodal Vivaldi given in Fig. 5.1 and described by (5.1)	106
Table 5.7 Summary of H-plane co-pol pattern characteristics of the balanced antipodal Vivaldi given in Fig. 5.1 and described by (5.1)	109
Table 5.8 Summary of H-plane cross-pol pattern characteristics of the balanced antipodal Vivaldi given in Fig. 5.1 and described by (5.1)	109
Table 5.9 Summary of E-plane co-pol pattern characteristics of the balanced antipodal Vivaldi with substrate elongation of 12.80mm given in Fig. 5.10	112
Table 5.10 Summary of E-plane cross-pol pattern characteristics of the balanced	112

antipodal Vivaldi with substrate elongation of 12.80mm given in
Fig. 5.10

Table 5.11 Summary of H-plane co-pol pattern characteristics of the balanced antipodal Vivaldi with substrate elongation of 12.80mm given in Fig. 5.10	113
Table 5.12 Summary of H-plane cross-pol pattern characteristics of the balanced antipodal Vivaldi with substrate elongation of 12.80mm given in Fig. 5.10	113
Table 5.13 Summary of E-plane co-pol pattern characteristics of the balanced antipodal Vivaldi with substrate elongation of 30mm given in Fig. 5.11	115
Table 5.14 Summary of E-plane cross-pol pattern characteristics of the balanced antipodal Vivaldi with substrate elongation of 30mm given in Fig. 5.11	115
Table 5.15 Summary of H-plane co-pol pattern characteristics of the balanced antipodal Vivaldi with substrate elongation of 30mm given in Fig. 5.11	116
Table 5.16 Summary of H-plane cross-pol pattern characteristics of the balanced antipodal Vivaldi with substrate elongation of 30mm given in Fig. 5.11	116
Table 5.17 Summary of E-plane co-pol pattern characteristics of the sharp tip substrate model given in Fig. 5.14	121
Table 5.18 Summary of E-plane cross-pol pattern characteristics of the sharp tip substrate model given in Fig. 5.14	121
Table 5.19 Summary of H-plane co-pol pattern characteristics of the sharp tip substrate model given in Fig. 5.14	122
Table 5.20 Summary of H-plane cross-pol pattern characteristics of the sharp tip substrate model given in Fig. 5.14	122

Table 5.21 Summary of E-plane co-pol pattern characteristics of the curved tip substrate model given in Fig. 5.15	124
Table 5.22 Summary of E-plane cross-pol pattern characteristics of the curved tip substrate model given in Fig. 5.15	124
Table 5.23 Summary of H-plane co-pol pattern characteristics of the curved tip substrate model given in Fig. 5.15	125
Table 5.24 Summary of H-plane cross-pol pattern characteristics of the sharp tip substrate model given in Fig. 5.15	125
Table 5.25 Summary of E-plane co-pol pattern characteristics of the curved sharp tip substrate model given in Fig. 5.16	127
Table 5.26 Summary of E-plane cross-pol pattern characteristics of the curved sharp tip substrate model given in Fig. 5.16	127
Table 5.27 Summary of H-plane co-pol pattern characteristics of the curved sharp tip substrate model given in Fig. 5.16	128
Table 5.28 Summary of H-plane cross-pol pattern characteristics of the curved sharp tip substrate model given in Fig. 5.16	128
Table 6.1 Summary of the simulated and measured E-plane co-pol pattern characteristics of the balanced antipodal Vivaldi given in Fig. 5.10 and Fig. 6.1 respectively	144
Table 6.2 Summary of the simulated and measured E-plane cross-pol pattern characteristics of the balanced antipodal Vivaldi given in Fig. 5.10 and Fig. 6.1 respectively	144
Table 6.3 Summary of the simulated and measured H-plane co-pol pattern characteristics of the balanced antipodal Vivaldi given in Fig. 5.10 and	152

Fig. 6.1 respectively

Table 6.4 Summary of the simulated and measured H-plane cross-pol pattern characteristics of the balanced antipodal Vivaldi given in Fig. 5.10 and Fig. 6.1 respectively 152

CHAPTER 1

INTRODUCTION

1.1 Preface

The Vivaldi antenna is a member of the class of aperiodic, continuously scaled, end-fire traveling wave antenna structures and was first introduced by Gibson in 1979 [1]. It consists of an exponentially tapered flare, and at different frequencies, different parts of the antenna radiate, while the size of the radiating part is constant in wavelength. As such, it has a theoretically unlimited operating frequency range. However, this infinite operating bandwidth is limited due to certain practical factors such as feed to slotline transition, finite dimensions of the antenna etc. [2]. In practice, the Vivaldi antenna can provide multioctave operation and is therefore designated under the class of ultra-wide band (UWB) antennas. These antennas are used for several applications such as satellite communication systems, radio astronomy, microwave imaging, feeds for reflectors and wide-band phased array systems [3]. In all these applications, it is important to know the radiation characteristics of this antenna as well as its phase centre location. This thesis investigates the radiation characteristics and location of phase centre for two different types of Vivaldi antennas.

1.2 Literature Review

Increasing operating frequency and bandwidth required for commercial and military communication systems have been considered as the main drives for advances in ultra-wideband (UWB) technology [4]. UWB systems transmit extremely narrow pulses on the order of 1 nano second or less, resulting in bandwidths in excess of 1 GHz [5]. The applications of such antennas include satellite communication, remote sensing, microwave imaging, wide band scanning arrays and radio astronomy. In all these applications, there is a growing need for integrated technology, as fabrication of a large number of metal waveguide feeds is expensive and leads to feed clusters for antennas which have very appreciable weight [6].

To overcome these problems, planar antennas with end-fire radiation were introduced. The first of its kind was introduced by Lewis *et al.* in [7] where a stripline fed tapered notch antenna capable of multioctave bandwidths was presented. In [1] an exponentially tapered slot antenna, namely the Vivaldi was introduced by Gibson, which demonstrated a bandwidth of 8 to 40 GHz.

Many numerical methods of analysis have been used to study the performance of these tapered slot antennas. In [8] a moment method model was presented for the radiation characteristics of the tapered slot antenna. In [9] a FD-TD analysis of the Vivaldi antenna was carried out.

Extensive study on Vivaldi antennas has been carried out by Schaubert. Characteristics of tapered slot antennas in general were discussed in [3] and [6]. In [10] a thorough parametric study of stripline fed Vivaldi antenna arrays was presented in which the effects of substrate thickness, stripline/slotline transition, slot parameters and array

grid spacing was investigated. In [11], wideband Vivaldi arrays for large aperture antennas were studied and the method of interleaving two orthogonal single polarized arrays to form dual polarized arrays was introduced.

The bandlimiting effect of feed line to slotline transition was overcome by the introduction of the antipodal Vivaldi in [2] where a tapered transition from microstrip to symmetric double sided slot line exhibiting a very wide operating frequency range was presented. The very high cross-polarization exhibited by this antenna was overcome with the development of the balanced antipodal Vivaldi which was presented in [12].

Only a few papers dealing with the study of location of phase centre of the Vivaldi antenna have been published in the past. In [13] an approach to finding a 3-D phase center was presented. In [14] a method in which a dielectric rod was inserted into a Vivaldi antenna in order to minimize phase center variations was introduced. Results in [15] showed that the H-plane phase center was located near the feed of the antenna where as the E plane phase center was located toward the wider end of the slot and tended to move towards the feed with increase in frequency.

This thesis investigates the radiation characteristics and phase centre location of two different types of Vivaldi antennas. A parametric study of a single sided Vivaldi antenna of existing design is carried out from which a compact design is developed which exhibits a performance superior to that of the former. Using this compact design, a balanced antipodal Vivaldi is developed and it is seen to exhibit a commendable performance as well. In order to achieve a wider bandwidth of operation, a balanced antipodal Vivaldi with a larger aperture is studied. Elongation of substrate and shaping of substrate are found to be suitable methods for enhancement of the gain of this antenna

and several models implementing these techniques are presented. Lastly, experimental investigations are also carried out and it is seen that the measured far-field radiation patterns and phase centre location are in close agreement with the simulated results.

1.3 Structure of the Thesis

The thesis is divided into seven chapters. Chapter one gives an introduction and literature review on the topic and describes its overall goals. Chapter two gives a brief overview of tapered slot antennas which includes the various types and their feeding techniques. The Vivaldi antenna and its properties are discussed in detail and the definition of the term phase centre is also included in this chapter. A parametric study on the length of the flare of a single sided Vivaldi antenna is presented in chapter three. The simulated radiation patterns along with the location of phase centre for each model is discussed. In chapter four, another parametric study on the same antenna is presented in which the rate of taper of the flare is varied and corresponding simulated radiation patterns and phase centre locations are studied. The effect of truncation of width on the antenna performance is also studied and a compact design which has a better performance than those of the former designs is developed. From this compact design, a balanced antipodal Vivaldi antenna is developed and its radiation patterns and phase centre location are studied in chapter five. Also, a balanced antipodal Vivaldi antenna which exhibits a larger bandwidth than the previous is also modeled and the effect of elongation and substrate shaping on its gain is investigated. In chapter six, an experimental verification is presented in which a comparison is made between measured and simulated results of a fabricated balanced antipodal Vivaldi antenna whose dimensions are chosen from one of the models presented in chapter five. The location of

the phase centre of this fabricated antenna is studied and compared to the simulated results. Finally, the conclusion and future work are given in chapter seven.

CHAPTER 2

BRIEF OVERVIEW OF TAPERED SLOT ANTENNAS

2.1 Introduction

Tapered slot antennas (TSA) exhibit attractive features such as light weight, ease of fabrication by photo-etching, conformal installation and compatibility with microwave integrated circuits (MIC). A TSA consists of a tapered slot cut in a thin film of metal with or without an electrically thin substrate on one side of the film. The slot is narrow toward one end for efficient coupling to devices such as mixer diodes. Away from this region, the slot is tapered and a traveling wave propagating along the slot radiates in the end-fire direction [16].

The stripline fed tapered slot antenna was the first TSA to be introduced by Lewis *et al.* [7] in 1974. The linearly tapered slot antenna was introduced by Prasad and Mahapatra [17], in 1979, and shortly there after, Gibson [1] introduced the Vivaldi antenna. Many variations of these simple structures were later on fabricated by using standard printed circuit techniques, and the dimensional tolerances were easily maintained for operation at frequencies of up to 100 GHz and higher [3].

In this chapter a brief introduction to the various types of tapered slot antennas, their feeding methods and an overview of the Vivaldi is presented. The term 'phase centre' is defined and its significance in this thesis is also mentioned.

2.2 Tapered Slot Antennas (TSAs)

2.2.1 Characteristics of TSAs

Tapered slot antennas belong to the class of traveling-wave antennas of the ‘surface wave’ type [18] and radiate predominantly in the end-fire direction. Such antennas utilize a traveling-wave propagating along the antenna structure with a phase velocity $v_{ph} < c$ where c is the velocity of light in free space. The energy in the traveling wave is tightly bound to the conductors when the separation is very small compared to a free space wavelength and becomes progressively weaker and more coupled to the radiation field as the separation increases [1]. Surface wave antennas are slow wave antennas and generally produce end-fire radiation [19].

The major advantage of tapered slot antennas is that they are known to exhibit a good performance over a very wide bandwidth [20]. They have moderately high gain for a given cross section by virtue of their traveling-wave nature. They also offer qualities such as efficiency, light weight and geometric simplicity [6].

2.2.2 Taper Profiles

The three basic taper profiles of TSAs are linear taper (LTSA), constant width taper (CWSA) and non-linear taper (exponential, tangential and parabolic). Though they differ in taper profile of the slot (which is the main radiating region of these antennas), the basic radiation mechanism of all these antennas is similar. Fig. 2.1 depicts some of these taper profiles.

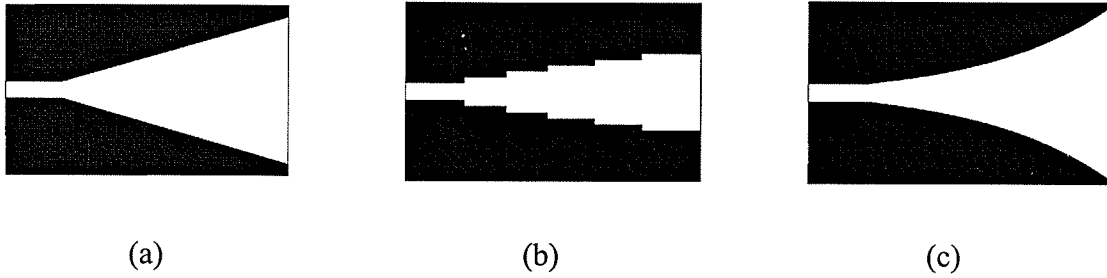


Fig. 2.1 Three basic taper profiles (a) Linear taper (b) Constant Width taper (c) Non-linear taper

These various taper profiles can be used in the fabrication of either single or double sided TSAs. Single sided TSAs are those in which a tapered slotline is etched on only one side of a dielectric slab. Double sided TSAs refer to antennas in which a tapered slotline is etched on both sides of the slab.

2.2.3 Feeding Techniques

Tapered slotline antennas can be fed by various techniques. The slotline section (radiating section) of the antenna is a balanced line, whereas the feed (such as a microstrip line or coaxial cable) is an unbalanced line. Hence, a proper transition section is required to act as a balun which translates the unbalanced feed to the balanced radiating section [21]. These transitions must be compact, easy to fabricate and have low loss. In practice, it has been observed that a very wideband transition is difficult to design and that it mainly affects the higher frequency limit of the antenna [22].

There are two types of transitions namely electromagnetically coupled transitions and directly coupled transitions. In electromagnetically coupled transitions, the coupling takes place through electromagnetic fields rather than through direct electrical contact. Examples of feeds which use such transitions are microstrip line, stripline, coplanar

waveguide, etc. The microstrip/stripline to slotline transition will be discussed in detail further on in this chapter. In directly coupled transitions, the coupling takes place through a direct current path. Examples of such feeds are coaxial cables, bond wires or ribbons [23].

2.3 The Vivaldi Antenna

2.3.1 Introduction

As previously mentioned, Gibson [1] proposed the Vivaldi antenna as a new member of the class of frequency independent antennas in 1979. It is an exponentially tapered slot antenna. At different frequencies, different sections of the exponentially tapered slot radiate efficiently and hence the Vivaldi antenna has theoretically infinite bandwidth [2]. In Fig. 2.2 a basic model of a Vivaldi antenna is shown.

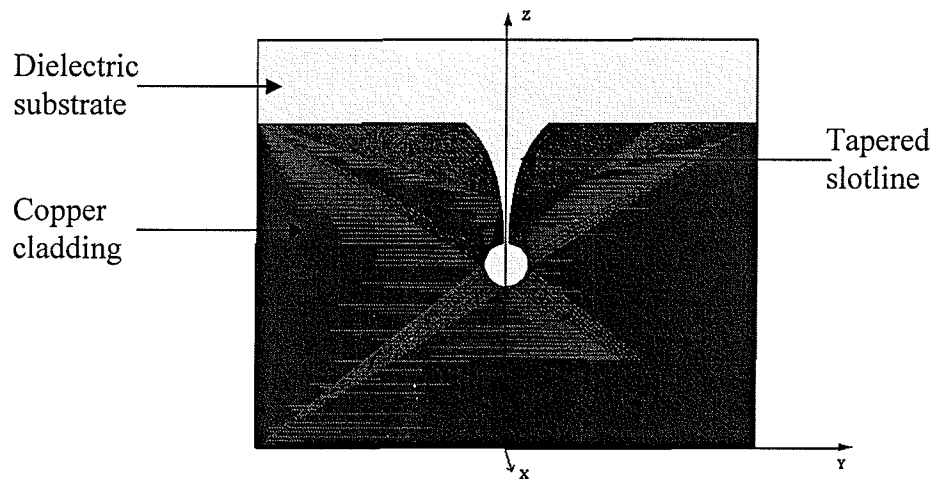


Fig. 2.2 Basic model of the Vivaldi antenna

Supposing the antenna shown in Fig. 2.2 is positioned in the y - z plane of a three dimensional Cartesian coordinate system, the general equation for the taper is given by the equation

$$y = \pm Ae^{pz} \quad (2.1)$$

The constant p dictates the gradualness of the exponential taper and is known as taper rate. The maximum separation between the slot line conductors, namely the aperture of the antenna, is equivalent to a free space half wavelength of the lowest frequency of operation. While the aperture size determines the lowest frequency of operation, the feed generally determines the highest frequency of operation of the antenna [21].

There are several variations in the design of this antenna namely; dielectric free, double sided and single sided. A dielectric free Vivaldi antenna, as the name itself implies, does not have any backing substrate and consists only of a tapered slot cut in a thin metal film. Double sided Vivaldi antennas consist of two copper-clad substrates bonded together with a stripline conductor in the middle and ground planes having flared slots on the outer surfaces [24]. Single sided Vivaldi antennas consist of one substrate with a ground plane on one side and a microstrip line conductor on the other. The microstrip to slotline transition of a single sided Vivaldi antenna will be discussed in detail in the next section.

Two other types of Vivaldi antennas which cannot be classified under any of the three previously mentioned categories are the antipodal Vivaldi antenna and the balanced antipodal Vivaldi antenna. They will be discussed in detail further on in this chapter.

2.3.2 Microstrip/Stripline to Slotline Transitions

Microstrip and stripline feeds are the most commonly used for single sided and double sided Vivaldi antennas respectively. The simplest broadband transition used is one in which the microstrip (or stripline) and the slotline cross each other at right angles. The slotline, which is etched on one side of the substrate, is crossed at a right angle by a microstrip conductor on the opposite side. If λ_m and λ_s are the lengths of the microstrip and slotline respectively in terms of wavelengths at a certain frequency of operation, then the microstrip line extends about $\lambda_m/4$ beyond the slot and similarly the slot extends about $\lambda_s/4$ beyond the microstrip. The transition can be fabricated using the usual photo-etching process and is thus easily reproducible [23]. Such a transition can be seen in Fig. 2.3.

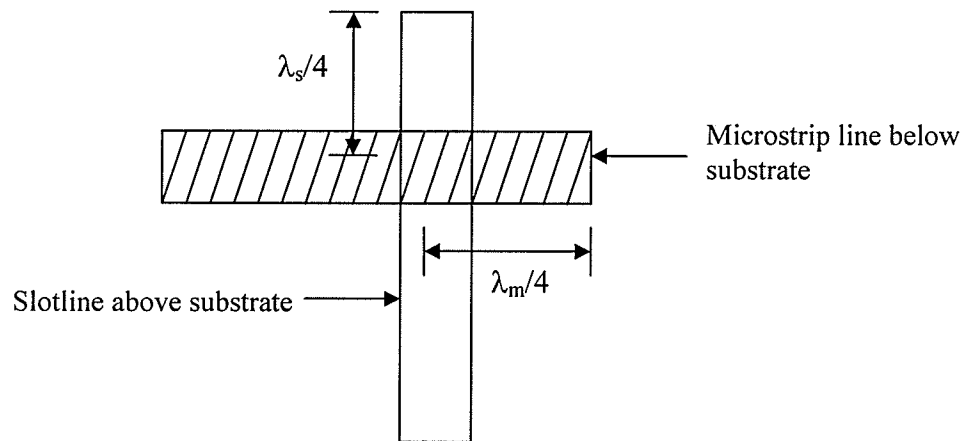


Fig. 2.3 Microstrip to slotline transition

Here λ_s and λ_m are the lengths of the slotline and microstrip respectively, in terms of wavelengths.

The microstrip line may be terminated by soldering it short or by using virtual shorts such as circular or radial stubs. Also, the slotline may be terminated by a circular

cavity which acts as an open circuit and facilitates radiation in the forward direction. It has been noticed that the bandwidth of a transition with a microstrip virtual short is always lower than the bandwidth of a transition with a soldered microstrip short. However, the bandwidth reduction is rather low and as virtual shorts may be easily fabricated completely by photolithographic techniques, they are generally preferred over soldered shorts [25]. Figure 2.4 shows a broadband transition in which a microstrip line terminated by a radial stub and a slotline with a circular cavity cross each other at right angles.

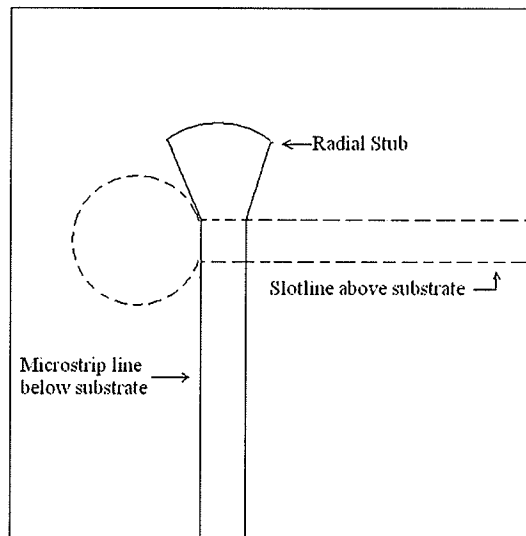


Fig. 2.4 Microstrip to slotline transition with radial stub

Stripline fed structures have three conductor layers. They comprise of two copper clad substrates with etched flares that are bonded together with a stripline in the middle. Stripline to slotline transitions are generally identical to those of microstrip to slotline transitions in which the stripline and slotline cross each other at right angles and extend

about quarter wavelengths beyond one another. Similar to microstrip lines, circular or radial stubs may be used to terminate stripline feeds as well.

2.3.3 Antipodal Vivaldi Antenna

Though microstrip (or stripline) feeds are commonly used, the slotline to feed line transition limits the broadband performance of the antenna. Another disadvantage is that a one sided slotline etched on a low dielectric constant substrate has a relatively high characteristic impedance which makes impedance matching to a microstrip feed line quite difficult. Also, the open feed line of a one sided Vivaldi may radiate and perturb the radiation pattern of the antenna [20]. To overcome all these problems, a new type of Vivaldi antenna, namely, the antipodal Vivaldi was proposed by Gazit [2].

If the feed transition is made as a collinear extension of the slot, then the band limiting effect is removed giving a very wide bandwidth of operation. In an antipodal Vivaldi antenna, one side of a dielectric substrate slab is etched to give a microstrip line which is then flared to produce one half of a conventional Vivaldi. On the other side, the ground plane is reduced to give a twin line. This is then flared in the opposite direction to the top, thus generating a Vivaldi antenna, but with wings on opposite sides of the substrate. The smooth microstrip to twin line to Vivaldi transition has very wide bandwidth capability and therefore the ultra-wide bandwidth potential of the antenna can be realized [12].

This antenna however, exhibits very high cross-polarization levels at high frequencies. The reason for such behavior and the method to overcome it is discussed in the next section. Figure 2.5 shows the basic geometry of an antipodal Vivaldi antenna.

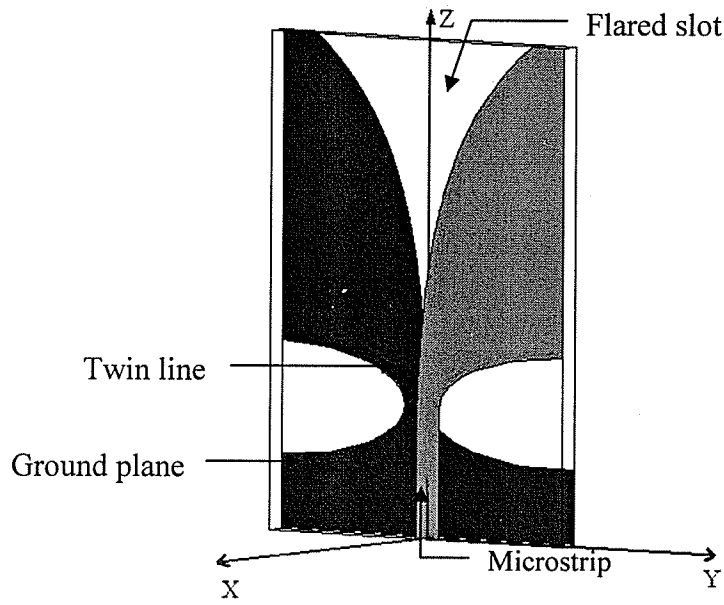


Fig. 2.5 Antipodal Vivaldi antenna

2.3.4 Balanced Antipodal Vivaldi Antenna

As mentioned in the previous section, the major drawback of the antipodal Vivaldi antenna is that it gives rise to very high levels of cross-polarization at high frequencies due to the skew in the slot fields close to the throat of the flare. Figure 2.6 is a cross sectional view of the top of the antipodal Vivaldi and it shows the skew in the E-field across the slot of the antenna.

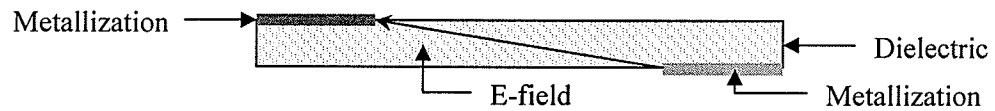


Fig. 2.6 Cross sectional view of the top of the antipodal Vivaldi depicting the E-field skew across the slot of the antenna

To overcome this problem, it is necessary to balance the currents on each radiating element and thereby negate the E-field skew. By applying another dielectric

layer and a further layer of metallization, a triplate or balanced antipodal Vivaldi antenna is formed as shown in Fig. 2.7.

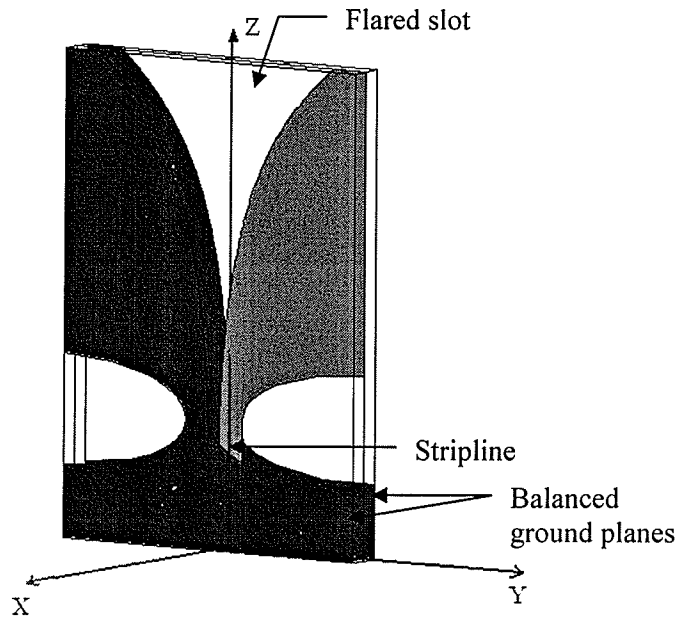


Fig. 2.7 Balanced antipodal Vivaldi antenna

In contrast to the antipodal Vivaldi, this antenna has a stripline feed to balanced twin line to balanced Vivaldi transition. But in common with the antipodal Vivaldi antenna, this feed arrangement is not band limited. With the addition of this balancing layer, the E-fields are no longer skewed as the resultant field is now parallel to the substrate at all frequencies as seen in Fig. 2.8. Hence, this antenna exhibits much better cross-polarization characteristics than the antipodal Vivaldi [12].

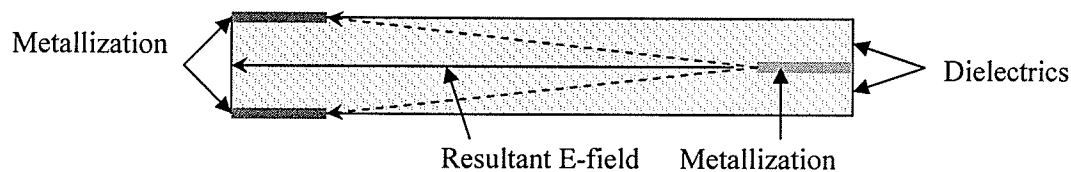


Fig. 2.8 Cross sectional view of the top of the balanced antipodal Vivaldi depicting the resultant E-field across the slot of the antenna

2.4 Phase Centre

The term ‘phase centre’ has been defined by IEEE standard 145-1993 as ‘the location of a point associated with an antenna such that, if it is taken as the centre of a sphere whose radius extends into the far-field, the phase of a given field component over the surface of the radiation sphere is essentially constant, at least over that portion of the surface where the radiation is significant’ [26].

A few studies on the location of the phase centre for various Vivaldi antenna geometries have been published in the past. These publications were discussed in brief in section 1.2 of chapter one. Most of the previous studies confirm that a fixed phase centre for both E and H-planes does not exist and also that its location varies with frequency.

In this thesis, we have studied the location of the phase centre along the axis of the Vivaldi which is aligned with the z -axis of the coordinate system. The study was mainly carried out for the models presented in chapters three and four as well as for one of the models presented in chapter five. In chapter six, the H-plane phase centre location for a fabricated antenna was determined.

2.5 Summary

In this chapter, an introduction to tapered slot antennas, their characteristics, taper types, and feeding techniques were presented. Specifically, the Vivaldi antenna and its concepts were introduced and the microstrip/stripline to slotline transition was described in detail. The term ‘antenna phase centre’ based on IEEE standards was defined and its significance in this thesis was mentioned.

CHAPTER 3

PARAMETRIC STUDY OF VIVALDI ANTENNA –I

3.1 Introduction

In this chapter a parametric study of a Vivaldi antenna based on the model presented by Thiele and Taflove in [9] is carried out. The model presented in [9] however, is a double sided stripline fed Vivaldi, whereas the models studied in this chapter and the next are all single sided microstrip line fed Vivaldis. All three models under investigation in this chapter share the same equation to describe their exponential tapers. Simulations were carried out by using a finite element method design and analysis package, Ansoft HFSS v 10.1. The simulated return loss and far-field radiation patterns of each model are plotted for a frequency range of 6 to 20 GHz. The location of the phase centre, represented as the distance d (in mm) from the starting of the slotline is also studied for all three models.

3.2 Original Model (Model 1)

3.2.1 Antenna Model

The first model (Model 1) under investigation is given in Fig. 3.1. In order to reduce computation time, the length of the antenna was truncated by 27.94 mm. It was verified that this truncation did not cause any change in the radiation patterns of the antenna. The dielectric substrate used in the simulations of all six models of this chapter and the next was Duroid 5880 with $\epsilon_r = 2.2$, height $h = 0.508$ mm and $\tan\delta = 0.001$.

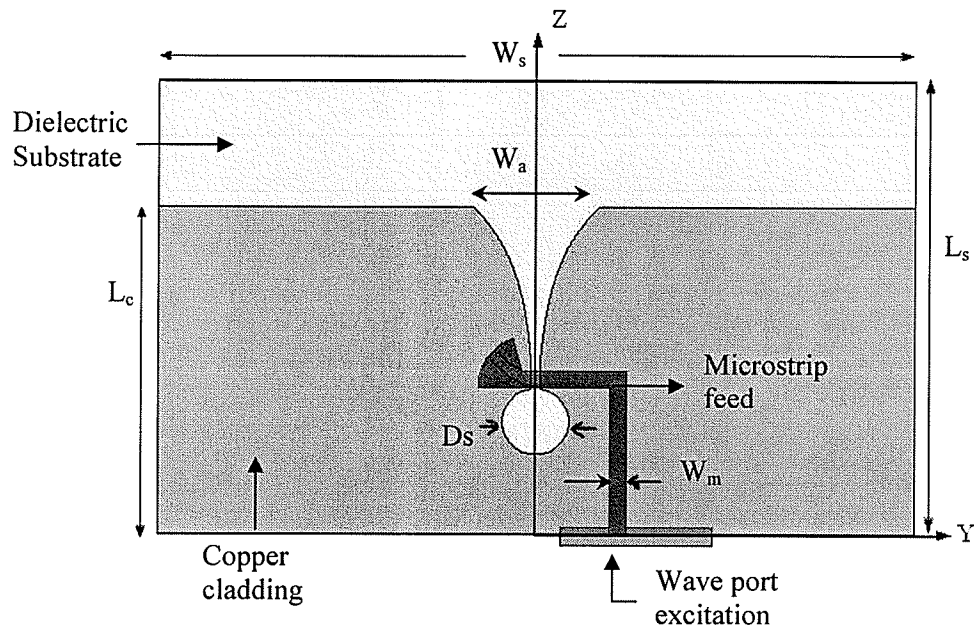


Fig. 3.1 The geometry of the Vivaldi antenna (Model 1) including the microstrip feed along with the co-ordinate system: $L_s = 22.86\text{mm}$, $W_s = 38.10\text{mm}$, $L_c = 16.51\text{mm}$, $W_m = 0.81\text{mm}$, $W_a = 6.35\text{mm}$, $D_s = 3.30\text{mm}$, with $\epsilon_r = 2.2$, $h = 0.508\text{mm}$ and $\tan\delta = 0.001$

It can be observed from Fig. 3.1 that the antenna axis is aligned with the z -axis of the coordinate system. The antenna flare is identical to that in [9] and its equation is

$$y = \pm 0.254e^{(0.33(z-8.9))}, \quad 8.90\text{mm} \leq z \leq 16.51\text{mm} \quad (3.1)$$

A microstrip to slotline transition as described in the previous chapter was used as the feeding technique for this antenna. The feed line is actually on the bottom side of the substrate, but is made visible in Fig. 3.1 for a better understanding of its geometry. Its characteristic impedance was found to be 75Ω based on the relative permittivity and height of the dielectric substrate.

The microstrip feed line was excited by using a wave port as shown in Fig. 3.1. Ansoft HFSS assumes that the defined wave port is connected to a semi-infinitely long waveguide that has the same cross section and material properties as the port.

3.2.2 Antenna Performance

As previously mentioned, the simulations were performed over a frequency range of 6 to 20 GHz (a bandwidth slightly greater than 3:1) using Ansoft HFSS v 10.1. The simulated S_{11} and input impedance plots of Model 1 are given in Fig. 3.2 (a) and (b).

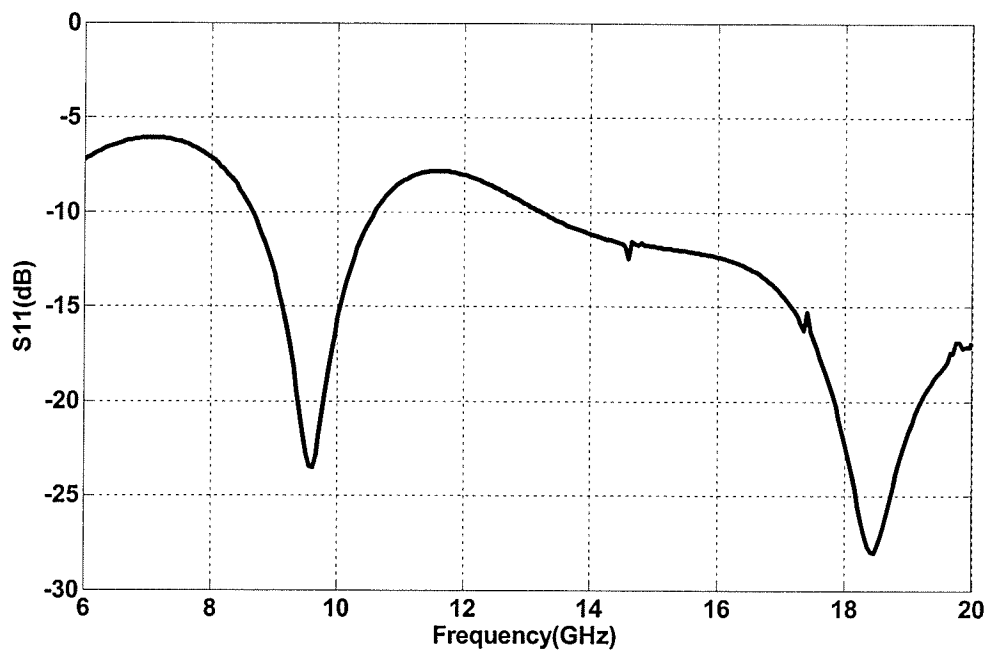


Fig. 3.2 (a)

Fig. 3.2 contd.

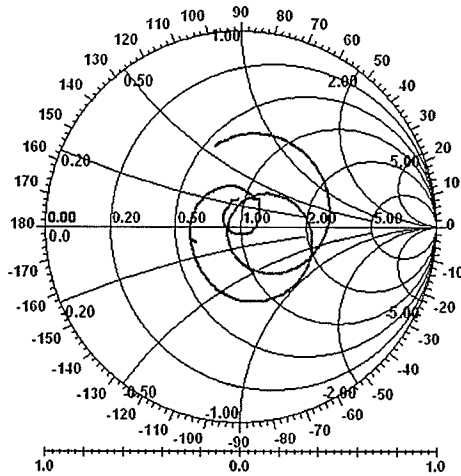


Fig. 3.2 (b)

Fig. 3.2 Simulated (a) S_{11} and (b) input impedance plot measured with respect to 75Ω for antenna Model 1 shown in Fig. 3.1 and described by (3.1)

From Fig. 3.2 (a) it can be seen that the antenna has a reasonably good performance over the entire frequency band under consideration. The discrepancy in S_{11} at the lower end of the frequency band in the return loss plot of Fig. 3.2 (a) is due to the band limiting effect of the microstrip to slotline transition of the antenna as mentioned in the previous chapter. In the Smith chart of Fig. 3.2 (b) it can be observed that the input impedance locus traces a loop, which represents the wide band property of this antenna. Also, the loop is located near the centre of the Smith chart which indicates proper matching between the feed line and excitation.

The co-pol and cross-pol radiation patterns in both principle planes were simulated for the 6 to 20 GHz range with a frequency step of 1 GHz. The plane in which the antenna is situated (yz plane, i.e. $\phi=90^\circ$ plane) is the E-plane and its perpendicular plane (xz plane, i.e. $\phi=0^\circ$ plane) is the H-plane of the antenna. The E-plane radiation patterns are given in Fig. 3.3. It is interesting to note that as frequency increases, the appearance of a null at boresight is observed for the E-plane co-pol patterns of this antenna. This null at boresight conforms to the patterns given in [9].

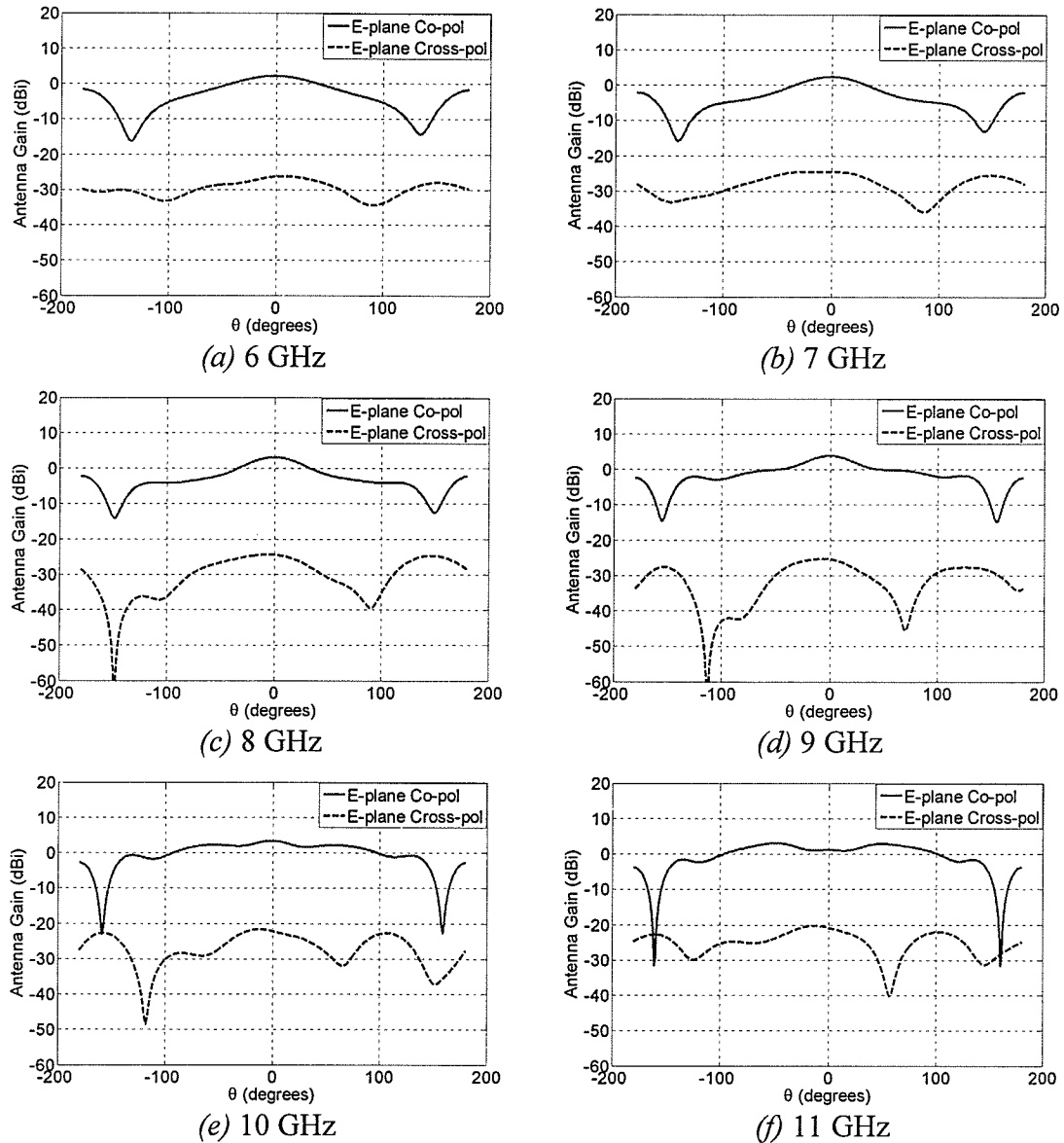


Fig. 3.3 (a)-(f)

Fig. 3.3 contd.

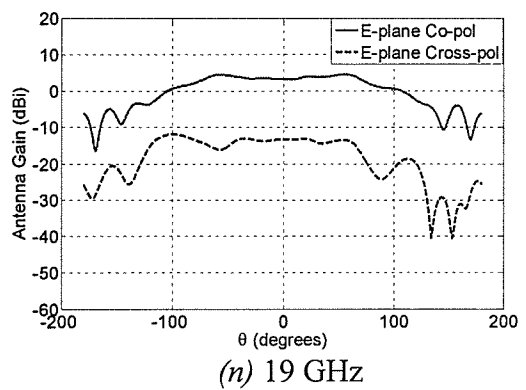
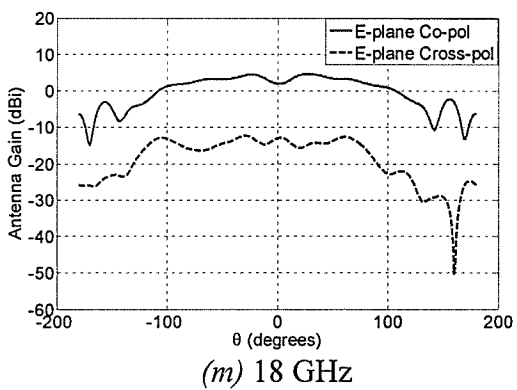
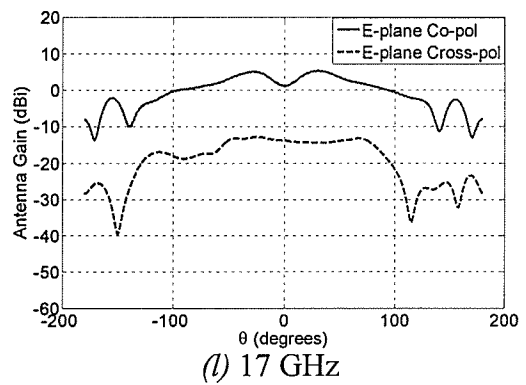
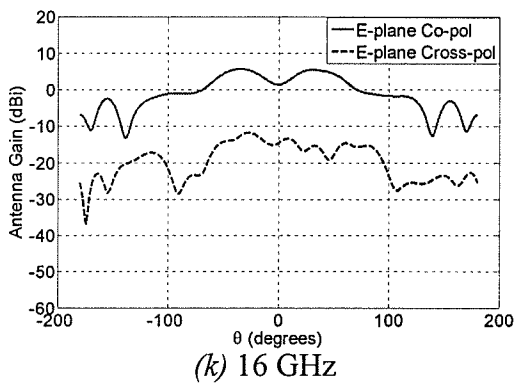
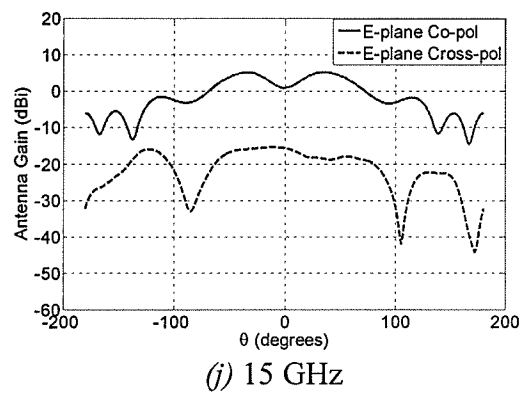
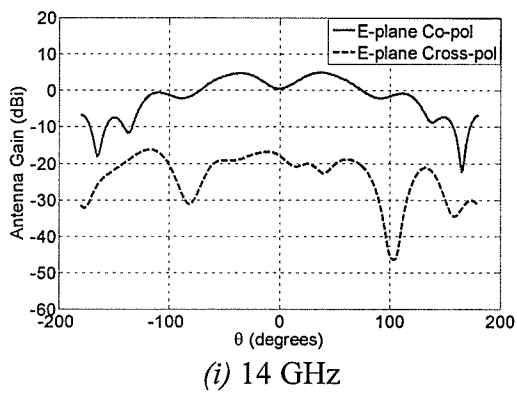
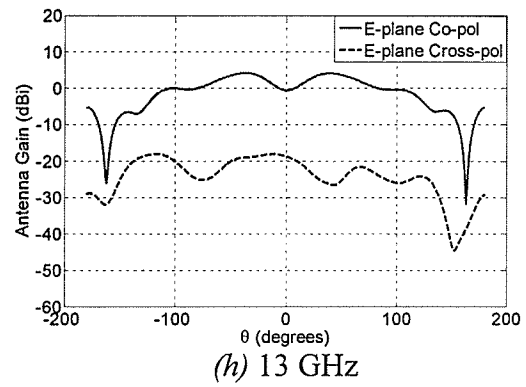
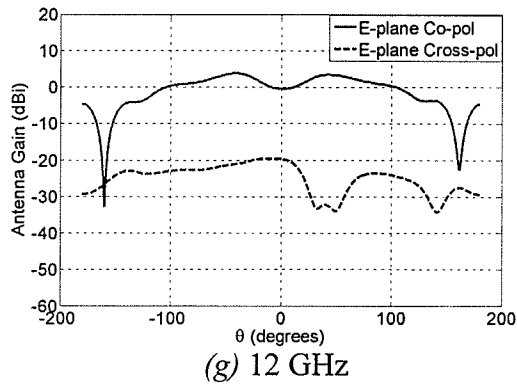


Fig. 3.3 (g)-(n)

Fig. 3.3 contd.

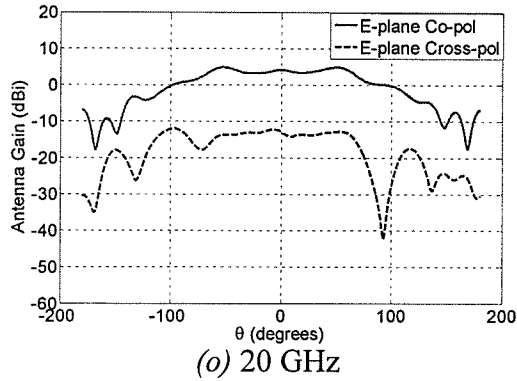


Fig. 3.3 Simulated E-plane ($\phi=90^\circ$ plane) co-pol and cross-pol patterns of Model 1 shown in Fig. 3.1 and described by (3.1)

In Tables 3.1 and 3.2 a summary of the important E-plane co-pol and cross-pol pattern characteristics (respectively) of Model 1 such as boresight and peak gains, 3 dB and 10 dB beamwidths (BW), boresight and peak cross-polarization, etc are given.

Frequency (GHz)	Boresight gain (dBi)	Peak gain (dBi)	Position of Peak gain	3 dB BW	10 dB BW
6	2.222	2.225	-1°	98°	228°
7	2.380	2.380	0°	77°	247°
8	3.130	3.130	0°	65°	271°
9	3.851	3.852	-1°	66°	289°
10	3.413	3.418	-1°	182°	300°
11	1.197	3.091	-49°	226°	306°
12	1.310	3.766	-44°	230°	304°
13	0.549	4.474	-41°	241°	306°
14	0.356	5.083	-38°	246°	312°
15	0.591	5.737	-35°	177°	322°
16	1.026	5.843	-32°	210°	276°
17	1.525	5.456	31°	227°	270°
18	1.890	4.937	29°	135°	276°
19	2.696	4.825	53°	221°	282°
20	3.603	5.478	49°	176°	283°

Table 3.1 Summary of E-plane co-pol pattern characteristics of Model 1 given in Fig. 3.1 and described by (3.1)

Frequency (GHz)	Boresight Cross-pol (dBi)	Peak Cross-pol (dBi)	Position of Peak Cross-pol
6	-26.218	-26.132	7°
7	-24.550	-24.447	-25°
8	-24.423	-24.355	-6°
9	-25.405	-25.284	-7°
10	-22.164	-21.651	-13°
11	-20.772	-20.209	-13°
12	-21.124	-20.867	-11°
13	-19.257	-18.728	-13°
14	-17.241	-16.735	-17°
15	-16.147	-15.736	-13°
16	-14.072	-12.915	-17°
17	-13.093	-12.083	-18°
18	-13.811	-13.031	-16°
19	-13.239	-11.067	-102°
20	-13.357	-12.055	-99°

Table 3.2 Summary of E-plane cross-pol pattern characteristics of Model 1 given in Fig. 3.1 and described by (3.1)

From Table 3.1 it can be seen that the antenna has a very moderate peak gain ranging from 2.2 to 5.8 dBi. Also, peak gain does not occur at boresight for most of the cases due to the occurrence of null at boresight with increase in frequency. It can be observed that the antenna has very wide 3 dB and 10 dB beamwidths. The cross-pol levels seem to increase with increase in frequency of operation as seen from Table 3.2.

The H-plane (xz plane, i.e. $\phi = 0^\circ$ plane) radiation patterns are given in Fig. 3.4.

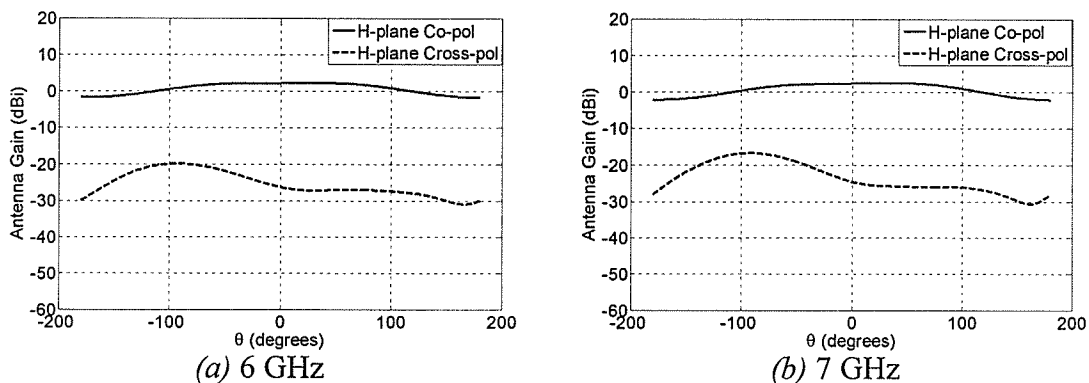


Fig. 3.4 (a), (b)

Fig. 3.4 contd.

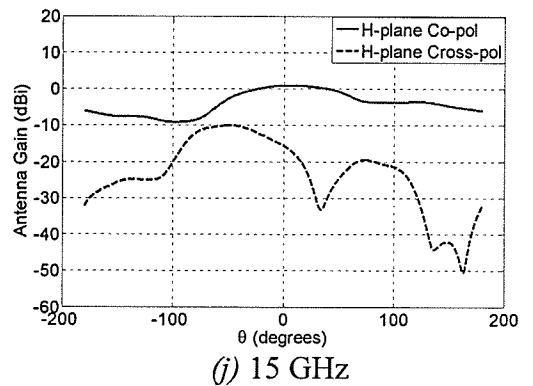
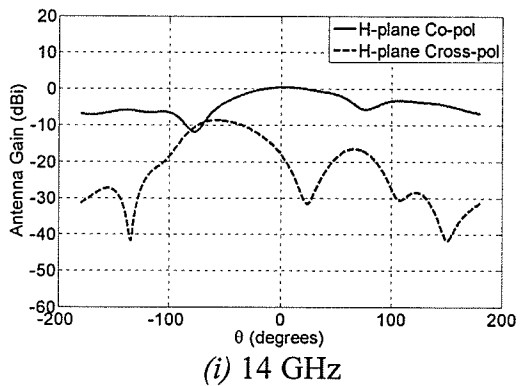
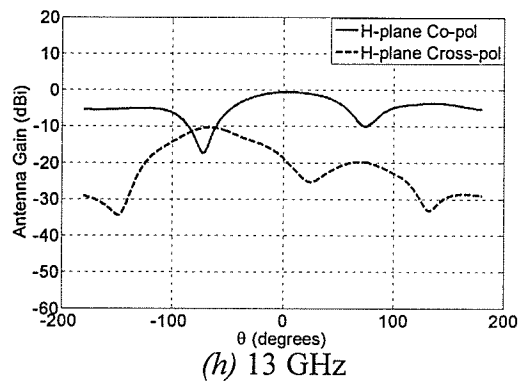
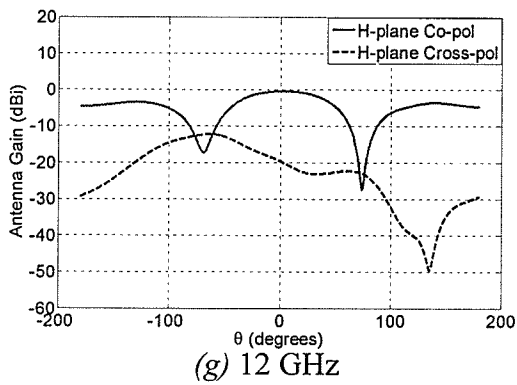
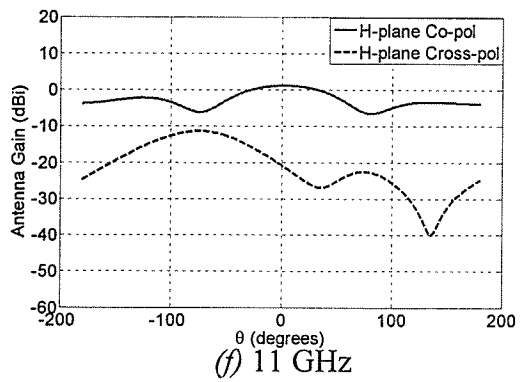
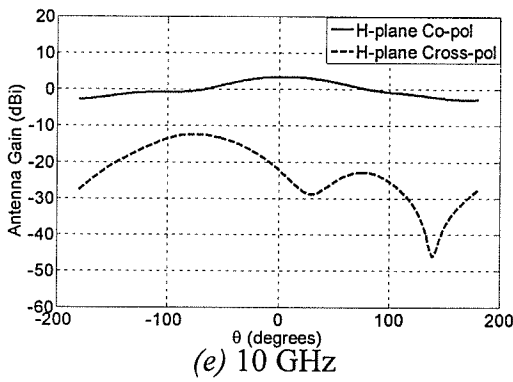
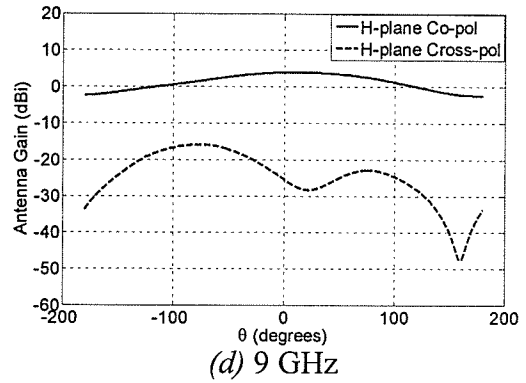
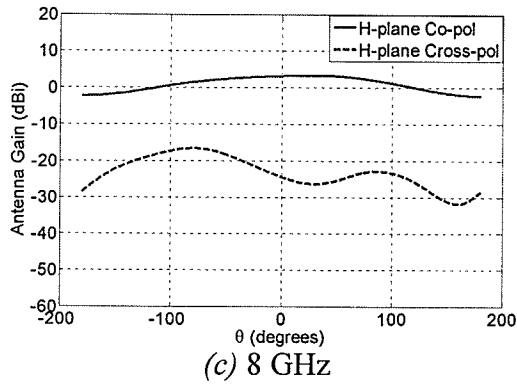


Fig. 3.4 (c)-(j)

Fig. 3.4 contd.

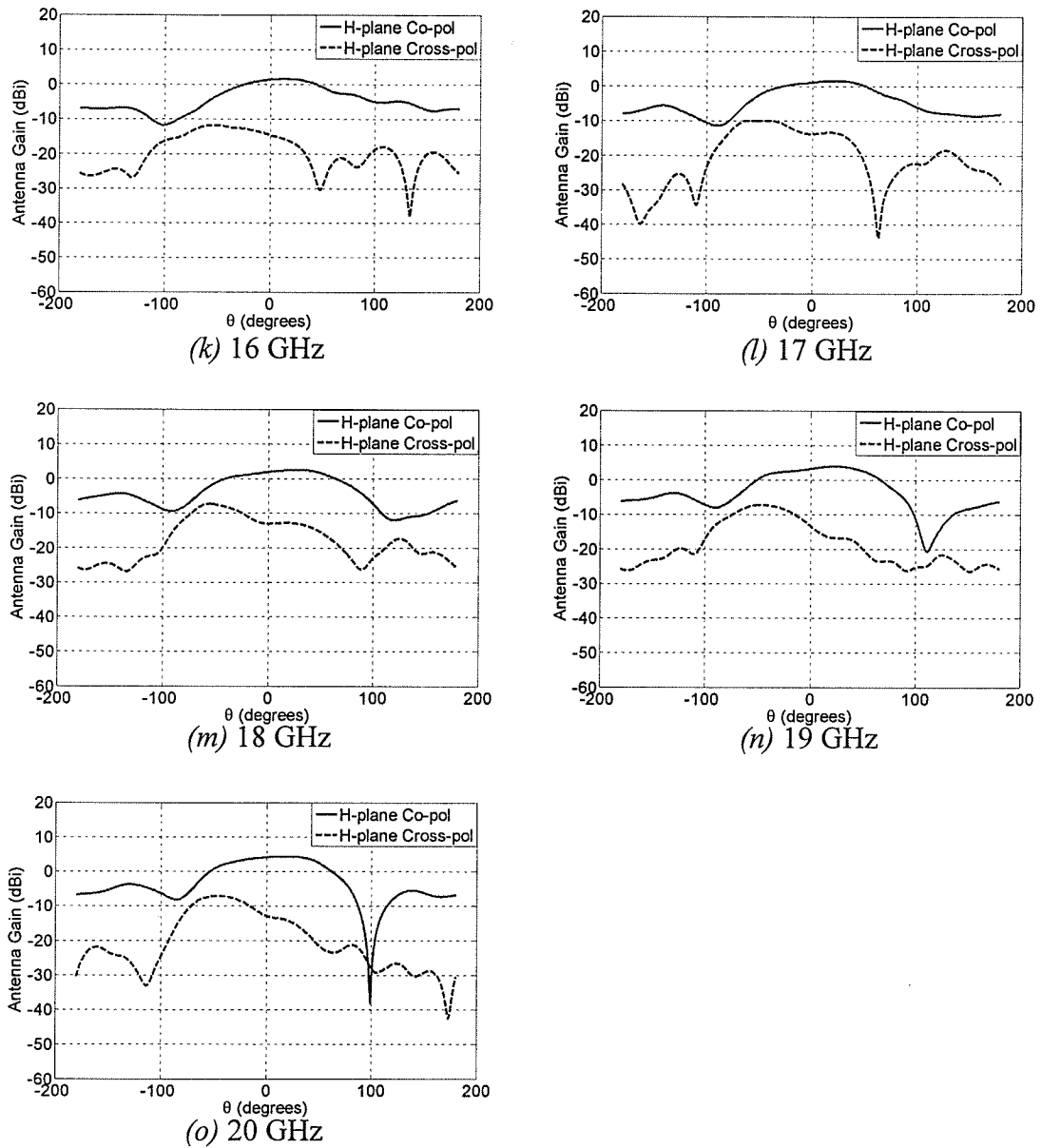


Fig. 3.4 Simulated H-plane ($\phi=0^\circ$ plane) co-pol and cross-pol patterns of Model 1 shown in Fig. 3.1 and described by (3.1)

A summary of the H-plane co-pol and cross-pol patterns characteristics are given in Tables 3.3 and 3.4 respectively.

Frequency (GHz)	Boresight gain (dBi)	Peak gain (dBi)	Position of Peak gain	3 dB BW	10 dB BW
6	2.222	2.295	32°	268°	--
7	2.380	2.522	35°	251°	--
8	3.130	3.282	30°	127°	--
9	3.851	3.891	12°	199°	--
10	3.413	3.429	5°	133°	--
11	1.197	1.204	3°	91°	--
12	1.310	1.345	6°	83°	142°
13	0.549	0.604	7°	90°	133°
14	0.356	0.436	8°	90°	--
15	0.591	0.718	11°	96°	--
16	1.026	1.210	14°	100°	--
17	1.525	1.703	13°	80°	235°
18	1.900	2.217	19°	109°	187°
19	2.696	2.985	19°	111°	178°
20	3.603	3.835	17°	114°	165°

Table 3.3 Summary of H-plane co-pol pattern characteristics of Model 1 given in Fig. 3.1 and described by (3.1)

Frequency (GHz)	Boresight Cross-pol (dBi)	Peak Cross-pol (dBi)	Position of Peak Cross-pol
6	-26.218	-19.908	-93°
7	-24.550	-16.758	-92°
8	-24.423	-16.596	-80°
9	-25.405	-15.879	-76°
10	-22.164	-12.343	-76°
11	-20.772	-11.348	-75°
12	-21.124	-11.502	-79°
13	-19.257	-11.076	-66°
14	-17.241	-10.239	-56°
15	-16.147	-9.226	-53°
16	-14.072	-9.225	-57°
17	-13.093	-9.233	-53°
18	-13.811	-7.893	-58°
19	-13.239	-6.294	-52°
20	-13.357	-6.329	-48°

Table 3.4 Summary of H-plane cross-pol pattern characteristics of Model 1 given in Fig. 3.1 and described by (3.1)

The blanks left at certain frequencies for 10 dB beamwidth of co-pol pattern is an indication that the gain did not fall 10 dB off boresight and hence the 10 dB beamwidth for such patterns could not be calculated.

3.2.3 Study of Phase Centre

The far field E and H-plane co-pol phase patterns of the antenna are not constant and change over the angles off the main beam axis. This means that the origin of the coordinate system is not located at the phase centre of the antenna. In order to find the phase centre location on the antenna axis, the antenna may be displaced along the z -axis of the coordinate system with respect to the origin, such that at this new location, the far field phase pattern is essentially constant.

As previously explained, the radiation from the Vivaldi antenna originates from various locations of its tapered slotline. Hence the starting of the slotline was chosen as the reference point for the study of the location of the phase centre for all the antenna models presented in this thesis. Here, the two principle planes' (E and H-planes) far field co-pol phase patterns were studied in the 6 to 20 GHz frequency range (with one GHz steps) for an angle off main beam axis θ ranging from 0 to 60°. At every considered frequency, the phase centre for each principle plane was located at a distance d from the starting of the slotline. It is important to mention that a completely constant far field phase pattern could not be achieved, and hence, the phase centre was identified as that location on the antenna axis at which the phase difference between any two points (in the mentioned angle off main beam axis range) of the far field copol phase pattern constrained to a specified maximum tolerable phase difference $\Delta\phi$. For every model, it was found that the phase centre location at each frequency (in either of the two principle

planes) did not confine itself to a fixed point on the antenna axis, but rather it was found to lie over a portion of the antenna axis.

Figure 3.5 (a) is a plot which depicts the lower and upper ends of the portion of the antenna axis of Model 1 where the phase centre was found to be situated for both principle planes for a maximum tolerable phase difference $\Delta\phi$ of 30° . The starting of the slotline is at a distance of 8.89 mm from the bottom of the antenna. This is taken as the reference point (i.e., 0 mm), and the phase centre locations are denoted as a distance d in mm from this reference. The lower end of the portion in each principle plane (at every frequency) is denoted as E_{min} (i.e., E-plane minimum) and H_{min} (i.e. H-plane minimum) while the upper end of the portion is denoted as E_{max} (i.e., E-plane maximum) and H_{max} (i.e., H-plane maximum). Figure 3.5 (b) shows the location of the phase centre in both principle planes on the antenna geometry.

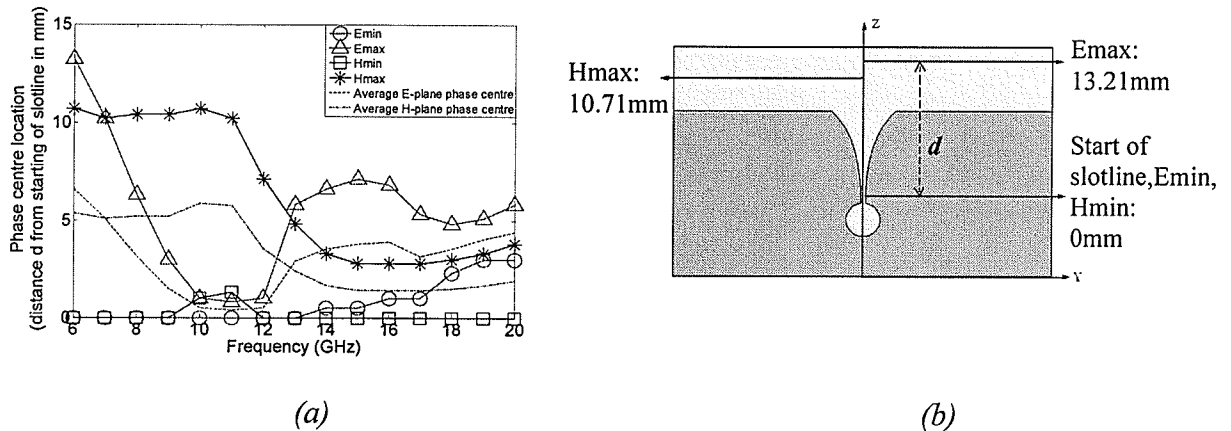


Fig. 3.5 (a) plot of E and H planes' phase centre location (for a maximum tolerable phase difference $\Delta\phi=30^\circ$ and θ ranging from 0 to 60°) of Model 1 given in Fig. 3.1; (b) geometry of Model 1 indicating the portion of antenna axis where phase centre lies for both E and H planes

As the phase centre was situated over a portion of the antenna axis as opposed to a particular point, the average of the E-plane maximum and minimum at each respective frequency was calculated in order to get a sense of the phase centre location point on an average on the antenna axis. This was carried out for the H-plane maximum and minimum at each respective frequency as well. These averages (at each frequency) are denoted as Average E-plane phase centre and Average H-plane phase centre respectively. A trace of these locations for both planes is shown in Fig. 3.5 (a). Figure 3.6 (a) shows a plot of the Average E and H-plane phase centre locations at each frequency and Fig. 3.6 (b) depicts these locations on the antenna geometry. AEmin and AEmax denote the Average E-plane the minimum and maximum phase centre locations respectively. Similarly AHmin and AHmax denote the Average H-plane minimum and maximum phase centres respectively.

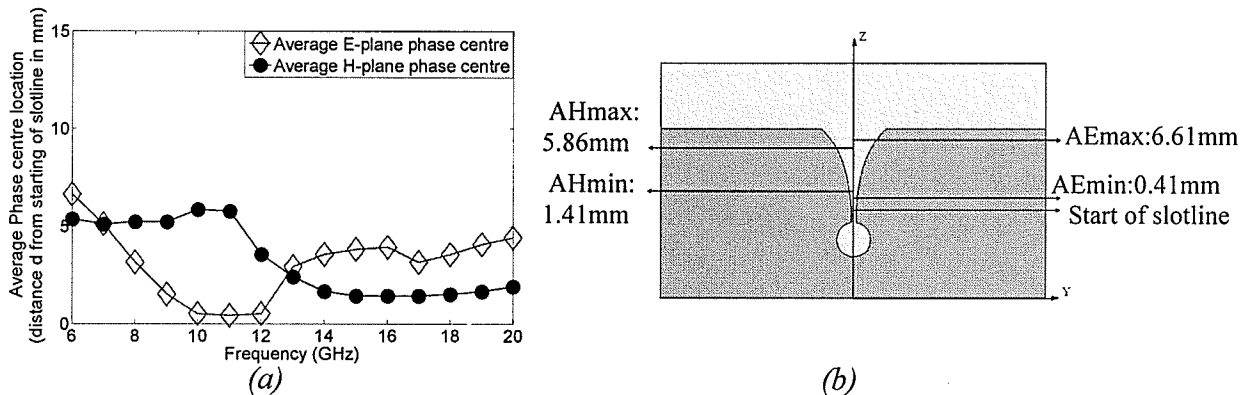


Fig. 3.6 (a) plot of Average E and H planes' phase centre location (for a maximum tolerable phase difference $\Delta\phi=30^\circ$ and θ ranging from 0 to 60°) of Model 1 given in Fig. 3.1; (b) geometry of Model 1 indicating the portion of antenna axis where these Average phase centres lie for both E and H planes

From Fig. 3.6 (a) it can be seen that the Average E-plane phase centre location on the antenna axis of Model 1 are quite stable in the 14 to 20 GHz range while the Average H-

plane phase centre is stable in the 6 to 10 GHz range as well as the 14 to 20 GHz range. Also, it can be observed that the maximum distance between the Average E-plane phase centre and Average H-plane phase centre is 5.45 mm.

3.3 Extended Flare Model (Model 2)

3.3.1 Antenna Model

The second model under study (Model 2) can be seen in Fig. 3.7. The dimensions of this model are identical to that of Model 1, as is the equation describing its exponential taper except that the length of the flare was increased by 2.54 mm.

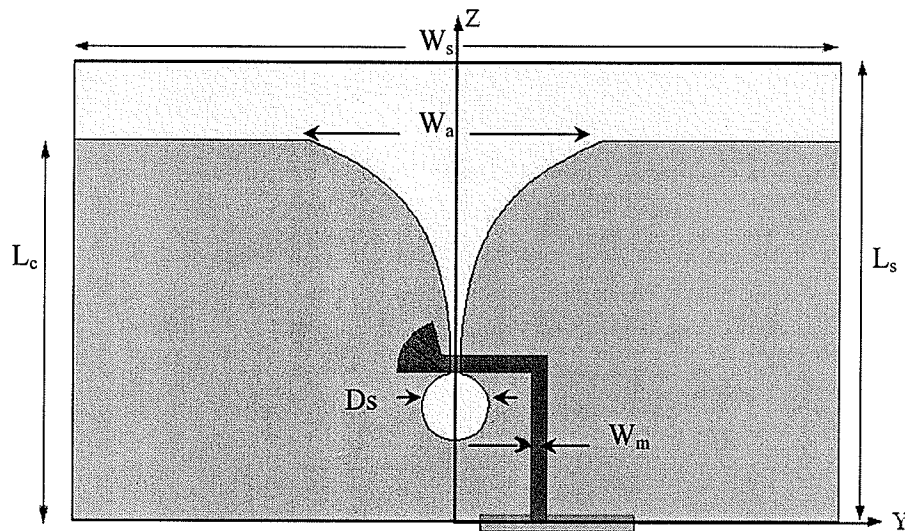


Fig. 3.7 The geometry of the Vivaldi antenna (Model 2) including the microstrip feed along with the co-ordinate system: $L_s = 22.86\text{mm}$, $W_s = 38.10\text{mm}$, $L_c = 19.05\text{mm}$, $W_m = 0.81\text{mm}$, $W_a = 14.73\text{mm}$, $D_s = 3.30\text{mm}$, with $\epsilon_r = 2.2$, $h = 0.508\text{mm}$ and $\tan\delta = 0.001$

The equation of the exponential taper is

$$y = \pm 0.254e^{(0.33(z-8.9))}, \quad 8.90\text{mm} \leq z \leq 19.05\text{mm} \quad (3.2)$$

Apart from the increase in taper length, all other parameters in this model were kept identical to that of Model 1 given in Fig. 3.1 including microstrip line width, method of feed excitation, etc.

3.3.2 Antenna Performance

The simulated S_{11} and input impedance plots of Model 2 are given in Fig. 3.8 (a) and (b).

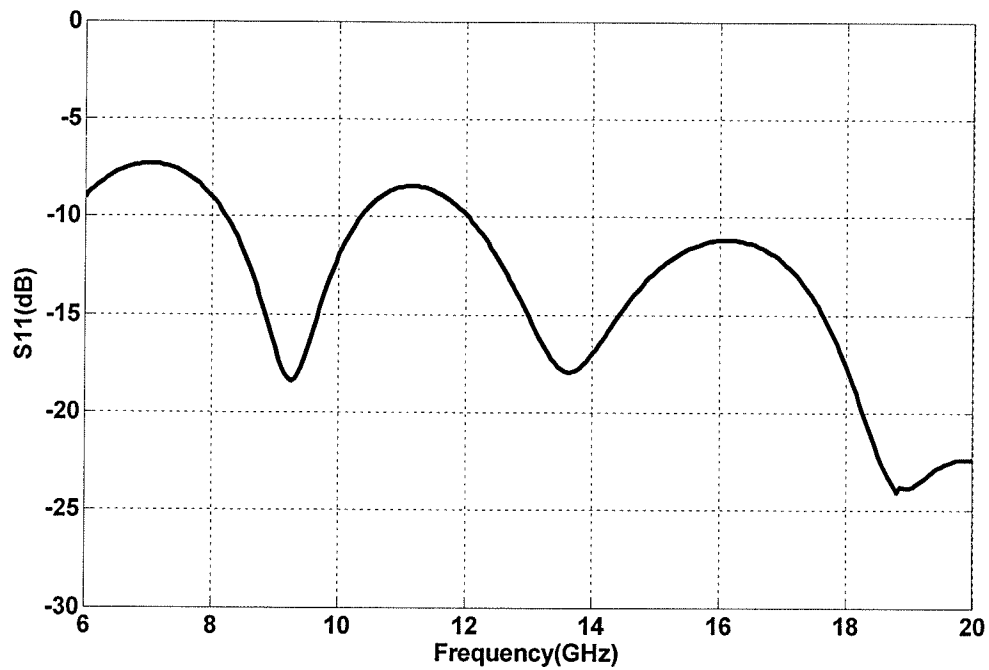


Fig. 3.8 (a)

Fig. 3.8 contd.

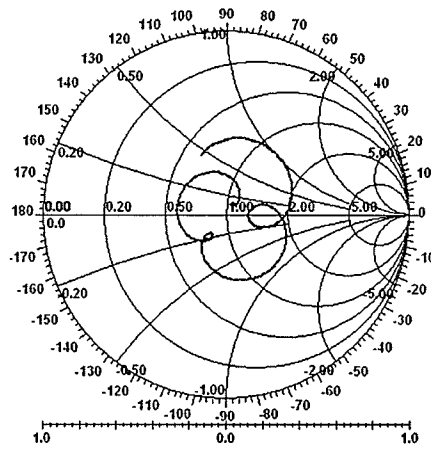


Fig. 3.8 (b)

Fig. 3.8 Simulated (a) S_{11} and (b) input impedance plot measured with respect to 75Ω for antenna Model 2 shown in Fig. 3.7 and described by (3.2)

From Fig. 3.8 (a), it can be observed that the increase in the length of the flare slightly improves the wide band performance of the antenna when compared to Model 1. From Fig. 3.8 (b) it can be seen that there is proper matching between the feed line and excitation.

The E-plane radiation patterns for Model 2 are given in Fig. 3.9. As in Model 1, a null at boresight for the co-pol patterns are observed with increase in frequency for this model also.

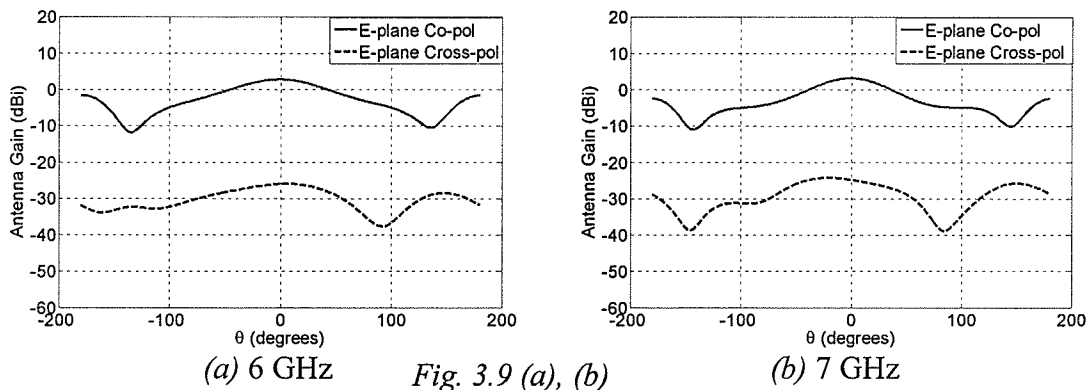


Fig. 3.9 (a), (b)

Fig. 3.9 contd.

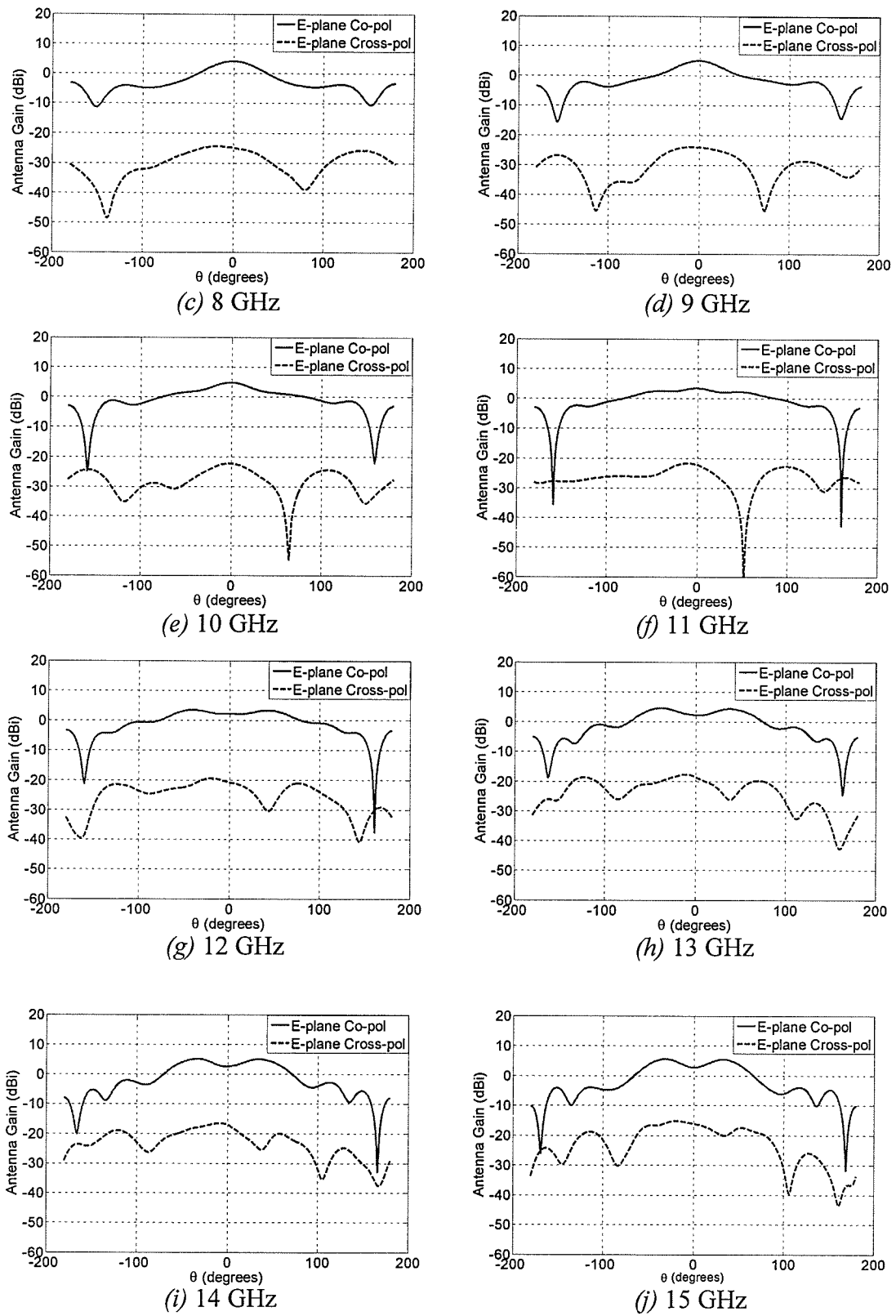


Fig. 3.9 (c)-(j)

Fig. 3.9 contd.

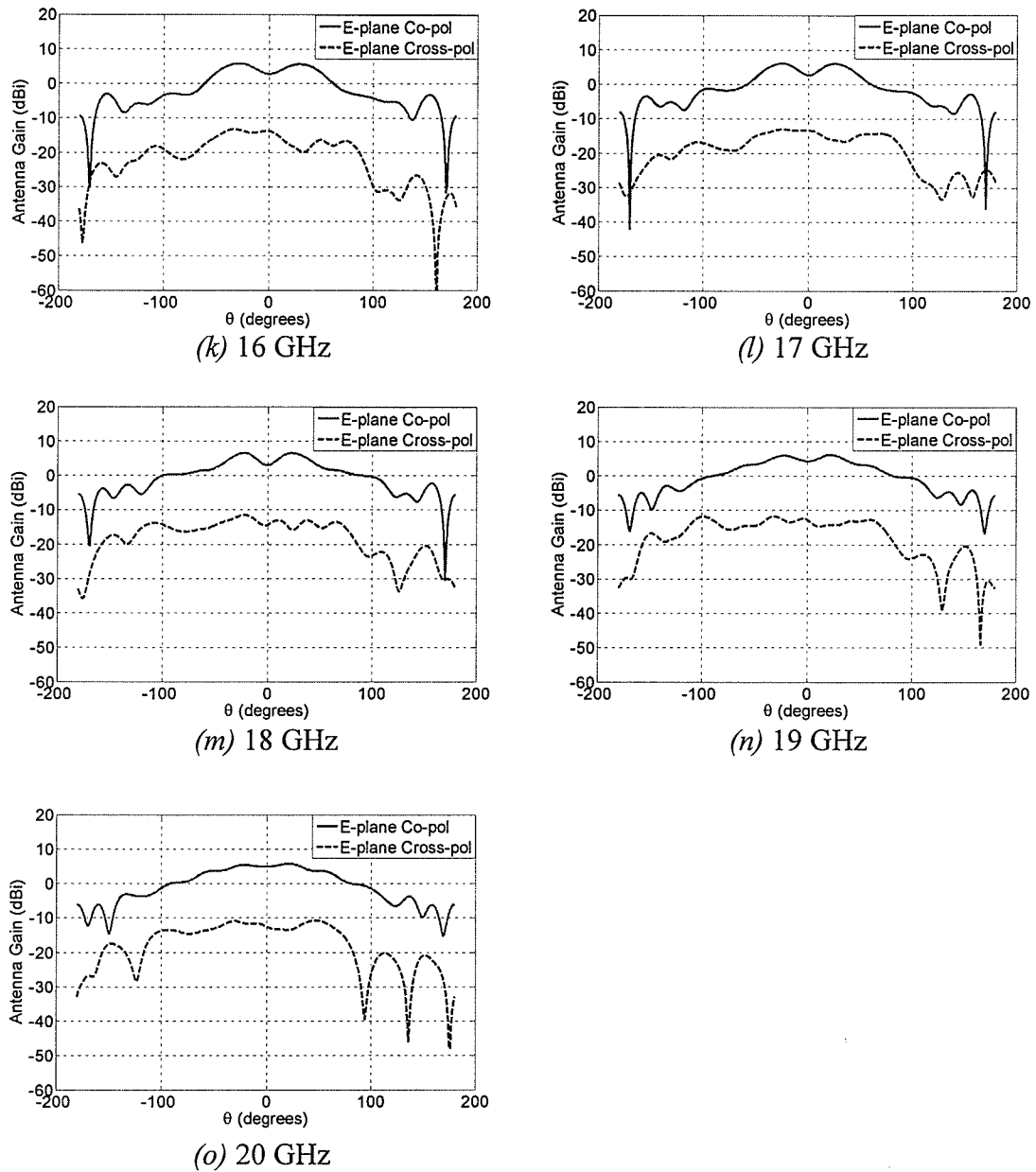


Fig. 3.9 Simulated E-plane ($\phi=90^\circ$ plane) co-pol and cross-pol patterns of Model 2 shown in Fig. 3.7 and described by (3.2)

Tables 3.5 and 3.6 summarize the important E-plane co-pol and cross-pol patterns characteristics respectively.

Frequency (GHz)	Boresight gain (dBi)	Peak gain (dBi)	Position of Peak gain	3 dB BW	10 dB BW
6	2.849	2.850	-1°	91°	232°
7	3.214	3.216	-1°	72°	252°
8	4.141	4.141	-1°	69°	273°
9	5.048	5.054	-1°	61°	287°
10	4.823	4.826	-1°	76°	295°
11	3.476	3.481	-1°	156°	301°
12	3.723	3.734	-2°	150°	292°
13	3.386	4.803	-39°	148°	302°
14	3.101	5.626	-36°	143°	289°
15	3.079	6.044	-33°	136°	259°
16	3.178	6.281	-28°	129°	262°
17	3.225	6.444	-27°	130°	248°
18	3.558	6.527	-25°	145°	234°
19	3.976	6.326	23°	160°	284°
20	4.440	5.981	22°	151°	285°

Table 3.5 Summary of E-plane co-pol pattern characteristics of Model 2 given in Fig. 3.7 and described by (3.2)

Frequency (GHz)	Boresight Cross-pol (dBi)	Peak Cross-pol (dBi)	Position of Peak Cross-pol
6	-25.925	-25.893	5°
7	-24.786	-24.214	-21°
8	-24.930	-24.376	-18°
9	-24.069	-23.965	-8°
10	-22.271	-22.253	-2°
11	-22.239	-21.759	-11°
12	-20.788	-20.102	-18°
13	-18.678	-18.419	-11°
14	-17.023	-16.736	-11°
15	-16.144	-15.440	-27°
16	-14.479	-13.698	-14°
17	-14.045	-11.902	-26°
18	-12.729	-12.252	-10°
19	-13.179	-11.502	-99°
20	-12.644	-11.304	-27°

Table 3.6 Summary of E-plane cross-pol pattern characteristics of Model 2 given in Fig. 3.7 and described by (3.2)

From Table 3.5, it is observed that the E-plane peak gain of Model 2 at various frequencies is slightly higher than that of Model 1. This is an indication that an increase in flare length increases the gain of the antenna.

The H-plane co-pol and cross-pol patterns of Model 2 are given in Fig. 3.10.

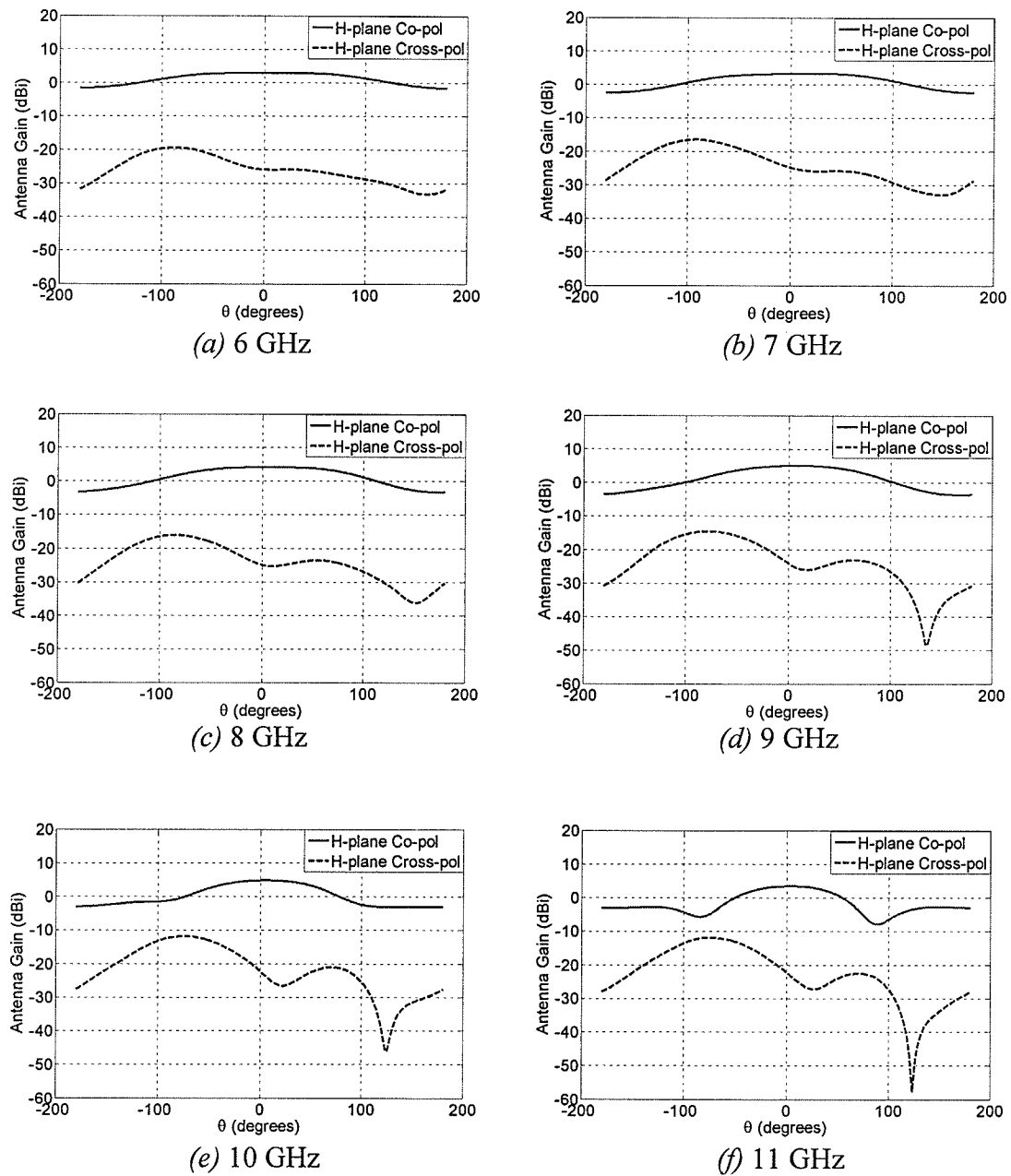


Fig. 3.10 (a)-(f)

Fig. 3.10 contd.

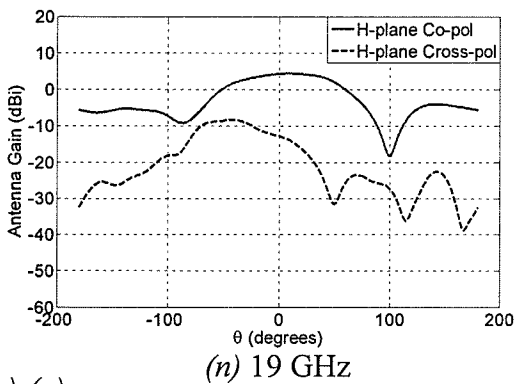
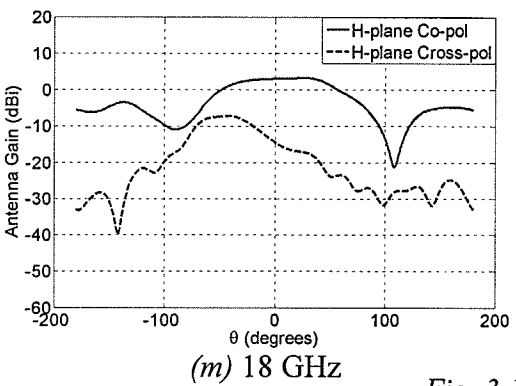
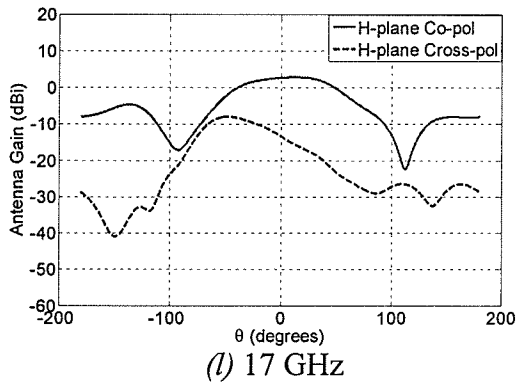
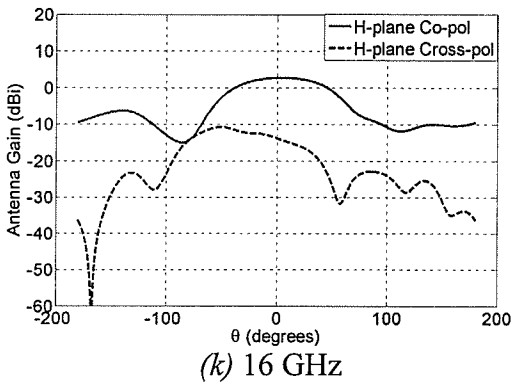
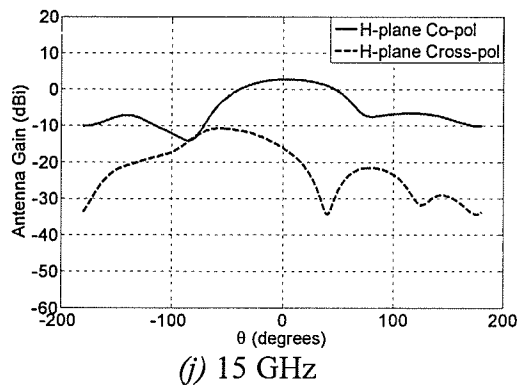
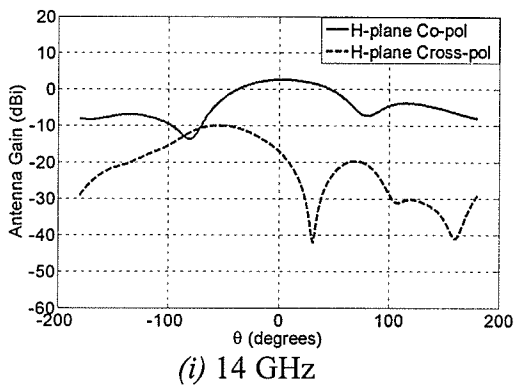
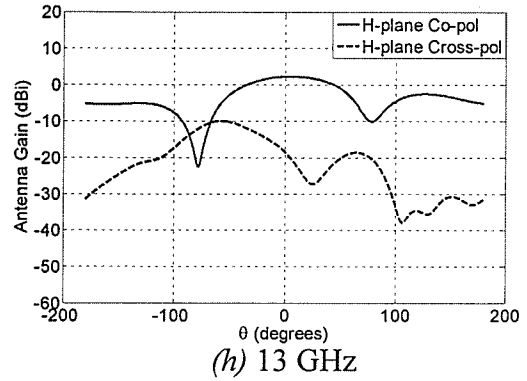
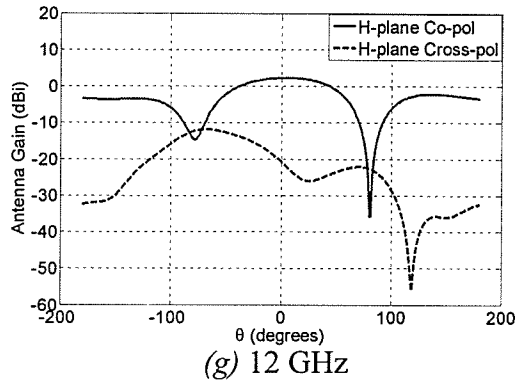


Fig. 3.10 (g)-(n)

Fig. 3.10 contd.

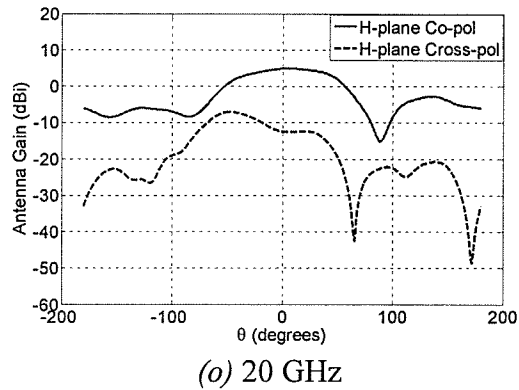


Fig. 3.10 Simulated H-plane ($\phi=0^\circ$ plane) co-pol and cross-pol patterns of Model 2 shown in Fig. 3.7 and described by (3.2)

Tables 3.7 and 3.8 give a summary of the important H-plane co-pol and cross-pol characteristics respectively. Again, blanks are left at certain frequencies for 10 dB beamwidth as they could not be calculated.

Frequency (GHz)	Boresight gain (dBi)	Peak gain (dBi)	Position of Peak gain	3 dB BW	10 dB BW
6	2.849	2.908	31°	254°	--
7	3.214	3.268	24°	219°	--
8	4.141	4.151	9°	191°	--
9	5.048	5.070	8°	157°	--
10	4.823	4.842	6°	121°	--
11	3.476	3.489	4°	99°	--
12	3.723	3.754	6°	97°	147°
13	3.386	3.430	6°	90°	137°
14	3.101	3.148	6°	87°	136°
15	3.079	3.131	6°	85°	137°
16	3.178	3.236	7°	85°	139°
17	3.225	3.307	8°	87°	141°
18	3.558	3.712	11°	88°	135°
19	3.976	4.125	12°	91°	145°
20	4.440	4.528	9°	90°	137°

Table 3.7 Summary of H-plane co-pol pattern characteristics of Model 2 given in Fig. 3.7 and described by (3.2)

Frequency (GHz)	Boresight Cross-pol (dBi)	Peak Cross-pol (dBi)	Position of Peak Cross-pol
6	-25.925	-19.398	-87°
7	-24.786	-16.463	-92°
8	-24.930	-16.069	-86°
9	-24.069	-14.492	-78°
10	-22.271	-11.810	-75°
11	-22.239	-11.902	-75°
12	-20.788	-12.502	-67°
13	-18.678	-11.263	-57°
14	-17.023	-9.942	-56°
15	-16.144	-9.925	-53°
16	-14.479	-9.839	-50°
17	-14.045	-8.176	-52°
18	-12.729	-7.230	-49°
19	-13.179	-6.989	-51°
20	-12.644	-7.275	-51°

Table 3.8 Summary of H-plane cross-pol pattern characteristics of Model 2 given in Fig. 3.7 and described by (3.2)

3.3.3 Study of Phase Centre for Model 2

A study of the phase centre location of Model 2 was carried out, and similar to Model 1, the phase centre in both the E and H-planes could not be located at a single point but rather it was found to situate on a certain portion of the antenna axis for a maximum tolerable phase difference $\Delta\phi$ of 25°. Figure 3.11 (a) shows a plot of the Average E and H-plane phase centre locations at each frequency and Fig. 3.11 (b) depicts these locations on the antenna geometry.

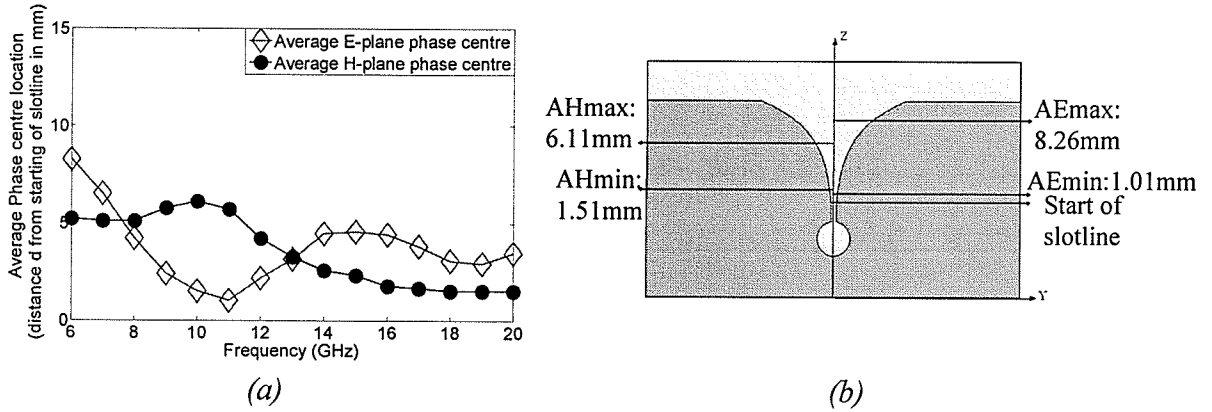


Fig. 3.11 (a) plot of Average E and H planes' phase centre location (for a maximum tolerable phase difference $\Delta\phi=25^\circ$ and θ ranging from 0 to 60°) of Model 2 given in Fig. 3.7; (b) geometry of Model 2 indicating the portion of antenna axis where these Average phase centres lie for both E and H planes

From Fig. 3.11 (a) it is observed that the Average E and H-plane phase centre locations on the axis of Model 2 are quite stable in the 14 to 20 GHz range. It is can also be seen that the maximum distance between the Average E and H-plane phase centres is 6.75 mm.

3.4 Truncated Flare Model (Model 3)

3.4.1 Antenna Model

In the last model under investigation in this chapter (Model 3), the effect of truncation of flare length was studied. The equation describing the flare was maintained the same as that of Model 1, but its length was truncated by 1.27 mm. All other dimensions were unaltered. Figure 3.12 shows the geometry of Model 3.

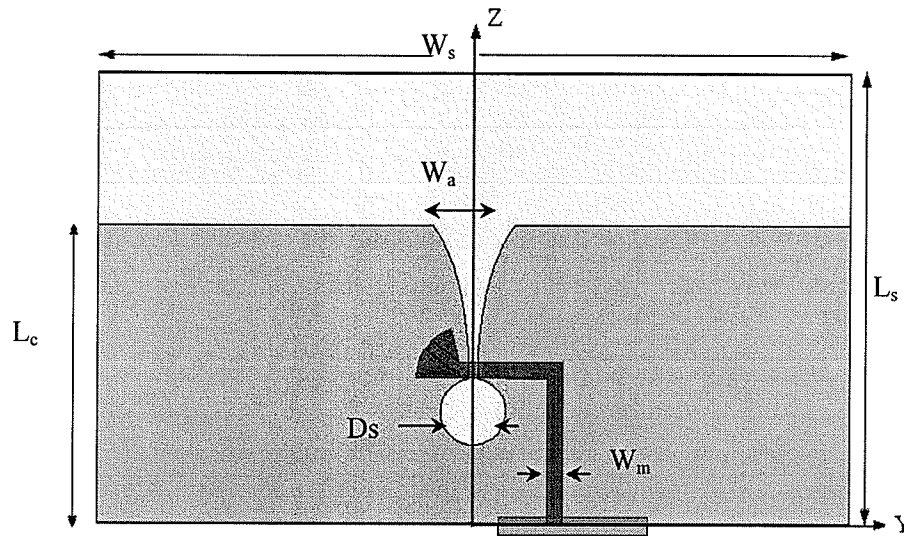


Fig. 3.12 The geometry of the Vivaldi antenna (Model 3) including the microstrip feed along with the co-ordinate system: $L_s = 22.86\text{mm}$, $W_s = 38.10\text{mm}$, $L_c = 15.24\text{mm}$, $W_m = 0.81\text{mm}$, $W_a = 4.06\text{mm}$, $D_s = 3.30\text{mm}$, with $\epsilon_r = 2.2$, $h = 0.508\text{mm}$, and $\tan\delta = 0.001$

The equation describing the flare is

$$y = \pm 0.254e^{(0.33(z-8.9))}, \quad 8.90\text{mm} \leq z \leq 15.24\text{mm} \quad (3.3)$$

3.4.2 Antenna Performance

The simulated S_{11} and input impedance plots of this model are given in Fig. 3.13. It can be observed that the truncation of the flare leads to a deterioration in the wide band performance of the antenna over the considered frequency range.

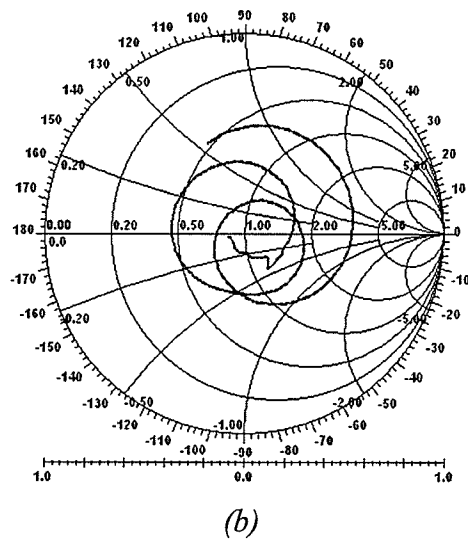
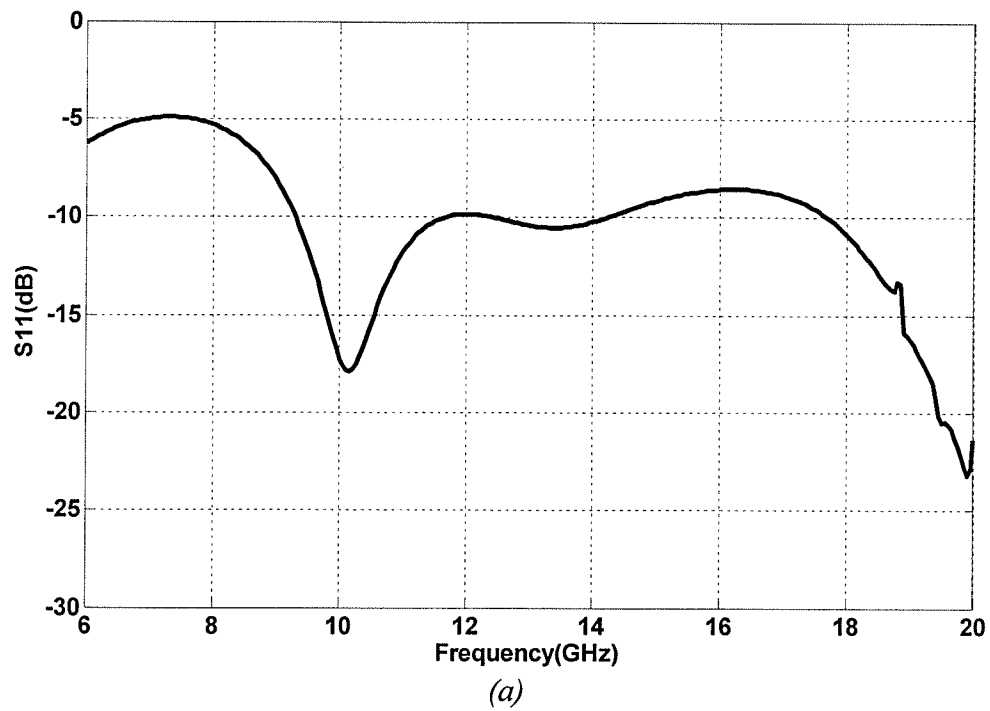


Fig. 3.13 Simulated (a) S_{11} and (b) input impedance plot measured with respect to 75Ω for antenna Model 3 shown in Fig. 3.12 and described by (3.3)

The E-plane co-pol and cross-pol patterns are shown in Fig. 3.14. As in the previous two models, the appearance of a null at boresight occurs in the co-pol patterns with an increase in frequency.

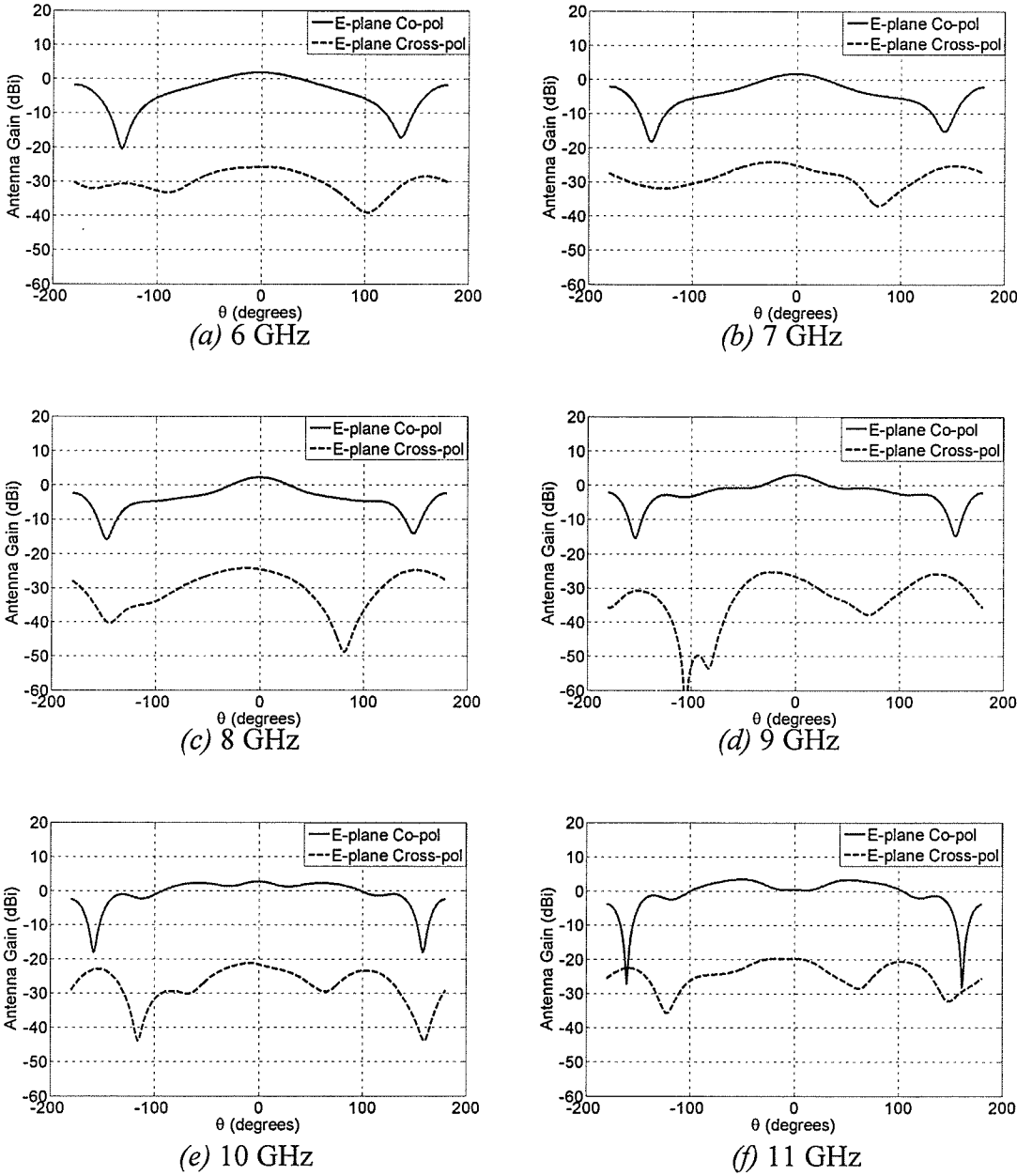


Fig. 3.14 (a)-(f)

Fig. 3.14 contd.

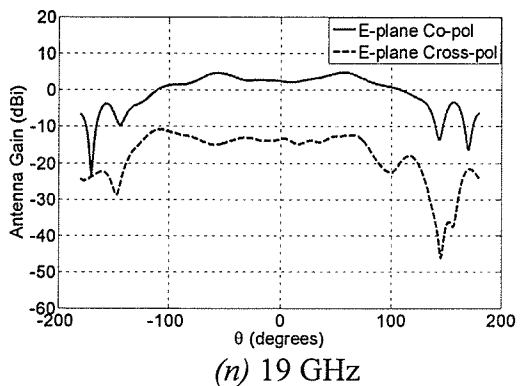
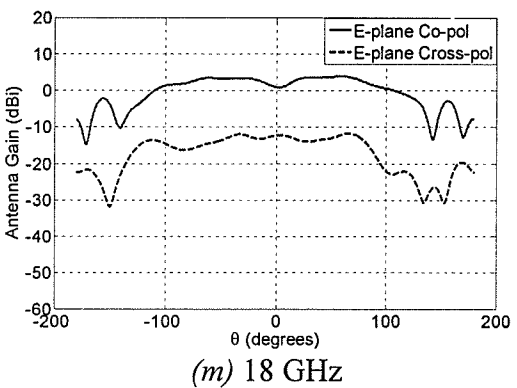
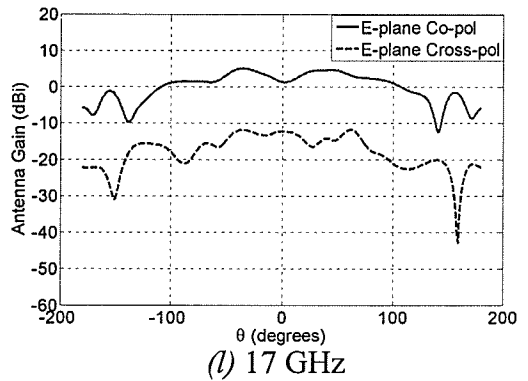
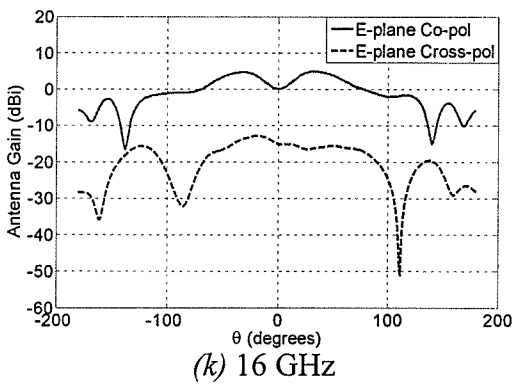
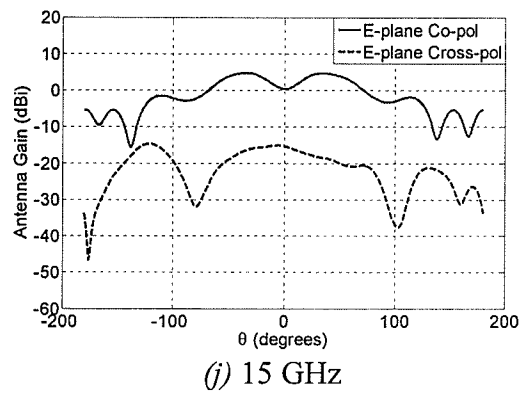
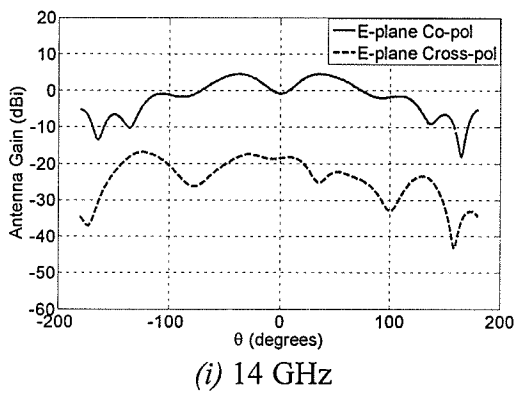
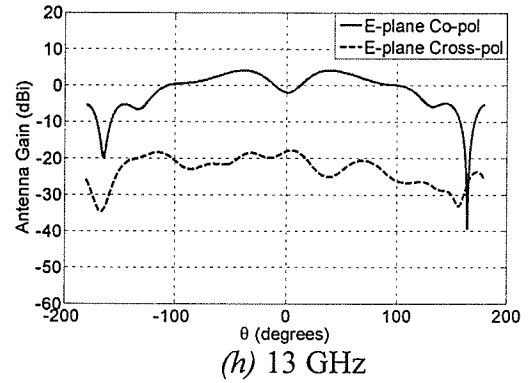
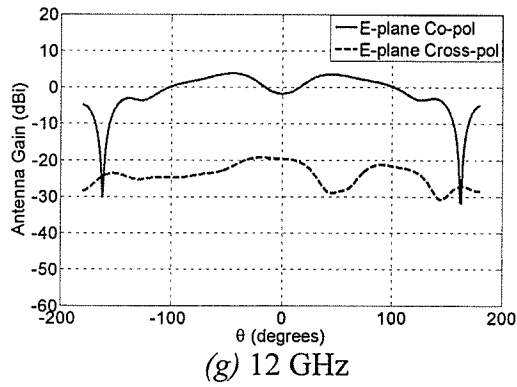


Fig. 3.14 (g)-(n)

Fig. 3.14 contd.

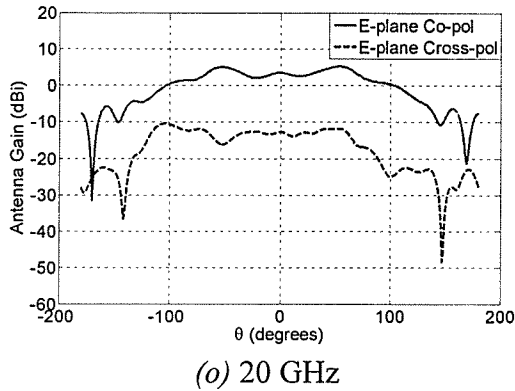


Fig. 3.14 Simulated E-plane ($\phi=90^\circ$ plane) co-pol and cross-pol patterns of Model 3 shown in Fig. 3.12 and described by (3.3)

Tables 3.9 and 3.10 summarize the important characteristics of the E-plane co-pol and cross-pol patterns.

Frequency (GHz)	Boresight gain (dBi)	Peak gain (dBi)	Position of Peak gain	3 dB BW	10 dB BW
6	1.857	1.859	-1°	104°	226°
7	1.721	1.723	-1°	82°	245°
8	2.249	2.249	0°	67°	268°
9	3.046	3.048	-1°	63°	286°
10	2.774	2.776	-1°	194°	301°
11	0.478	3.511	-50°	290°	310°
12	0.561	3.903	-46°	242°	308°
13	-0.458	4.390	-41°	252°	311°
14	-0.836	5.015	-37°	252°	315°
15	0.048	5.070	-35°	246°	272°
16	0.415	5.058	34°	247°	268°
17	0.697	4.929	-32°	249°	269°
18	1.167	4.294	31°	249°	272°
19	1.852	5.095	53°	241°	277°
20	2.985	5.495	51°	221°	281°

Table 3.9 Summary of E-plane co-pol pattern characteristics of Model 3 given in Fig. 3.12 and described by (3.3)

Frequency (GHz)	Boresight Cross-pol (dBi)	Peak Cross-pol (dBi)	Position of Peak Cross-pol
6	-25.757	-25.754	2°
7	-25.153	-24.146	-24°
8	-24.569	-24.235	-14°
9	-26.656	-25.220	-23°
10	-21.626	-21.290	-9°
11	-19.964	-19.878	-20°
12	-19.322	-18.874	-12°
13	-19.250	-18.866	-14°
14	-17.456	-16.855	-125°
15	-15.992	-15.139	-18°
16	-14.825	-13.644	-21°
17	-12.849	-12.537	-11°
18	-13.289	-12.007	61°
19	-12.875	-11.675	-105°
20	-12.981	-10.960	-101°

Table 3.10 Summary of E-plane cross-pol pattern characteristics of Model 3 given in Fig. 3.12 and described by (3.3)

From Table 3.9 it can be observed that the boresight and peak gains of Model 3 are slightly lower than that of Model 1 at some frequencies. This implies that a truncation in length of the flare leads to a reduction in gain of the antenna.

The H-plane co-pol and cross-pol patterns of Model 3 are given in Fig. 3.15.

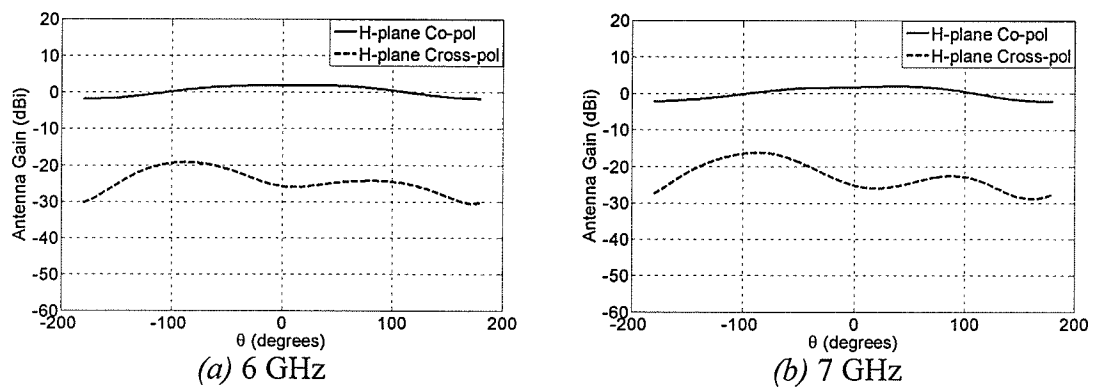


Fig. 3.15 (a), (b)

Fig. 3.15 contd.

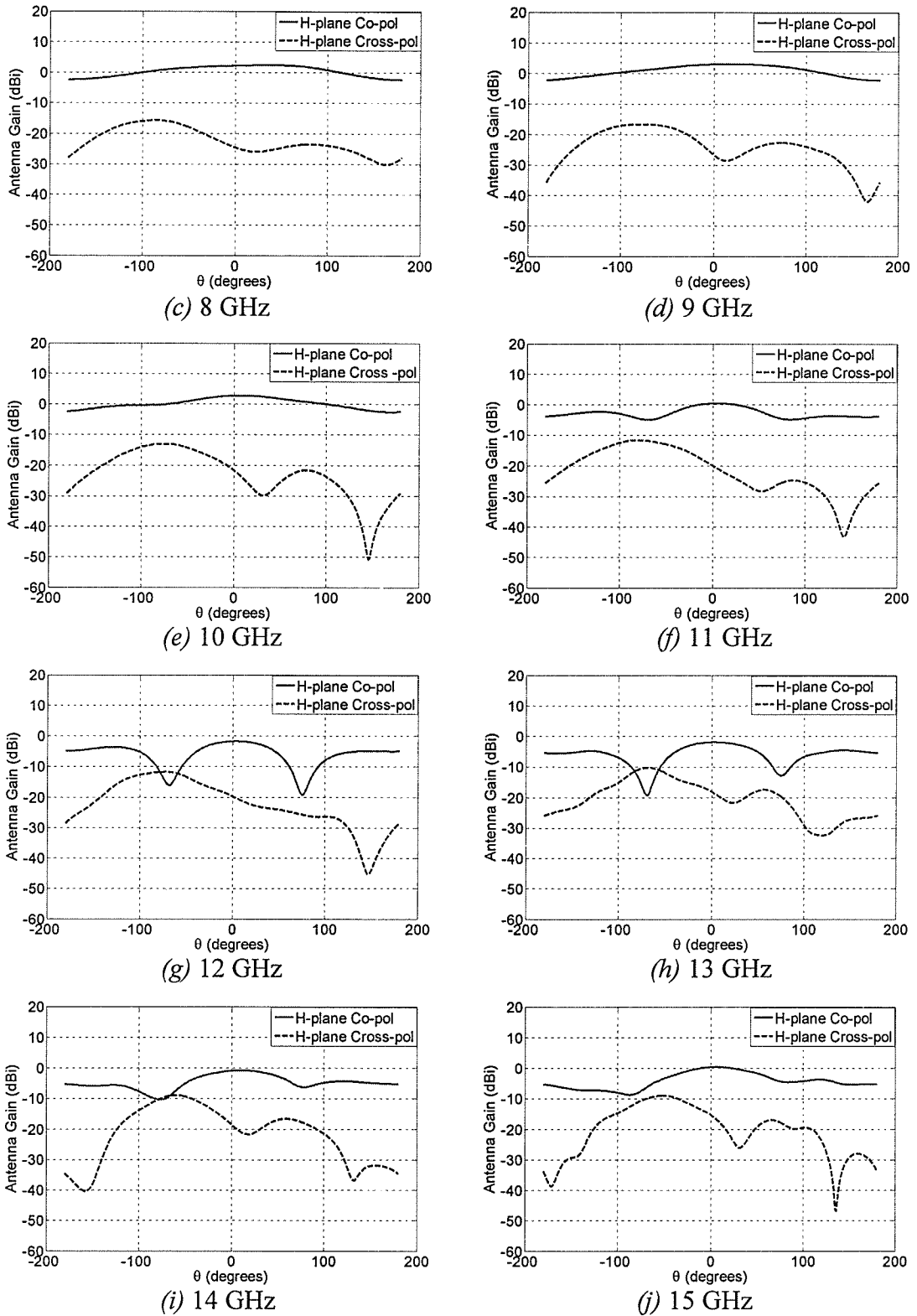


Fig. 3.15 (c)-(j)

Fig. 3.15 contd.

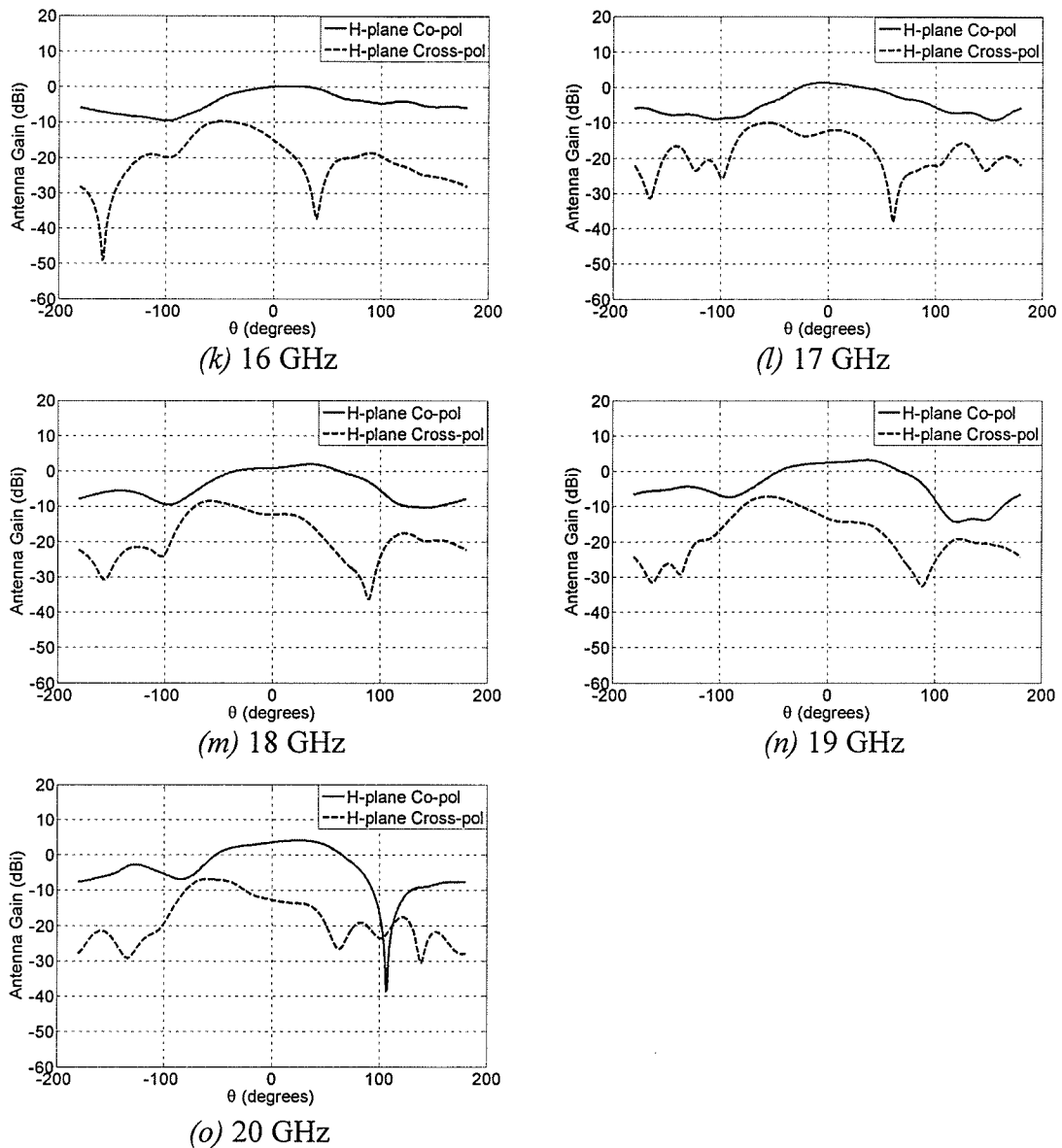


Fig. 3.15 Simulated H-plane ($\phi=0^\circ$ plane) co-pol and cross-pol patterns of Model 3 shown in Fig. 3.12 and described by (3.3)

Tables 3.11 and 3.12 summarize the important characteristics of the H-plane co-pol and cross-pol patterns. It can be observed that the truncation of flare length has reduced both

H-plane boresight and peak gains of Model 3 to some extent when compared to those of Model 1.

Frequency (GHz)	Boresight gain (dBi)	Peak gain (dBi)	Position of Peak gain	3 dB BW	10 dB BW
6	1.857	1.883	23°	278°	--
7	1.721	1.961	38°	268°	--
8	2.249	2.436	37°	246°	--
9	3.046	3.131	20°	229°	--
10	2.774	2.812	8°	248°	--
11	0.478	0.495	4°	97°	--
12	0.561	0.594	5°	92°	151°
13	-0.458	-0.397	7°	87°	132°
14	-0.836	-0.755	8°	86°	140°
15	0.048	0.120	8°	90°	--
16	0.415	0.522	10°, 11°	94°	--
17	0.697	0.986	16°	110°	--
18	1.167	1.546	20°	118°	212°
19	1.852	2.361	25°	121°	--
20	2.985	3.412	21°	110°	179°

Table 3.11 Summary of H-plane co-pol pattern characteristics of Model 3 given in Fig. 3.12 and described by (3.3)

Frequency (GHz)	Boresight Cross-pol (dBi)	Peak Cross-pol (dBi)	Position of Peak Cross-pol
6	-25.757	-19.224	-88°
7	-25.153	-16.213	-87°
8	-24.569	-15.674	-86°
9	-26.656	-16.663	-79°
10	-21.626	-12.955	-75°
11	-19.964	-11.590	-81°
12	-19.322	-11.392	-78°
13	-19.250	-11.274	-71°
14	-17.456	-10.087	-59°
15	-15.992	-9.055	-60°
16	-14.825	-10.057	-49°
17	-12.849	-10.489	-51°
18	-13.289	-9.321	-56°
19	-12.875	-7.026	-56°
20	-12.981	-6.390	-53°

Table 3.12 Summary of H-plane cross-pol pattern characteristics of Model 3 given in Fig. 3.12 and described by (3.3)

3.4.3 Study of Phase centre for Model 3

Figure 3.16 (a) shows a plot of the Average E and H-plane phase centre locations at each frequency and Fig. 3.16 (b) depicts these locations on the antenna geometry. The maximum tolerable phase difference $\Delta\phi$ at the phase centre location was found to be 35° . This implies that there is a larger variation in phase of the co-pol radiation at the phase centre location in both the planes when compared to that of Model 1.

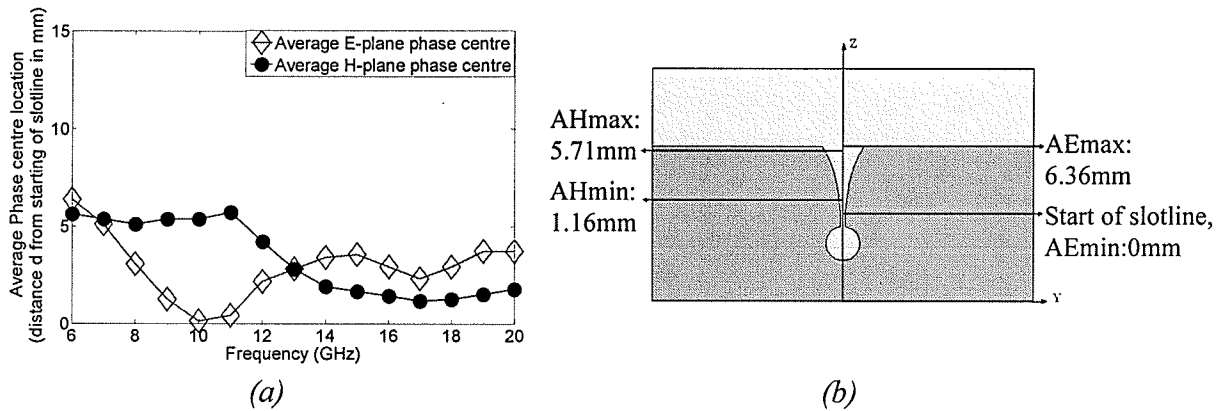


Fig. 3.16 (a) plot of Average E and H planes' phase centre location (for a maximum tolerable phase difference $\Delta\phi=35^\circ$ and θ ranging from 0 to 60°) of Model 3 given in Fig. 3.12; (b) geometry of Model 3 indicating the portion of antenna axis where these Average phase centres lie for both E and H planes

From Fig. 3.16 (a) it is observed the Average E-plane phase centre is stable in the 14 to 20 GHz range while the Average H-plane phase centre is stable in the 6 to 11 GHz range as well as the 14 to 20 GHz range. The maximum separation between the Average E and H-plane phase centres is 5.20 mm.

3.5 Summary

In this chapter a parametric study of a single sided Vivaldi antenna was carried out by maintaining the same equation to describe the flare of the taper while varying its length. The simulated return loss plots and radiation patterns for all three models were presented. An appearance of a null at boresight in the E-plane co-pol patterns was observed for all three models. From Model 2, it was seen that an increase in flare length increased the gain of the antenna, whereas from Model 3, it was observed that a decrease in flare length lead to a slight decrease in gain. A study of the phase centre location for all three models was carried out. It was observed for all three models that the phase centre did not lie at a single point on the axis of the antenna, but rather, it situated itself on a portion of the antenna axis. The phase centre location of Model 2 was seen to exhibit the smallest maximum tolerable phase difference $\Delta\phi$ while Model 3 exhibited the largest. From the radiation patterns and phase centre study, it may be concluded that Model 2 has the best performance amongst the three models presented in this chapter.

CHAPTER 4

PARAMETRIC STUDY OF VIVALDI ANTENNA –II

4.1 Introduction

In this chapter, a study on the rate of taper of the flare and also on the width of the same Vivaldi presented in [9] is presented. As in the previous chapter, all three models presented in this chapter are also single sided microstrip line fed Vivaldi antennas. Two cases deal with the variation in the rate of taper of the flare of the antenna. In the third case, the width of the Vivaldi was truncated and the results were studied. The simulations were once again carried out by using Ansoft HFSS v.10 and the frequency range under consideration was also maintained as that of the previous chapter. A study of the phase centre location is also carried out in this chapter for all three models.

4.2 Fast Opening Flare Model (Model 4)

4.2.1 Antenna Model

As previously mentioned, for all three models of chapter three, the equation of the flare was unaltered. In order to observe the effect of change in rate of taper on the antenna's performance, two models with flare equations different from that given in [9] were studied and are presented here. The first model under study in this chapter (and the fourth model of its kind under parametric study) is given in Fig. 4.1

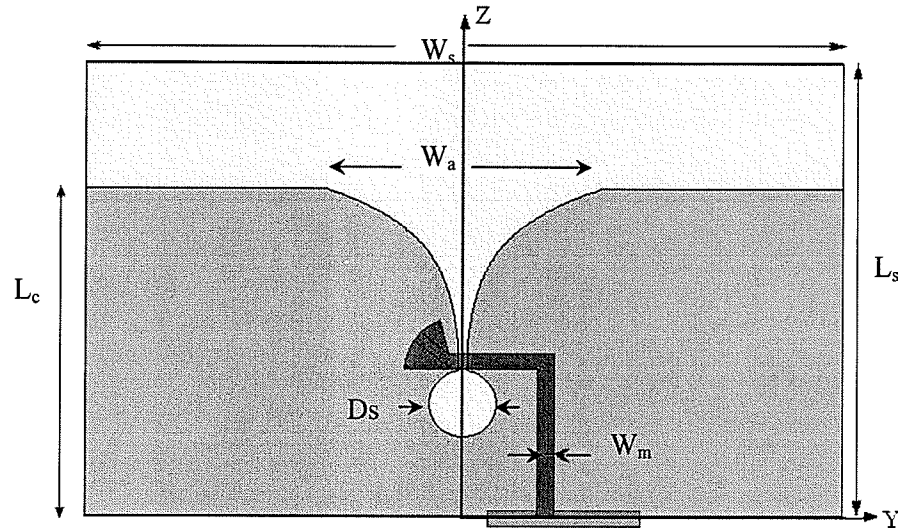


Fig. 4.1 The geometry of the Vivaldi antenna (Model 4) including the microstrip feed along with the co-ordinate system: $L_s = 22.86\text{mm}$, $W_s = 38.10\text{mm}$, $L_c = 16.51\text{mm}$, $W_m = 0.81\text{mm}$, $W_a = 13.72\text{mm}$, $D_s = 3.30\text{mm}$, with $\epsilon_r = 2.2$, $h = 0.508\text{mm}$ and $\tan\delta = 0.001$

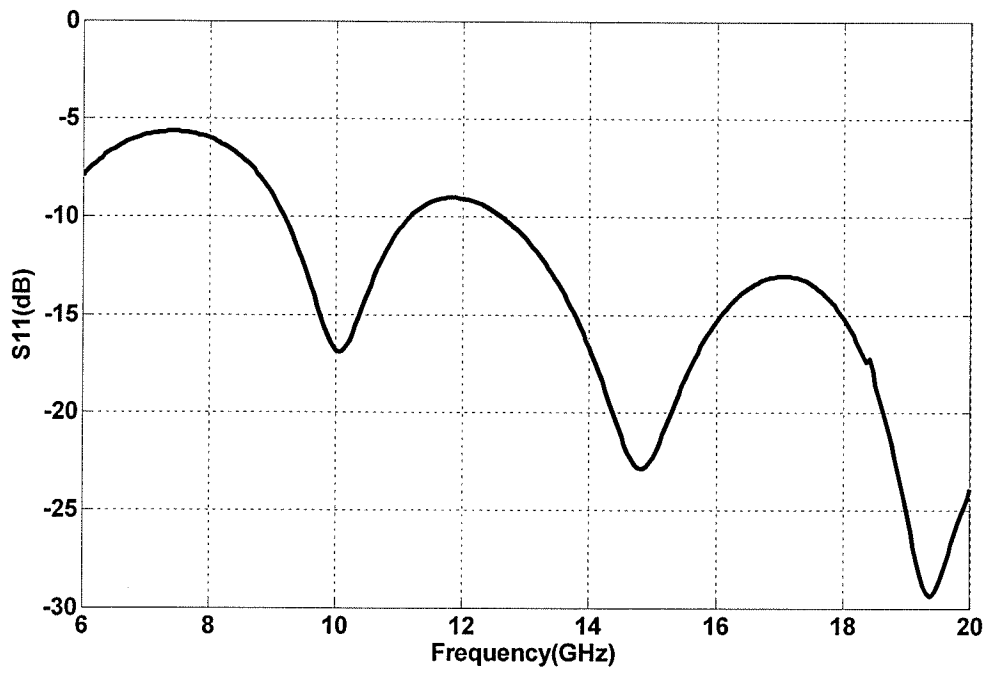
In this model (Model 4), the rate of taper of the flare was increased when compared to that given in [9] and the equation describing the flare is

$$y = \pm 0.254e^{(0.43(z-8.9))}, \quad 8.90\text{mm} \leq z \leq 16.51\text{mm} \quad (4.1)$$

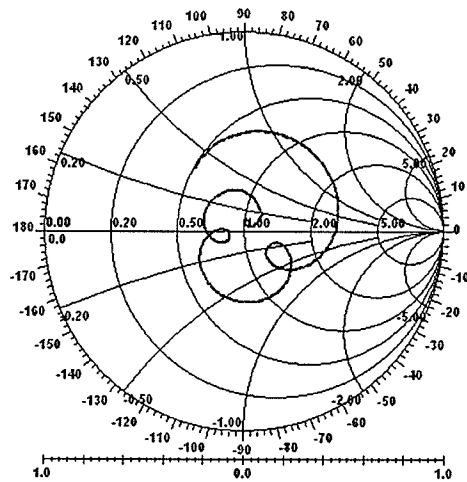
This increase in rate of taper increases the width of the aperture of the antenna. All other parameters such as microstrip feed width; antenna length, etc. were maintained as those in the previous chapter.

4.2.2 Antenna Performance

The simulated S_{11} and input impedance plots of Model 4 are given in Fig. 4.2. It can be observed that mid-band performance of this model slightly better than that of Model 1 of chapter three.



(a)



(b)

Fig. 4.2 Simulated (a) S_{11} and (b) input impedance plot measured with respect to 75Ω for antenna Model 4 shown in Fig. 4.1 and described by (4.1)

The E-plane co-pol and cross-pol patterns are shown in Fig. 4.3. From the plots it is evident that a change in the rate of taper of the flare of the antenna does not prevent the appearance of a null at boresight with an increase in frequency in the co-pol patterns.

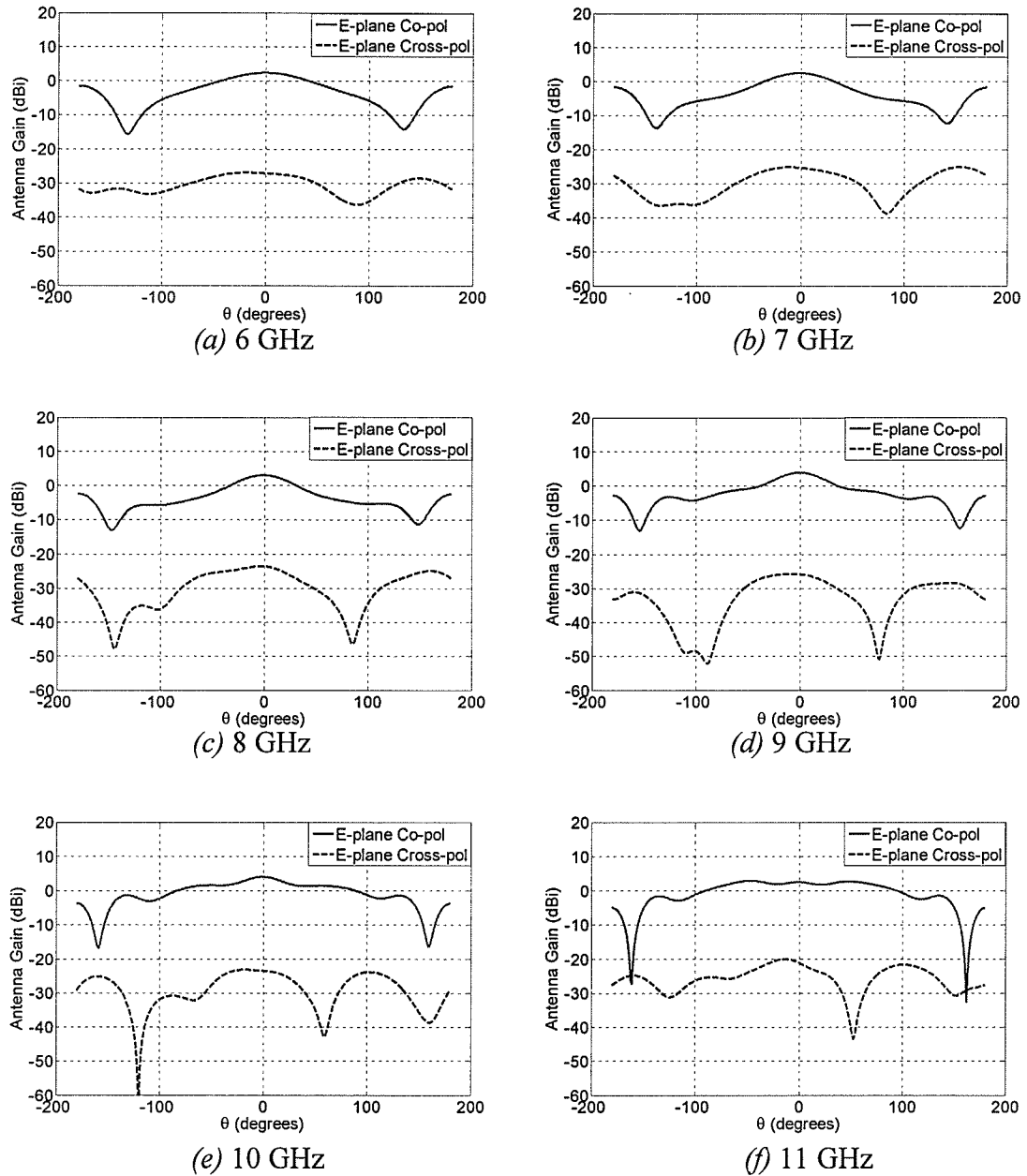


Fig. 4.3 (a)-(f)

Fig. 4.3 contd.

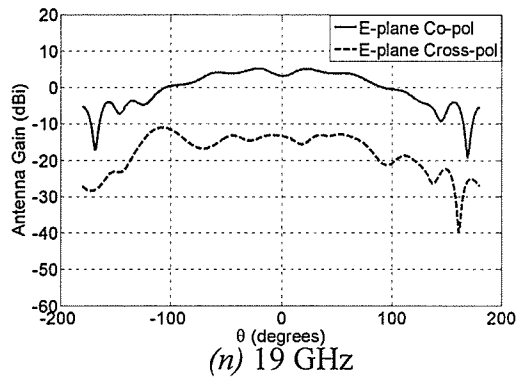
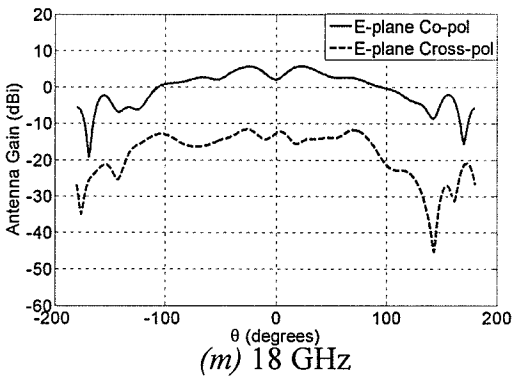
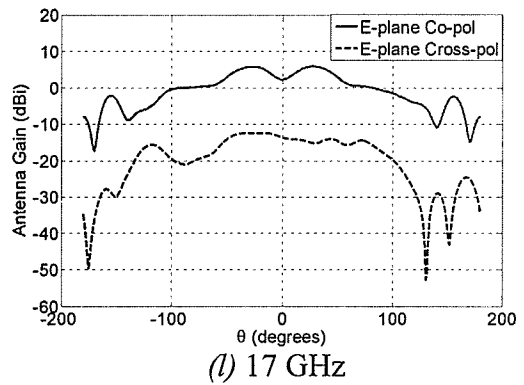
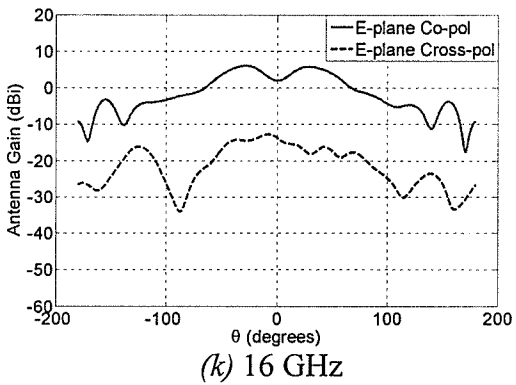
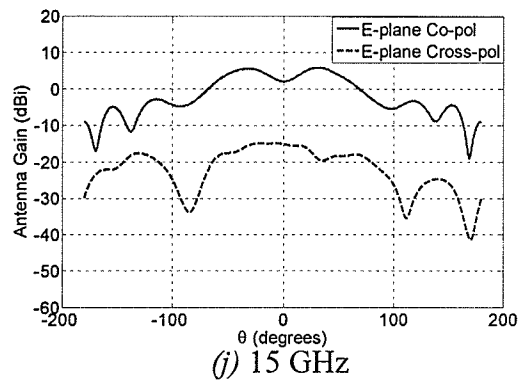
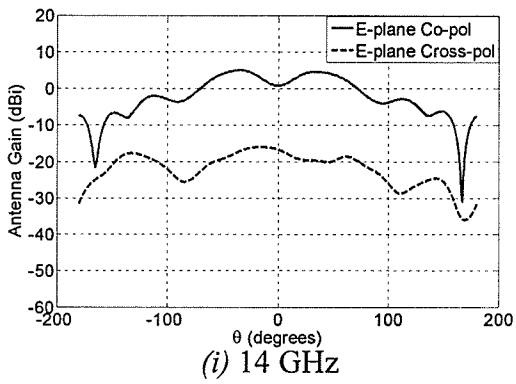
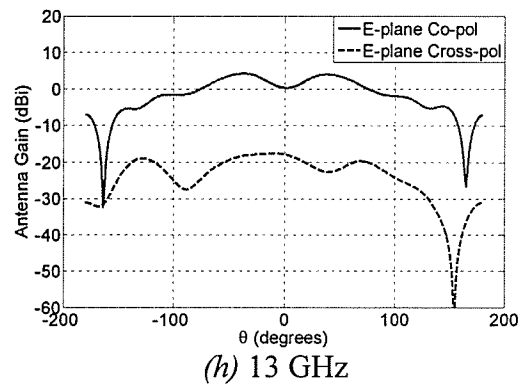
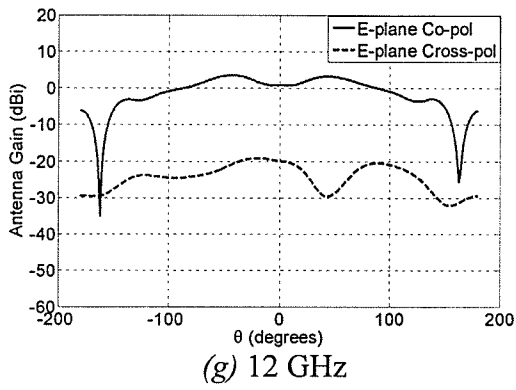


Fig. 4.3 (g)-(n)

Fig. 4.3 contd.

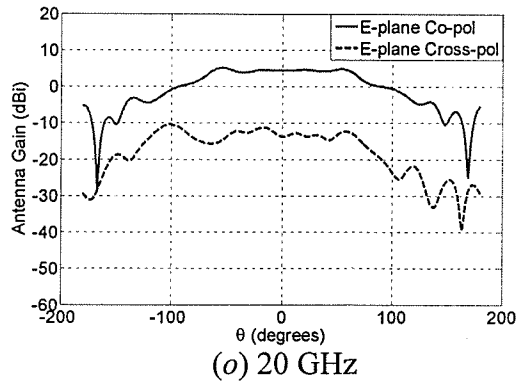


Fig. 4.3 Simulated E-plane ($\phi=90^\circ$ plane) co-pol and cross-pol patterns of Model 4 shown in Fig. 4.1 and described by (4.1)

The note worthy characteristics of the E-plane co-pol and cross-pol patterns of Model 4 are summarized in Tables 4.1 and 4.2.

Frequency (GHz)	Boresight gain (dBi)	Peak gain (dBi)	Position of Peak gain	3 dB BW	10 dB BW
6	2.400	2.400	0°	98°	218°
7	2.453	2.460	-2°	76°	241°
8	3.012	3.018	-1°	64°	264°
9	3.897	3.897	0°	61°	285°
10	4.089	4.091	-1°	144°	298°
11	2.578	2.938	-47°	193°	307°
12	2.507	3.635	-44°	192°	305°
13	1.742	4.520	-40°	188°	308°
14	1.480	5.472	-38°	162°	313°
15	1.721	5.898	-34°	153°	318°
16	1.964	6.084	-31°	155°	275°
17	2.247	6.096	-29°	169°	265°
18	2.599	6.060	-27°	208°	273°
19	2.943	5.401	25°	212°	280°
20	3.479	4.991	-52°	181°	284°

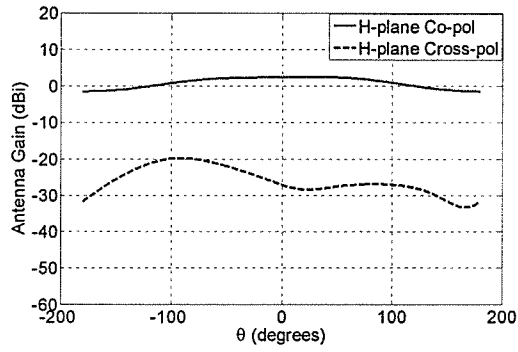
Table 4.1 Summary of E-plane co-pol pattern characteristics of Model 4 given in Fig. 4.1 and described by (4.1)

Frequency (GHz)	Boresight Cross-pol (dBi)	Peak Cross-pol (dBi)	Position of Peak Cross-pol
6	-27.106	-26.874	-18°
7	-25.367	-25.106	154°
8	-23.573	-23.537	-3°
9	-25.807	-25.683	-8°
10	-23.502	-23.180	-18°
11	-21.168	-20.048	-14°
12	-20.290	-19.815	-13°
13	-18.336	-17.595	-16°
14	-16.799	-16.757	-14°
15	-15.521	-14.978	-12°
16	-15.230	-14.343	-19°
17	-13.846	-12.630	-23°
18	-13.498	-12.476	-24°
19	-13.895	-11.538	-106°
20	-13.266	-10.665	-106°

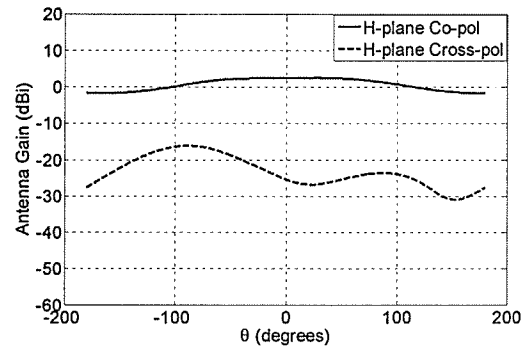
Table 4.2 Summary of E-plane cross-pol pattern characteristics of Model 4 given in Fig. 4.1 and described by (4.1)

From a brief inspection of Table 4.1, it can be observed that the boresight and peak gains of Model 4 are slightly higher than those of Model 1 of chapter three. This indicates that an increase in rate of taper of the flare of the antenna plays a role in the increase of its gain. However, from Table 4.2 it can be seen that the cross-pol levels of Model 4 are quite similar to those of Model 1.

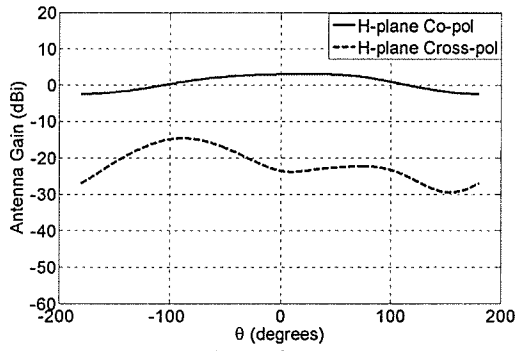
The H-plane co-pol and cross-pol patterns of Model 4 are given in Fig. 4.4. Similar to all the previous models, the co-pol patterns are quite flat with very wide 3 dB and 10 dB beamwidths.



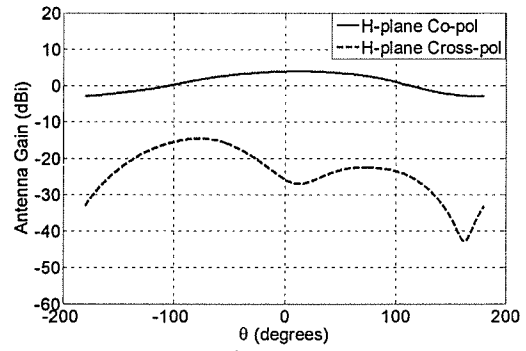
(a) 6 GHz



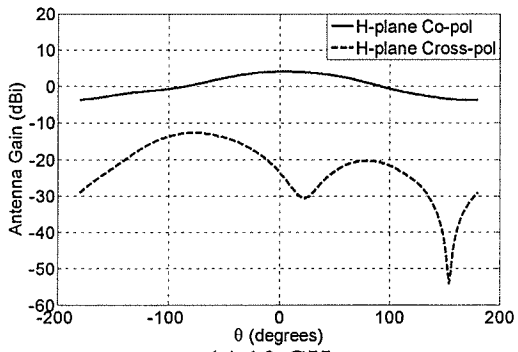
(b) 7 GHz



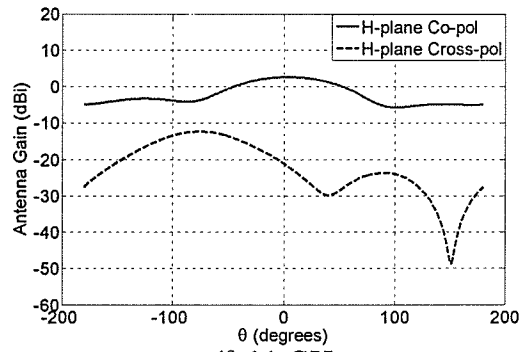
(c) 8 GHz



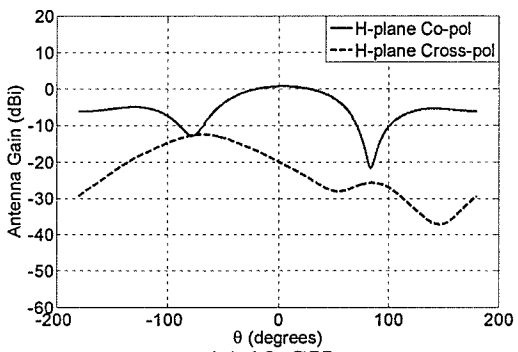
(d) 9 GHz



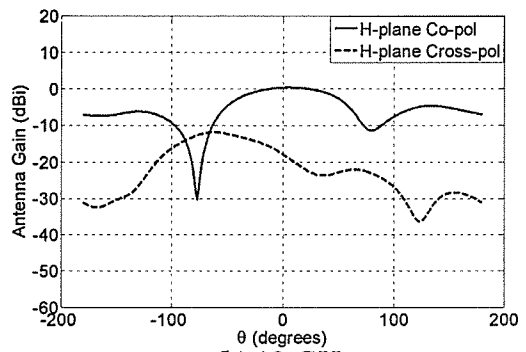
(e) 10 GHz



(f) 11 GHz



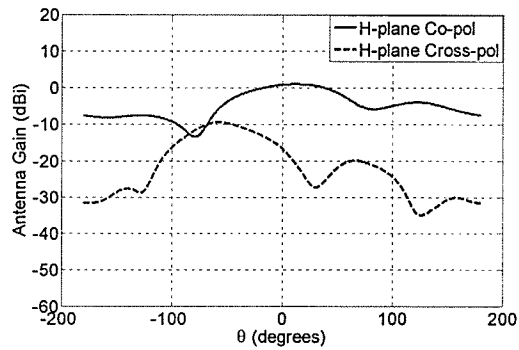
(g) 12 GHz



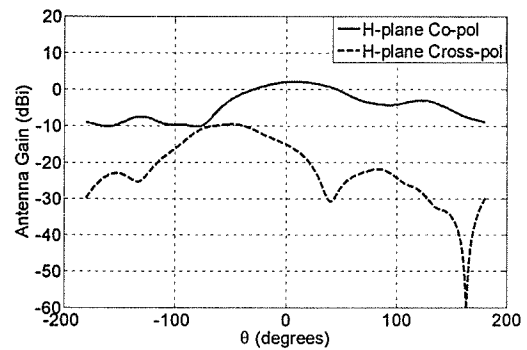
(h) 13 GHz

Fig. 4.4 (a)-(h)

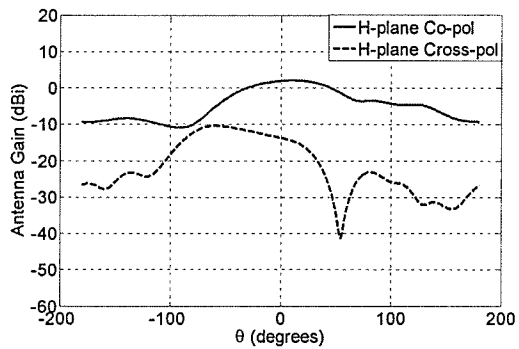
Fig. 4.4 contd.



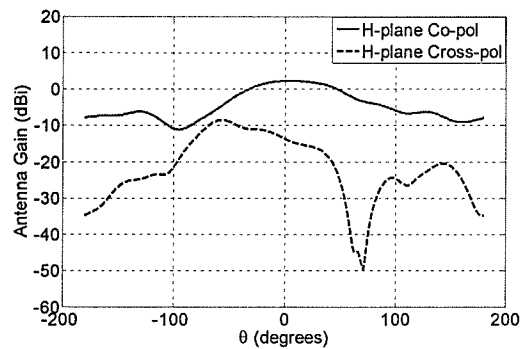
(i) 14 GHz



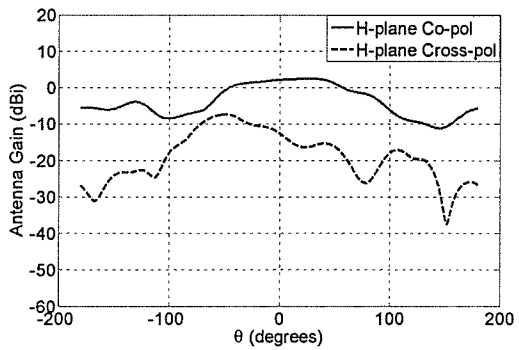
(j) 15 GHz



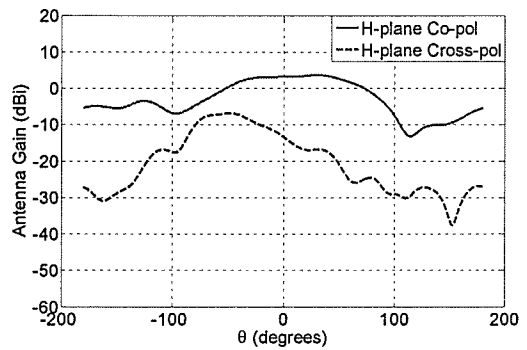
(k) 16 GHz



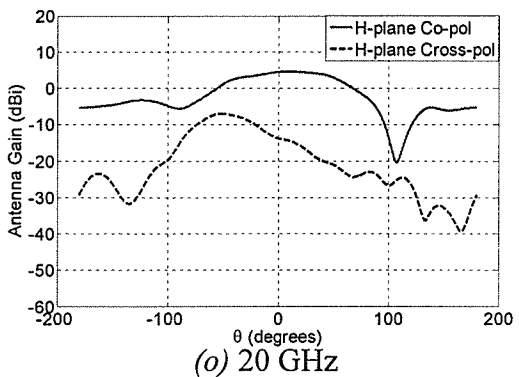
(l) 17 GHz



(m) 18 GHz



(n) 19 GHz



(o) 20 GHz

Fig. 4.4 Simulated H-plane ($\phi=0^\circ$ plane) co-pol and cross-pol patterns of Model 4 shown in Fig. 4.1 and described by (4.1)

Tables 4.3 and 4.4 summarize the important H-plane co-pol and cross-pol patterns characteristics respectively.

Frequency (GHz)	Boresight gain (dBi)	Peak gain (dBi)	Position of Peak gain	3 dB BW	10 dB BW
6	2.400	2.461	31°	269°	--
7	2.453	2.530	28°	242°	--
8	3.012	3.078	25°	219°	--
9	3.897	3.942	13°	192°	--
10	4.089	4.096	4°	147°	--
11	2.578	2.590	4°	105°	--
12	2.507	2.551	7°	112°	160°
13	1.742	1.799	7°	93°	142°
14	1.480	1.545	7°	90°	144°
15	1.721	1.825	9°	89°	--
16	1.964	2.046	8°	91°	233°
17	2.247	2.345	9°	94°	208°
18	2.599	2.758	12°	99°	180°
19	2.943	3.164	15°	106°	179°
20	3.479	3.700	16°	110°	179°

Table 4.3 Summary of H-plane co-pol pattern characteristics of Model 4 given in Fig. 4.1 and described by (4.1)

Frequency (GHz)	Boresight Cross-pol (dBi)	Peak Cross-pol (dBi)	Position of Peak Cross-pol
6	-25.925	-19.760	-91°
7	-24.786	-16.140	-88°
8	-24.930	-14.584	-89°
9	-24.069	-14.534	-76°
10	-22.271	-12.700	-78°
11	-22.239	-12.314	-75°
12	-20.788	-12.974	-72°
13	-18.678	-12.293	-62°
14	-17.023	-11.123	-57°
15	-16.144	-9.415	-58°
16	-14.479	-9.712	-58°
17	-14.045	-9.650	-53°
18	-12.729	-7.078	-50°
19	-13.179	-6.811	-55°
20	-12.644	-6.645	-52°

Table 4.4 Summary of H-plane cross-pol pattern characteristics of Model 4 given in Fig. 4.1 and described by (4.1)

4.2.3 Study of Phase centre for Model 4

The procedure used to find the location of the phase centre of all three models in this chapter was exactly the same as that of chapter three. The phase centre location for Model 4 (and for the remaining two models presented here) was again found to lie on a portion of its axis as opposed to lying at a single point. The maximum tolerable phase difference $\Delta\phi$ was found to be identical to that of Model 1 (i.e. 30°), indicating that the increase in rate of taper did not help in minimizing the phase variation of the co-pol radiation at the phase centre location. Figure 4.5 (a) shows a plot of the Average E and H-plane radiation at the phase centre location. Figure 4.5 (a) shows a plot of the Average E and H-plane phase centre locations at each frequency and Fig. 4.5 (b) depicts these locations on the antenna geometry.

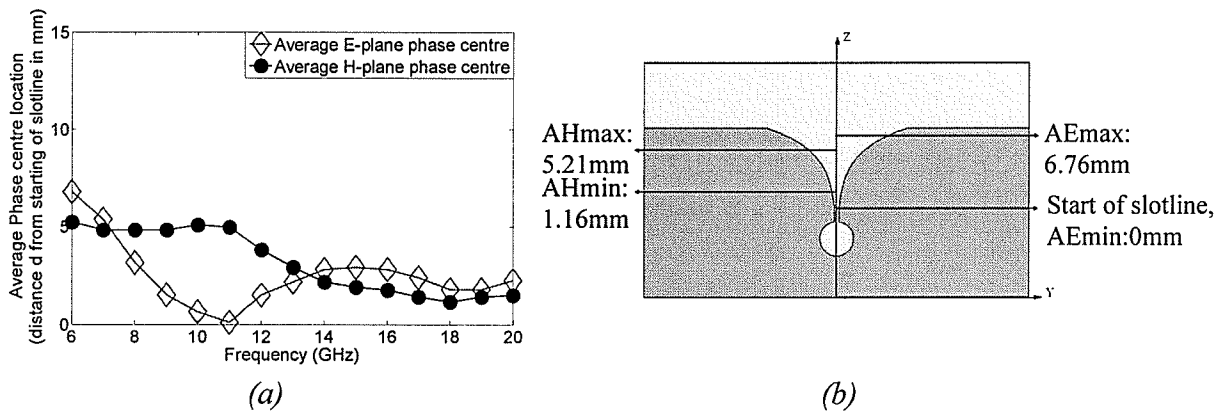


Fig. 4.5 (a) plot of Average E and H planes' phase centre location (for a maximum tolerable phase difference $\Delta\phi=30^\circ$ and θ ranging from 0 to 60°) of Model 4 given in Fig. 4.1; (b) geometry of Model 4 indicating the portion of antenna axis where these Average phase centres lie for both E and H planes

From Fig. 4.5 (a) it can be seen that the stability of the Average E and H-plane phase centres of Model 4 with respect to frequency are more or less similar to those of the

previous three models of chapter three. It is also observed that the maximum distance between the Average E and H-plane phase centres is 5.60 mm.

4.3 Slow Opening Flare Model (Model 5)

4.3.1 Antenna Model

In this model (Model 5), the rate of taper of the flare was decreased from that of the original model (Model 1) and its geometry is given in Fig. 4.6.

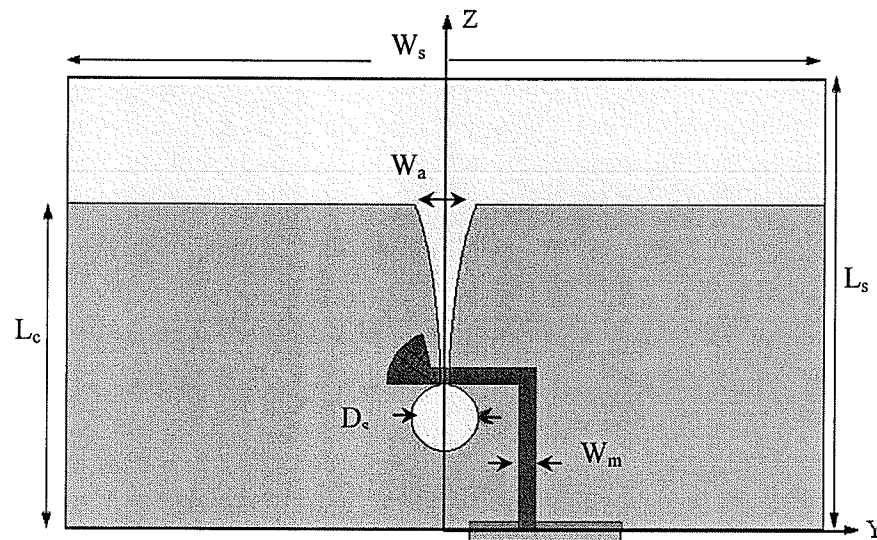


Fig. 4.6 The geometry of the Vivaldi antenna (Model 5) including the microstrip feed along with the co-ordinate system: $L_s = 22.86\text{mm}$, $W_s = 38.10\text{mm}$, $L_c = 16.51\text{mm}$, $W_m = 0.81\text{mm}$, $W_a = 3.05\text{mm}$, $D_s = 3.30\text{mm}$, with $\epsilon_r = 2.2$, $h = 0.508\text{mm}$ and $\tan\delta = 0.001$

As can be seen from Fig. 4.6, the width of the aperture, W_a , is smaller than that of Model 1. All other dimensions were maintained the same as Model 1. The equation of the flare is given below

$$y = \pm 0.254e^{(0.23(z-8.9))}, \quad 8.90\text{mm} \leq z \leq 16.51\text{mm} \quad (4.2)$$

4.3.2 Antenna Performance

The simulated S_{11} and input impedance plots of this model are given in Fig. 4.7. From the figure it is observed that the wide band performance of the antenna is significantly deteriorated due to the decrease in taper rate of the flare.

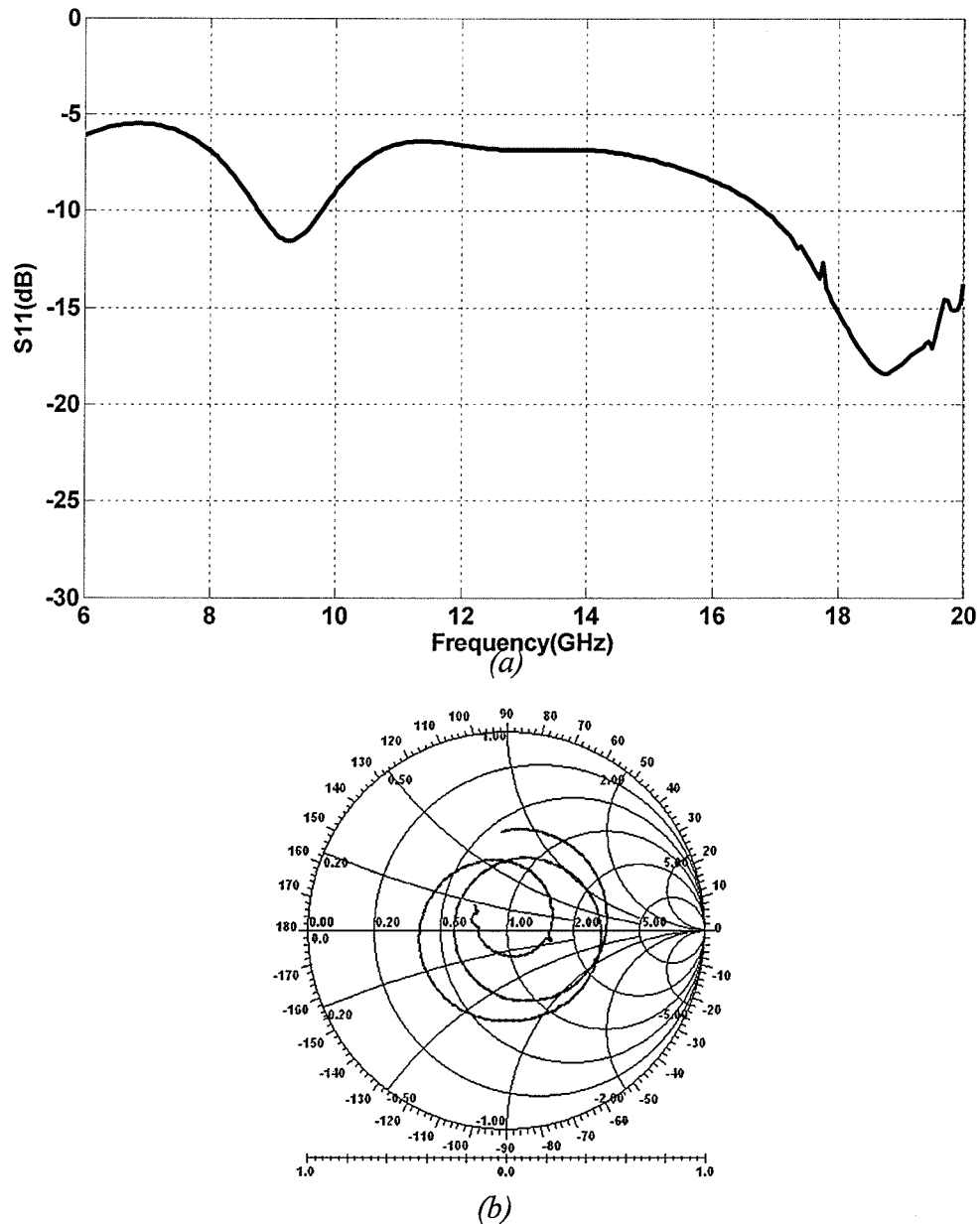


Fig. 4.7 Simulated (a) S_{11} and (b) input impedance plot measured with respect to 75Ω for antenna Model 5 shown in Fig. 4.6 and described by (4.2)

The E-plane co-pol and cross-pol patterns of Model 5 are given in Fig. 4.8. As in all the previous models, an appearance of a null at boresight occurs in the co-pol patterns with increase in frequency of operation.

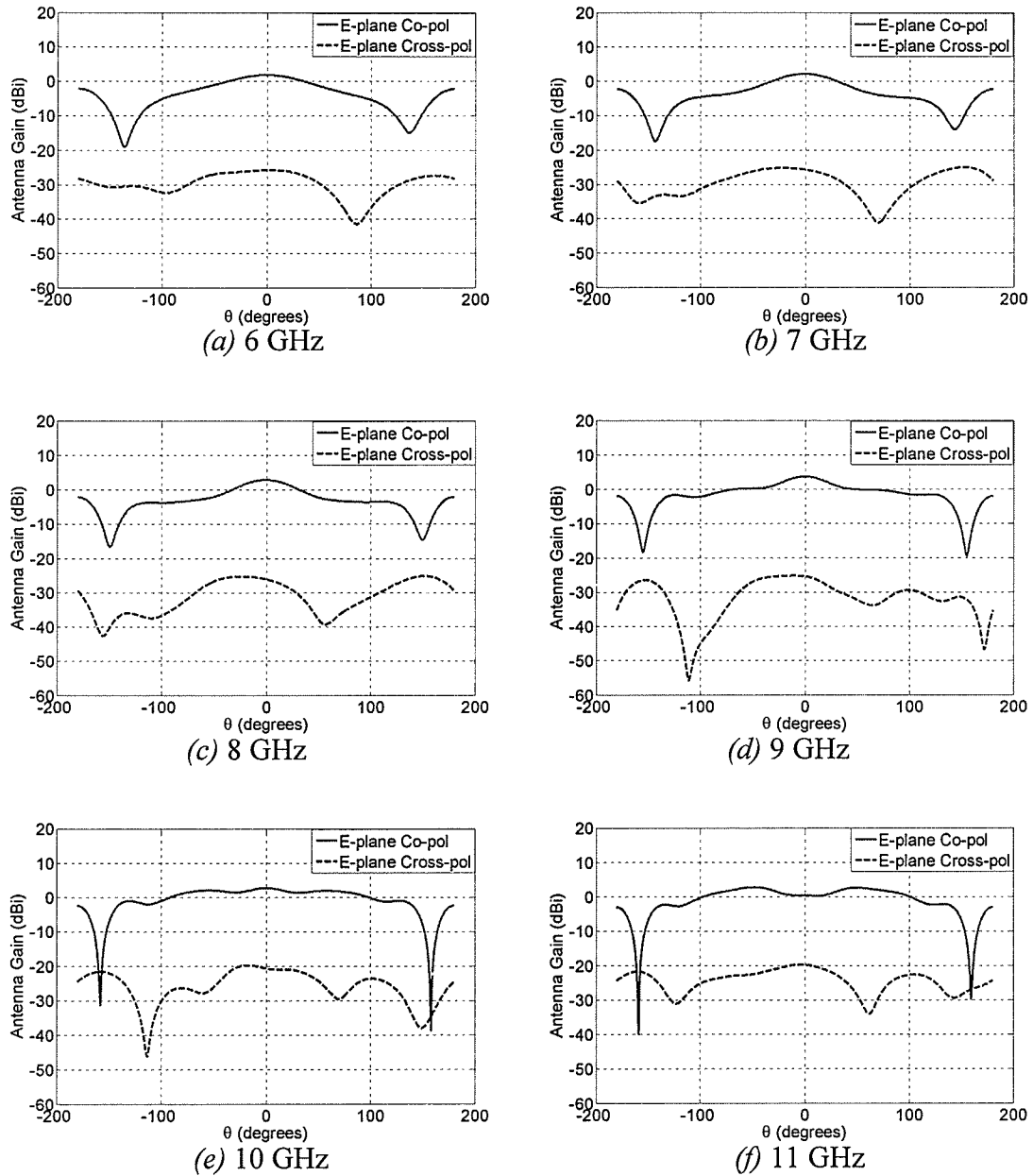


Fig. 4.8 (a)-(f)

Fig. 4.8 contd.

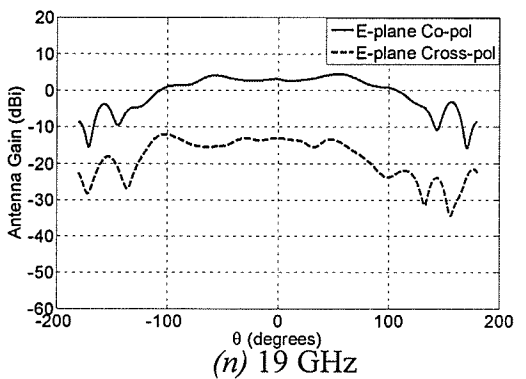
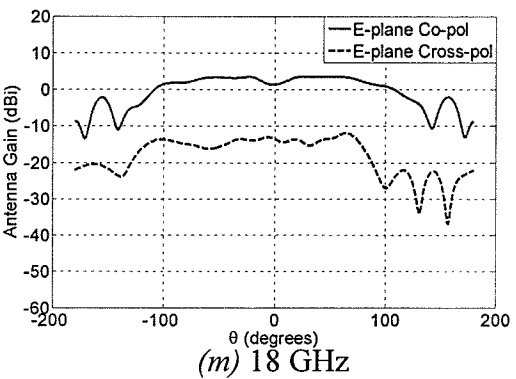
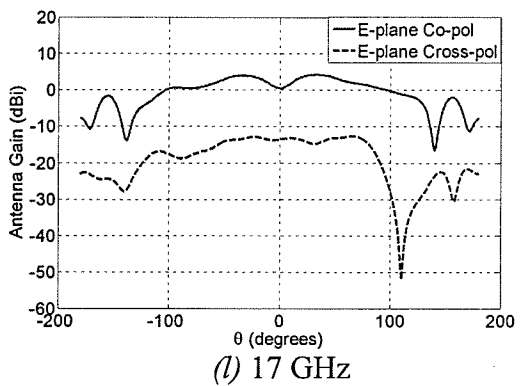
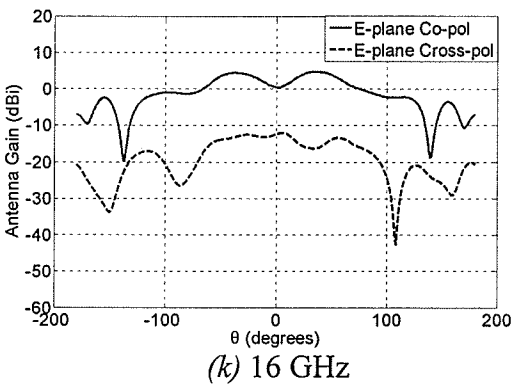
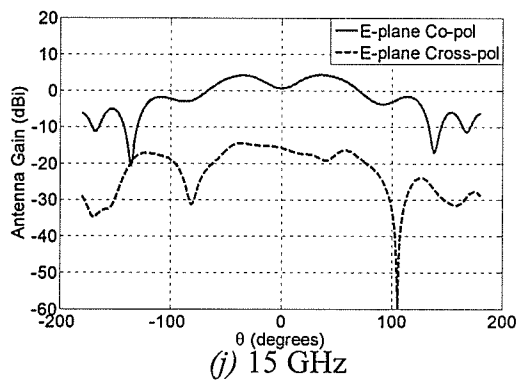
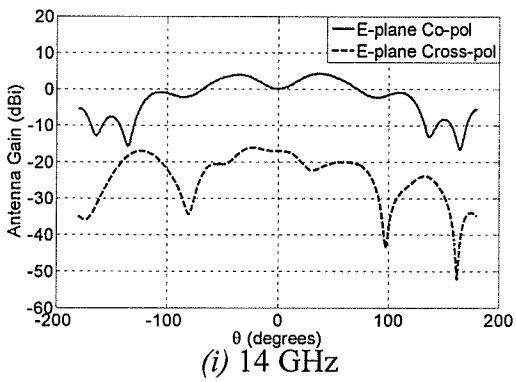
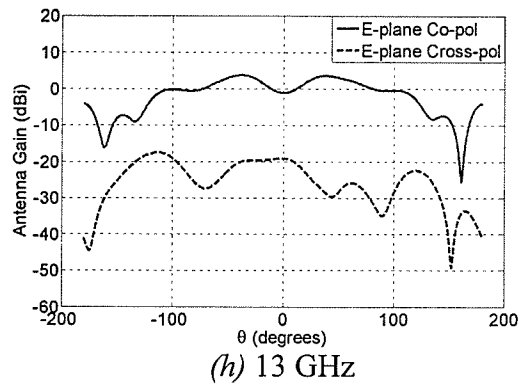
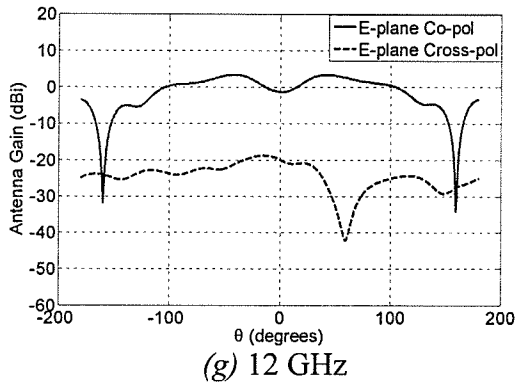


Fig. 4.8 (g)-(n)

Fig. 4.8 contd.

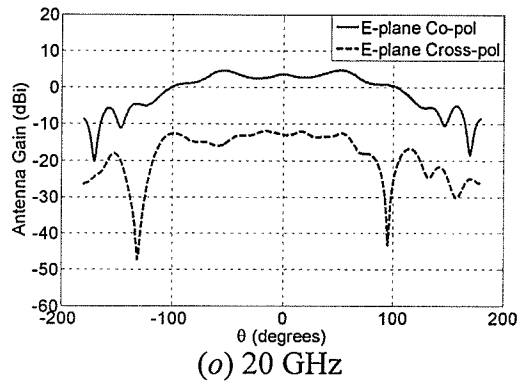


Fig. 4.8 Simulated E-plane ($\phi=90^\circ$ plane) co-pol and cross-pol patterns of Model 5 shown in Fig. 4.6 and described by (4.2)

Tables 4.5 and 4.6 summarize the important E-plane co-pol and cross-pol patterns characteristics.

Frequency (GHz)	Boresight gain (dBi)	Peak gain (dBi)	Position of Peak gain	3 dB BW	10 dB BW
6	1.862	1.862	-1°	98°	233°
7	2.127	2.129	-1°	76°	253°
8	2.903	2.907	-1°	66°	273°
9	3.732	3.732	0°	67°	288°
10	2.830	2.830	0°	193°	300°
11	0.503	2.838	-48°	278°	306°
12	0.497	3.367	-44°	238°	300°
13	-0.302	3.980	-40°	245°	302°
14	-0.609	4.553	-38°	248°	291°
15	-0.249	4.817	-35°	246°	264°
16	0.655	4.796	34°	243°	265°
17	0.681	4.646	33°	244°	268°
18	1.120	4.046	32°	241°	274°
19	2.186	4.732	53°	227°	277°
20	3.138	5.357	50°	208°	281°

Table 4.5 Summary of E-plane co-pol pattern characteristics of Model 5 given in Fig. 4.6 and described by (4.2)

Frequency (GHz)	Boresight Cross-pol (dBi)	Peak Cross-pol (dBi)	Position of Peak Cross-pol
6	-25.770	-25.761	3°
7	-25.684	-24.964	152°
8	-26.081	-25.138	151°
9	-25.409	-25.203	-10°
10	-26.065	-19.753	-18°
11	-19.786	-19.726	-4°
12	-20.877	-20.458	-13°
13	-20.188	-19.424	-16°
14	-17.686	-16.586	-16°
15	-15.623	-14.887	-26°
16	-13.881	-12.623	-19°
17	-13.479	-12.155	-33°
18	-13.419	-12.435	61°
19	-13.204	-12.169	-98°
20	-12.202	-12.177	-2°

Table 4.6 Summary of E-plane cross-pol pattern characteristics of Model 5 given in Fig. 4.6 and described by (4.2)

From Table 4.5 it can be observed that the boresight and peak gains of Model 5 are slightly lower than that of Model 1 indicating that the decrease in rate of taper reduces the gain of the antenna.

The H-plane co-pol and cross-pol patterns of Model 5 are given in Fig. 4.9.

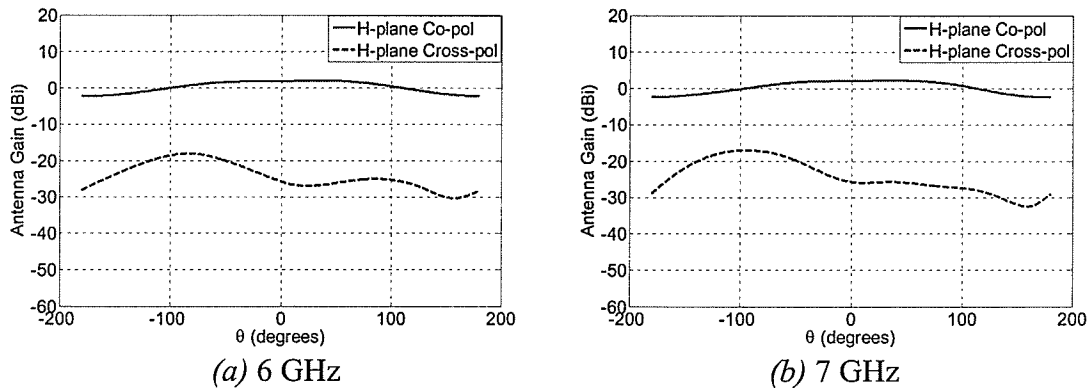
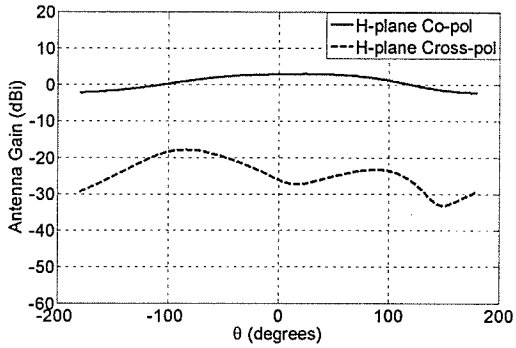
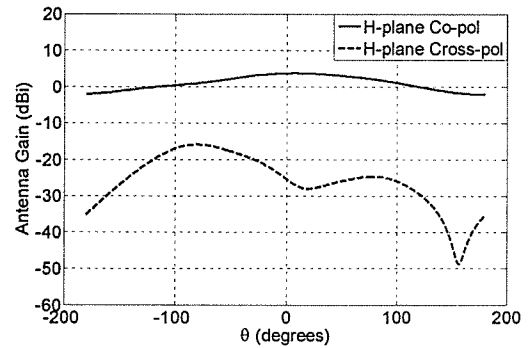


Fig. 4.9 (a), (b)

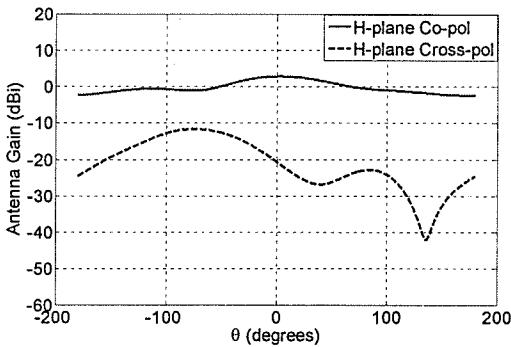
Fig. 4.9 contd.



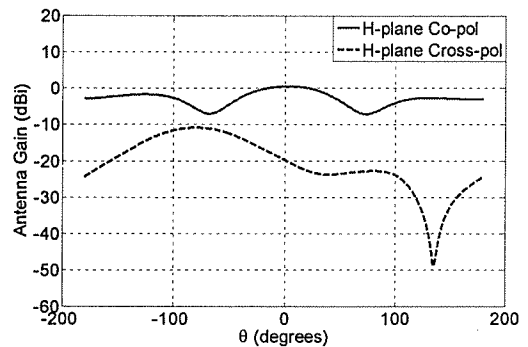
(c) 8 GHz



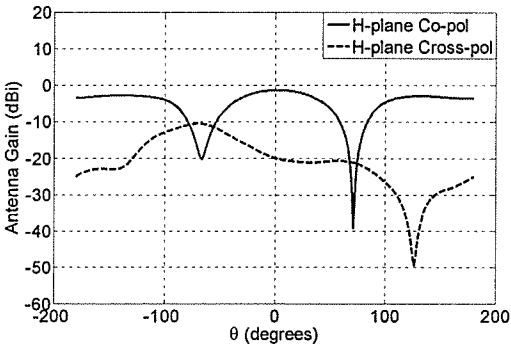
(d) 9 GHz



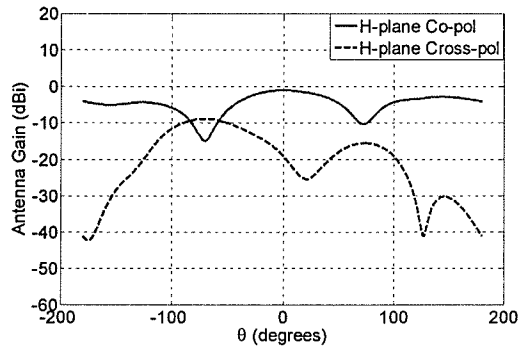
(e) 10 GHz



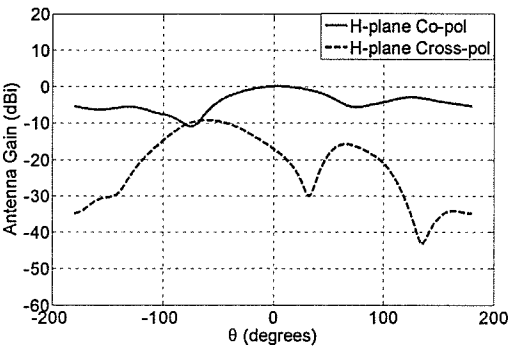
(f) 11 GHz



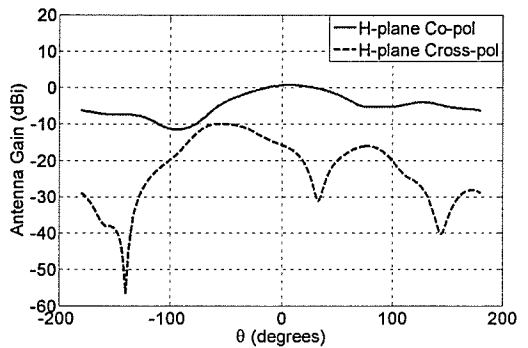
(g) 12 GHz



(h) 13 GHz



(i) 14 GHz



(j) 15 GHz

Fig. 4.9 (c)-(j)

Fig. 4.9 contd.

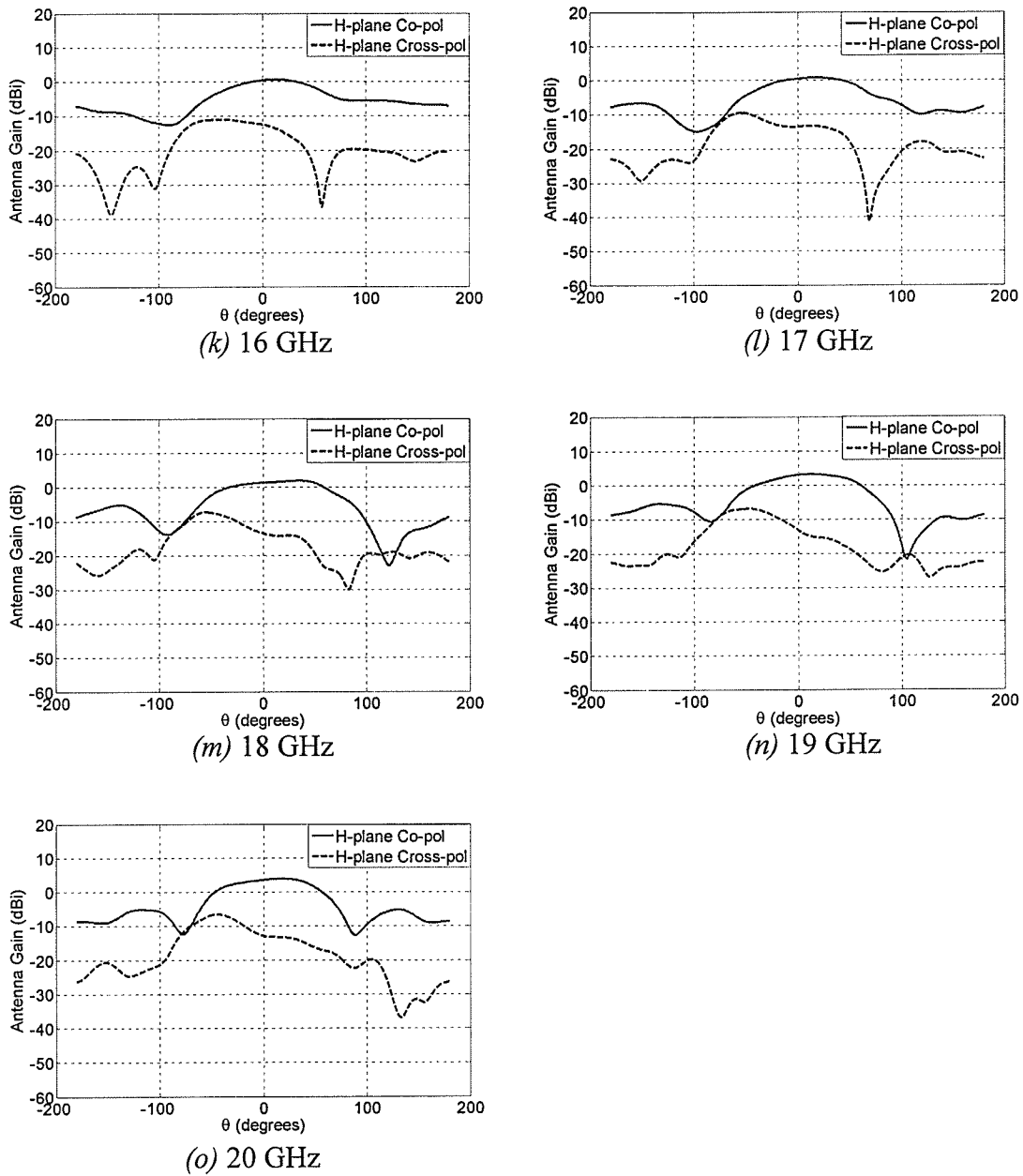


Fig. 4.9 Simulated H-plane ($\phi=0^\circ$ plane) co-pol and cross-pol patterns of Model 5 shown in Fig. 4.6 and described by (4.2)

A summary of the important characteristics of the H-plane co-pol and cross-pol patterns are given in Tables 4.7 and 4.8.

Frequency (GHz)	Boresight gain (dBi)	Peak gain (dBi)	Position of Peak gain	3 dB BW	10 dB BW
6	1.862	2.024	37°	263°	--
7	2.127	2.274	36°	247°	--
8	2.903	2.989	24°	230°	--
9	3.732	3.759	8°	198°	--
10	2.830	2.840	3°	124°	--
11	0.503	0.518	3°	83°	--
12	0.497	0.513	4°	96°	132°
13	-0.302	-0.272	5°	84°	127°
14	-0.609	-0.531	8°	88°	--
15	-0.249	-0.176	8°	92°	--
16	0.655	0.777	11°	93°	--
17	0.681	1.016	18°	90°	--
18	1.120	1.618	23°	86°	177°
19	2.186	2.529	19°	105°	163°
20	3.138	3.447	17°	96°	144°

Table 4.7 Summary of H-plane co-pol pattern characteristics of Model 5 given in Fig. 4.6 and described by (4.2)

Frequency (GHz)	Boresight Cross-pol (dBi)	Peak Cross-pol (dBi)	Position of Peak Cross-pol
6	-25.770	-18.076	-84°
7	-25.684	-16.977	-95°
8	-26.081	-17.854	-84°
9	-25.409	-15.837	-81°
10	-26.065	-11.672	-76°
11	-19.786	-10.922	-81°
12	-20.877	-10.756	-76°
13	-20.188	-11.019	-70°
14	-17.686	-10.469	-58°
15	-15.623	-10.045	-56°
16	-13.881	-10.955	-54°
17	-13.479	-9.497	-55°
18	-13.419	-7.409	-57°
19	-13.204	-6.300	-52°
20	-12.202	-5.975	-50°

Table 4.8 Summary of H-plane cross-pol pattern characteristics of Model 5 given in Fig. 4.6 and described by (4.2)

4.3.3 Study of Phase centre for Model 5

Figure 4.10 (a) shows a plot of the Average E and H-plane phase centre locations at each frequency and Fig. 4.10 (b) depicts these locations on the antenna geometry. It was found that the maximum tolerable phase difference $\Delta\phi$ for this model was 30° , indicating that the decrease in the rate of taper of the antenna flare had no effect on the variation of phase of the principle planes' far-field co-pol radiation patterns at the phase centre location.

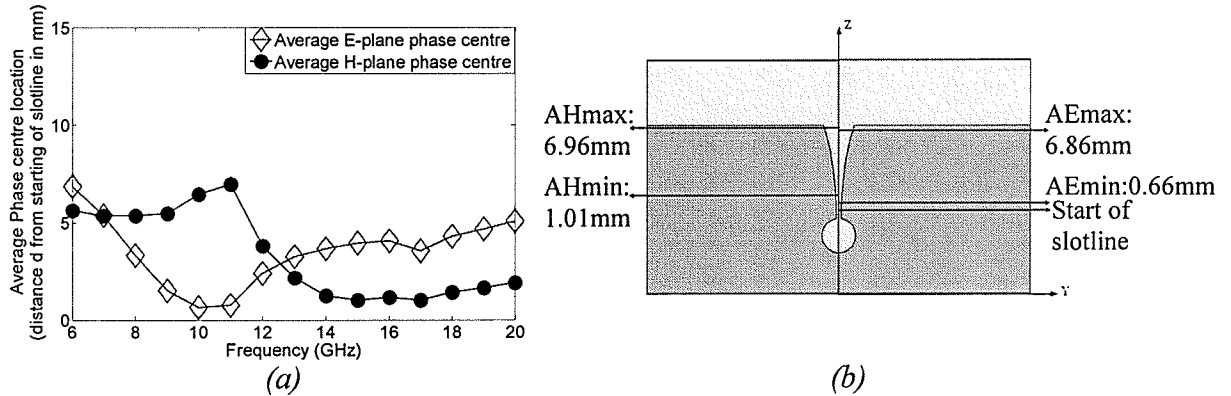


Fig. 4.10 (a) plot of Average E and H planes' phase centre location (for a maximum tolerable phase difference $\Delta\phi=30^\circ$ and θ ranging from 0 to 60°) of Model 5 given in Fig. 4.6; (b) geometry of Model 5 indicating the portion of antenna axis where these Average phase centres lie for both E and H planes

From Fig. 4.10 (a) it can be seen that similar to the previous models, the Average E and H-plane phase centres are more stable in the higher frequencies of operation for this model as well. The maximum distance between the Average E and H-plane phase centres is 6.30 mm.

4.4 Width Truncated Model (Model 6)

4.4.1 Antenna Model

Up until this point, the study carried out was focused on different types of tapers for the antenna flare. Another study of interest was to observe the effect of variation of antenna width on the original model (Model 1) from [9]. In order to do this, a parametric study was carried out in which the antenna was truncated to different widths and the effect of each truncation on the far-field radiation pattern was observed. From this study, the antenna model with optimum gain performance in both principle planes was chosen and is presented in this section, while all the other truncated models are excluded for the sake of brevity.

The truncated model (Model 6) is given in Fig. 4.11. In this model, the width of the antenna has been reduced by 10.16 mm on either side.

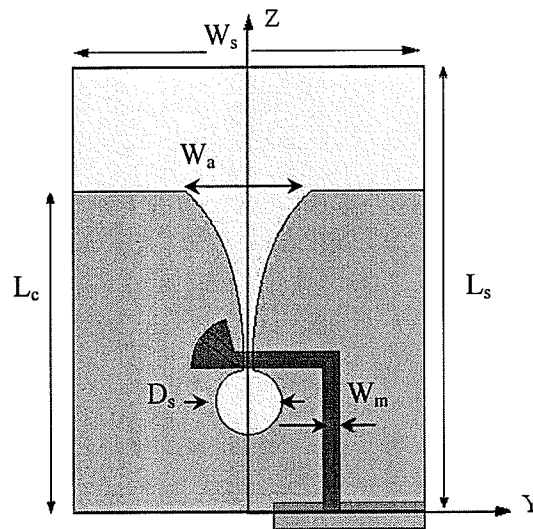


Fig. 4.11 The geometry of the Vivaldi antenna (Model 6) including the microstrip feed along with the co-ordinate system: $L_s = 22.86\text{mm}$, $W_s = 17.94\text{mm}$, $L_c = 16.51\text{mm}$, $W_m = 0.81\text{mm}$, $W_a = 6.35\text{mm}$, $D_s = 3.30\text{mm}$, with $\epsilon_r = 2.2$, $h = 0.508\text{mm}$ and $\tan\delta = 0.001$

The equation describing the flare and all other parameters except antenna width are identical to that of Model 1.

4.4.2 Antenna Performance

The simulated S_{11} and input impedance plots of Model 6 are given in Fig. 4.12. From the figure it is observed that its performance is quite similar to that of original model (Model 1) through out the frequency range under consideration, indicating that the truncation did not significantly alter the return loss of the antenna.

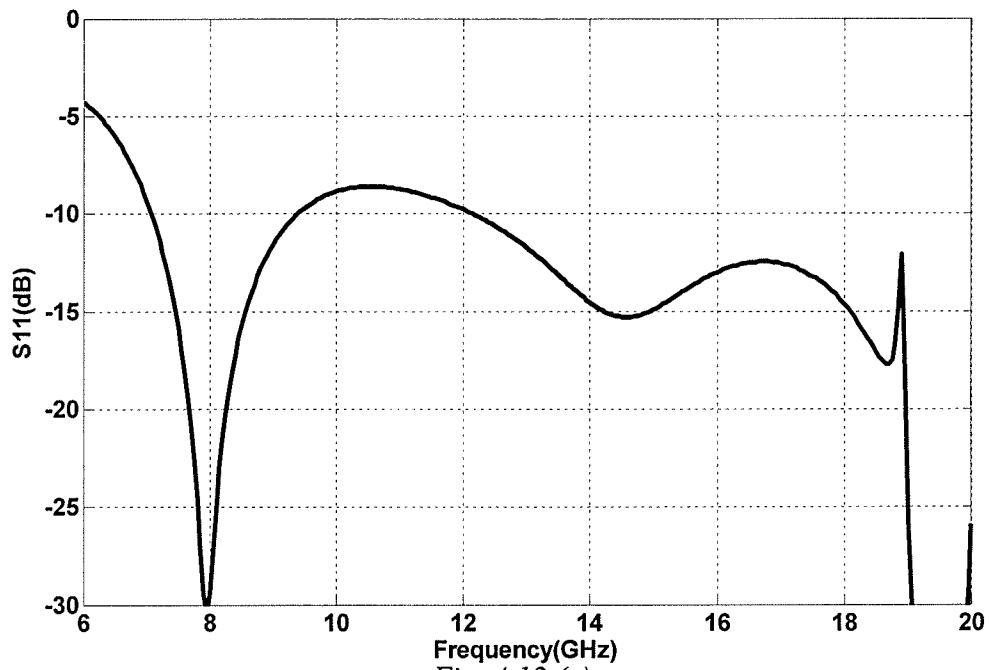


Fig. 4.12 (a)

Fig. 4.12 contd.

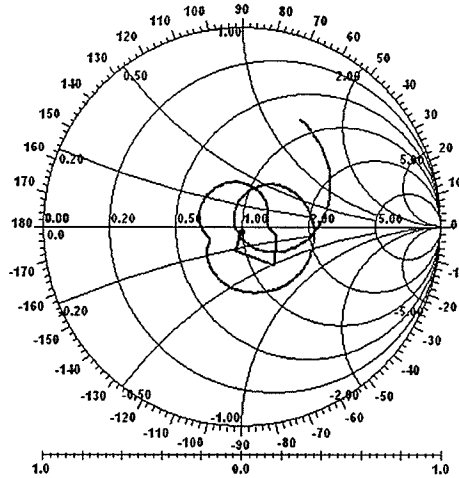


Fig. 4.12 (b)

Fig. 4.12 Simulated (a) S_{11} and (b) input impedance plot measured with respect to 75Ω for antenna Model 6 shown in Fig. 4.11 and described by (3.1)

The E-plane co-pol and cross-pol patterns of this model are given in Fig. 4.13. It is interesting to note that the null at boresight in the co-pol patterns which appeared with increase in frequency operation for all the previous models does not appear in this model.

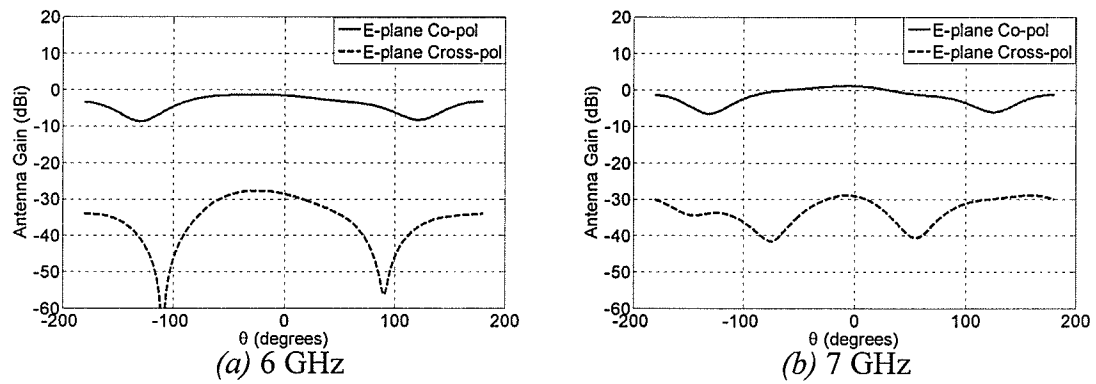
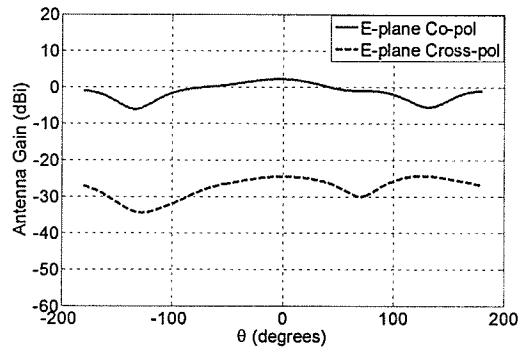
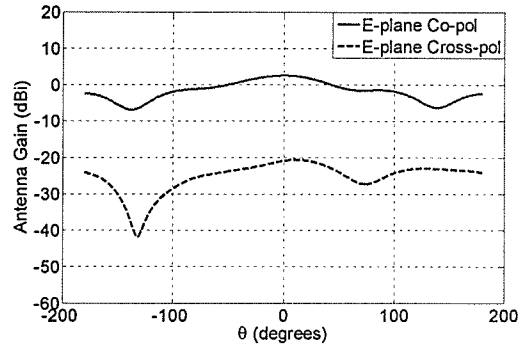


Fig. 4.13 (a), (b)

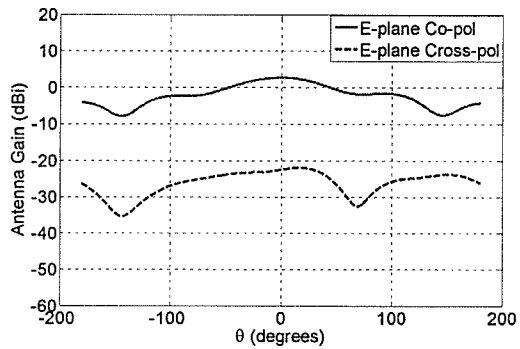
Fig. 4.13 contd.



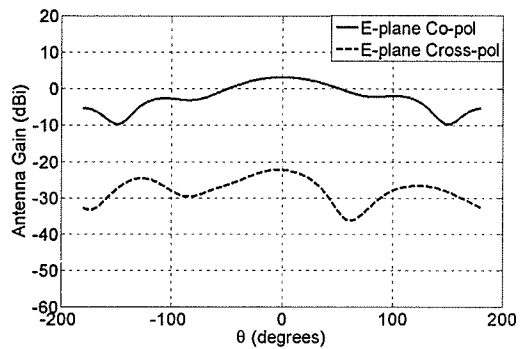
(c) 8 GHz



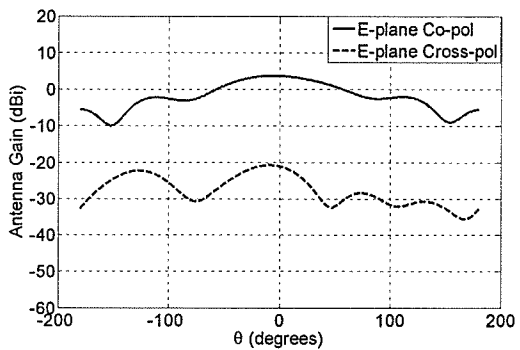
(d) 9 GHz



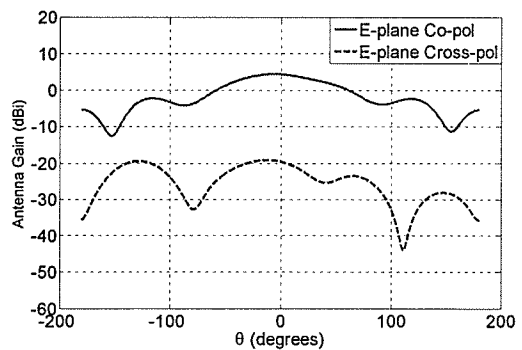
(e) 10 GHz



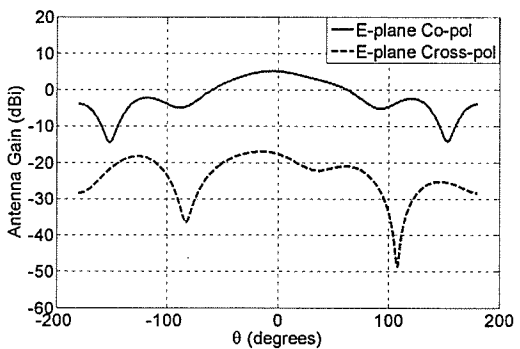
(f) 11 GHz



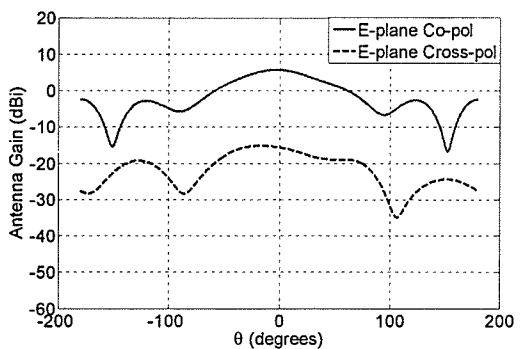
(g) 12 GHz



(h) 13 GHz



(i) 14 GHz



(j) 15 GHz

Fig. 4.13 (c)-(j)

Fig. 4.13 contd.

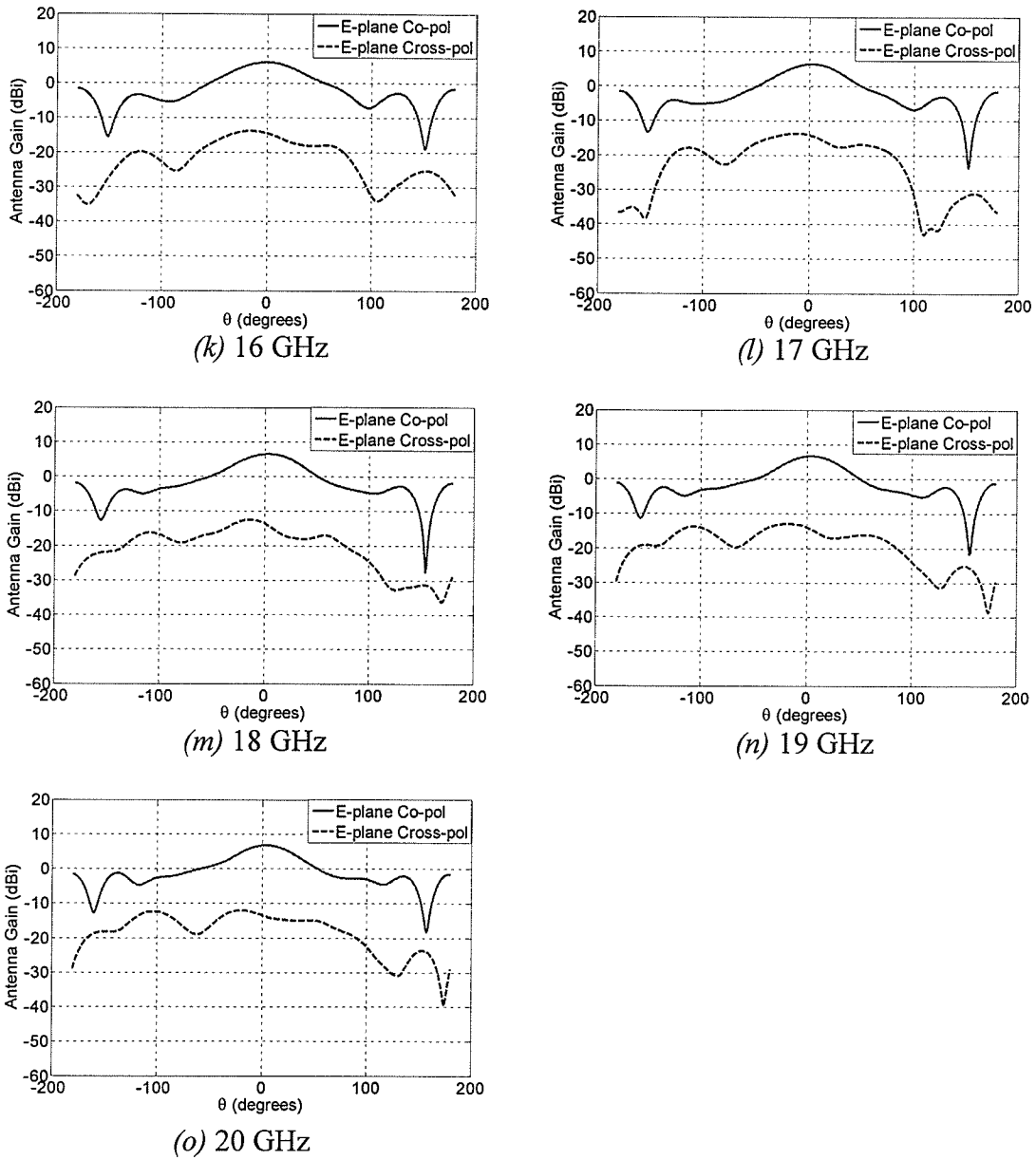


Fig. 4.13 Simulated E-plane ($\phi=90^\circ$ plane) co-pol and cross-pol patterns of Model 6 shown in Fig. 4.11

Tables 4.9 and 4.10 summarize the important E-plane co-pol and cross-pol pattern characteristics of Model 6.

Frequency (GHz)	Boresight gain (dBi)	Peak gain (dBi)	Position of Peak gain	3 dB BW	10 dB BW
6	-1.528	-1.318	-24°	184°	--
7	1.131	1.162	-6°	173°	--
8	2.253	2.263	-3°	146°	--
9	2.551	2.551	1°	116°	--
10	2.717	2.717	0°	97°	280°
11	3.137	3.137	0°	98°	273°
12	3.712	3.751	-6°	103°	281°
13	4.382	4.440	-6°	100°	276°
14	5.099	5.152	-5°	111°	175°
15	5.691	5.711	-3°	78°	160°
16	6.069	6.069	0°	68°	159°
17	6.352	6.381	3°	61°	155°
18	6.491	6.538	4°	64°	182°
19	6.645	6.704	4°	59°	186°
20	6.728	6.776	4°	59°	208°

Table 4.9 Summary of E-plane co-pol pattern characteristics of Model 6 given in Fig. 4.11

Frequency (GHz)	Boresight Cross-pol (dBi)	Peak Cross-pol (dBi)	Position of Peak Cross-pol
6	-28.600	-27.686	-25°
7	-29.095	-28.942	-7°
8	-24.444	-24.304	126°
9	-20.944	-20.646	12°
10	-22.449	-21.883	16°
11	-22.261	-22.219	-4°
12	-21.075	-20.752	-9°
13	-19.603	-19.171	-12°
14	-17.641	-16.999	-15°
15	-15.672	-15.191	-17°
16	-14.437	-13.797	-15°
17	-14.090	-13.688	-12°
18	-13.543	-12.489	-14°
19	-13.900	-12.892	-18°
20	-13.461	-12.022	-20°

Table 4.10 Summary of E-plane cross-pol pattern characteristics of Model 6 given in Fig. 4.11

From Table 4.9 it can be observed that there is a significant increase (about 3 dB at certain frequencies of operation) in boresight as well as peak gain of the E-plane radiation patterns. Also, as previously mentioned, the null that appeared at boresight in the co-pol patterns with increase in frequency of operation for all other models does not occur for this model as can be seen in Fig. 4.13.

For a better understanding of this increase in gain, the simulated surface current density (both magnitude and direction) distribution on the copper cladding of the original model (Model 1) as well as on Model 6 are given in Fig. 4.14 and Fig. 4.15 respectively for a frequency of 15 GHz.

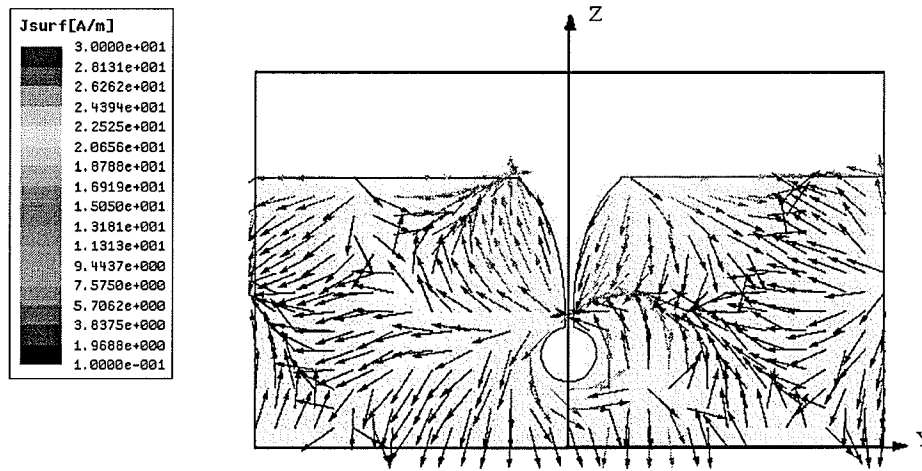


Fig. 4.14 Simulated surface current at 15 GHz on the copper cladding of Model 1 given in Fig. 3.1 and described by (3.1)

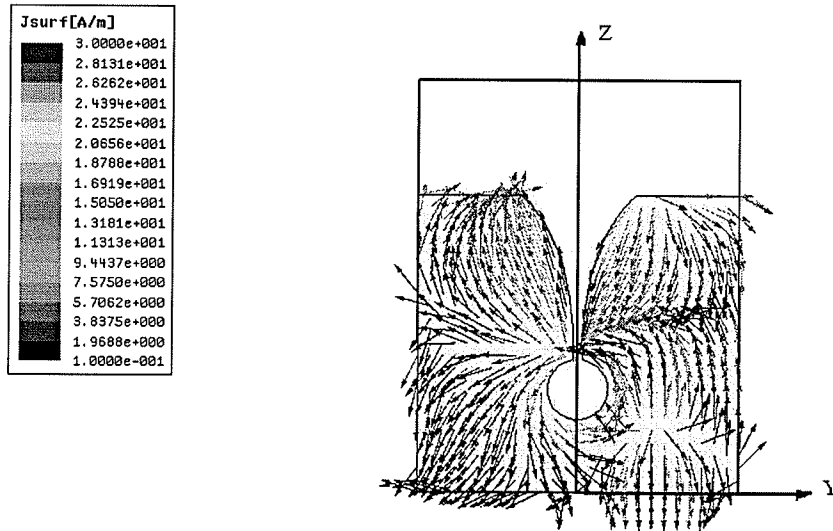


Fig. 4.15 Simulated surface current at 15 GHz on the copper cladding of Model 6 given in Fig. 4.11 and described by (3.1)

From Fig. 4.14 it can be observed that there is a phase reversal in the current distribution on the metallization of the Model 1 on either side of its axis (i.e., z -axis). This results in a cancellation of currents and therefore reduces the gain of the antenna, and is also the cause for the appearance of a null at boresight in the E-plane co-pol patterns. Also, from Fig. 4.15 it can be seen that the current density magnitude variation along the y -axis for Model 6 from the edge of the flare to the end of the antenna is lower than that of Model 1 in Fig. 4.14. Due to this, Model 6 exhibits higher gain than that of Model 1.

The H-plane co-pol and cross-pol patterns of Model 6 are given in Fig. 4.16. From the figure, it is clear that the truncation of the width of the antenna does not affect the shape of the co-pol radiation patterns.

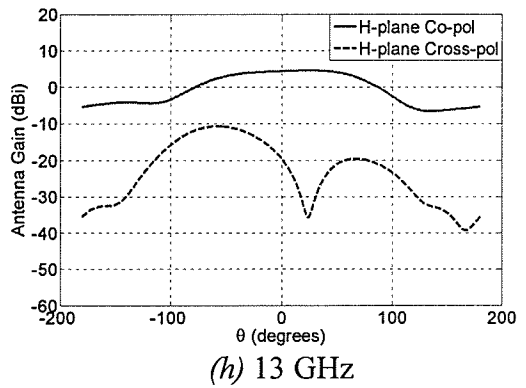
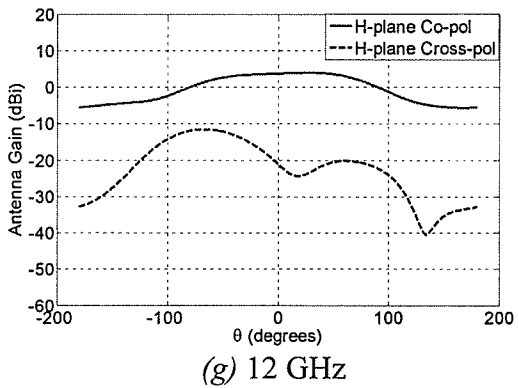
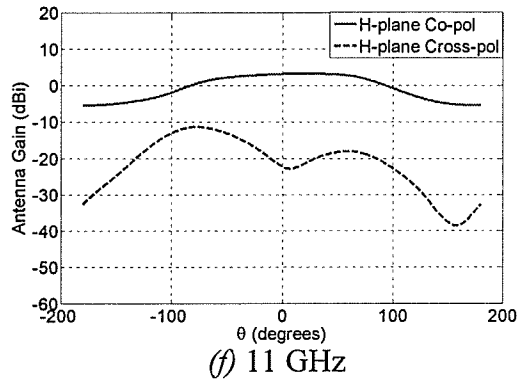
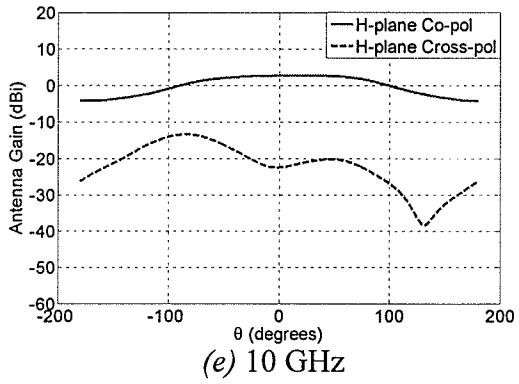
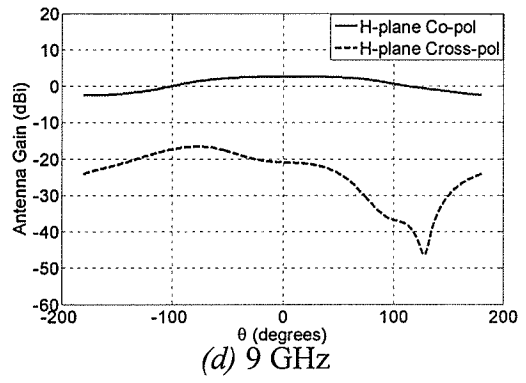
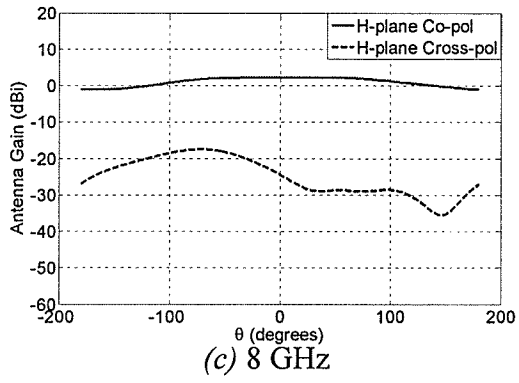
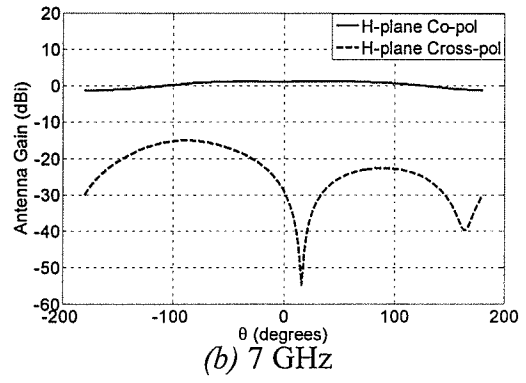
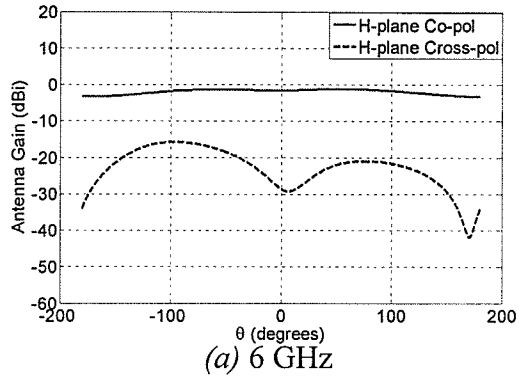


Fig. 4.16 (a)-(d)

Fig. 4.16 contd.

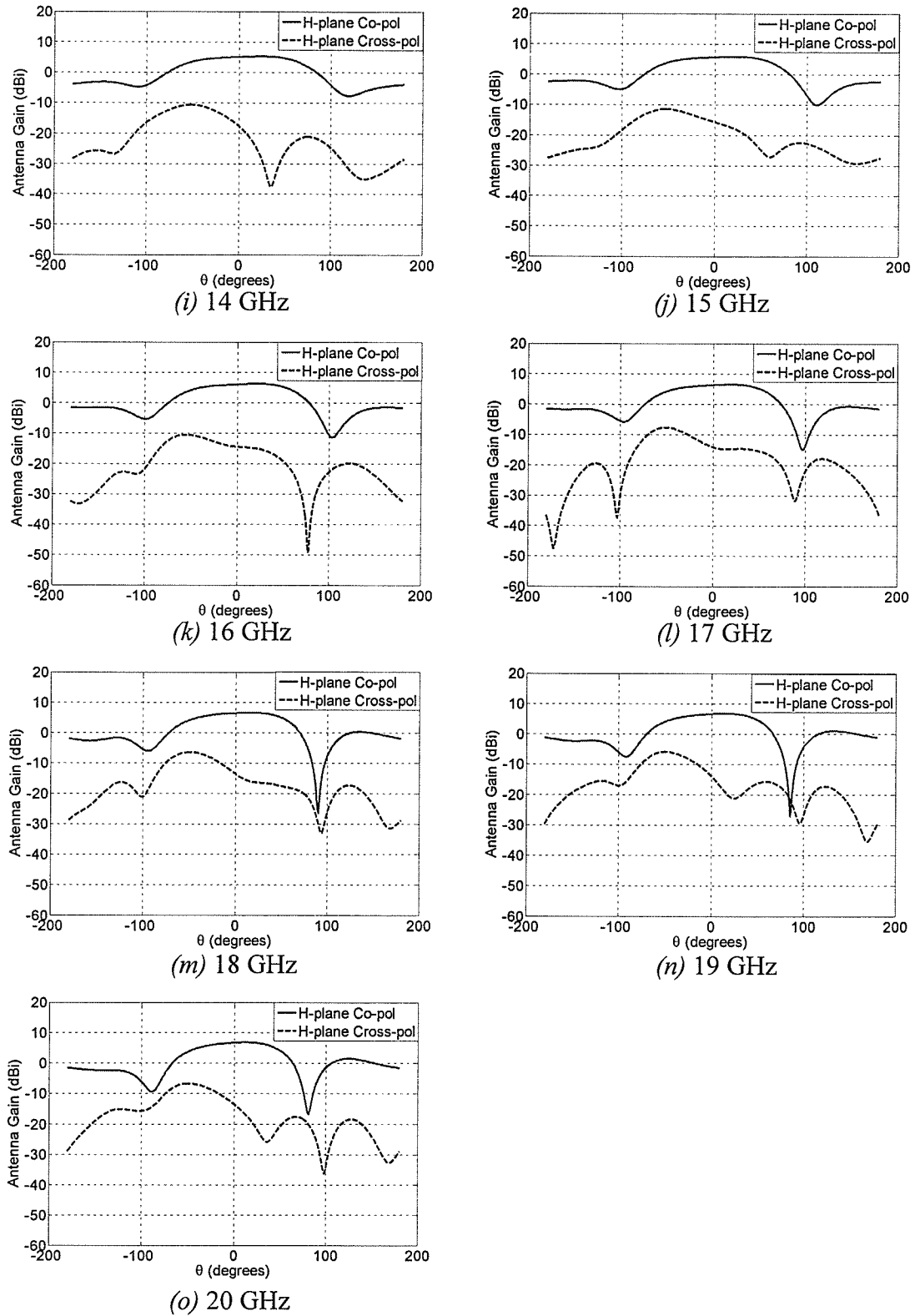


Fig. 4.16 Simulated H-plane ($\phi=0^\circ$ plane) co-pol and cross-pol patterns of Model 6 shown in Fig. 4.11

Tables 4.11 and 4.12 summarize the important characteristics of the H-plane co-pol and cross-pol patterns of Model 6.

Frequency (GHz)	Boresight gain (dBi)	Peak gain (dBi)	Position of Peak gain	3 dB BW	10 dB BW
6	-1.528	-1.163	57°	--	--
7	1.131	1.249	40°	--	--
8	2.253	2.347	36°	308°	--
9	2.551	2.578	23°	230°	--
10	2.717	2.800	24°	197°	--
11	3.137	3.221	21°	174°	--
12	3.712	3.931	28°	157°	--
13	4.382	4.571	25°	145°	--
14	5.099	5.313	25°	138°	--
15	5.691	5.878	23°	132°	200°
16	6.069	6.295	22°	125°	177°
17	6.352	6.556	20°	119°	167°
18	6.491	6.622	17°	114°	160°
19	6.645	6.783	14°	109°	152°
20	6.728	6.839	12°	102°	144°

Table 4.11 Summary of H-plane co-pol pattern characteristics of Model 6 given in Fig. 4.11

Frequency (GHz)	Boresight Cross-pol (dBi)	Peak Cross-pol (dBi)	Position of Peak Cross-pol
6	-28.600	-15.729	-97°
7	-29.095	-15.047	-88°
8	-24.444	-17.499	-71°
9	-20.944	-16.574	-77°
10	-22.449	-13.342	-84°
11	-22.261	-11.340	-77°
12	-21.075	-11.575	-67°
13	-19.603	-10.724	-58°
14	-17.641	-10.625	-52°
15	-15.672	-11.461	-52°
16	-14.437	-10.543	-56°
17	-14.090	-7.621	-51°
18	-13.543	-6.405	-49°
19	-13.900	-5.870	-50°
20	-13.461	-6.681	-50°

Table 4.12 Summary of H-plane cross-pol pattern characteristics of Model 6 given in Fig. 4.11

4.4.3 Study of Phase centre for Model 6

Figure 4.17 (a) shows a plot of the Average E and H-plane phase centre locations at each frequency and Fig. 4.17 (b) depicts these locations on the geometry of the antenna. Interestingly, it was found that the maximum tolerable phase difference $\Delta\phi$ for this model was 10° . This indicates that the truncation in width of the antenna resulted in a decrease in phase variation of the principle planes' far-field co-pol radiation patterns and hence led to more 'flat' co-pol phase patterns at the phase centre location; a requirement which is desirable.

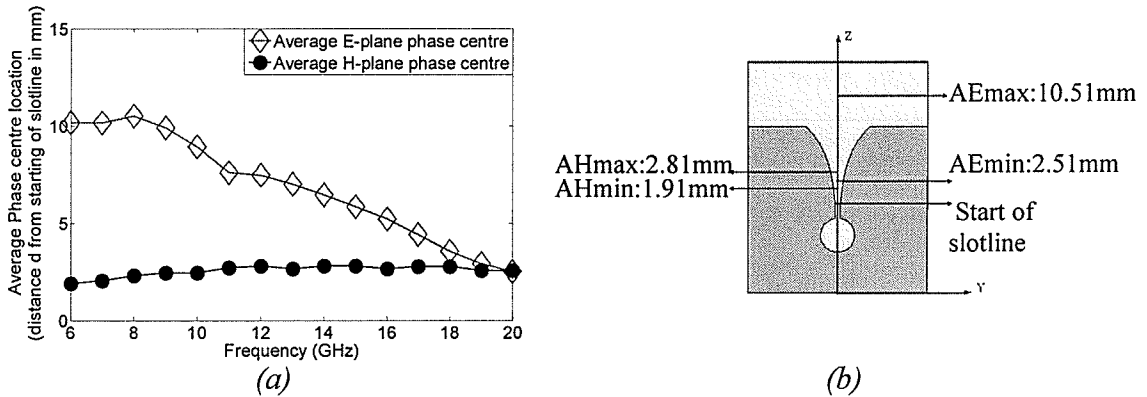


Fig. 4.17 (a) plot of Average E and H planes' phase centre location (for a maximum tolerable phase difference $\Delta\phi=10^\circ$ and θ ranging from 0 to 60°) of Model 6 given in Fig. 4.11; (b) geometry of Model 6 indicating the portion of antenna axis where these Average phase centres lie for both E and H planes

From Fig. 4.17 (a) it is observed that the Average H-plane phase centre is very stable through out the entire frequency range of operation. In the case of the Average E-plane phase centre, its behavior is comparatively more stable than the other models and tends to move closer to the Average H-plane phase centre with increase in frequency. The maximum distance of separation between the Average E and H-plane phase centres is

8.60 mm. Though this distance is larger than any of the previous models, the fact that this model exhibits the best stability in E and H-plane phase centres through out the entire frequency range of operation, and also the smallest $\Delta\phi$ of 10° , it may be considered to have the optimum phase centre behavior amongst all six models presented in this chapter and the previous.

From an overall inspection of the parametric study performed on the single sided Vivaldi antenna of [9], it may be concluded that a compact model (i.e. Model 6) with optimum gain and phase centre behavior was developed and that it exhibits a performance superior to that of the remaining five models.

4.5 Summary

In this chapter a parametric study of a single sided Vivaldi antenna was carried out by varying the rate of taper of its flare and also by truncating its width. The simulated return loss plots and radiation patterns for all three models were presented. It was observed that a truncation in width of the antenna (Model 6) led to a significant increase in its gain and also to a disappearance of the null at boresight in the E-plane co-pol patterns which was observed in all the previous models. A study of the phase centre location for all three models was carried out. It was seen that Model 6 had the smallest maximum tolerable phase difference $\Delta\phi$ out of all six models. The phase centre (in both principle planes) behavior for Model 6 through out the entire considered frequency range was also observed to be the most stable. From the radiation patterns and phase centre study, it may be concluded that Model 6 exhibits the best performance out of all six models presented in chapters three and four and hence may be considered the optimum design for the single sided Vivaldi antenna chosen for study.

CHAPTER 5

STUDY OF BALANCED ANTIPODAL VIVALDI ANTENNA

5.1 Introduction

In the previous two chapters, a single sided Vivaldi antenna fed by a microstrip line was investigated. In this chapter, a balanced antipodal Vivaldi antenna developed from the compact Model 6 of chapter four is first studied. A balanced antipodal Vivaldi was chosen as opposed to an antipodal Vivaldi due to its better cross-polarization performance as mentioned in chapter two. Next, a balanced antipodal Vivaldi antenna with a larger aperture was studied. Simulations were again carried out using Ansoft HFSS v 10.1. While conducting this study, it was observed that elongation and shaping of the supporting substrate led to an increase in the gain of the antenna. Models implementing these two techniques are also presented in this chapter.

5.2 Balanced Antipodal Vivaldi Antenna

5.2.1 Antenna Model 1

As previously described in chapter two, a balanced antipodal Vivaldi antenna is a triplate structure which consists of a stripline feed to balanced twin line to balanced Vivaldi transition. This type of antenna overcomes the limitation of broadband performance due to slotline to feed line transition as seen in single as well as double sided Vivaldi antennas. Also, the balanced antipodal Vivaldi eliminates the E-field skew that is observed in the antipodal Vivaldi and hence has lower cross-polarization levels than the latter. From the parametric studies of chapters three and four, it was observed that Model

6 of chapter four exhibited the best performance with regard to both radiation characteristics as well as phase centre behavior, and was concluded to be the optimum design out of the six single sided Vivaldi models. Hence this model's dimensions were the first choice for the design of a balanced antipodal Vivaldi antenna.

Fig. 5.1 (a) gives a 3-dimensional view depicting the various layers of the balanced Vivaldi antenna that was simulated using HFSS v.10.1. A front view of this antenna is given in Fig. 5.1 (b). It must be noted that in reality, the middle flare cannot be seen, and that it is made visible here for a better understanding of the exponential taper of the antenna.

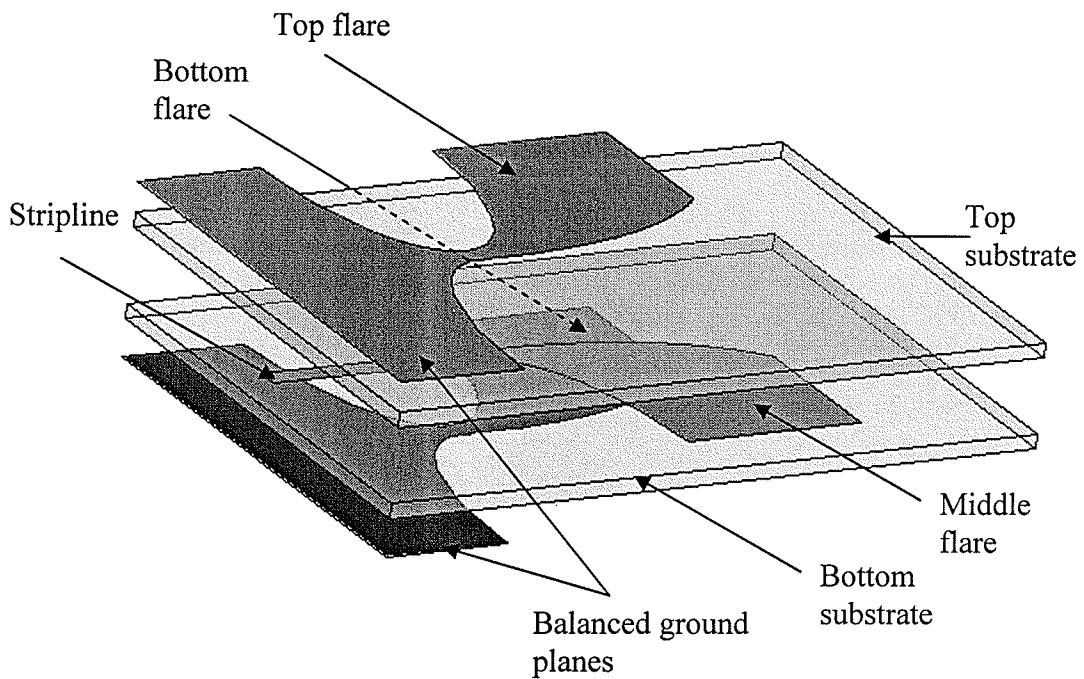


Fig. 5.1 (a)

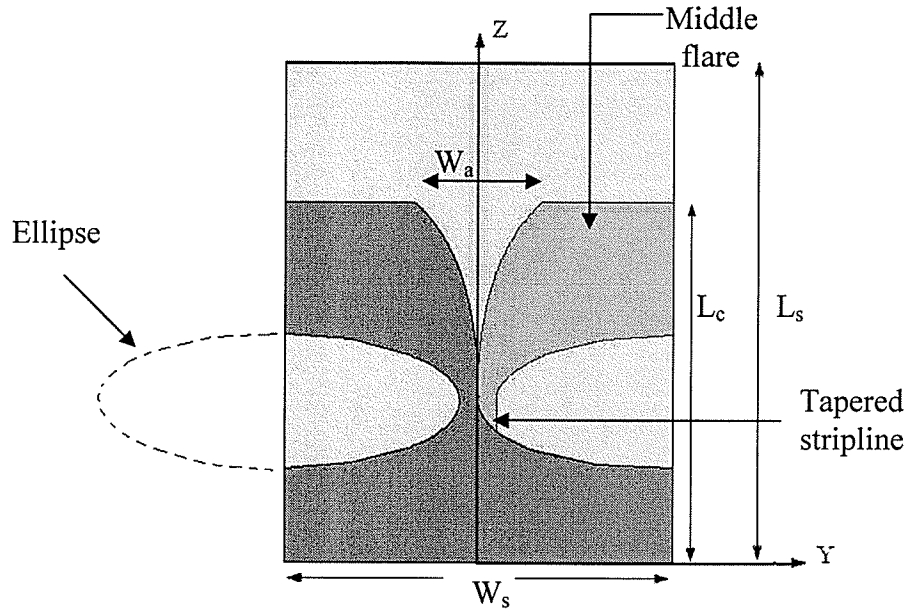


Fig. 5.1 (b)

Fig. 5.1 (a) Three dimensional view of the balanced antipodal Vivaldi depicting the various layers (b) Front view of the antenna along with co-ordinate system: $L_s = 22.86\text{mm}$, $W_s = 17.94\text{mm}$, $L_c = 16.51\text{mm}$, $W_a = 6.35\text{mm}$ and described by (3.1), with $\epsilon_r = 2.2$, height of each dielectric $h = 0.508\text{mm}$ and $\tan\delta = 0.001$

The equation describing the flare as well as the dielectric substrate properties of this antenna are identical to that of Model 6 of chapter four. The tapered stripline and shaped ground plane were modeled by subtracting an ellipse having a major axis of 8.05 mm and axial ratio of 0.38. These dimensions were chosen such that the width of the stripline feed was 0.84 mm so that it had a characteristic impedance of 50 Ω . Similar to the antenna models in the previous two chapters; a waveport was used to excite the feed line.

5.2.2 Antenna Performance

The simulated S_{11} and input impedance plots of this antenna are given in Fig. 5.2.

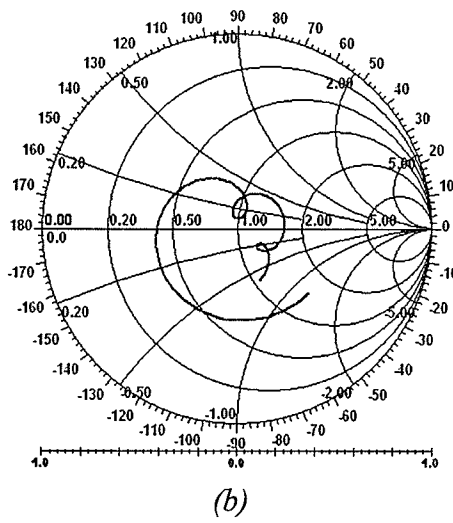
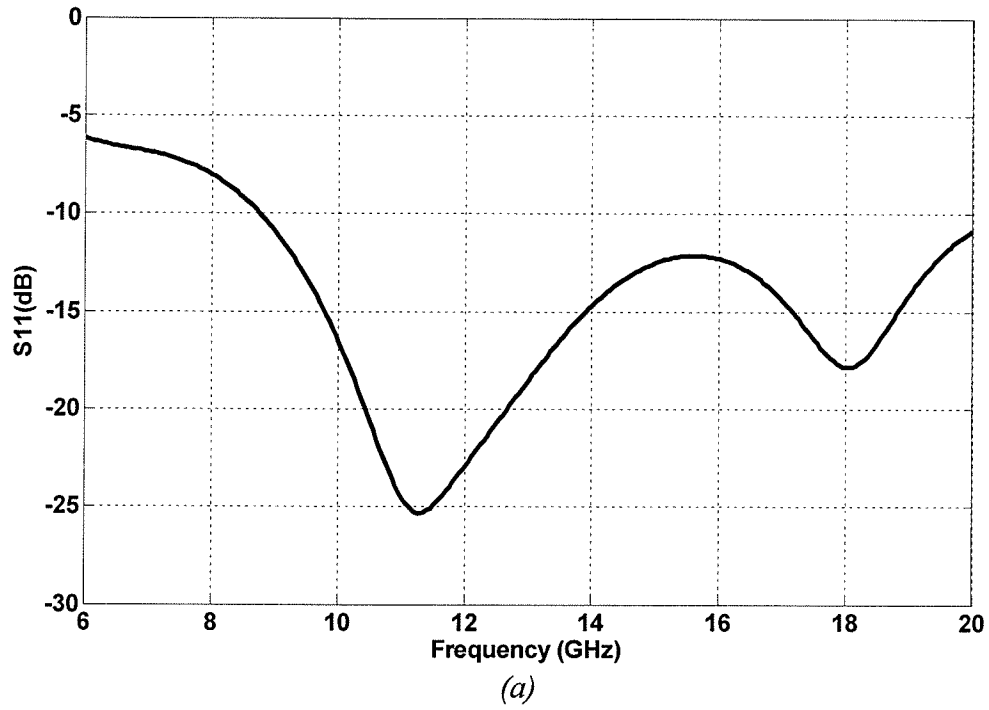


Fig. 5.2 Simulated (a) S_{11} and (b) input impedance plot measured with respect to 50Ω for the balanced antipodal Vivaldi antenna shown in Fig. 5.1 and described by (3.1)

From Fig. 5.2 (a) it can be seen that the S_{11} performance of this antenna is more or less like that of its single sided counterpart (Model 6). The Smith chart in Fig. 5.2 (b) indicates proper matching between the feed line and excitation.

The E-plane (yz plane, i.e. $\phi=90^\circ$ plane) radiation patterns are shown in Fig. 5.3. The geometrical asymmetry of the antenna (two metal flares etched in one direction, and one metal flare etched in the other direction) is believed to be the cause of the asymmetrical nature as well as squint in the co-pol patterns of this plane [20].

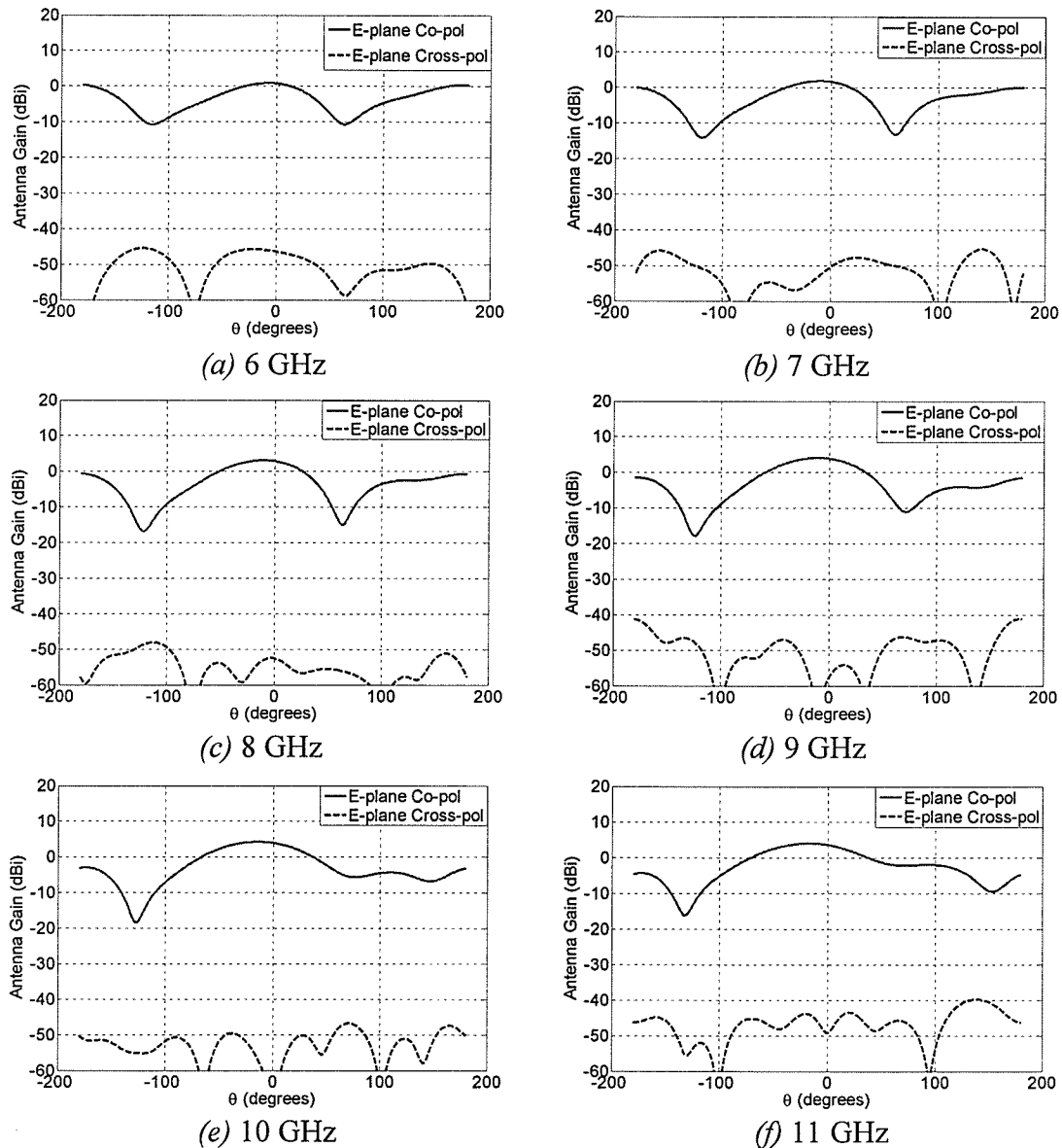


Fig. 5.3 (a)-(f)

Fig. 5.3 contd.

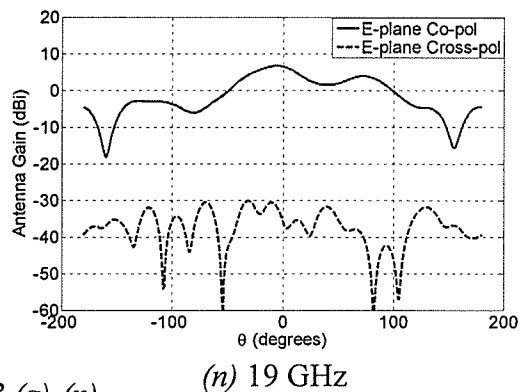
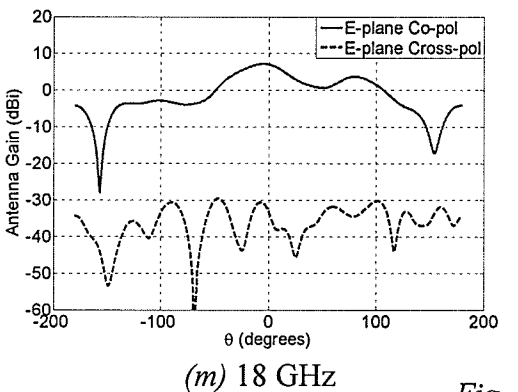
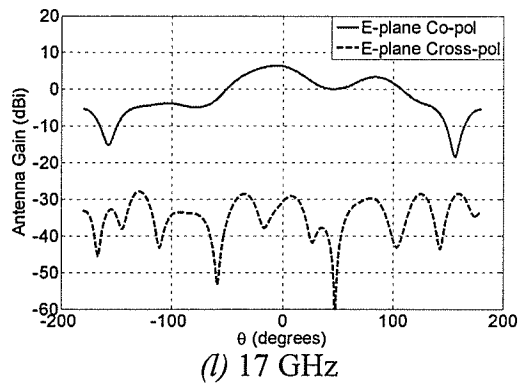
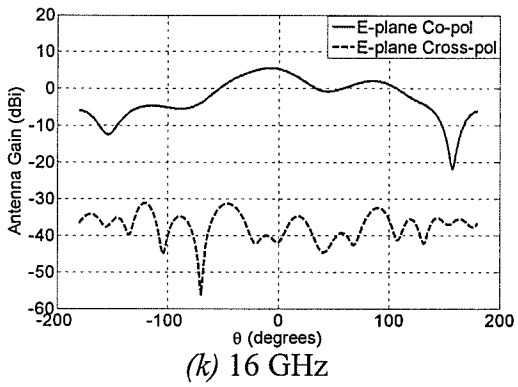
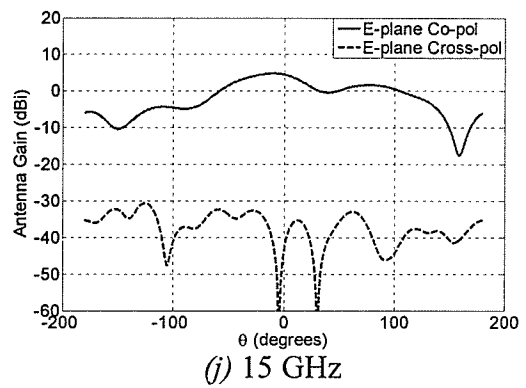
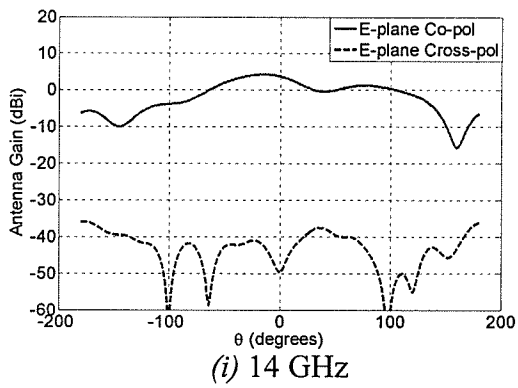
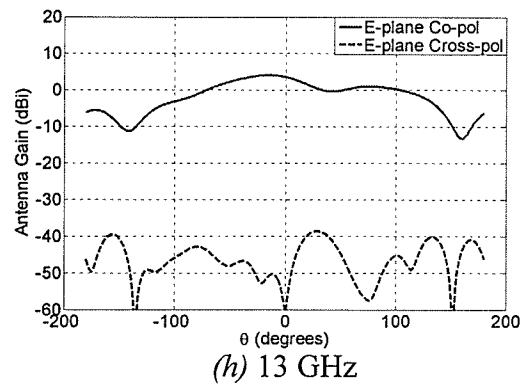
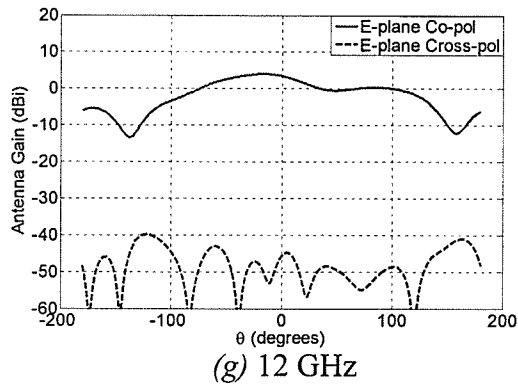


Fig. 5.3 (g)-(n)

Fig. 5.3 contd.

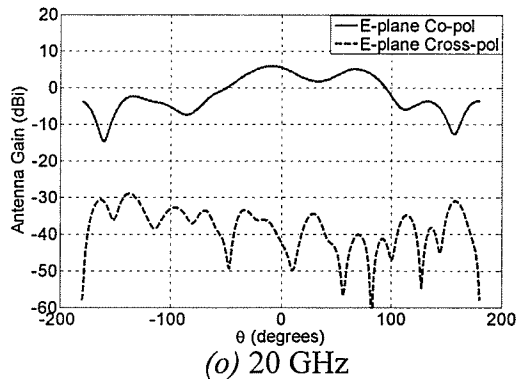


Fig. 5.3 Simulated E-plane ($\phi=90^\circ$ plane) co-pol and cross-pol patterns of the balanced antipodal Vivaldi shown in Fig. 5.1 and described by (3.1)

From the plots of Fig. 5.3 it can be clearly observed that the cross-pol levels of this antipodal Vivaldi antenna are much lower than those of Model 6 of chapter four. However, they increase with increase in frequency of operation. The important E-plane co-pol and cross-pol patterns characteristics are summarized in Tables 5.1 and 5.2 respectively.

Frequency (GHz)	Boresight gain (dBi)	Peak gain (dBi)	Position of Peak gain	3 dB BW	10 dB BW
6	0.780	0.891	-7°	81°	158°
7	1.704	1.908	-10°	79°	144°
8	2.883	3.102	-10°	79°	139°
9	3.921	4.132	-11°	82°	144°
10	3.960	4.275	-14°	91°	233°
11	3.689	4.106	-17°	99°	243°
12	3.463	3.999	-17°	101°	260°
13	3.594	4.106	-15°	94°	267°
14	3.736	4.286	-15°	84°	271°
15	4.513	4.840	-10°	72°	265°
16	5.336	5.540	-7°	64°	210°
17	6.290	6.439	-6°	68°	190°
18	7.069	7.220	-5°	53°	179°
19	6.611	6.830	-6°	54°	179°
20	5.565	5.987	-9°	60°	177°

Table 5.1 Summary of E-plane co-pol pattern characteristics of the balanced antipodal Vivaldi given in Fig. 5.1 and described by (3.1)

Frequency (GHz)	Boresight Cross-pol (dBi)	Peak Cross-pol (dBi)	Position of Peak Cross-pol
6	-46.346	-45.382	-124°
7	-50.377	-45.355	141°
8	-52.500	-48.059	-112°
9	-57.739	-41.120	178°
10	-72.157	-46.697	71°
11	-49.161	-39.730	139°
12	-45.564	-39.813	-122°
13	-60.260	-38.578	29°
14	-49.717	-35.869	-176°
15	-43.194	-30.594	-125°
16	-41.869	-31.151	-121°
17	-30.662	-27.862	-129°
18	-33.127	-29.563	-47°
19	-35.851	-30.057	-31°
20	-42.250	-28.888	-138°

Table 5.2 Summary of E-plane cross-pol pattern characteristics of the balanced antipodal Vivaldi given in Fig. 5.1 and described by (3.1)

From Table 5.1, it can be observed that the gain (boresight and peak) of the balanced antipodal Vivaldi throughout the considered frequency range is quite appreciable for such a compact design. Overall, its co-pol radiation characteristics are quite similar to those of Model 6 of chapter four. As previously mentioned, the cross-pol performance of this antenna is however significantly better than that of Model 6.

The H-plane (xz plane, i.e. $\phi=0^\circ$ plane) radiation patterns are given in Fig. 5.4.

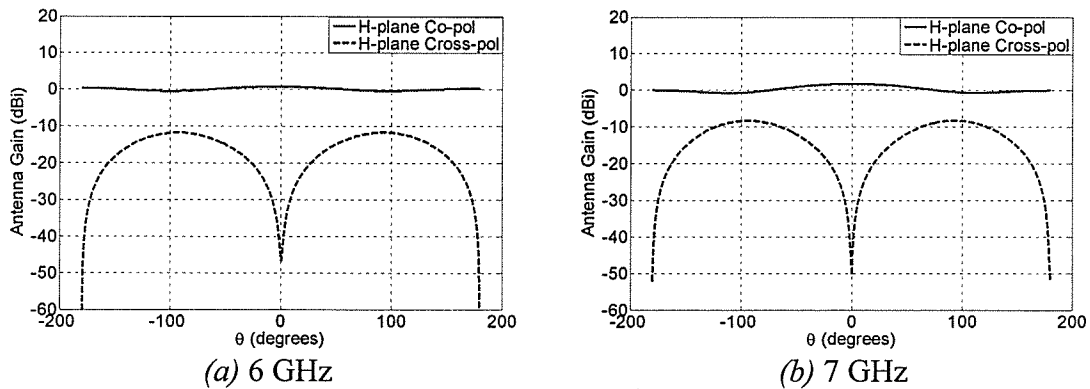


Fig. 5.4 (a), (b)

Fig. 5.4 contd.

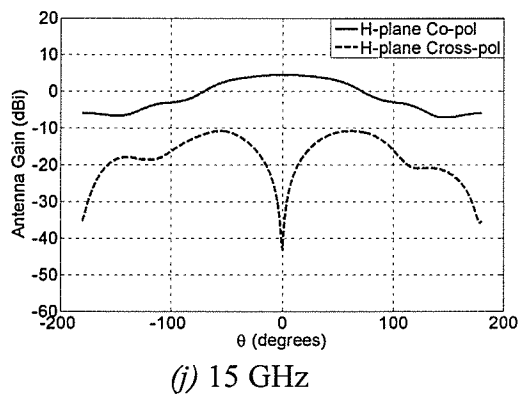
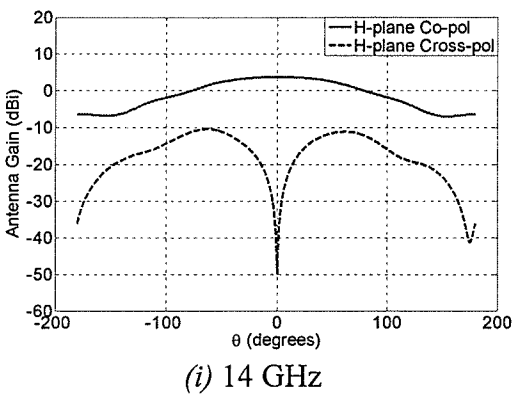
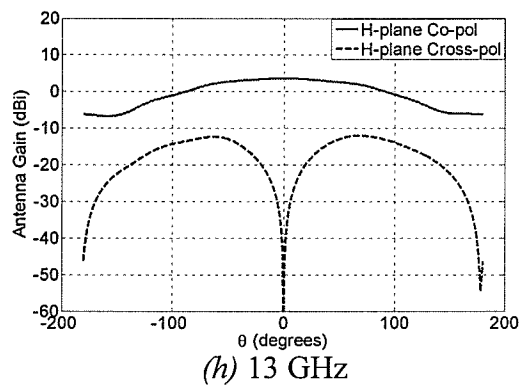
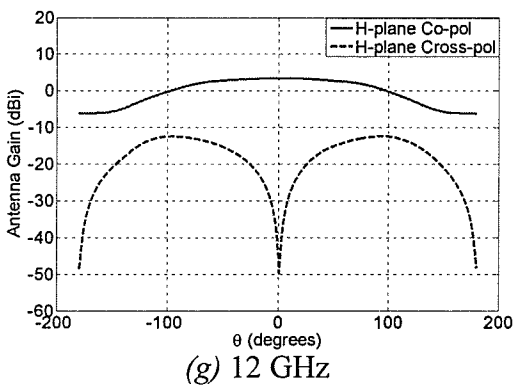
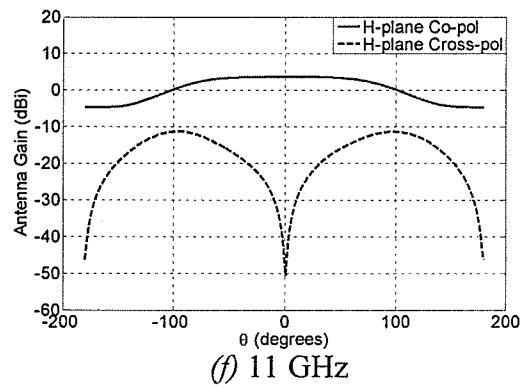
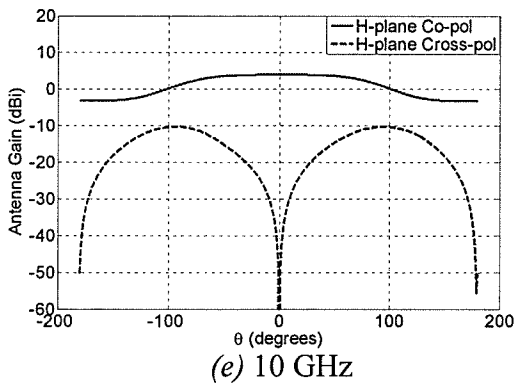
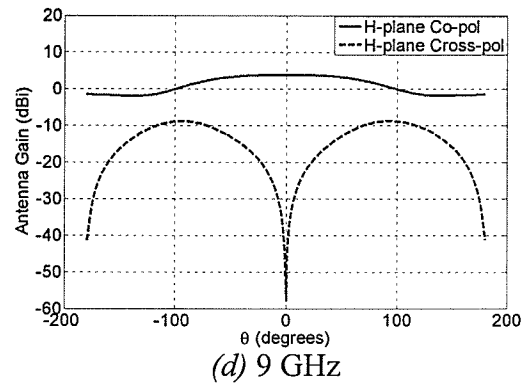
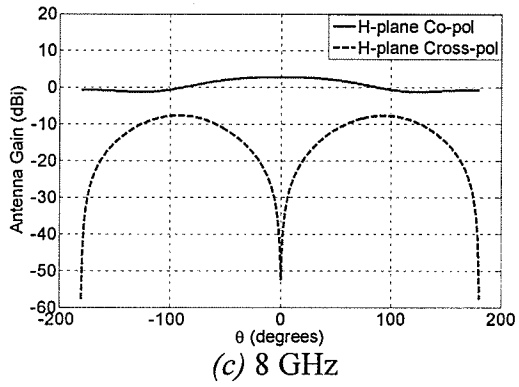


Fig. 5.4 (c)-(j)

Fig. 5.4 contd.

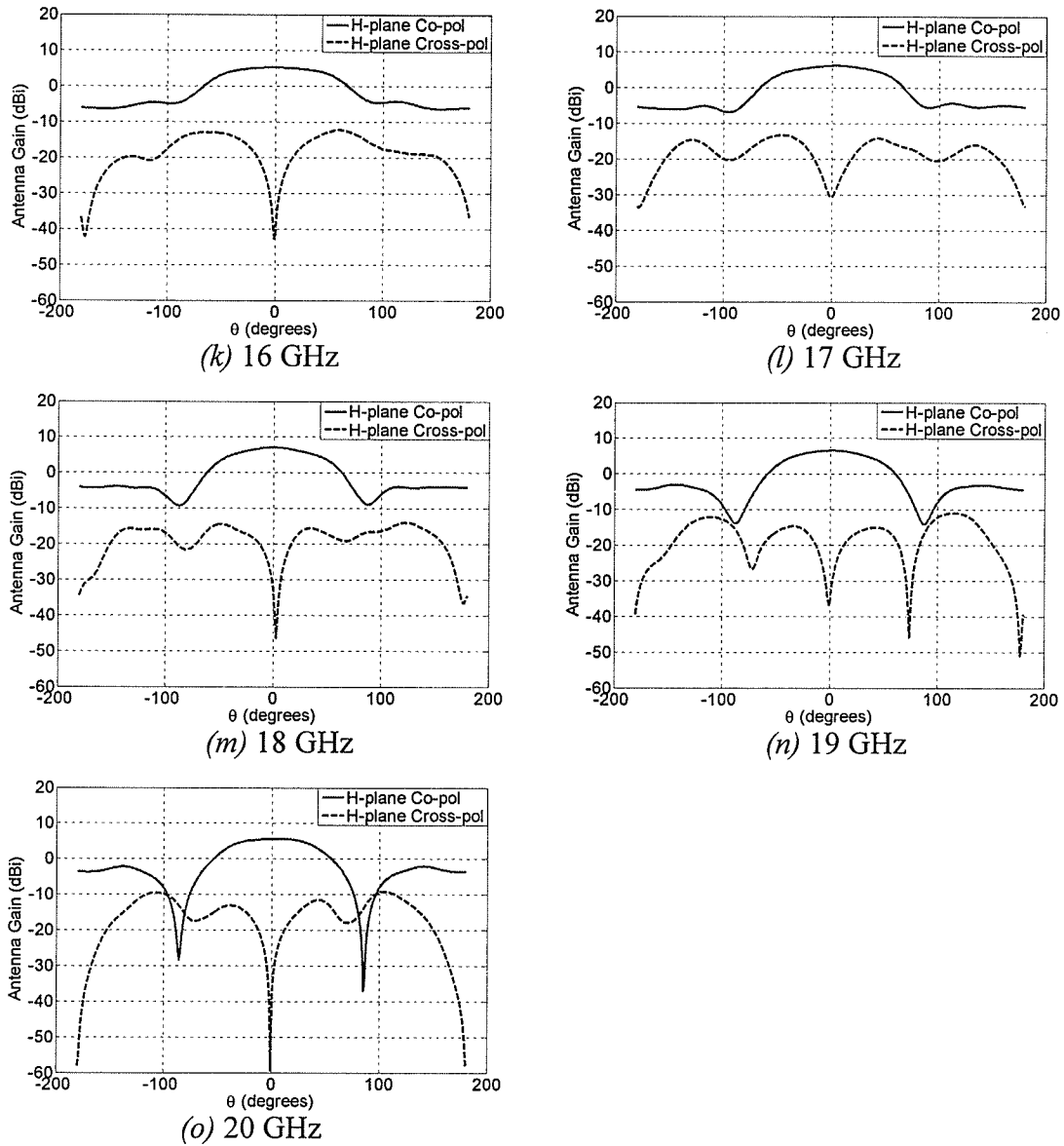


Fig. 5.4 Simulated H-plane ($\phi=0^\circ$ plane) co-pol and cross-pol patterns of the balanced antipodal Vivaldi shown in Fig. 5.1 and described by (3.1)

Tables 5.3 and 5.4 summarize the simulated H-plane co-pol and cross-pol patterns characteristics.

Frequency (GHz)	Boresight gain (dBi)	Peak gain (dBi)	Position of Peak gain	3 dB BW	10 dB BW
6	0.780	0.782	-3°	--	--
7	1.704	1.704	1°	--	--
8	2.883	2.883	0°	182°	--
9	3.921	3.921	0°	177°	--
10	3.960	3.961	9°	186°	--
11	3.689	3.702	12°	192°	--
12	3.463	3.467	4°	187°	--
13	3.594	3.594	0°	167°	--
14	3.736	3.736	-1°	143°	281°
15	4.513	4.513	1°	122°	260°
16	5.336	5.339	-2°	112°	182°
17	6.290	6.312	4°	106°	158°
18	7.069	7.069	0°	92°	140°
19	6.611	6.617	2°	88°	136°
20	5.565	5.594	6°	88°	135°

Table 5.3 Summary of H-plane co-pol pattern characteristics of the balanced antipodal Vivaldi given in Fig. 5.1 and described by (3.1)

Frequency (GHz)	Boresight Cross-pol (dBi)	Peak Cross-pol (dBi)	Position of Peak Cross-pol
6	-46.346	-11.653	93°
7	-50.377	-8.238	92°
8	-52.500	-7.614	-92°
9	-57.739	-8.709	93°
10	-72.157	-10.262	-94°
11	-49.161	-11.293	-96°
12	-45.564	-12.330	93°
13	-60.260	-12.000	68°
14	-49.717	-10.344	-63°
15	-43.194	-10.779	-55°
16	-41.869	-12.248	59°
17	-30.662	-13.248	-46°
18	-33.127	-13.902	123°
19	-35.851	-10.989	115°
20	-42.250	-9.183	104°

Table 5.4 Summary of H-plane cross-pol pattern characteristics of the balanced antipodal Vivaldi given in Fig. 5.1 and described by (3.1)

From the plots of Fig. 5.4 and Tables 5.3 and 5.4, it can be observed that the H-plane 3 dB and 10 dB beamwidths of this antenna are more or less similar to those of Model 6. The boresight cross-pol levels however are significantly better than those of Model 6.

5.2.3 Study of Phase centre for the balanced antipodal Vivaldi antenna 1

A study of the phase centre location was carried out in the same manner as that of the single sided Vivaldi antennas previously studied. However, the angle off main beam axis θ ranged from -30° to 30° . It was found that for this antenna also, phase centre location did not confine itself to a single point on the antenna axis and varied with frequency of operation. The maximum tolerable phase difference $\Delta\phi$ was 15° , which is quite close to that of Model 6. Fig. 5.5 (a) shows a plot of the Average E and H-plane phase centre locations at each frequency and Fig. 5.5 (b) depicts these locations on the antenna axis and their distances from the starting of the slotline (which is 8.89 mm from bottom of the antenna). The maximum distance of separation between the Average E and H-plane phase centres is 5.09 mm.

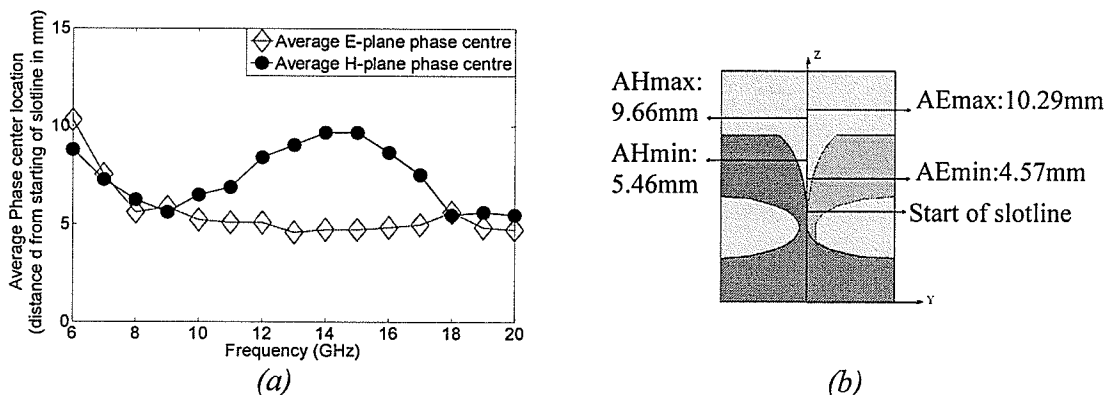


Fig. 5.5 (a) plot of Average E and H planes' phase centre location (for a maximum tolerable phase difference $\Delta\phi=15^\circ$ and θ ranging from -30° to 30°) of the balanced antipodal Vivaldi given in Fig. 5.1; (b) geometry of the antenna indicating the portion of antenna axis where Average E and H-plane phase centres lie

From an overall inspection of the performance of this balanced antipodal Vivaldi, it can be concluded that it exhibits a remarkable performance for such a compact design.

5.2.4 Antenna Model 2

Though the overall performance of the balanced antipodal Vivaldi studied in the previous section was very good, it exhibits bandwidth limitations. It may be assessed that the width of the aperture was not large enough for a reasonable performance at lower frequencies for this antenna. Also, the radiating section of a balanced antipodal Vivaldi antenna is the tapered slotline, and the transition between this section and the feed line is the most critical part in the antenna's design. The antenna's performance at higher frequencies is very sensitive to structure discontinuities, and therefore the gradual transition from the feed line to the radiating section must be as smooth as possible to avoid any such discontinuities [21]. For this reason, the flare and stripline feed are preferably longer than a regular unilateral Vivaldi antenna. As these factors (i.e., width of aperture and smoothness in transition) were not sufficient for a proper S_{11} performance of this balanced antipodal Vivaldi in the 6 to 20 GHz frequency range, a balanced antipodal Vivaldi antenna which had a significant performance in this desired range was designed for simulations. An exponential taper given in [27] was chosen which provided a considerably smooth transition from the flare to feed line as well as a sufficiently wide aperture for the antenna. The equation for the flare is given below

$$y = \pm 0.8652e^{(0.0578z)}, \quad 20\text{mm} \leq z \leq 75.90\text{mm} \quad (5.1)$$

From (5.1) it can be seen that the length of the flare of this balanced antipodal Vivaldi is 50 mm whereas that of (3.1) was only 7.61 mm. A front view of this antenna is

given in Fig. 5.6. The substrate used was Ultralam 1250 with $\epsilon_r = 2.5$, height of each slab $h = 1.5$ mm and $\tan\delta = 0.001$. The substrate specifications were chosen to match those of the dielectric material available at the University of Manitoba so that if a model was to be fabricated, the simulated and measured results could be easily compared.

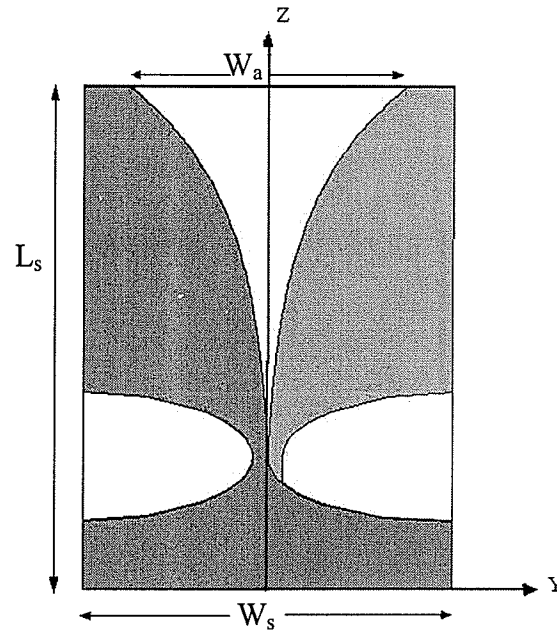


Fig. 5.6 Front view of the balanced antipodal Vivaldi antenna 2 along with co-ordinate system: $L_s = 75.90$ mm, $W_s = 55.90$ mm, $W_a = 43$ mm and described by (5.1), with $\epsilon_r = 2.5$, height of each dielectric $h = 1.5$ mm and $\tan\delta = 0.001$

From Fig. 5.6 it can be seen this antenna is 75.90 mm \times 55.90 mm which is much larger than the Vivaldi of Fig. 5.1 which was only 22.86 mm \times 17.94 mm. Also it can be seen that the aperture width of this model is 43 mm, which is adequate to radiate frequencies as low as 3 GHz [27]. The width of the stripline feed was 2.24 mm so that it had a characteristic impedance of 50 Ω .

5.2.5 Antenna Performance

The simulated S_{11} and input impedance plots of this antenna are given in Fig. 5.7.

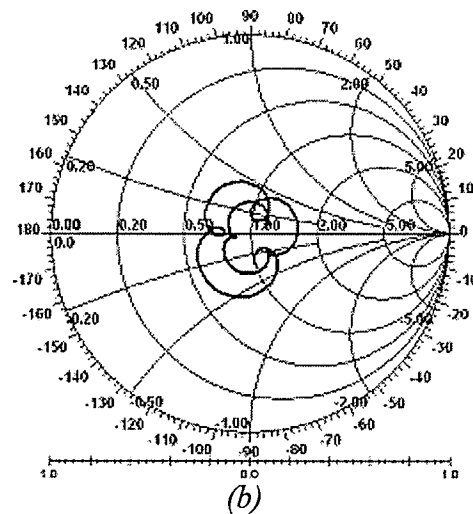
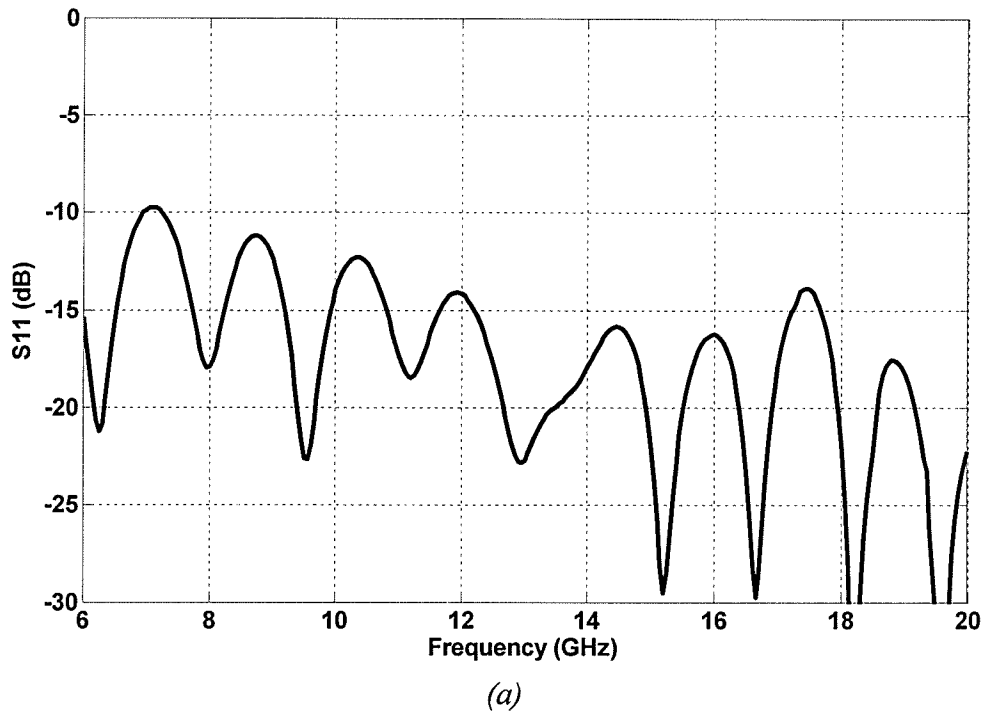


Fig. 5.7 Simulated (a) S_{11} and (b) input impedance plot measured with respect to 50Ω for the balanced antipodal Vivaldi antenna 2 shown in Fig. 5.6 and described by (5.1)

From Fig. 5.7 (a) it is observed that the limitation of bandwidth seen in the balanced antipodal Vivaldi model of Fig. 5.1 as well as in the single sided models of the previous chapters (due to the microstrip/slot transition) is overcome in this antenna. The Smith chart of Fig. 5.7 (b) indicates proper matching between the feed line and excitation.

The E-plane radiation patterns are shown in Fig. 5.8.

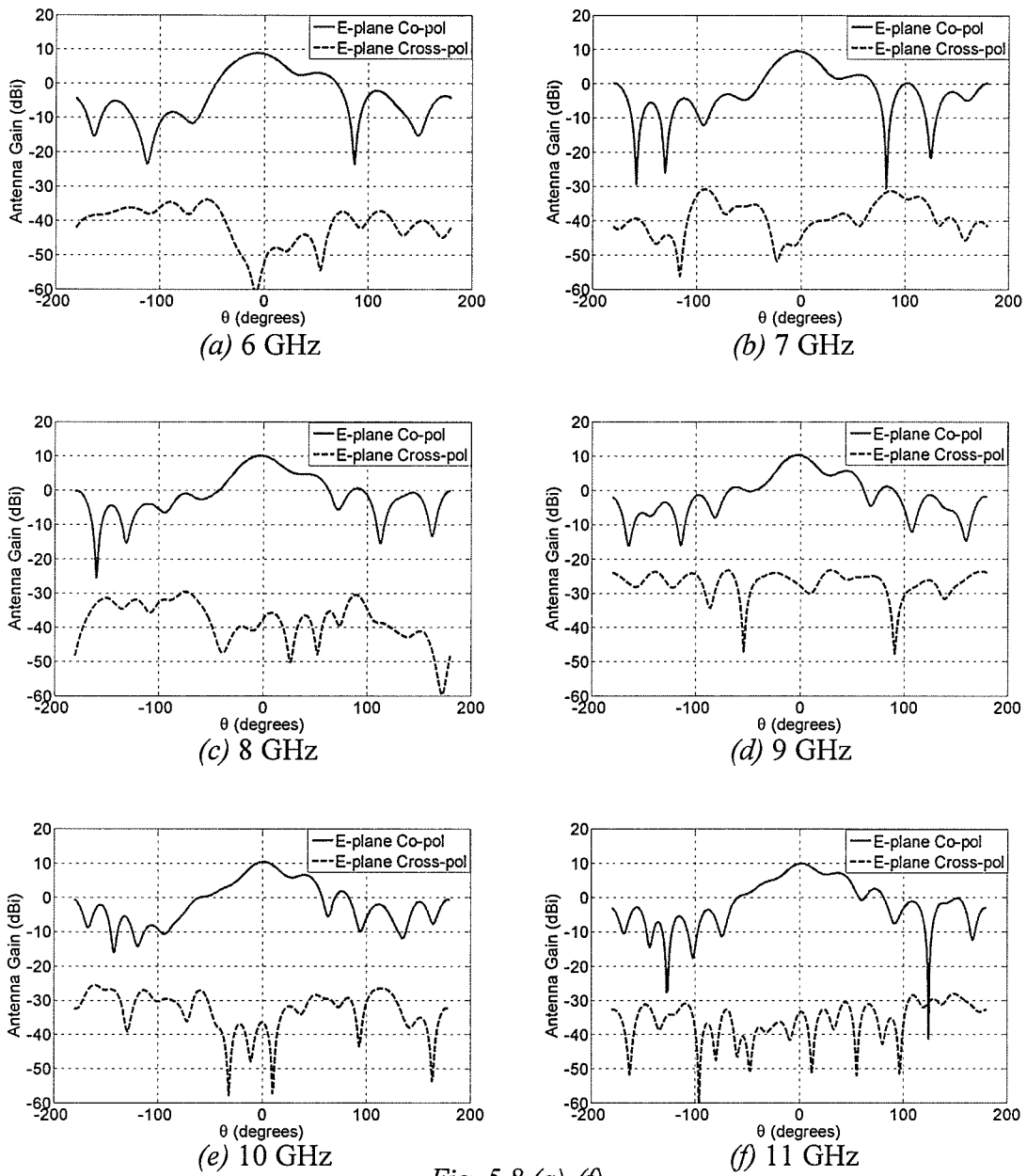


Fig. 5.8 (a)-(f)

Fig. 5.8 contd.

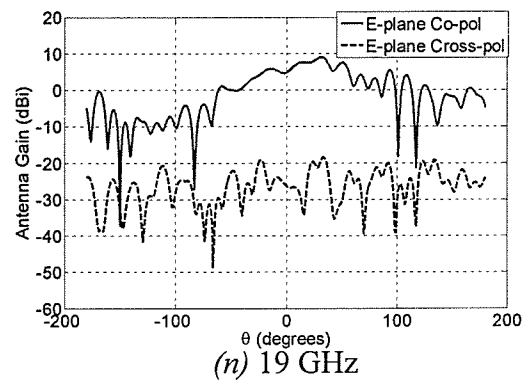
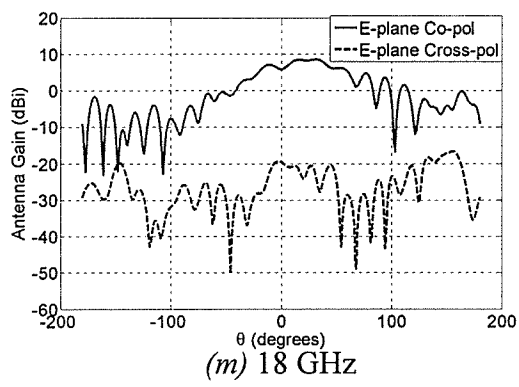
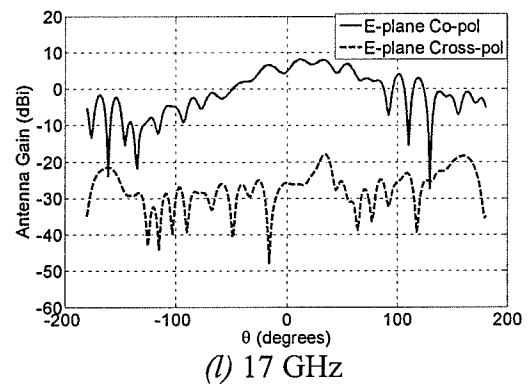
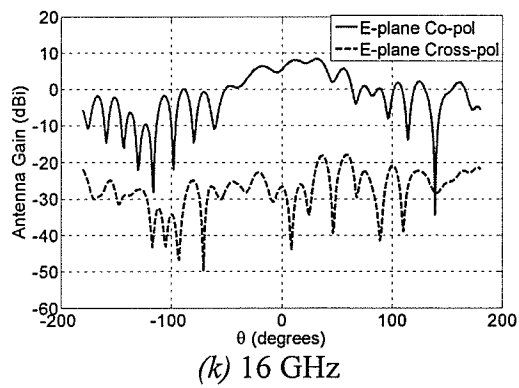
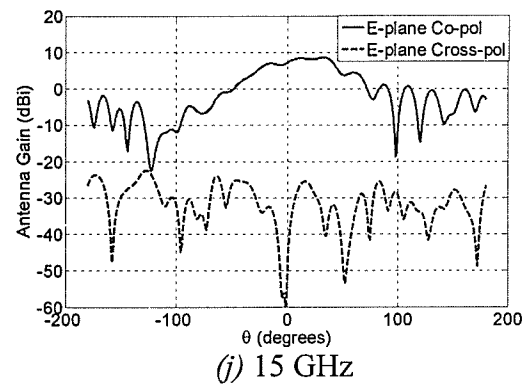
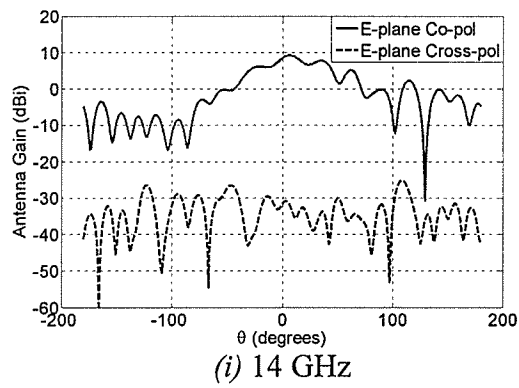
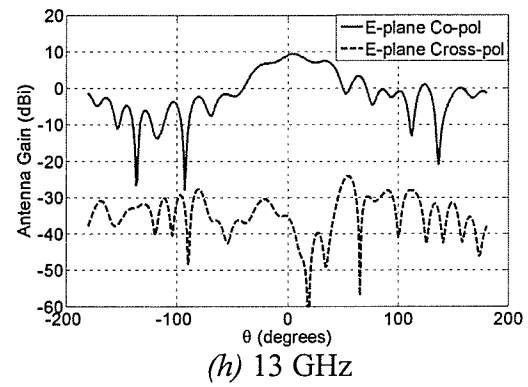
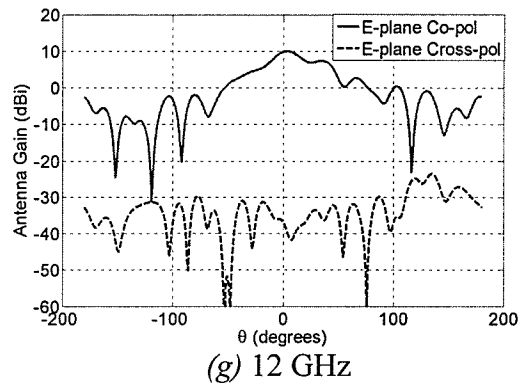


Fig. 5.8 (g)-(n)

Fig. 5.8 contd.

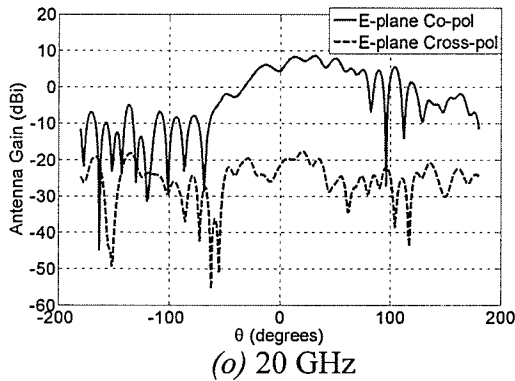


Fig. 5.8 Simulated E-plane ($\phi=90^\circ$ plane) co-pol and cross-pol patterns of the balanced antipodal Vivaldi antenna 2 shown in Fig. 5.6 and described by (5.1)

Tables 5.5 and 5.6 summarize the important E-plane co-pol and cross-pol patterns characteristics respectively.

Frequency (GHz)	Boresight gain (dBi)	Peak gain (dBi)	Position of Peak gain	3 dB BW	10 dB BW
6	8.630	8.826	-6°	48°	122°
7	9.378	9.472	-4°	40°	111°
8	10.076	10.122	-2°	40°	104°
9	10.259	10.319	-2°	34°	102°
10	10.380	10.392	1°	35°	108°
11	9.859	9.892	2°	37°	117°
12	9.882	10.034	3°	52°	131°
13	9.099	9.416	5°	67°	93°
14	8.525	9.192	6°	75°	132°
15	7.154	8.645	33°	79°	141°
16	5.436	8.377	32°	76°	150°
17	4.805	8.113	12°	126°	184°
18	5.831	8.525	31°	108°	157°
19	4.787	9.027	31°	95°	164°
20	4.486	8.579	31°	108°	140°

Table 5.5 Summary of E-plane co-pol pattern characteristics of the balanced antipodal Vivaldi antenna 2 given in Fig. 5.6 and described by (5.1)

Frequency (GHz)	Boresight Cross-pol (dBi)	Peak Cross-pol (dBi)	Position of Peak Cross-pol
6	-52.296	-33.918	-55°
7	-44.807	-30.847	-91°
8	-37.559	-29.563	-74°
9	-27.866	-23.283	30°
10	-36.368	-25.600	-161°
11	-33.434	-27.986	149°
12	-36.859	-23.514	135°
13	-35.268	-24.068	55°
14	-31.622	-25.199	108°
15	-49.748	-22.468	-127°
16	-26.685	-17.962	58°
17	-25.699	-17.946	34°
18	-19.584	-16.622	155°
19	-26.325	-18.437	33°
20	-21.476	-17.716	20°

Table 5.6 Summary of E-plane cross-pol pattern characteristics of the balanced antipodal Vivaldi antenna 2 given in Fig. 5.6 and described by (5.1)

From Fig. 5.6 it can be seen that there is an asymmetry and squint in the E-plane patterns of this antenna as well. Table 5.5 indicates that the peak gain of this model at each frequency of operation is much greater than that of the antenna given in Fig. 5.1. However, the cross-pol levels of this antenna are higher than that of the previous model as can be seen from Table 5.6.

The H-plane radiation patterns are given in Fig. 5.9.

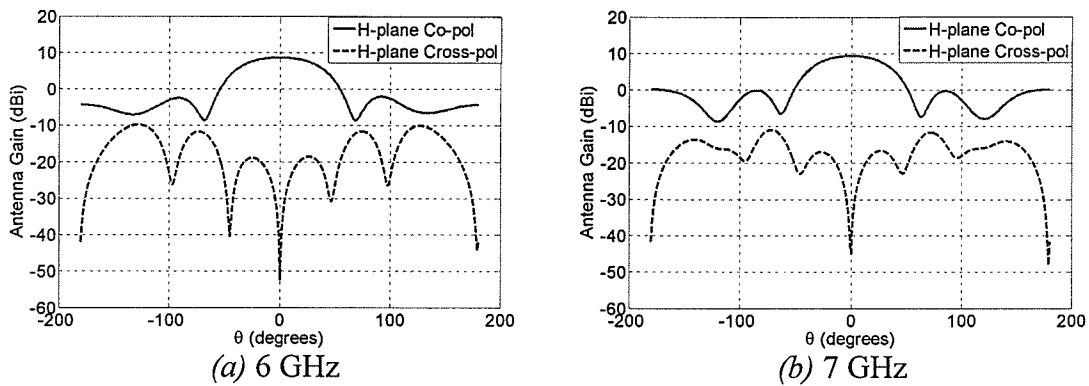


Fig. 5.9 (a), (b)

Fig. 5.9 contd.

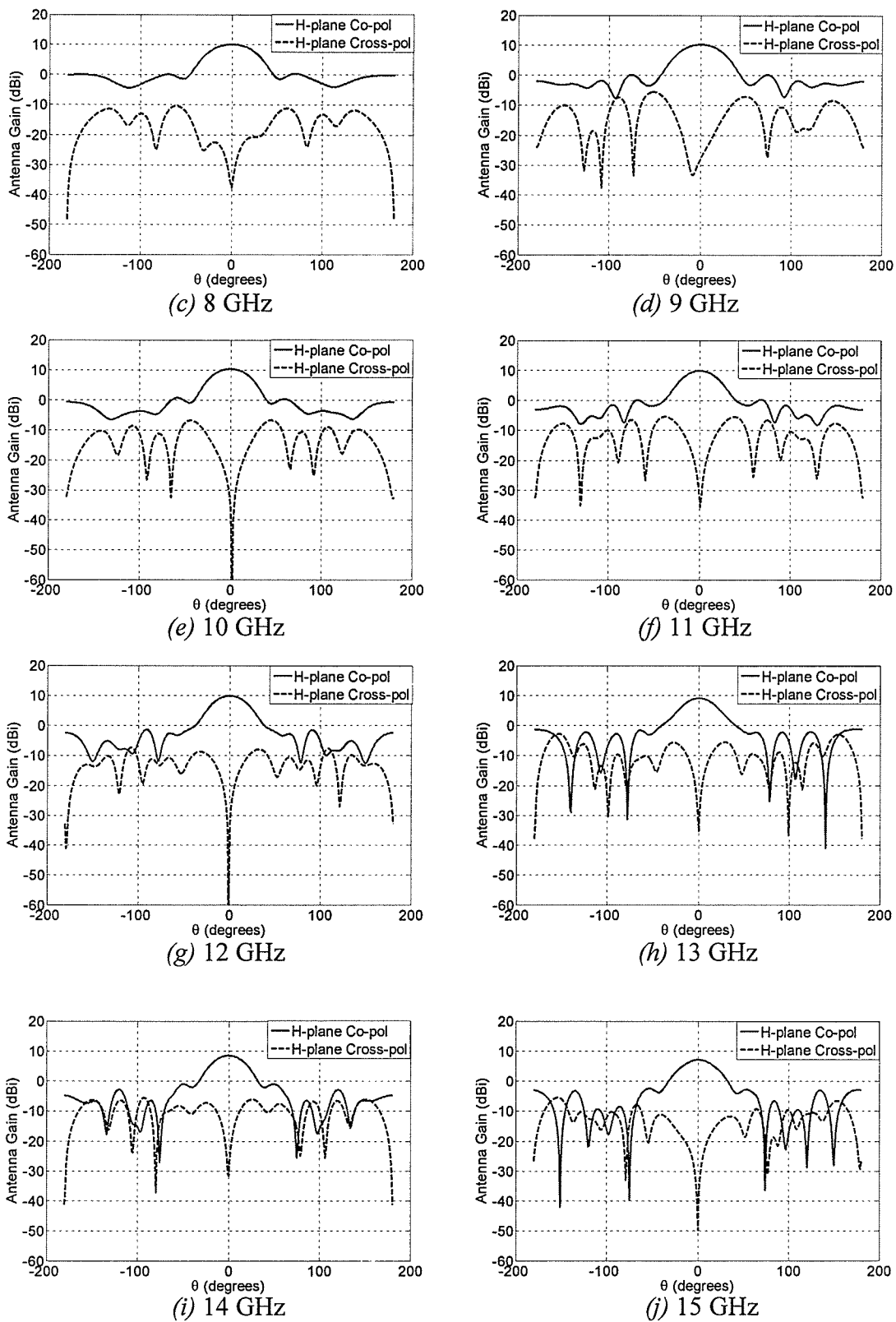


Fig. 5.9 (c)-(j)

Fig. 5.9 contd.

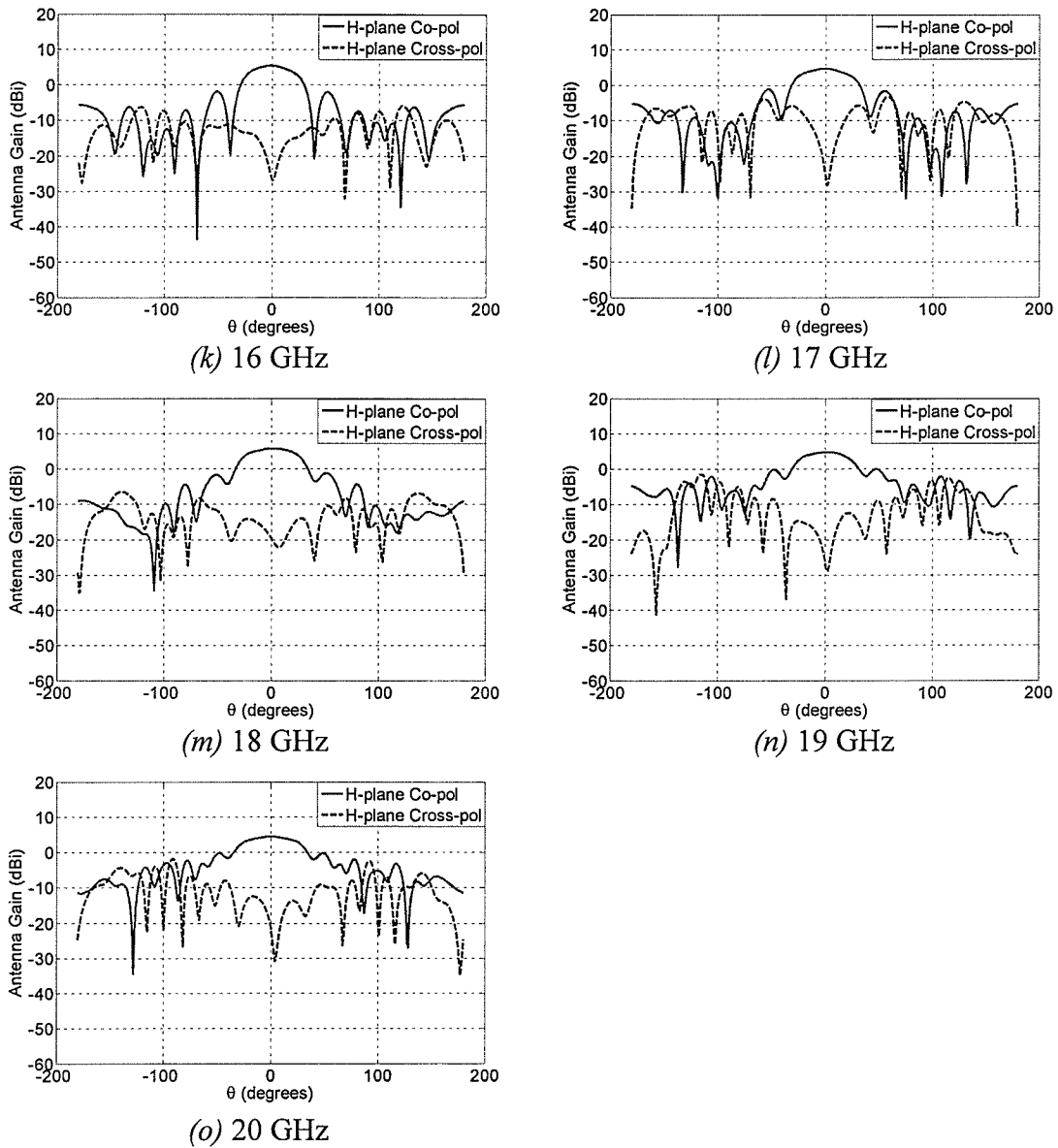


Fig. 5.9 Simulated H-plane ($\phi=0^\circ$ plane) co-pol and cross-pol patterns of the balanced antipodal Vivaldi antenna 2 shown in Fig. 5.6 and described by (5.1)

Tables 5.7 and 5.8 summarize the simulated H-plane co-pol and cross-pol patterns characteristics.

Frequency (GHz)	Boresight gain (dBi)	Peak gain (dBi)	Position of Peak gain	3 dB BW	10 dB BW
6	8.630	8.630	0°	76°	112°
7	9.378	9.378	0°	69°	105°
8	10.076	10.076	0°	54°	90°
9	10.259	10.259	0°	50°	86°
10	10.380	10.380	0°	46°	78°
11	9.859	9.859	0°	42°	80°
12	9.882	9.882	0°	41°	76°
13	9.099	9.099	0°	39°	89°
14	8.525	8.525	0°	39°	71°
15	7.154	7.154	0°	49°	76°
16	5.436	5.445	-1°	50°	68°
17	4.805	4.805	0°	55°	74°
18	5.831	5.839	1°	56°	81°
19	4.787	4.808	2°	54°	127°
20	4.486	4.486	0°	61°	137°

Table 5.7 Summary of H-plane co-pol pattern characteristics of the balanced antipodal Vivaldi antenna 2 given in Fig. 5.6 and described by (5.1)

Frequency (GHz)	Boresight Cross-pol (dBi)	Peak Cross-pol (dBi)	Position of Peak Cross-pol
6	-52.296	-9.740	-128°
7	-44.807	-10.965	-72°
8	-37.559	-10.397	-61°
9	-27.866	-5.547	-51°
10	-36.368	-6.646	45°
11	-33.434	-5.406	-38°
12	-36.859	-7.327	-108°
13	-35.268	-2.792	-153°
14	-31.622	-5.583	-93°
15	-49.748	-5.522	-154°
16	-26.685	-5.925	122°
17	-25.699	-3.210	58°
18	-19.584	-6.435	-140°
19	-26.325	-1.457	-115°
20	-21.476	-18.429	-91°

Table 5.8 Summary of H-plane cross-pol pattern characteristics of the balanced antipodal Vivaldi antenna 2 given in Fig. 5.6 and described by (5.1)

From Table 5.8 it is seen that the H-plane boresight cross-pol levels of this antenna are also quite low just as in the previous model.

From an overall inspection of the performance of this antenna and the balanced antipodal Vivaldi presented in the previous section, it can be concluded that both models have a very good performance in the considered frequency range. Though the antenna in Fig. 5.6 has a better S_{11} performance than the model in Fig. 5.1, it must be highlighted that the latter has a remarkable performance for such a compact design.

5.3 Increase in Length of Substrate

As the Vivaldi is a traveling wave antenna, any change in its geometrical parameters will change the phase velocity and guided wavelength of the antenna, which in turn impacts its radiation characteristics. The gain of a TSA increases with increase in its length, typically from a few dB to over 10 dB depending on the extent of elongation [28].

The balanced antipodal Vivaldi antenna 2 shown in Fig. 5.6 was chosen for the study on the effect of increase in substrate length. This model was chosen over the model given in Fig. 5.1 because, as previously mentioned, the dielectric substrate specifications of the former were suitable for practical purposes. In order to observe this effect, the substrate length of the antenna was increased beyond its aperture. Two models were studied. In the first model, the length of the substrate was extended by 12.80 mm beyond the aperture of the antenna. In the second model, the length of the substrate was extended by 30 mm beyond its aperture. All other parameters including flare equation were

unaltered for both models. It must also be mentioned that there was no significant reason in choosing these specific elongation lengths and that it was merely by choice.

The antenna models are given in the next section along with their respective tabulations of important co-pol and cross-pol pattern characteristics for both principle planes. As the return loss and beam shapes of the radiation patterns (in both planes) were not affected due to elongation in either model, they have been omitted in the following section for the sake of brevity. The radiation patterns of the Vivaldi with an elongation of 12.80 mm however, are presented in the next chapter.

5.3.1 Elongated Antenna Models and Performance

A front view of the balanced antipodal Vivaldi antenna 2 which was elongated by 12.80 mm beyond its aperture is given in Fig. 5.10.

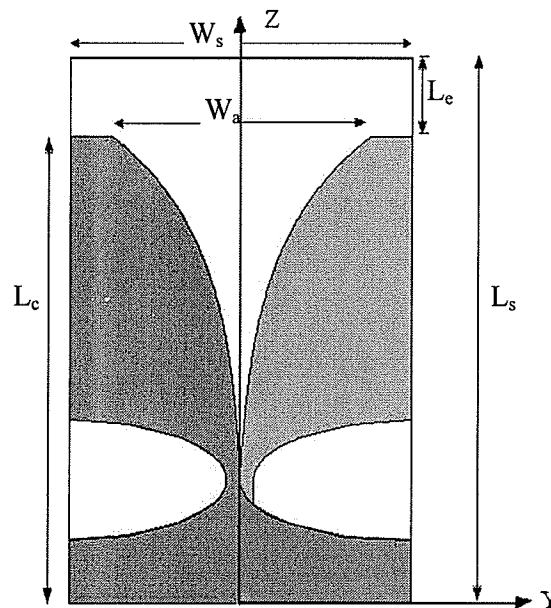


Fig. 5.10 Front view of the balanced antipodal Vivaldi antenna with substrate elongation of 12.80 mm along with co-ordinate system: $L_s = 88.70\text{mm}$, $L_c = 75.90\text{mm}$, $L_e = 12.80\text{mm}$, $W_s = 55.90\text{mm}$, $W_a = 43\text{mm}$ and described by (5.1), with $\epsilon_r = 2.5$, height of each dielectric $h = 1.5\text{ mm}$ and $\tan\delta = 0.001$

A summary of the simulated co-pol and cross-pol characteristics of this antenna in both principle planes are given in Tables 5.9 to 5.12.

Frequency (GHz)	Boresight gain (dBi)	Peak gain (dBi)	Position of Peak gain	3 dB BW	10 dB BW
6	9.218	9.392	-6°	40°	118°
7	9.608	9.728	-4°	40°	109°
8	10.319	10.356	-2°	41°	115°
9	10.757	10.821	-3°	37°	126°
10	10.707	10.707	0°	38°	114°
11	9.967	9.973	1°	62°	137°
12	9.988	10.080	3°	57°	125°
13	9.165	9.231	3°	68°	127°
14	8.409	9.280	32°	78°	131°
15	7.069	10.335	26°	86°	138°
16	6.686	8.930	29°	92°	162°
17	5.340	9.707	31°	105°	140°
18	3.414	10.420	27°	122°	154°
19	6.386	9.229	28°	96°	140°
20	5.111	10.744	30°	95°	136°

Table 5.9 Summary of E-plane co-pol pattern characteristics of the balanced antipodal Vivaldi with substrate elongation of 12.80 mm given in Fig. 5.10

Frequency (GHz)	Boresight Cross-pol (dBi)	Peak Cross-pol (dBi)	Position of Peak Cross-pol
6	-43.733	-38.916	161°
7	-44.174	-34.004	52°
8	-49.150	-36.993	34°
9	-35.500	-30.055	-28°
10	-52.190	-34.923	-144°
11	-42.672	-25.199	66°
12	-40.015	-21.892	62°
13	-27.705	-26.295	20°
14	-30.537	-23.371	-105°
15	-29.008	-21.058	-59°
16	-29.227	-24.929	-60°
17	-32.137	-19.786	31°
18	-28.933	-22.209	-81°
19	-27.458	-23.033	157°
20	-26.194	-19.794	107°

Table 5.10 Summary of E-plane cross-pol pattern characteristics of the balanced antipodal Vivaldi with substrate elongation of 12.80 mm given in Fig. 5.10

Frequency (GHz)	Boresight gain (dBi)	Peak gain (dBi)	Position of Peak gain	3 dB BW	10 dB BW
6	9.218	9.218	0°	70°	106°
7	9.608	9.608	0°	52°	98°
8	10.319	10.319	0°	50°	80°
9	10.757	10.757	0°	46°	78°
10	10.707	10.707	0°	42°	74°
11	9.967	9.967	0°	38°	131°
12	9.988	9.988	0°	38°	100°
13	9.165	9.165	0°	35°	123°
14	8.409	8.410	1°	37°	118°
15	7.069	7.069	0°	35°	112°
16	6.686	6.686	0°	43°	64°
17	5.340	5.340	0°	47°	106°
18	3.414	3.414	0°	44°	60°
19	6.386	6.389	1°	44°	92°
20	5.111	5.112	1°	69°	92°

Table 5.11 Summary of H-plane co-pol pattern characteristics of the balanced antipodal Vivaldi with substrate elongation of 12.80 mm given in Fig. 5.10

Frequency (GHz)	Boresight Cross-pol (dBi)	Peak Cross-pol (dBi)	Position of Peak Cross-pol
6	-43.733	-10.297	-124°
7	-44.174	-10.056	-73°
8	-49.150	-9.470	61°
9	-35.500	-6.481	50°
10	-52.190	-5.880	-47°
11	-42.672	-4.662	40°
12	-40.015	-7.788	108°
13	-27.705	-2.343	-149°
14	-30.537	-6.172	-28°
15	-29.008	-5.628	152°
16	-29.227	-3.931	-58°
17	-32.137	-3.079	55°
18	-28.933	-4.656	158°
19	-27.458	-3.293	117°
20	-26.194	-6.288	-138°

Table 5.12 Summary of H-plane cross-pol pattern characteristics of the balanced antipodal Vivaldi with substrate elongation of 12.80 mm given in Fig. 5.10

From the above tables it can be seen that the elongation of substrate by 12.80 mm only slightly increased the boresight gain (and E-plane peak gain) when compared to that of the antenna without elongation given in Fig. 5.6. But an overall increase of gain was observed in the entire frequency range of operation.

In order to observe the effect of further elongation, the balanced antipodal Vivaldi of Fig. 5.6 was elongated such that the substrate length beyond its aperture was 30 mm. Figure 5.11 gives a front view of this model and Tables 5.13 to 5.16 summarize the E and H-plane radiation pattern properties of interest.

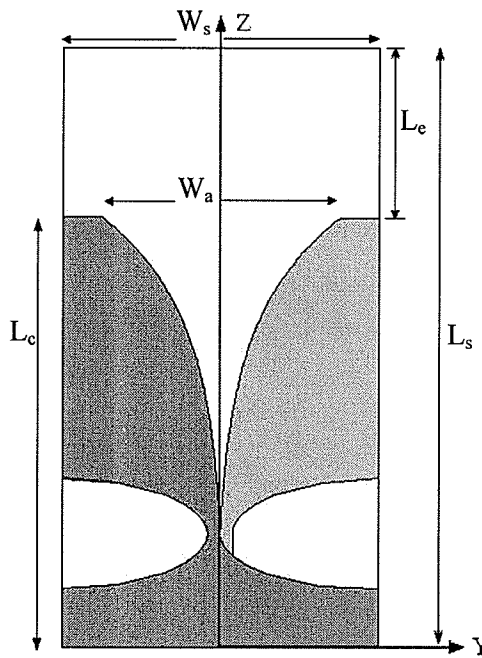


Fig. 5.11 Front view of the balanced antipodal Vivaldi with substrate elongation of 30 mm along with co-ordinate system: $L_s = 105.90\text{mm}$, $L_c = 75.90\text{mm}$, $L_e = 30\text{mm}$, $W_s = 55.90\text{mm}$, $W_a = 43\text{mm}$ and described by (5.1), with $\epsilon_r = 2.5$, height of each dielectric $h = 1.5\text{ mm}$ and $\tan\delta = 0.001$

Frequency (GHz)	Boresight gain (dBi)	Peak gain (dBi)	Position of Peak gain	3 dB BW	10 dB BW
6	9.660	9.829	-6°	50°	113°
7	10.315	10.443	-4°	40°	107°
8	11.157	11.197	-2°	39°	100°
9	11.720	11.777	-2°	35°	105°
10	11.810	11.819	-1°	33°	102°
11	11.412	11.412	0°	35°	100°
12	11.229	11.287	2°	50°	92°
13	10.404	10.421	1°	62°	81°
14	9.794	10.217	27°	67°	102°
15	8.574	11.673	23°	64°	98°
16	-5.383	4.129	27°	103°	179°
17	-2.849	5.238	26°	110°	132°
18	-1.609	6.417	23°	103°	124°
19	-4.550	6.862	21°	115°	119°
20	-1.929	7.110	20°	97°	159°

Table 5.13 Summary of E-plane co-pol pattern characteristics of the balanced antipodal Vivaldi with substrate elongation of 30 mm given in Fig. 5.11

Frequency (GHz)	Boresight Cross-pol (dBi)	Peak Cross-pol (dBi)	Position of Peak Cross-pol
6	-42.777	-41.629	79°
7	-47.337	-35.571	79°
8	-39.337	-32.264	-80°
9	-41.256	-32.379	37°
10	-36.695	-29.173	39°
11	-45.077	-28.502	65°
12	-45.386	-25.332	117°
13	-39.980	-23.085	133°
14	-24.170	-20.311	-111°
15	-26.152	-18.769	-60°
16	-41.006	-32.404	93°
17	-34.171	-30.222	161°
18	-31.635	-25.474	146°
19	-26.049	-22.592	129°
20	-36.031	-22.370	33°

Table 5.14 Summary of E-plane cross-pol pattern characteristics of the balanced antipodal Vivaldi with substrate elongation of 30 mm given in Fig. 5.11

Frequency (GHz)	Boresight gain (dBi)	Peak gain (dBi)	Position of Peak gain	3 dB BW	10 dB BW
6	9.660	9.660	0°	66°	99°
7	10.315	10.315	0°	56°	88°
8	11.157	11.157	0°	46°	74°
9	11.720	11.720	0°	42°	70°
10	11.810	11.810	0°	38°	98°
11	11.412	11.412	0°	34°	98°
12	11.229	11.229	0°	36°	102°
13	10.404	10.404	0°	36°	110°
14	9.794	9.794	0°	40°	104°
15	8.574	8.574	0°	72°	126°
16	-5.383	-1.392	37°	40°	127°
17	-2.849	-0.281	-35°	34°	122°
18	-1.609	0.261	32°	31°	118°
19	-4.550	0.484	30°	20°	139°
20	-1.929	0.832	-31°	25°	126°

Table 5.15 Summary of H-plane co-pol pattern characteristics of the balanced antipodal Vivaldi with substrate elongation of 30 mm given in Fig. 5.11

Frequency (GHz)	Boresight Cross-pol (dBi)	Peak Cross-pol (dBi)	Position of Peak Cross-pol
6	-42.777	-10.733	124°
7	-47.337	-10.159	71°
8	-39.337	-9.006	-58°
9	-41.256	-6.167	51°
10	-36.695	-5.535	-47°
11	-45.077	-3.624	40°
12	-45.386	-7.213	-33°
13	-39.980	-3.700	31°
14	-24.170	-5.308	31°
15	-26.152	-5.565	152°
16	-41.006	-11.120	-60°
17	-34.171	-8.948	56°
18	-31.635	-9.441	-31°
19	-26.049	-7.843	110°
20	-36.031	-7.222	-44°

Table 5.16 Summary of H-plane cross-pol pattern characteristics of the balanced antipodal Vivaldi with substrate elongation of 30 mm given in Fig. 5.11

From the above tables it can be seen that this model has a higher boresight (and peak) gain in the 6 to 15 GHz range than the balanced antipodal Vivaldi of Fig 5.6 and the model with substrate elongation of 12.80 mm given in Fig. 5.10. However, there is a drastic decrease in boresight (as well as peak) gain in this model for the 16 to 20 GHz range when compared to the previous two models. It can therefore be concluded that the increase in substrate length facilitated improvement only in the 6 to 15 GHz range.

5.3.2 Study of Phase centre for the 12.80 mm elongated substrate model

A study on the phase centre location was carried out for the balanced antipodal Vivaldi with substrate elongation of 12.80 mm given in Fig. 5.10. This model was chosen as it had a better overall performance in the considered frequency range when compared to the antenna with substrate elongation of 30 mm given in Fig. 5.11. Also, this model was chosen for fabrication, and hence it was appropriate to study its simulated phase centre location in order to compare with measured results.

The maximum tolerable phase difference $\Delta\phi$ in the E-plane was found to be 35° , whereas in the H-plane it was found to be 15° . As the goal was to find a phase centre location on the antenna axis which confined to a common phase difference tolerability for both principle planes, $\Delta\phi$ was chosen to be 35° . Due to such unnecessarily large phase tolerability in the H-plane, the phase centre location in this plane was found to lie over a very large portion of the antenna axis. Fig. 5.12 (a) shows a plot of the Average E and H-plane phase centre locations at each frequency and Fig. 5.12 (b) depicts these locations on the antenna axis and their distances from the starting of the slotline (which is 20 mm from the bottom of the antenna).

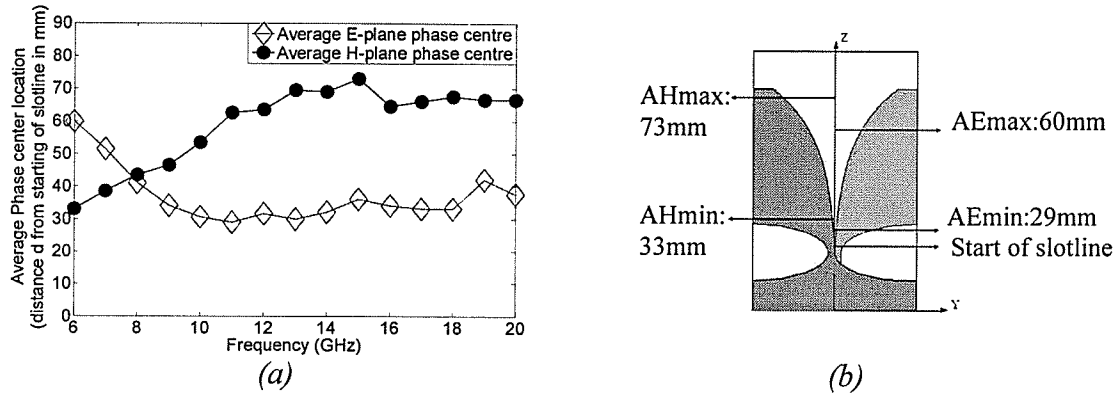


Fig. 5.12 (a) plot of Average E and H planes' phase centre location (for a maximum tolerable phase difference $\Delta\phi=35^\circ$ and θ ranging from -30° to 30°) of the balanced antipodal Vivaldi given in Fig. 5.10; (b) geometry of the antenna indicating the portion of antenna axis where Average E and H-plane phase centres lie

The maximum distance between the Average E and H-plane phase centres is 44 mm, which is quite large. However this is due to the fact of imposing an unnecessarily large $\Delta\phi$ on H-plane phase patterns.

As previously shown, the maximum tolerable phase difference $\Delta\phi$ of the compact balanced antipodal Vivaldi given in Fig. 5.1 was 15° which is much smaller than the $\Delta\phi$ of the model shown here. From an overall comparison of the Average E and H-plane phase centre plots of these two models, it can be concluded that the balanced antipodal Vivaldi antenna given in Fig. 5.1 has a better performance with regard to phase centre location. In order to comprehend the size difference of these two antennas, a comparison of the sizes of these two models is given in Fig. 5.13. It must be noted that Fig. 5.13 merely depicts a comparison of the relative size of one model to the other and should not be mistaken for the actual sizes of the antenna models.

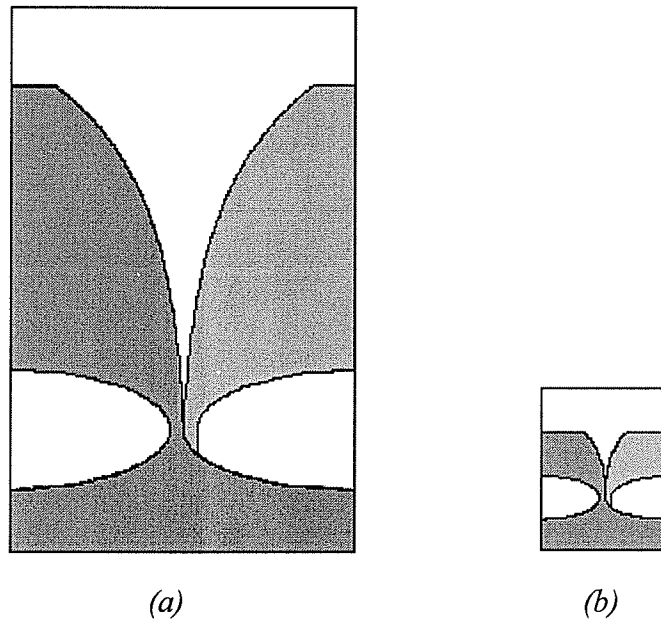


Fig. 5.13 Comparison of the relative sizes of (a) the balanced antipodal Vivaldi given in Fig. 5.10 and (b) the balanced antipodal Vivaldi given in Fig. 5.1

From Fig. 5.13 it can be seen the balanced antipodal Vivaldi given in Fig. 5.1 is much quite tiny in size when compared to the Vivaldi given in Fig. 5.10. It is very interesting to note that although the former is much smaller, it has a superior phase centre performance.

5.4 Shaping of Substrate

After studying the effect of elongation of the antenna, a study on the effect of shaping of the elongated substrate was considered. As the antenna model with substrate elongation of 30 mm given in Fig. 5.11 exhibited a higher gain in the 6 to 15 GHz frequency range than the prior elongation of 12.80 mm given in Fig. 5.10, it was chosen for this study.

The elongated substrate shapes were chosen to be simple in order to facilitate ease in modeling of the antenna in Ansoft HFSS v. 10.1. Three different models are presented

in the following sections along with tabulations of their radiation characteristics in the two principle planes. Once again, the simulated S_{11} and radiation plots have been omitted as their patterns were not significantly affected due to shaping of the substrate.

5.4.1 Antenna Substrate Shapes and Performance

As previously mentioned, the 30 mm elongated substrate was chosen for shaping. In the first model of this section, the extended substrate portion was shaped into an isosceles triangle of height 30 mm, and with the two equal sides having a length of 41 mm each. For ease of reference, this model will be called sharp tip substrate, and its front view is given in Fig. 5.14.

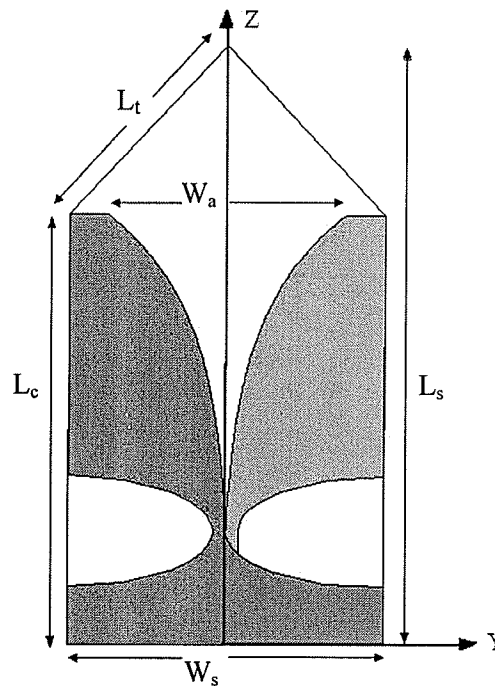


Fig. 5.14 Front view of the sharp tip substrate model along with co-ordinate system: $L_s = 105.90\text{mm}$, $L_c = 75.90\text{mm}$, $W_s = 55.90\text{mm}$, $W_a = 43\text{mm}$, $L_t = 41\text{mm}$ and described by (5.1), with $\epsilon_r = 2.5$, height of each dielectric $h = 1.5\text{mm}$ and $\tan\delta = 0.001$

The important E and H-plane characteristics of this model are given in Tables 5.17 to 5.20

Frequency (GHz)	Boresight gain (dBi)	Peak gain (dBi)	Position of Peak gain	3 dB BW	10 dB BW
6	9.302	9.456	-5°	48°	117°
7	9.883	9.974	-3°	41°	107°
8	10.822	10.857	-2°	40°	100°
9	11.147	11.201	-2°	34°	93°
10	11.123	11.179	-2°	37°	90°
11	11.478	11.478	0°	35°	93°
12	11.621	11.638	1°	28°	81°
13	11.043	11.063	1°	31°	83°
14	11.127	11.442	4°	30°	102°
15	10.592	10.764	3°	39°	118°
16	1.212	3.975	32°	65°	138°
17	2.971	5.564	33°	62°	101°
18	4.122	5.915	30°	48°	95°
19	5.564	6.112	4°	43°	90°
20	6.736	7.409	4°	18°	87°

Table 5.17 Summary of E-plane co-pol pattern characteristics of the sharp tip substrate model given in Fig. 5.14

Frequency (GHz)	Boresight Cross-pol (dBi)	Peak Cross-pol (dBi)	Position of Peak Cross-pol
6	-43.793	-37.853	-59°
7	-43.831	-37.221	-53°
8	-42.868	-27.326	-83°
9	-40.736	-31.660	18°
10	-51.586	-27.425	40°
11	-42.729	-28.039	-63°
12	-40.977	-21.617	123°
13	-42.066	-23.966	25°
14	-32.965	-23.992	68°
15	-29.996	-22.842	142°
16	-33.804	-27.336	-35°
17	-41.834	-29.615	157°
18	-40.045	-26.837	157°
19	-30.857	-25.282	-149°
20	-41.672	-27.631	36°

Table 5.18 Summary of E-plane cross-pol pattern characteristics of the sharp tip substrate model given in Fig. 5.14

Frequency (GHz)	Boresight gain (dBi)	Peak gain (dBi)	Position of Peak gain	3 dB BW	10 dB BW
6	9.302	9.302	0°	68°	102°
7	9.883	9.883	0°	62°	94°
8	10.822	10.822	0°	50°	80°
9	11.147	11.147	0°	46°	78°
10	11.123	11.123	0°	42°	116°
11	11.478	11.478	0°	38°	108°
12	11.621	11.621	0°	40°	107°
13	11.043	11.043	0°	38°	122°
14	11.127	11.128	-1°	42°	116°
15	10.592	10.592	0°	44°	115°
16	1.212	1.212	0°	45°	109°
17	2.971	2.971	0°	46°	101°
18	4.122	4.122	0°	44°	130°
19	5.564	5.566	-1°	38°	117°
20	6.736	6.737	-1°	42°	102°

Table 5.19 Summary of H-plane co-pol pattern characteristics of the sharp tip substrate model given in Fig. 5.14

Frequency (GHz)	Boresight Cross-pol (dBi)	Peak Cross-pol (dBi)	Position of Peak Cross-pol
6	-43.793	-10.584	130°
7	-43.831	-11.872	-73°
8	-42.868	-9.923	59°
9	-40.736	-7.727	50°
10	-51.586	-6.175	46°
11	-42.729	-4.135	40°
12	-40.977	-7.410	108°
13	-42.066	-2.991	150°
14	-32.965	-5.507	94°
15	-29.996	-6.140	149°
16	-33.804	-10.950	-63°
17	-41.834	-9.499	59°
18	-40.045	-10.818	-71°
19	-30.857	-6.446	-111°
20	-41.672	-6.776	91°

Table 5.20 Summary of H-plane cross-pol pattern characteristics of the sharp tip substrate model given in Fig. 5.14

From the tables we can see that this shape of the substrate does not greatly impact the gain of the antenna in the 6 to 15 GHz range. However, there is a drastic increase in boresight (and peak) gain in the 16 to 20 GHz range of operation when compared to the model with substrate elongation of 30 mm given in Fig. 5.11. Hence this substrate shape improved the gain of the antenna in the higher frequencies of operation.

In the second model presented in this section, the elongated substrate portion was shaped into a semicircle of radius 30 mm. This model will be referred to as curved substrate and its geometry is given in Fig. 5.15.

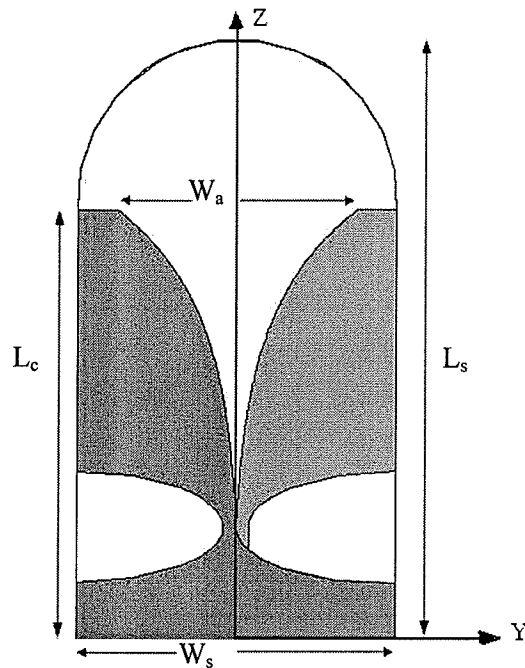


Fig. 5.15 Front view of the curved substrate model along with co-ordinate system: $L_s = 105.90\text{mm}$, $L_c = 75.90\text{mm}$, $W_s = 55.90\text{mm}$, $W_a = 43\text{mm}$ and described by (5.1), with $\epsilon_r = 2.5$, height of each dielectric $h = 1.5\text{mm}$ and $\tan\delta = 0.001$

The E and H-plane radiation characteristics of this model are given in Tables 5.21 to 5.24.

Frequency (GHz)	Boresight gain (dBi)	Peak gain (dBi)	Position of Peak gain	3 dB BW	10 dB BW
6	9.597	9.735	-5°	49°	113°
7	10.324	10.413	-3°	40°	107°
8	10.925	10.959	-2°	41°	99°
9	11.600	11.638	-2°	35°	93°
10	11.786	11.799	-1°	33°	93°
11	8.692	8.715	1°	35°	96°
12	8.261	8.350	3°	51°	118°
13	7.368	7.455	2°	52°	106°
14	6.698	7.090	31°	56°	147°
15	6.143	8.280	27°	69°	122°
16	-1.882	4.193	30°	68°	143°
17	0.820	6.014	30°	57°	137°
18	2.435	6.500	26°	110°	134°
19	2.559	5.488	25°	43°	131°
20	5.236	6.315	26°	39°	103°

Table 5.21 Summary of E-plane co-pol pattern characteristics of the curved substrate model given in Fig. 5.15

Frequency (GHz)	Boresight Cross-pol (dBi)	Peak Cross-pol (dBi)	Position of Peak Cross-pol
6	-46.394	-36.250	88°
7	-34.377	-31.814	72°
8	-40.457	-29.902	79°
9	-42.095	-30.514	105°
10	-34.356	-22.601	44°
11	-44.407	-31.518	117°
12	-44.259	-30.507	116°
13	-43.849	-30.613	129°
14	-41.073	-31.893	-170°
15	-26.595	-21.757	-174°
16	-34.693	-24.222	-76°
17	-29.112	-23.997	153°
18	-28.518	-23.444	145°
19	-38.816	-25.464	37°
20	-31.697	-20.631	35°

Table 5.22 Summary of E-plane cross-pol pattern characteristics of the curved substrate model given in Fig. 5.15

Frequency (GHz)	Boresight gain (dBi)	Peak gain (dBi)	Position of Peak gain	3 dB BW	10 dB BW
6	9.597	9.597	0°	66°	100°
7	10.324	10.324	0°	59°	90°
8	10.925	10.925	0°	48°	76°
9	11.600	11.600	0°	43°	74°
10	11.786	11.786	0°	40°	107°
11	8.692	8.692	0°	34°	54°
12	8.261	8.261	0°	30°	52°
13	7.368	7.368	0°	30°	104°
14	6.698	6.698	0°	32°	110°
15	6.143	6.143	0°	36°	134°
16	-1.882	-0.903	-39°	44°	136°
17	0.820	0.820	-1°	40°	128°
18	2.435	2.437	1°	37°	124°
19	2.559	2.559	0°	32°	134°
20	5.236	5.236	0°	35°	129°

Table 5.23 Summary of H-plane co-pol pattern characteristics of the curved substrate model given in Fig. 5.15

Frequency (GHz)	Boresight Cross-pol (dBi)	Peak Cross-pol (dBi)	Position of Peak Cross-pol
6	-46.394	-11.626	-126°
7	-34.377	-10.805	73°
8	-40.457	-8.355	-59°
9	-42.095	-7.248	50°
10	-34.356	-5.641	47°
11	-44.407	-8.736	-43°
12	-44.259	-8.862	39°
13	-43.849	-5.150	-149°
14	-41.073	-8.190	-142°
15	-26.595	-7.349	-152°
16	-34.693	-11.473	61°
17	-29.112	-8.167	-57°
18	-28.518	-9.429	53°
19	-38.816	-8.795	49°
20	-31.697	-6.083	46°

Table 5.24 Summary of H-plane cross-pol pattern characteristics of the curved substrate model given in Fig. 5.15

From the tables it is seen that there is a decrease in boresight (and peak) gain of this model at certain frequencies in the 6 to 15 GHz range when compared to the 30 mm elongated antenna without any substrate shaping of Fig. 5.11. Also, the gain of this model is higher in the 16 to 20 GHz range than the elongated antenna of Fig. 5.11 but lower than that of the sharp tip substrate model given in Fig. 5.14.

As the sharp tip substrate model slightly improved the gain of the antenna and both the sharp tip and curved models improved the gain of the antenna in the 16 to 20 GHz range, a model which integrated both shapes was chosen as the last case under this study. The basis for this model is the sharp tip substrate model. However, the two equal sides of the isosceles triangle portion of the elongated substrate were altered such that they were curved in shape. The resultant model is shown in Fig. 5.16 and will be called curved sharp tip substrate.

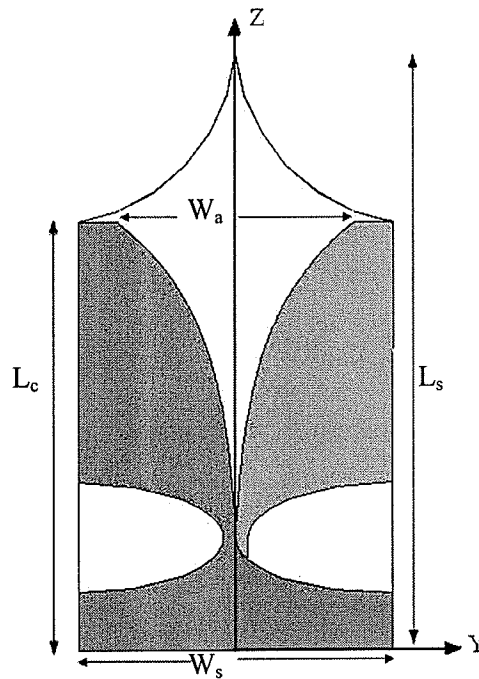


Fig. 5.16 Front view of the curved sharp tip substrate model along with co-ordinate system: $L_s = 105.90\text{mm}$, $L_c = 75.90\text{mm}$, $W_s = 55.90\text{mm}$, $W_a = 43\text{mm}$ and described by (5.1), with $\epsilon_r = 2.5$, height of each dielectric $h = 1.5\text{mm}$ and $\tan\delta = 0.001$

Tables 5.25 to 5.28 summarize the two principle planes' radiation characteristics of interest.

Frequency (GHz)	Boresight gain (dBi)	Peak gain (dBi)	Position of Peak gain	3 dB BW	10 dB BW
6	8.923	9.111	-6°	49°	121°
7	9.766	9.854	-3°	41°	110°
8	10.514	10.561	-2°	41°	101°
9	10.928	10.983	-2°	35°	94°
10	11.055	11.055	0°	37°	95°
11	10.786	10.792	1°	36°	93°
12	11.272	11.334	2°	34°	82°
13	10.552	10.630	2°	45°	82°
14	10.714	11.049	4°	29°	80°
15	10.505	10.697	4°	43°	102°
16	2.312	3.372	31°	67°	103°
17	3.163	4.965	34°	65°	138°
18	4.304	5.433	7°	62°	132°
19	5.254	6.548	6°	44°	121°
20	6.829	8.107	6°	44°	96°

Table 5.25 Summary of E-plane co-pol pattern characteristics of the curved sharp tip substrate model given in Fig. 5.16

Frequency (GHz)	Boresight Cross-pol (dBi)	Peak Cross-pol (dBi)	Position of Peak Cross-pol
6	-45.847	-36.695	-76°
7	-42.920	-30.744	89°
8	-44.594	-28.136	-81°
9	-26.076	-20.684	33°
10	-38.086	-26.067	-173°
11	-36.918	-27.581	135°
12	-34.161	-23.158	126°
13	-36.264	-22.406	129°
14	-35.400	-23.114	48°
15	-28.862	-22.090	-173°
16	-34.999	-24.480	-38°
17	-37.484	-23.804	42°
18	-28.508	-18.078	154°
19	-29.997	-22.923	-145°
20	-30.172	-23.315	55°

Table 5.26 Summary of E-plane cross-pol pattern characteristics of the curved sharp tip substrate model given in Fig. 5.16

Frequency (GHz)	Boresight gain (dBi)	Peak gain (dBi)	Position of Peak gain	3 dB BW	10 dB BW
6	8.923	8.923	0°	72°	106°
7	9.766	9.766	1°	64°	98°
8	10.514	10.514	0°	52°	84°
9	10.928	10.928	0°	48°	82°
10	11.055	11.055	0°	44°	124°
11	10.786	10.786	0°	40°	128°
12	11.272	11.272	0°	42°	116°
13	10.552	10.552	0°	39°	127°
14	10.714	10.714	0°	41°	115°
15	10.505	10.505	0°	44°	115°
16	2.312	2.312	0°	50°	92°
17	3.163	3.163	-1°	52°	107°
18	4.304	4.378	10°	51°	101°
19	5.254	5.265	-6°	47°	94°
20	6.829	6.832	2°	46°	90°

Table 5.27 Summary of H-plane co-pol pattern characteristics of the curved sharp tip substrate model given in Fig. 5.16

Frequency (GHz)	Boresight Cross-pol (dBi)	Peak Cross-pol (dBi)	Position of Peak Cross-pol
6	-45.847	-9.984	128°
7	-42.920	-12.199	72°
8	-44.594	-10.339	61°
9	-26.076	-6.691	-52°
10	-38.086	-7.309	45°
11	-36.918	-4.701	38°
12	-34.161	-7.307	-108°
13	-36.264	-2.416	152°
14	-35.400	-4.196	119°
15	-28.862	-5.155	-153°
16	-34.999	-12.453	141°
17	-37.484	-9.899	-127°
18	-28.508	-9.557	135°
19	-29.997	-5.059	-113°
20	-30.172	-6.803	-109°

Table 5.28 Summary of H-plane cross-pol pattern characteristics of the curved sharp tip substrate model given in Fig. 5.16

From the tables it is seen that the performance of this model is more or less like that of the sharp tip substrate model.

Overall, from this study, may be seen that all three elongated substrate shapes did not have a significant influence on the gain of the antenna in the 6 to 15 GHz range, but they did improve the antenna gain in the 16 to 20 GHz range. The sharp tip substrate model of Fig. 5.14 may be concluded to be the best design for the balanced antipodal Vivaldi in order to achieve an optimum gain performance.

5.5 Summary

In this chapter, a balanced antipodal Vivaldi developed from the compact Model 6 of chapter four was studied. Its radiation characteristics and phase centre location were presented and it was observed that this antenna exhibited a commendable performance like its single sided counterpart of chapter four. Though this compact antenna had a remarkable performance, it did not overcome bandwidth limitations. In order to appreciate the broadband nature of the Vivaldi, a balanced antipodal Vivaldi antenna with a much wider aperture than that of the former was designed and studied. The effect of substrate elongation on this antenna's performance was investigated, and it was seen that with the increase in length of substrate, its gain also increased. However, it was observed that for a substrate elongation of 30 mm, the gain of the antenna drastically decreased in the 16 to 20 GHz frequency range of operation. The effect of shaping of the elongated substrate was also studied and it was found that it did not have a prominent impact on antenna performance in the 6 to 15 GHz range, but significantly increased the gain in the 16 to 20 GHz range. From an overall inspection, it was concluded that the sharp tip substrate model of Fig. 5.14 was the best design to achieve optimum gain performance.

CHAPTER 6

EXPERIMENTAL VERIFICATION

6.1 Introduction

In this chapter, an experimental verification of one of the antenna models discussed in the previous chapter is presented. The chosen model was fabricated and its return loss and radiation patterns were measured in order to confirm the simulated results. A comparison of the measured and simulated results was carried out, and a study of the measured phase center location of the antenna is discussed in brief.

6.2 Fabricated Antenna

The antenna model chosen to be fabricated was the balanced antipodal Vivaldi presented in Fig. 5.10 of section 5.3.1 which had a substrate elongation of 12.80 mm, as it exhibited a very good performance over the entire considered frequency range and also due to the fact that the dielectric substrate available for fabrication matched its specifications. More importantly, it was of appropriate size for the vacuum table used to fabricate the antenna.

In order to fabricate the desired model, a $50\ \Omega$ stripline feed of width 2.24 mm was etched on one side of a copper clad substrate and it was flared out to produce one wing of the balanced antipodal Vivaldi. On the other side of the substrate, the ground plane was reduced to give a twin line which was then flared in the opposite direction of the first flare. On another dielectric slab, an identical ground plane to twin line to Vivaldi flare transition as the previous was etched on one side while on the other side, the copper

cladding was completely stripped off. These two substrates were sandwiched together and held in place with the help of nylon No. 6 screws to form the desired balanced antipodal Vivaldi antenna. Each dielectric slab used had a relative permittivity of $\epsilon_r = 2.5$, height $h = 1.5$ mm and a loss tangent $\tan\delta = 0.001$. A photograph of the etched stripline to flare transition on the first dielectric slab and the ground plane to twin line to flare transition on the second slab can be seen in Fig. 6.1 (a). It must be noted that the substrate with the etched stripline to flare transition also has an etched ground plane to flare transition on the other side in the opposite direction. The copper cladding on the other side of the second substrate is completely stripped off.

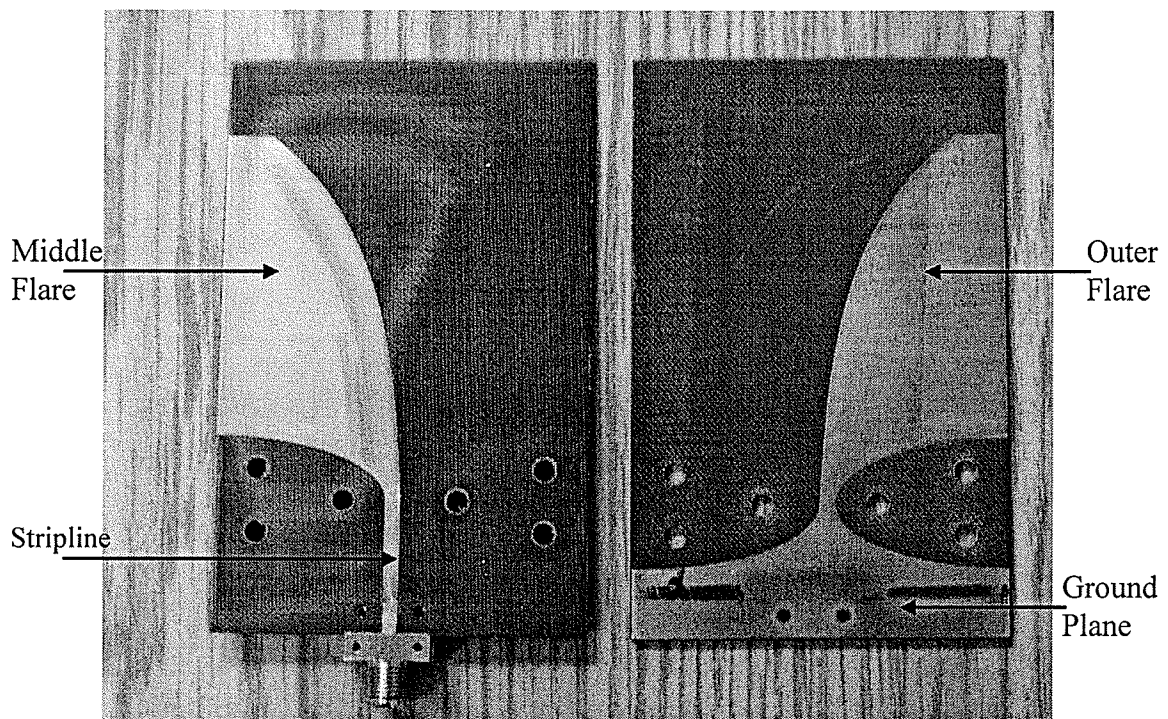


Fig. 6.1 (a) Photograph of the two dielectric substrates of the fabricated antenna showing the etched stripline to flare transition on one slab and the ground plane to flare transition on the other. Other dimensions are given in Fig. 6.1 (b)

Figure 6.1 (b) shows a photograph of the resultant fabricated balanced antipodal Vivaldi antenna after the two substrates are fastened together with the help of screws. The dimensions of this antenna are also given.

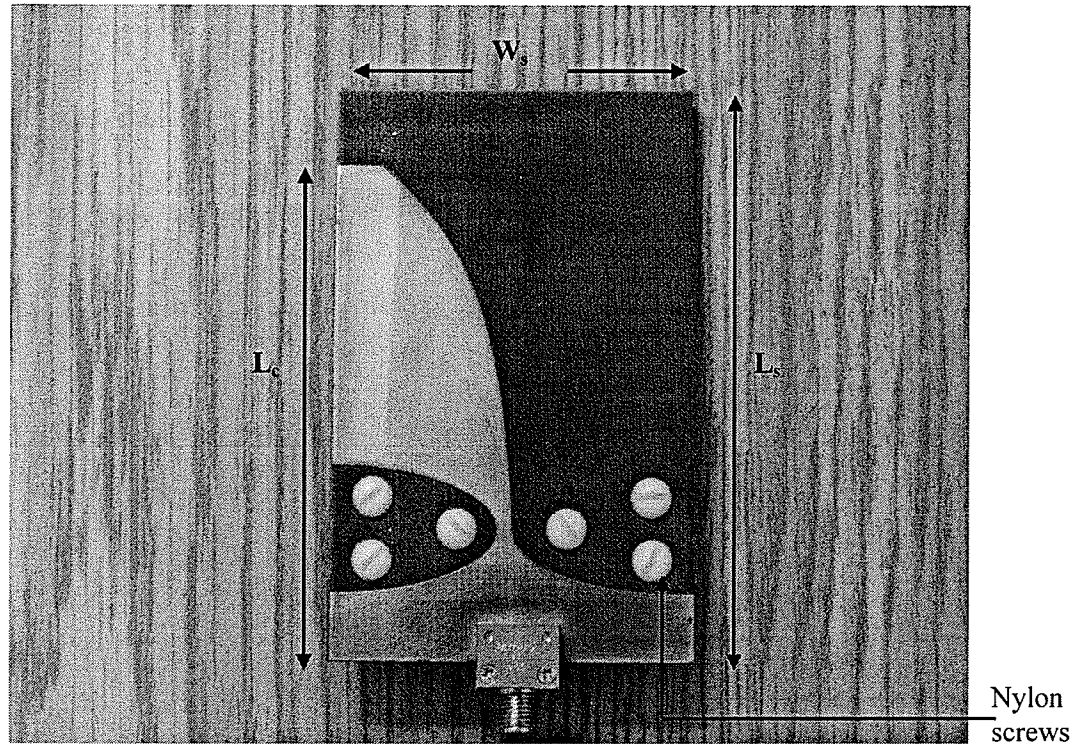


Fig. 6.1 (b) Fabricated balanced antipodal Vivaldi antenna described by (5.1) with substrate elongation of 12.80 mm: $L_s = 88.70\text{mm}$, $L_c = 75.90\text{mm}$, $W_s = 55.90\text{mm}$

6.3 Simulated vs. Measured Results

The fabricated Vivaldi was fed electromagnetically by the $50\ \Omega$ stripline, which was excited by a $50\ \Omega$ SMA probe. The antenna was tested in the Antenna Laboratory at the University of Manitoba. The S_{11} and input impedance were measured by ANRITSU ME7808A Network Analyzer. Fig. 6.2 shows a comparison between the measured and

simulated S_{11} . It can be seen that the fabricated antenna also exhibits a very good wideband performance in the 6 to 20 GHz frequency range.

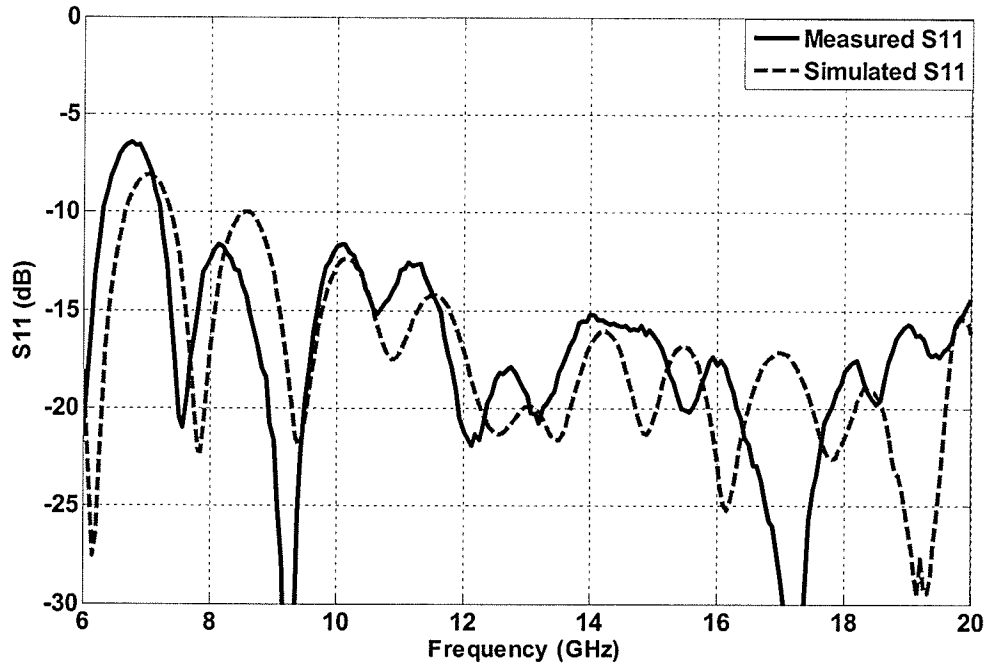


Fig. 6.2 Simulated and measured S_{11} patterns with respect to 50Ω for the balanced antipodal Vivaldi shown in Fig. 5.10 and Fig. 6.1 respectively and described by (5.1) with $\epsilon_r = 2.5$, $h = 1.5 \text{ mm}$, $\tan\delta = 0.001$. Other parameters are given in Fig. 6.1

As the fabricated Vivaldi comprises of two dielectric slabs, there is probability that air gaps exist between the two substrate layers. This causes a deviation of the measured return loss from that of the simulated, as this factor is not taken into account during simulations. With this practical issue taken into consideration, it can be said that the simulated and measured return loss results are in good agreement.

In the input impedance plots of this antenna are shown in Fig. 6.3 for three separate frequency ranges. From the figure it can be seen that the locus of the input

impedance at each frequency range is near the centre of the Smith chart, indicating that the antenna is well matched to the 50 Ω SMA probe in each range.

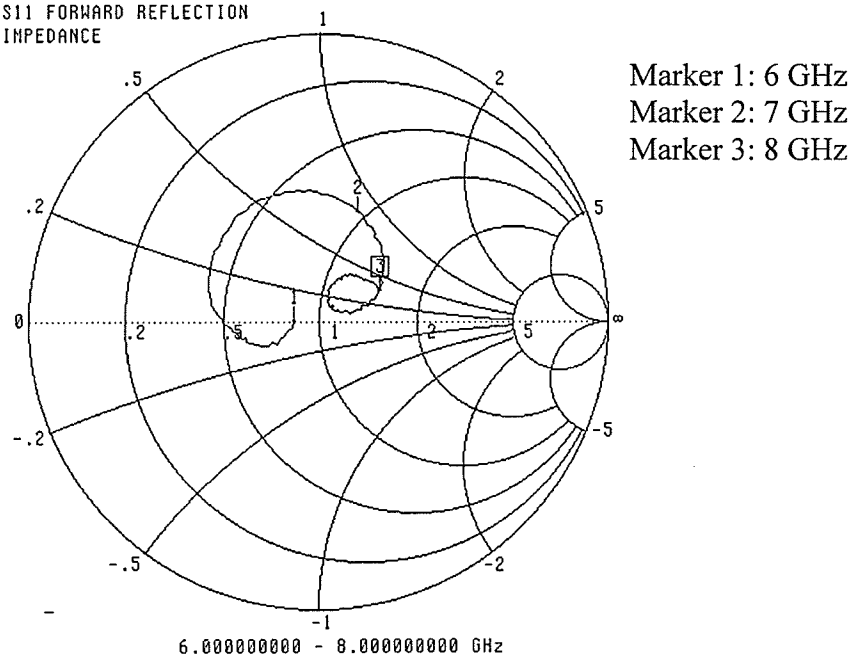


Fig. 6.3 (a)

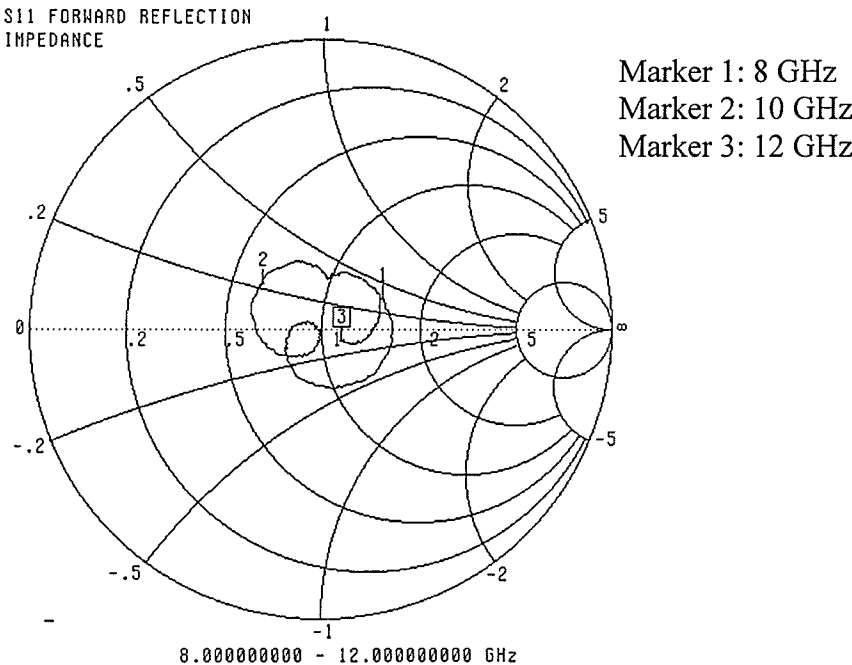


Fig. 6.3 (b)

Fig. 6.3 contd.

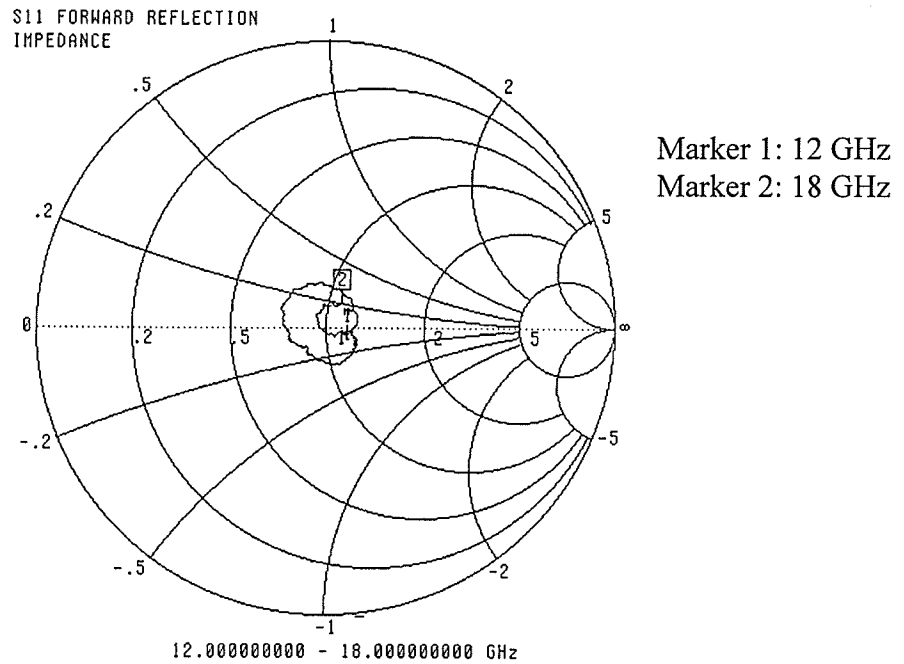


Fig. 6.3 (c)

Fig. 6.3 Measured input impedance plot of the antenna in Fig. 6.1 with respect to 50Ω on a substrate with $\epsilon_r=2.5$, $h=1.5\text{mm}$ and $\tan\delta=0.001$. Other parameters are mentioned in Fig. 6.1

The radiation characteristics of the fabricated antenna were measured in the anechoic chamber in the Antenna Laboratory at the University of Manitoba. Figures 6.4 and 6.5 show the positions in which the antenna was mounted in order to measure the E and H-plane radiation patterns respectively.

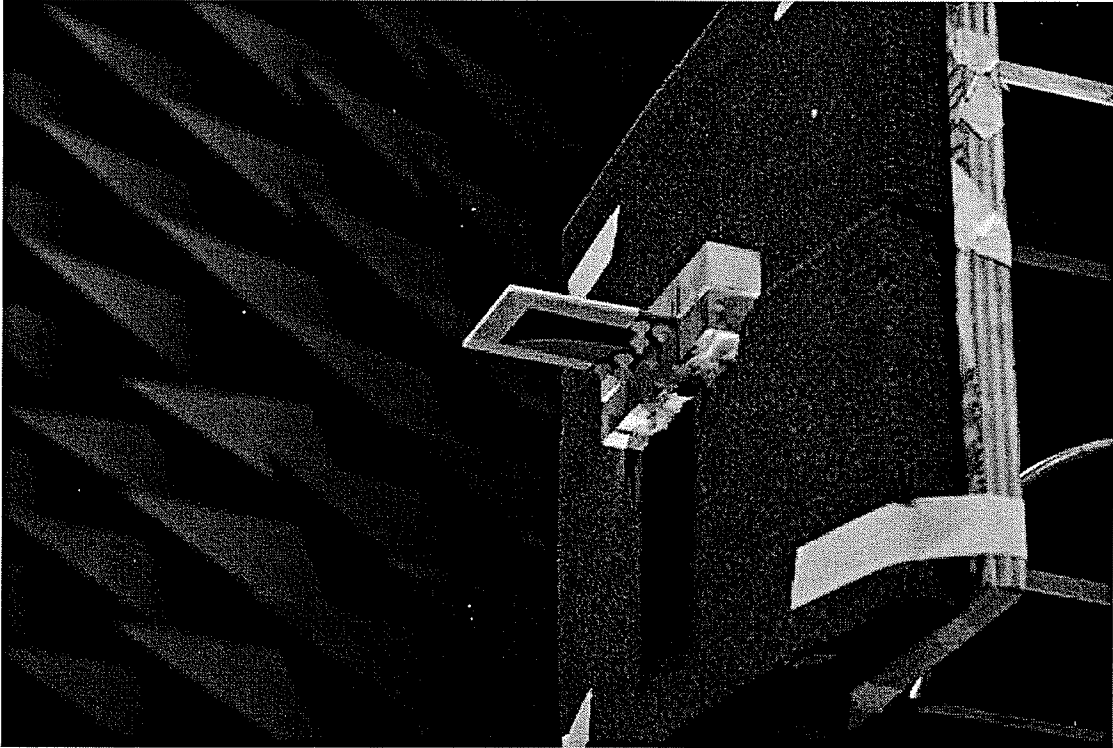


Fig. 6.4 Picture of the fabricated balanced antipodal Vivaldi showing the mounting position in the anechoic chamber for measuring E-plane radiation patterns

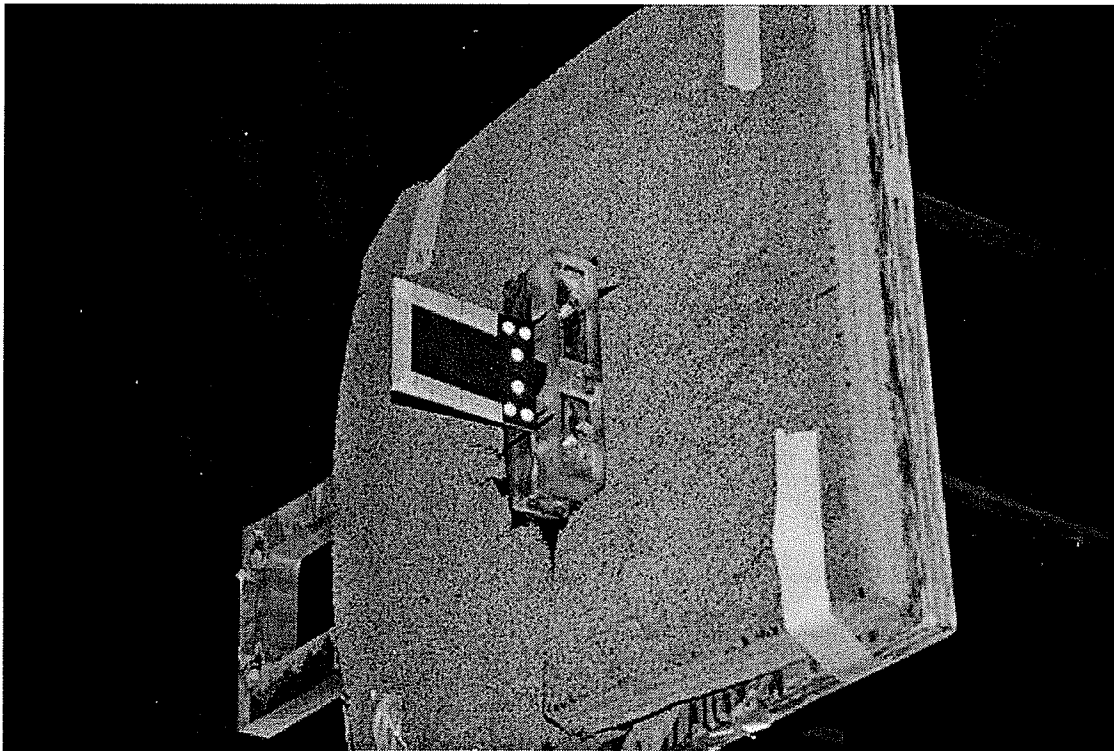
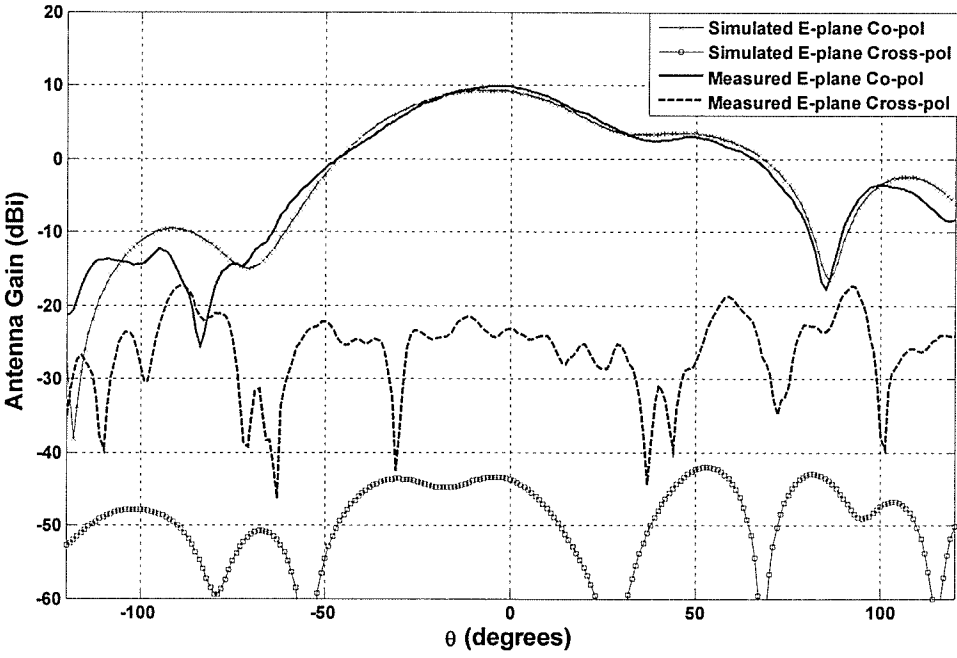


Fig. 6.5 Picture of the fabricated balanced antipodal Vivaldi showing the mounting position in the anechoic chamber for measuring H-plane radiation patterns

The far-field radiation patterns for both principle planes were measured in the frequency range of 6 to 18 GHz (with a one GHz frequency step). Figure 6.6 shows a comparison between the E-plane simulated and measured radiation patterns in this frequency range.



(a) 6 GHz

Fig. 6.6 (a)

Fig. 6.6 contd.

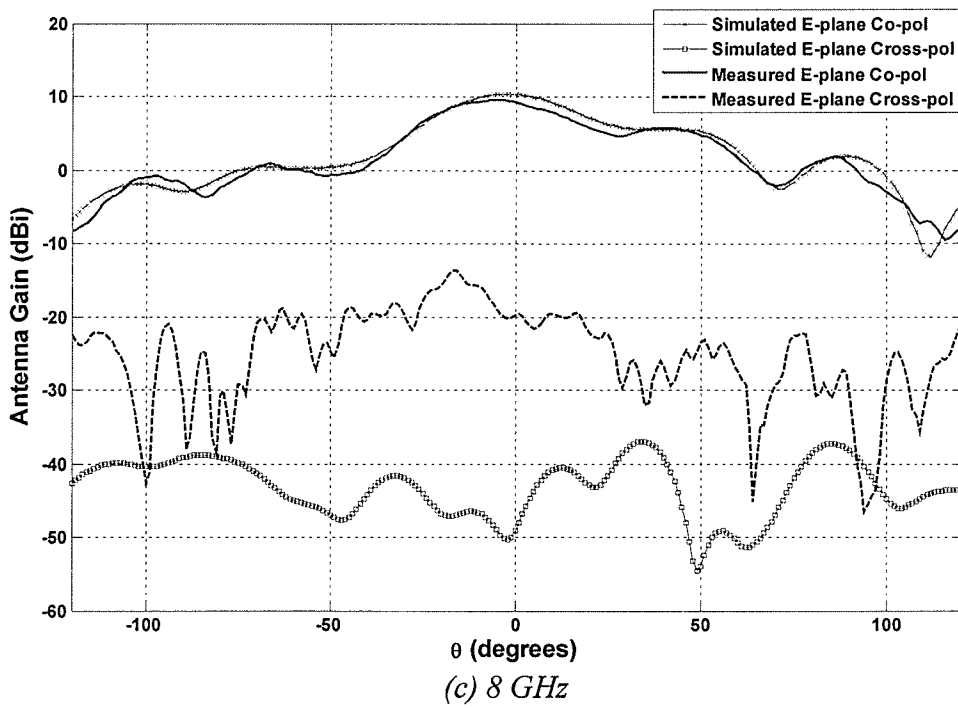
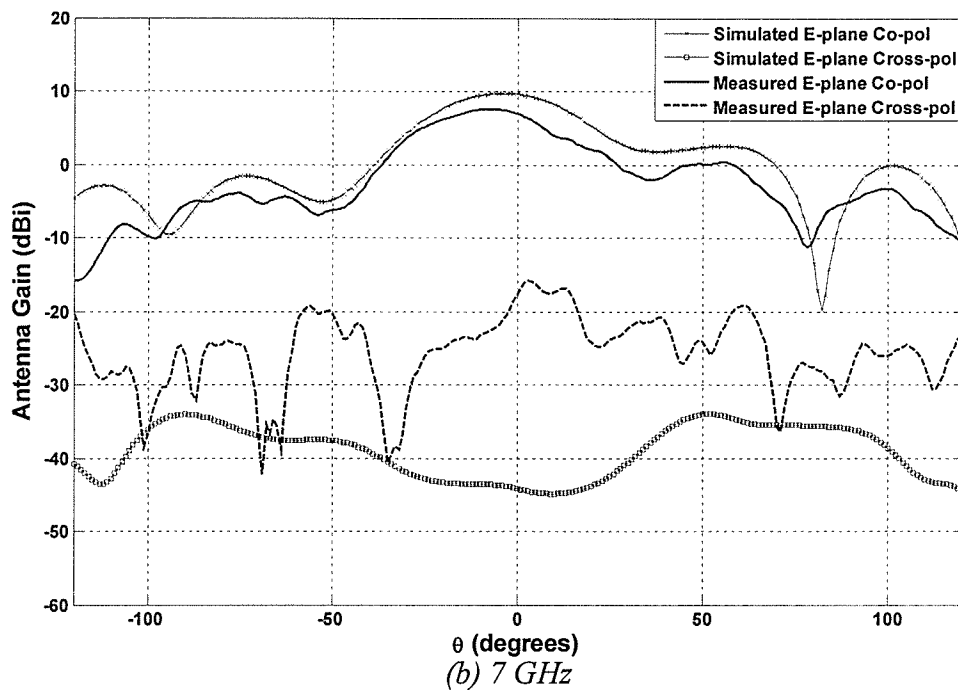


Fig. 6.6 (b), (c)

Fig. 6.6 contd.

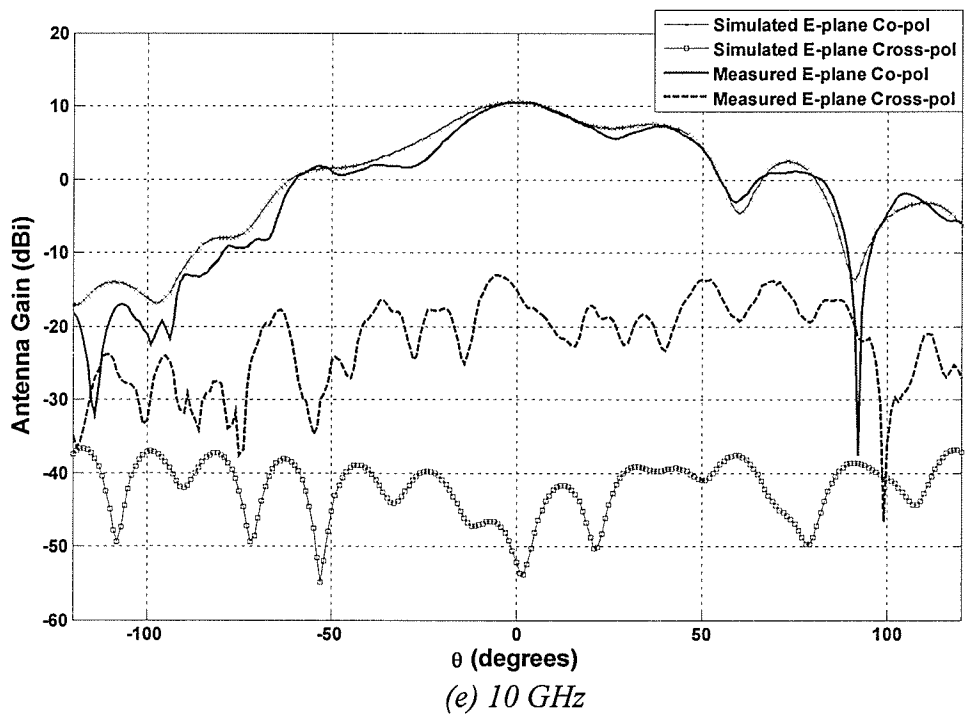
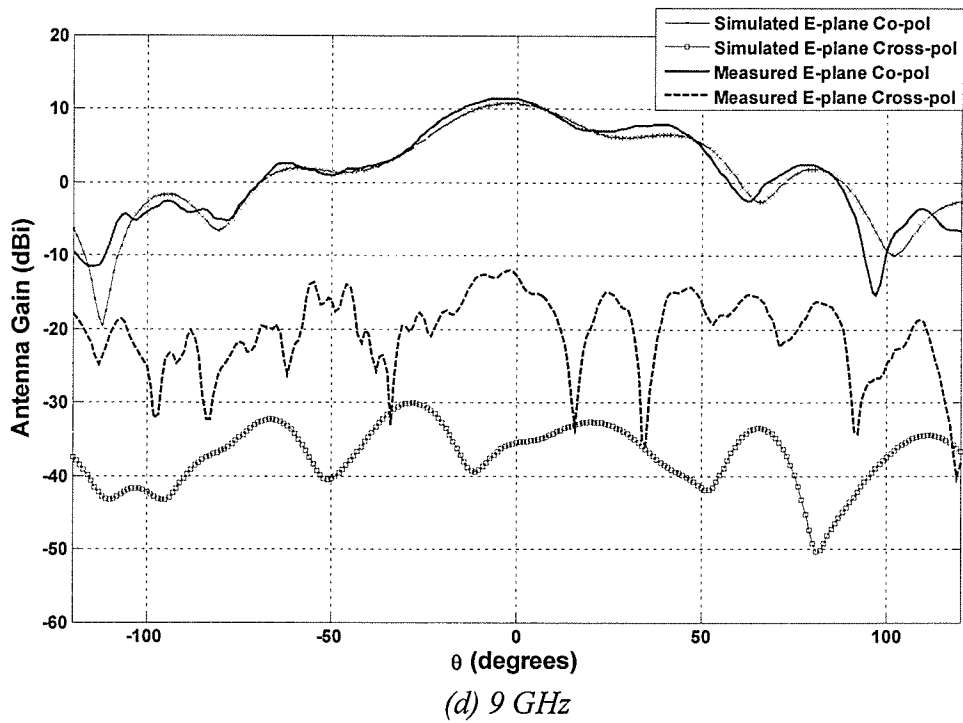


Fig. 6.6 (d), (e)

Fig. 6.6 contd.

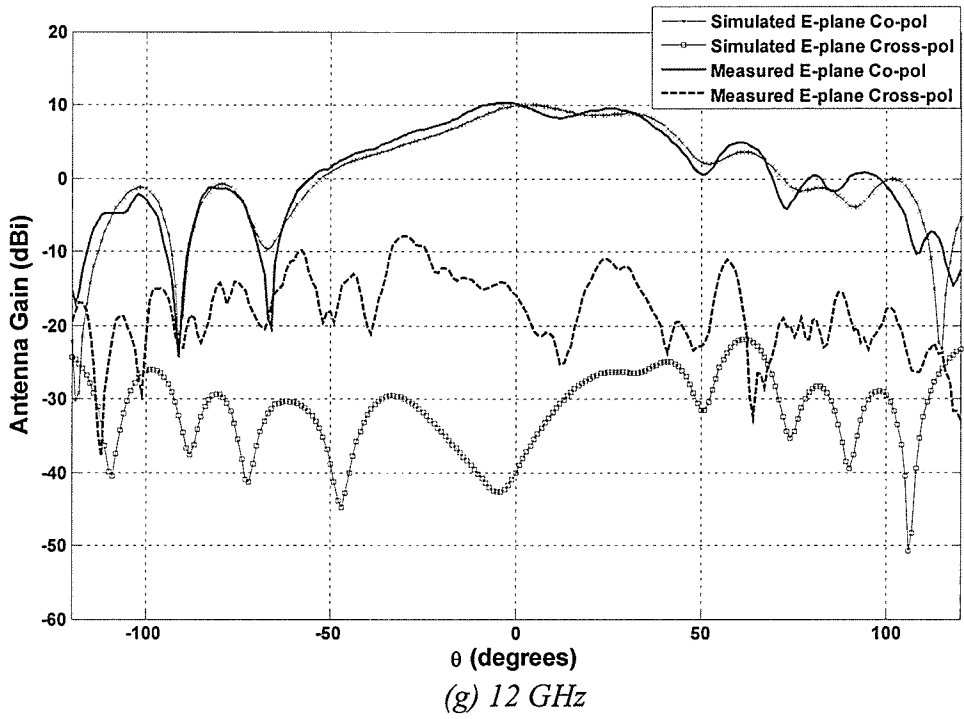
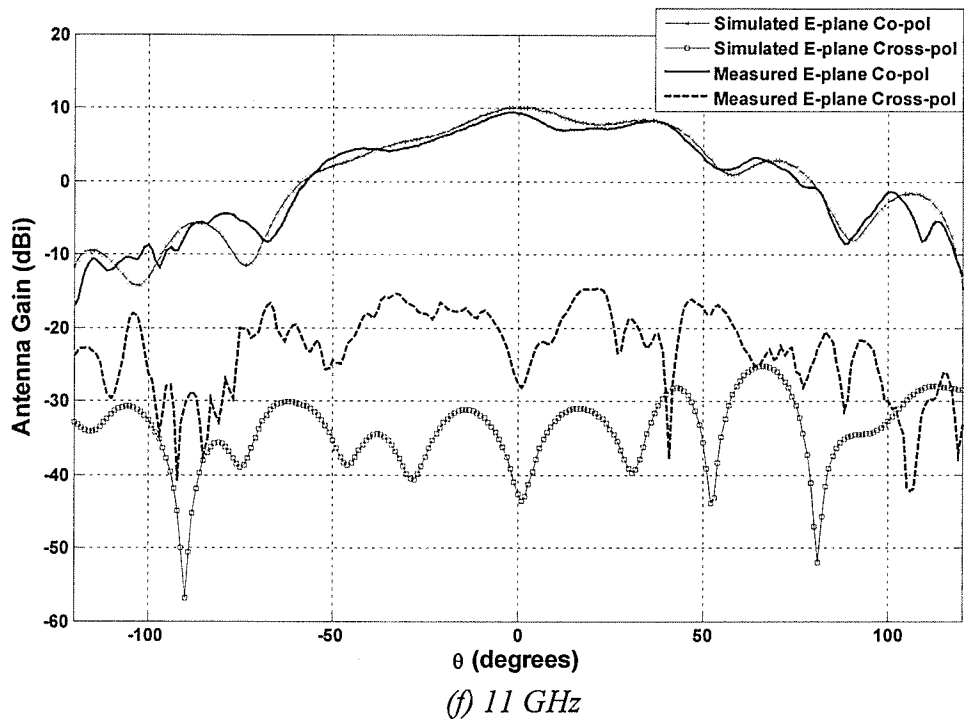


Fig. 6.6 (f), (g)

Fig. 6.6 contd.

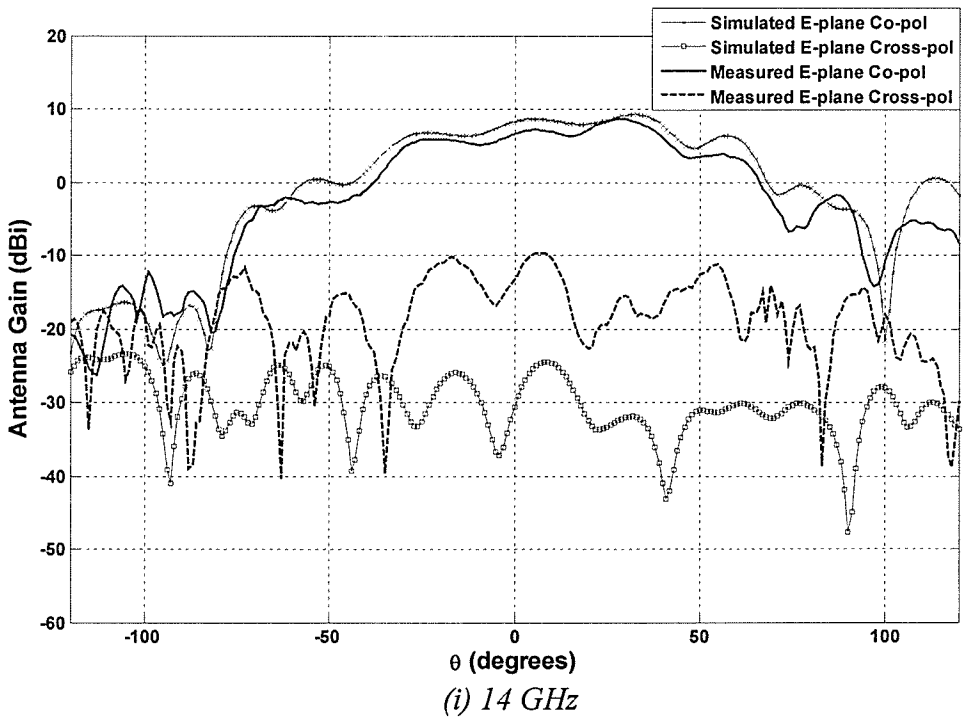
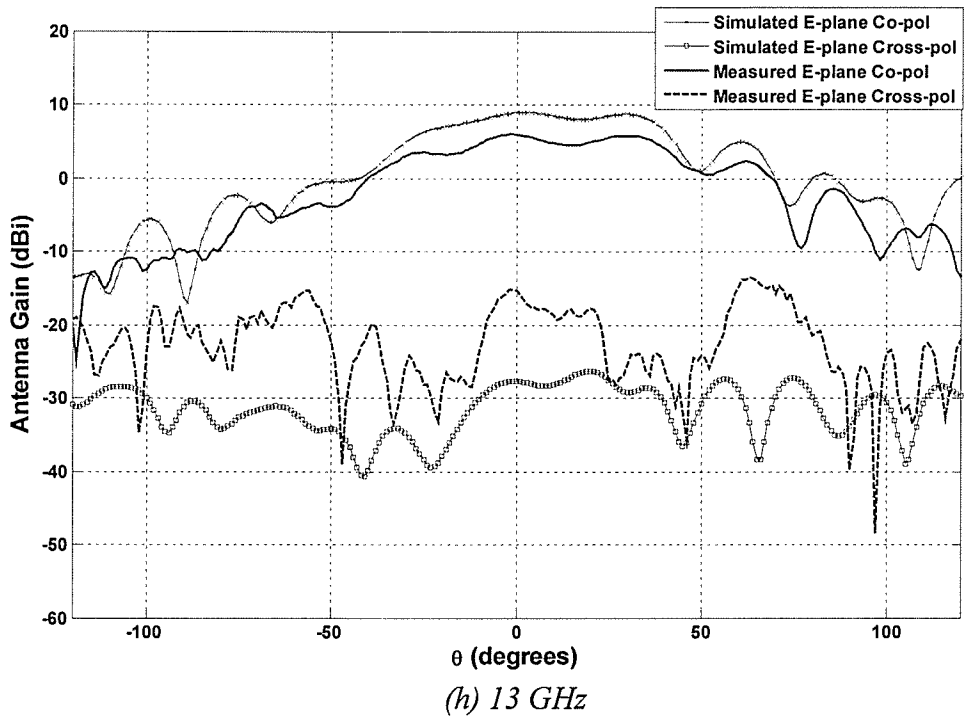


Fig. 6.6 (h), (i)

Fig. 6.6 contd.

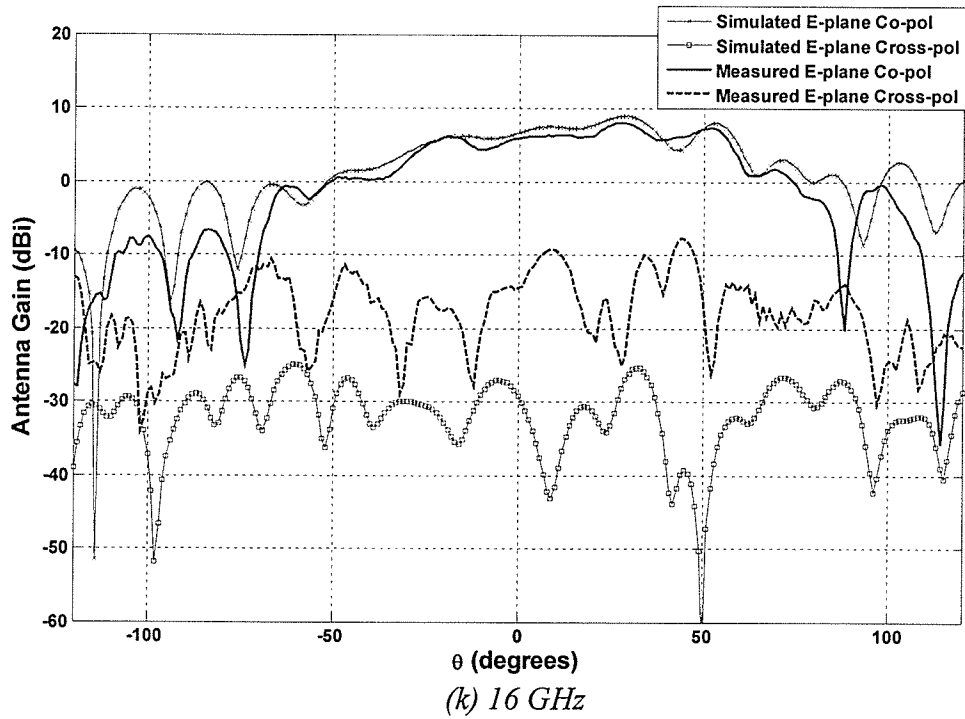
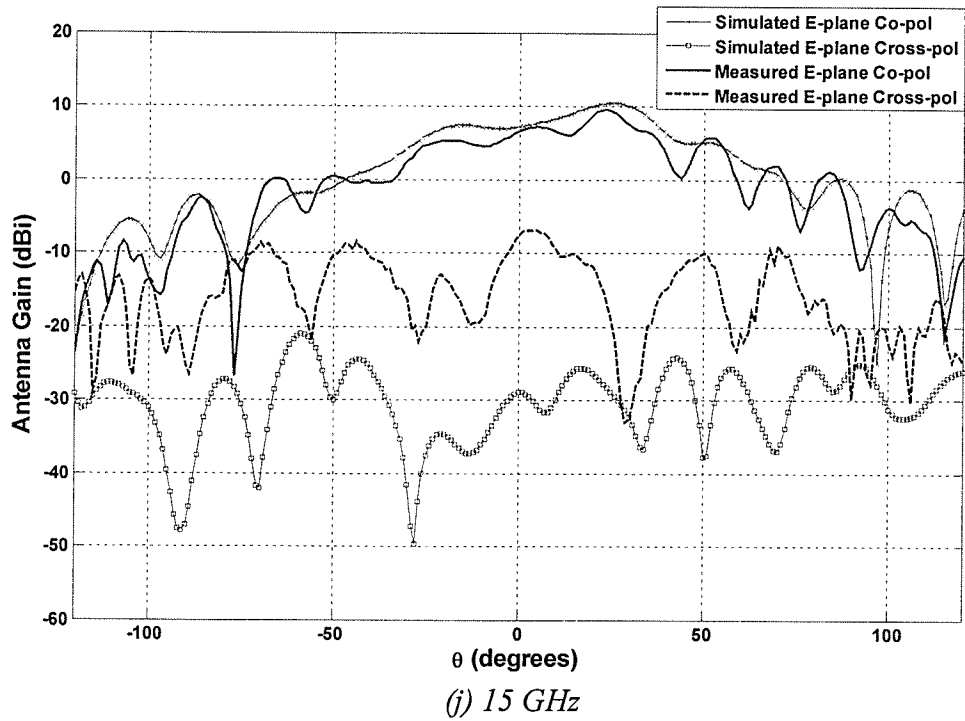


Fig. 6.6 (j), (k)

Fig. 6.6 contd.

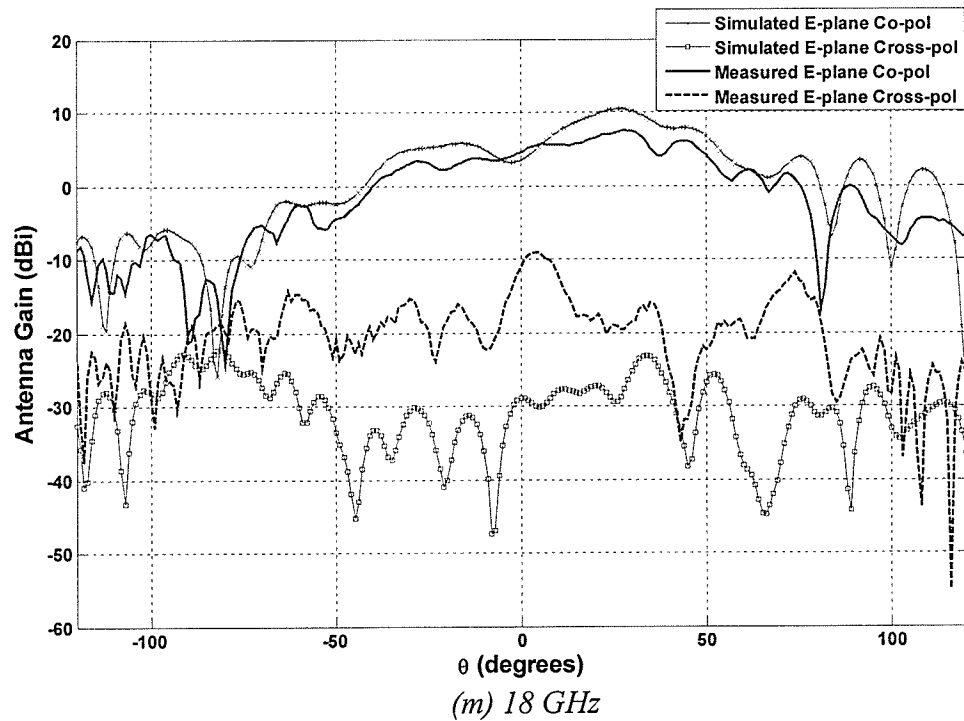
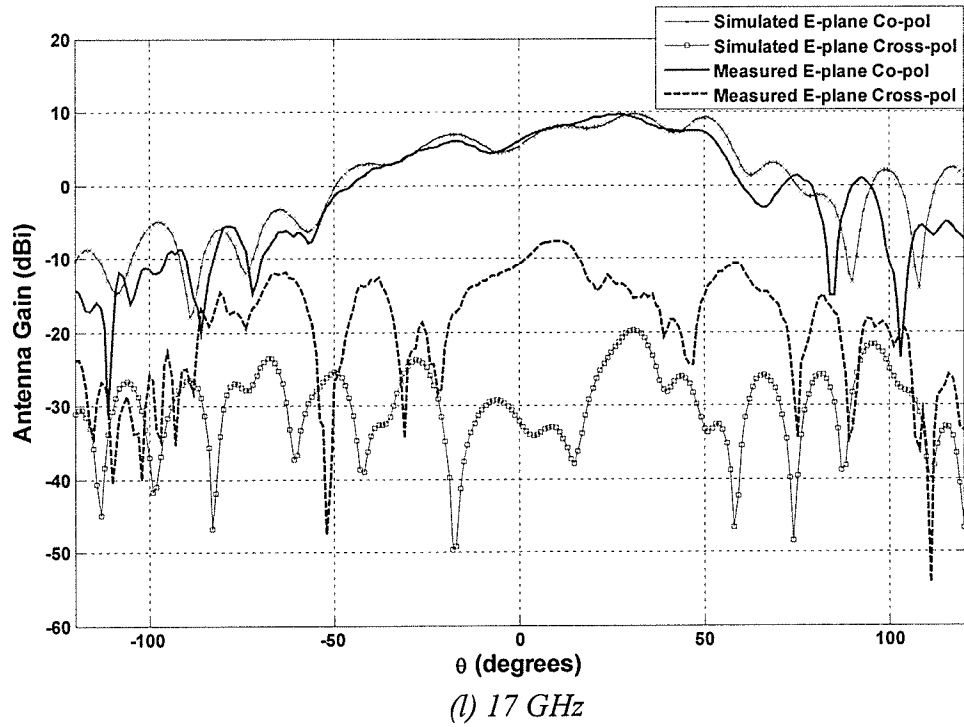


Fig. 6.6 Simulated and measured E-plane ($\phi=90^\circ$ plane) radiation patterns of the balanced antipodal Vivaldi given in Fig. 5.10 and Fig. 6.1 respectively with $\epsilon_r = 2.5$, $h = 1.5$ mm, $\tan\delta = 0.001$. Other parameters are given in Fig. 6.1

A comparison of the important simulated and measured E-plane co-pol and cross-pol characteristics are summarized in Tables 6.1 and 6.2. In the tables, Sim and Meas stand for simulated and measured results respectively.

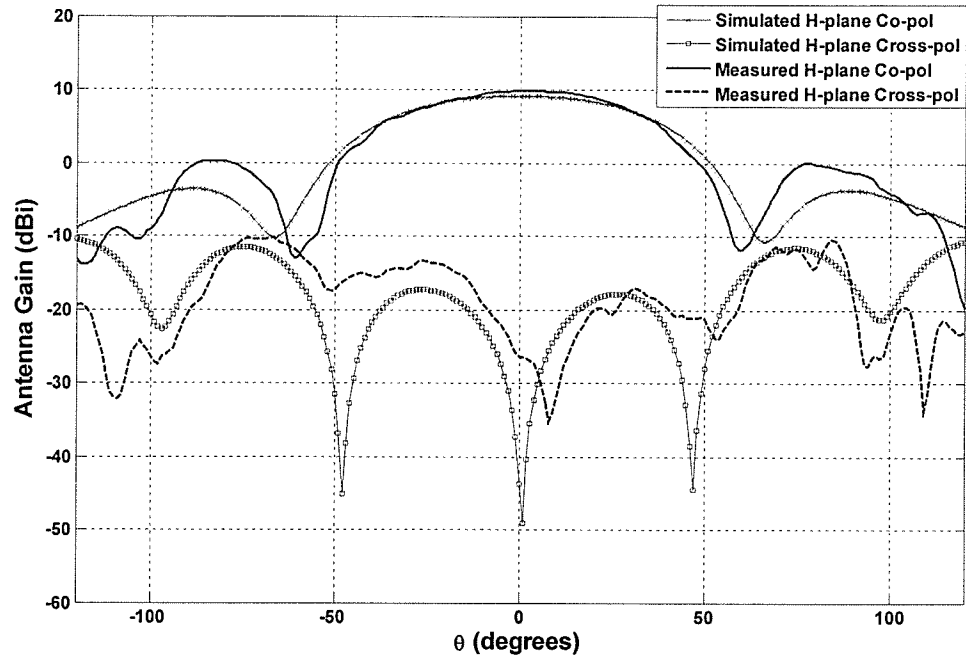
Frequency (GHz)	Boresight Gain (dBi)		Peak Gain (dBi)		Position of Peak Gain		3 dB BW		10 dB BW	
	Sim	Meas	Sim	Meas	Sim	Meas	Sim	Meas	Sim	Meas
6	9.218	9.778	9.392	9.915	-6°	-4°	40°	44°	118°	115°
7	9.608	6.912	9.728	7.587	-4°	-7°	40°	39°	109°	108°
8	10.319	9.257	10.356	9.538	-2°	-4°	41°	44°	115°	141°
9	10.757	11.336	10.821	11.430	-3°	-4°	37°	34°	126°	102°
10	10.707	10.472	10.707	10.480	0°	1°	38°	33°	114°	113°
11	9.967	9.285	9.973	9.369	1°	-2°	62°	64°	137°	130°
12	9.988	10.184	10.080	10.331	3°	-3°	57°	58°	125°	124°
13	9.165	5.907	9.231	5.974	3°	-2°	68°	74°	127°	131°
14	8.409	6.640	9.280	8.627	32°	28°	78°	79°	131°	139°
15	7.069	6.666	10.335	9.607	26°	24°	86°	68°	138°	118°
16	6.686	5.874	8.930	8.092	29°	28°	92°	91°	162°	152°
17	5.340	6.047	9.707	9.636	31°	27°	105°	91°	140°	135°
18	5.111	4.578	10.744	7.491	30°	28°	95°	91°	136°	131°

Table 6.1 Summary of the simulated and measured E-plane co-pol pattern characteristics of the balanced antipodal Vivaldi given in Fig. 5.10 and Fig. 6.1 respectively

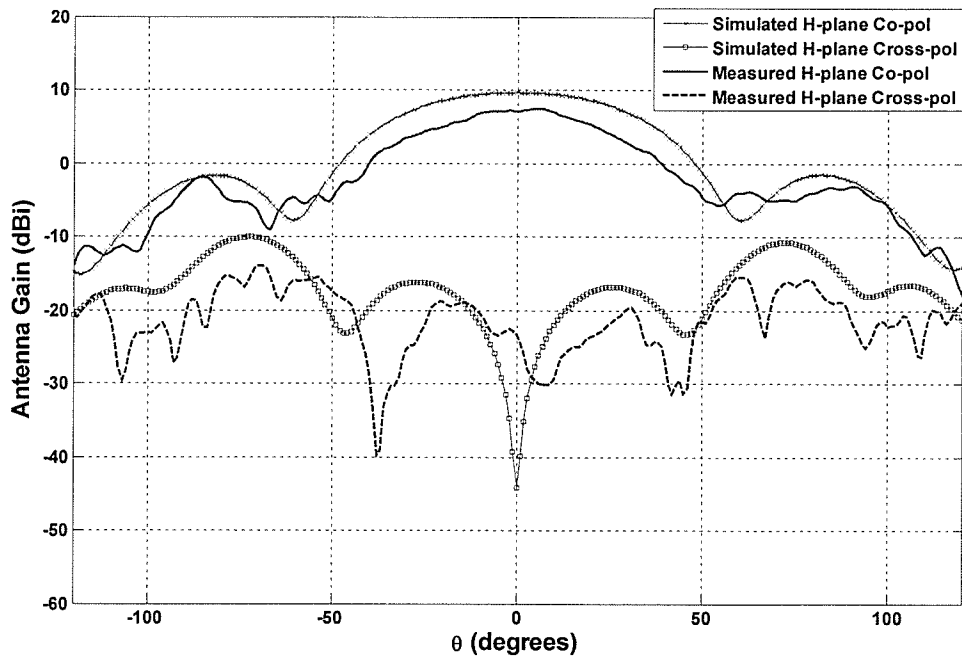
Frequency (GHz)	Boresight Cross-pol (dBi)		Peak Cross-pol (dBi)		Position of Peak Cross-pol	
	Sim	Meas	Sim	Meas	Sim	Meas
6	-43.733	-23.065	-38.916	-17.335	161°	92°
7	-44.174	-17.579	-34.004	-15.869	52°	3°
8	-49.150	-19.726	-36.993	-13.656	34°	-16°
9	-35.500	-12.810	-30.055	-11.979	-28°	-2°
10	-52.190	-15.231	-34.923	-13.035	-144°	-5°
11	-42.672	-27.688	-25.199	-14.593	66°	22°
12	-40.015	-15.983	-21.892	-7.823	62°	-30°
13	-27.705	-15.350	-26.295	-13.482	20°	63°
14	-30.537	-13.185	-23.371	-9.758	-105°	6°
15	-29.008	-7.615	-21.058	-6.906	-59°	3°
16	-29.227	-14.456	-24.929	-7.757	-60°	44°
17	-32.137	-10.772	-19.786	-7.658	31°	12°
18	-26.194	-11.002	-19.794	-9.106	107°	4°

Table 6.2 Summary of the simulated and measured E-plane cross-pol pattern characteristics of the balanced antipodal Vivaldi given in Fig. 5.10 and Fig. 6.1 respectively

Figure 6.7 shows a comparison between the H-plane simulated and measured radiation patterns in the 6 to 18 GHz frequency range.



(a) 6 GHz



(b) 7 GHz

Fig. 6.7 (a), (b)

Fig. 6.7 contd.

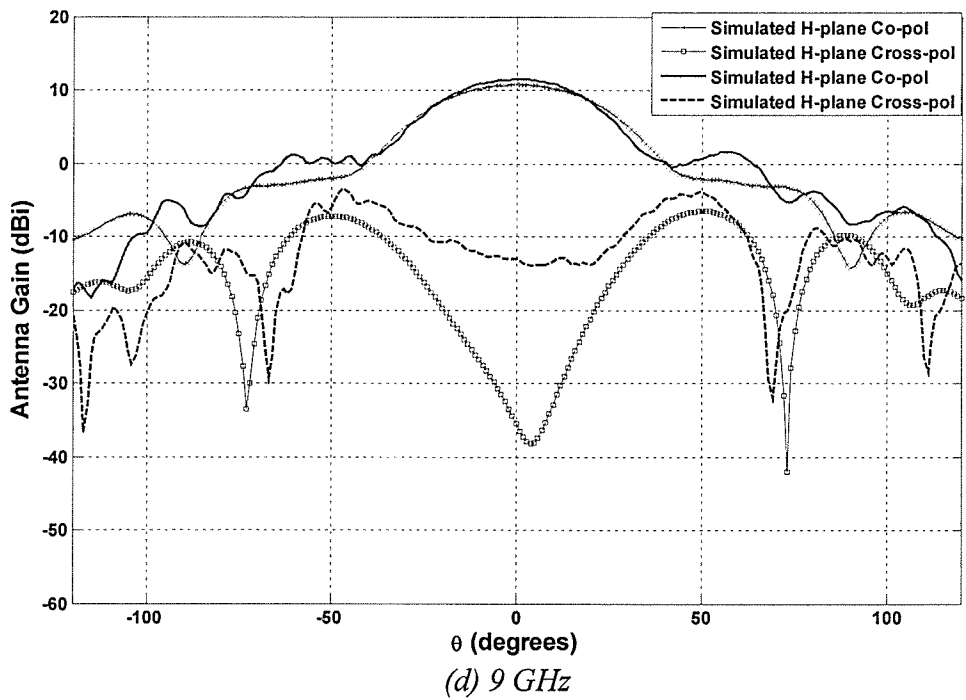
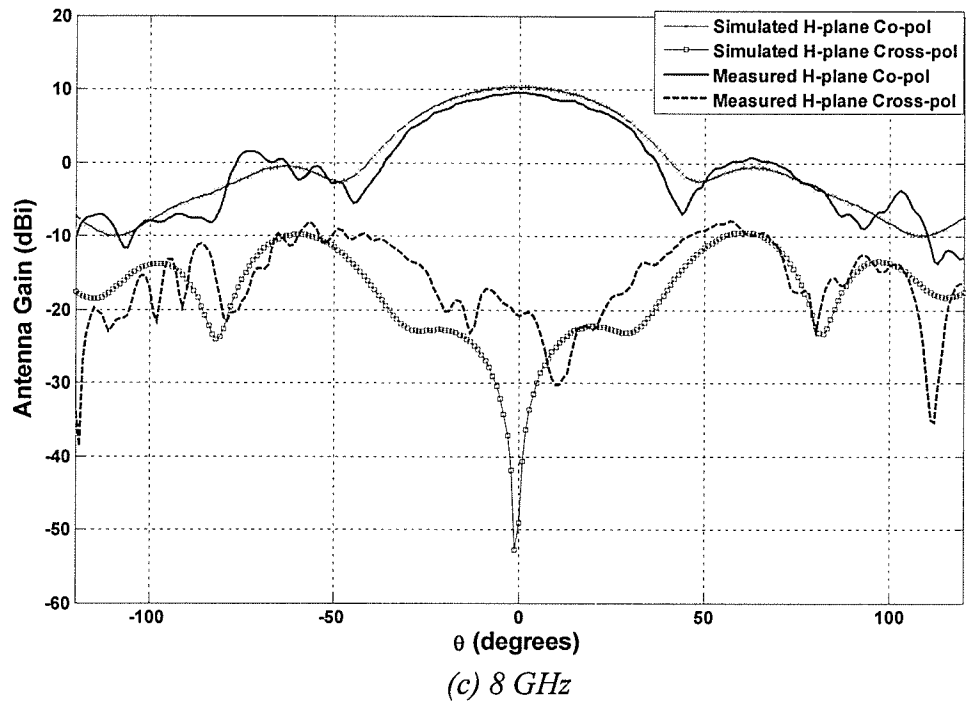


Fig. 6.7 (c), (d)

Fig. 6.7 contd.

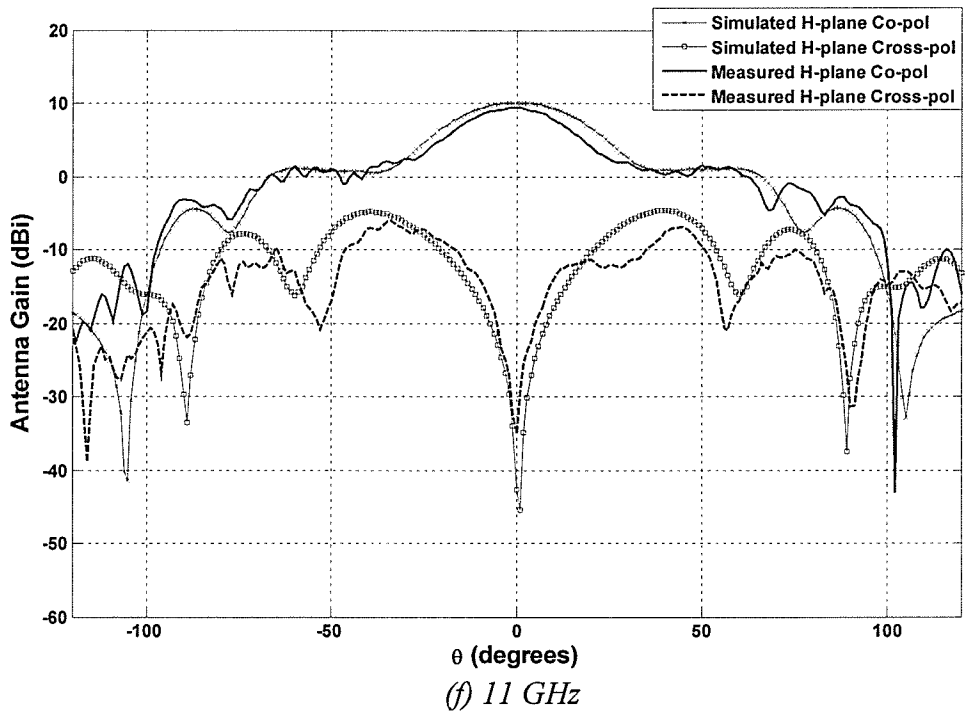
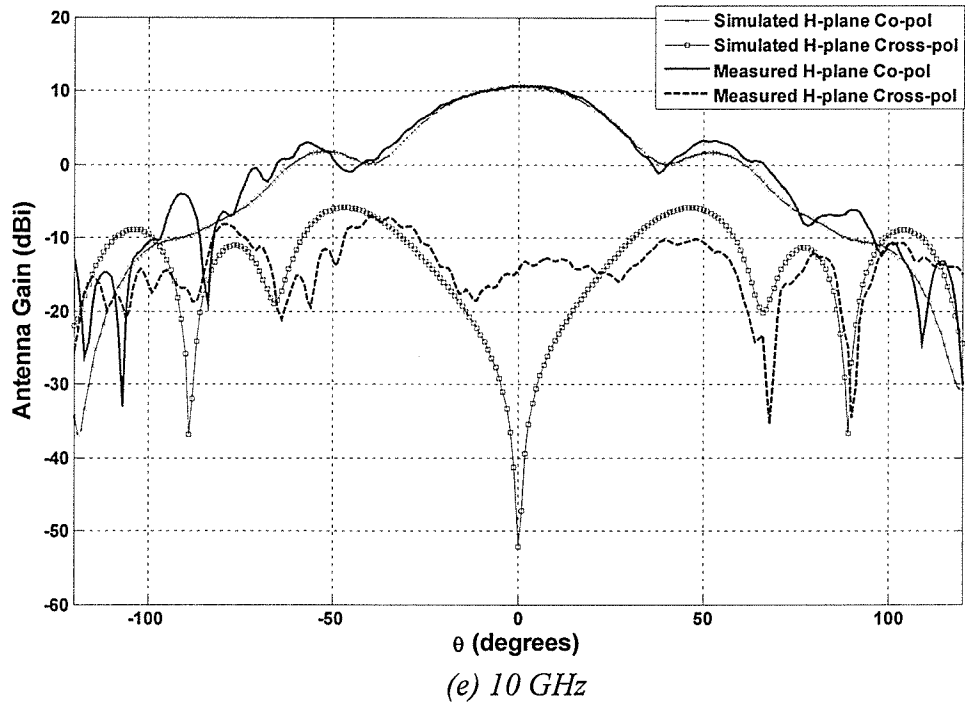


Fig. 6.7 (e), (f)

Fig. 6.7 contd.

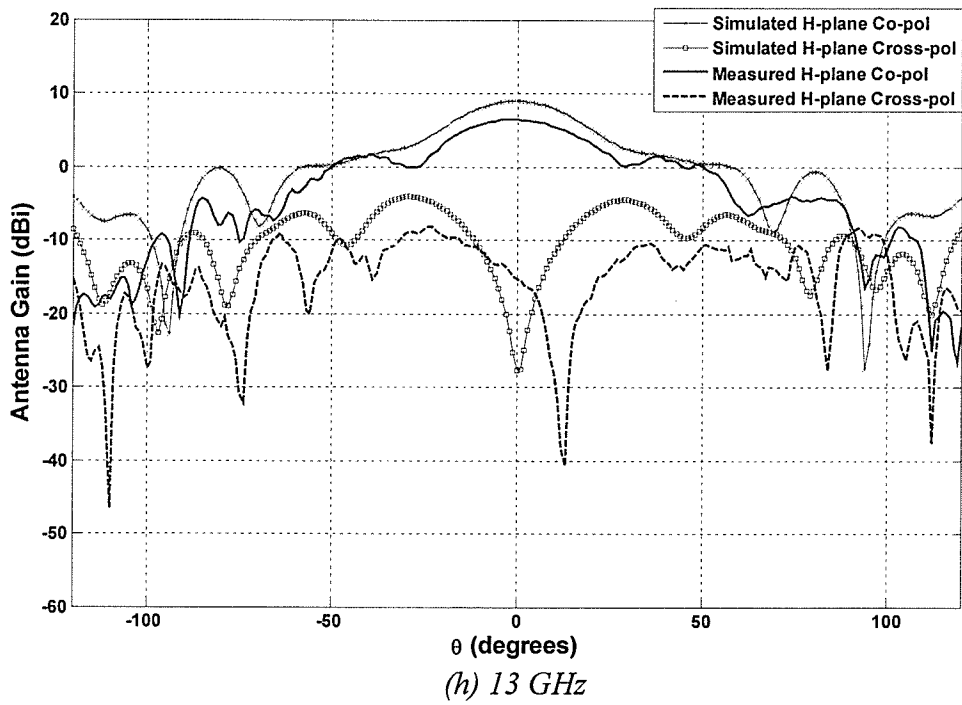
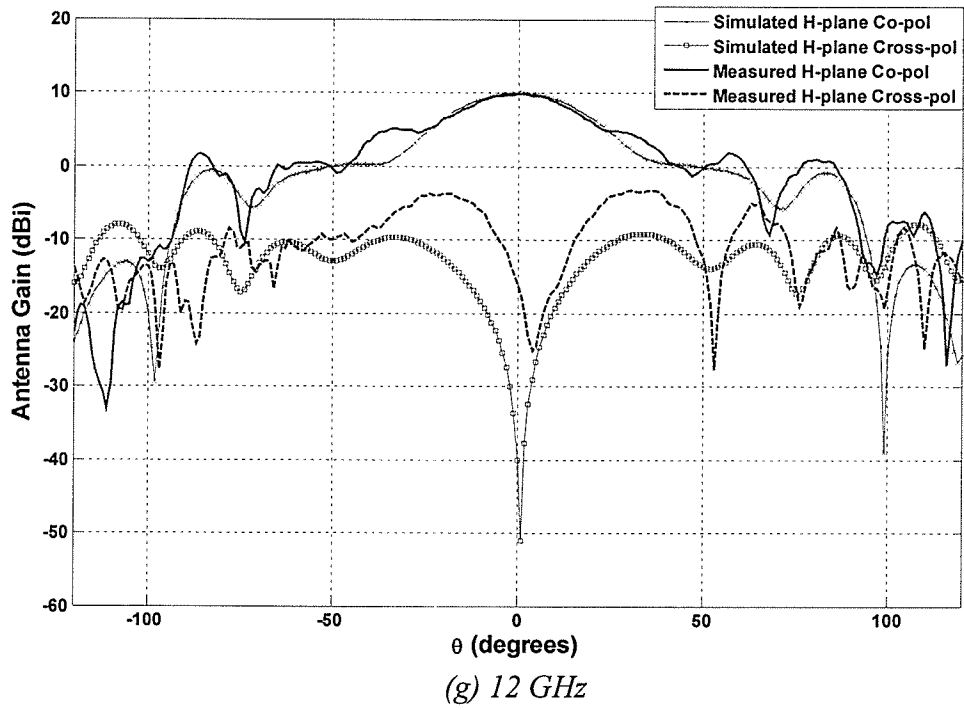


Fig. 6.7 (g), (h)

Fig. 6.7 contd.

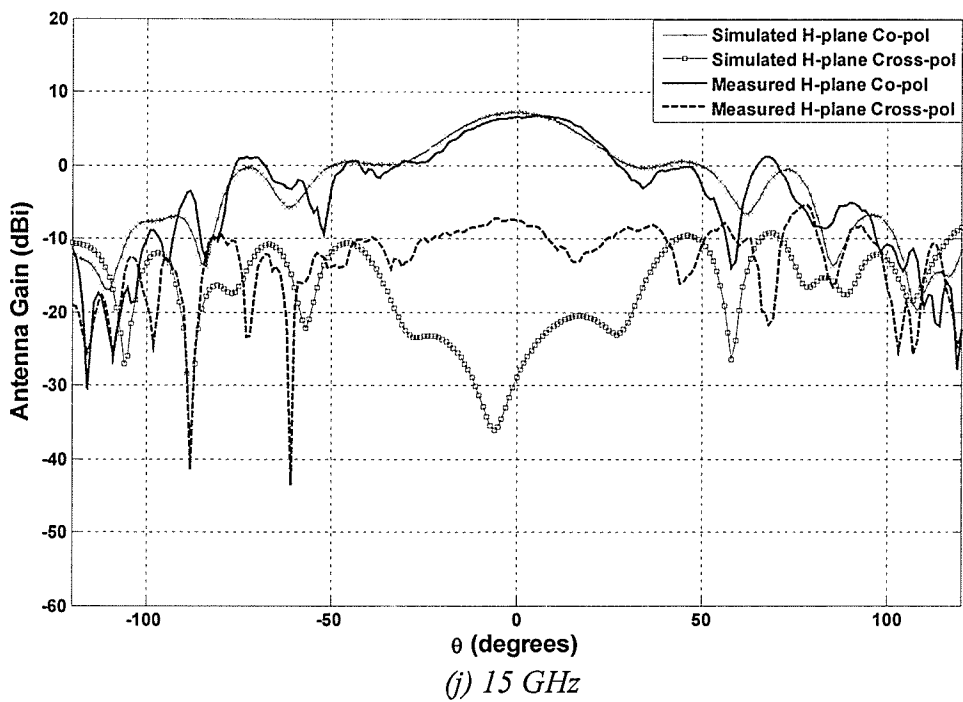
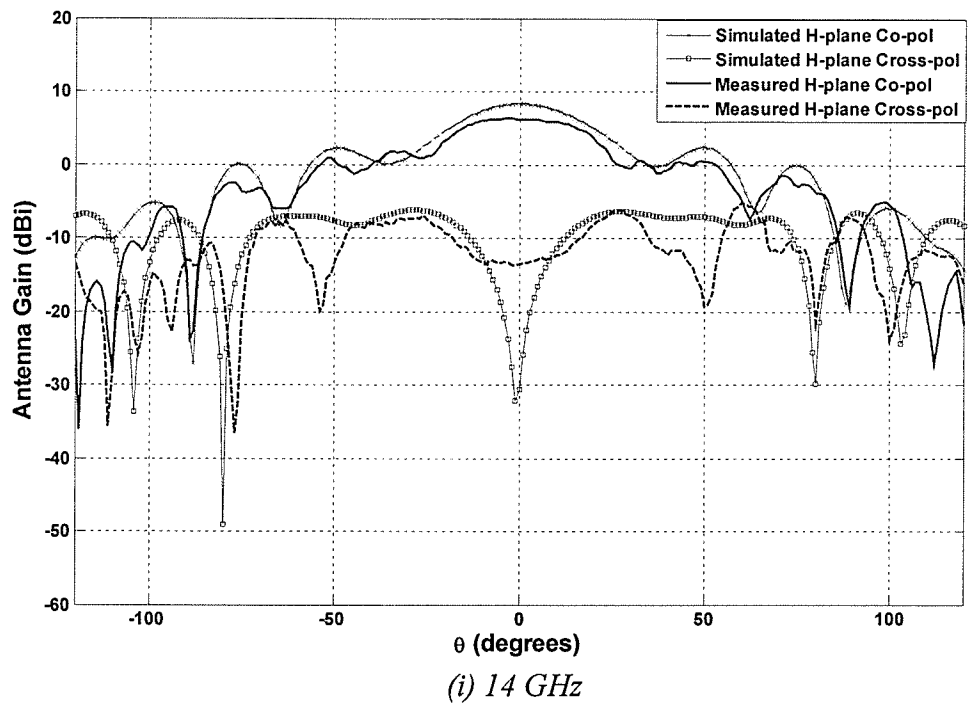


Fig. 6.7 (i), (j)

Fig. 6.7 contd.

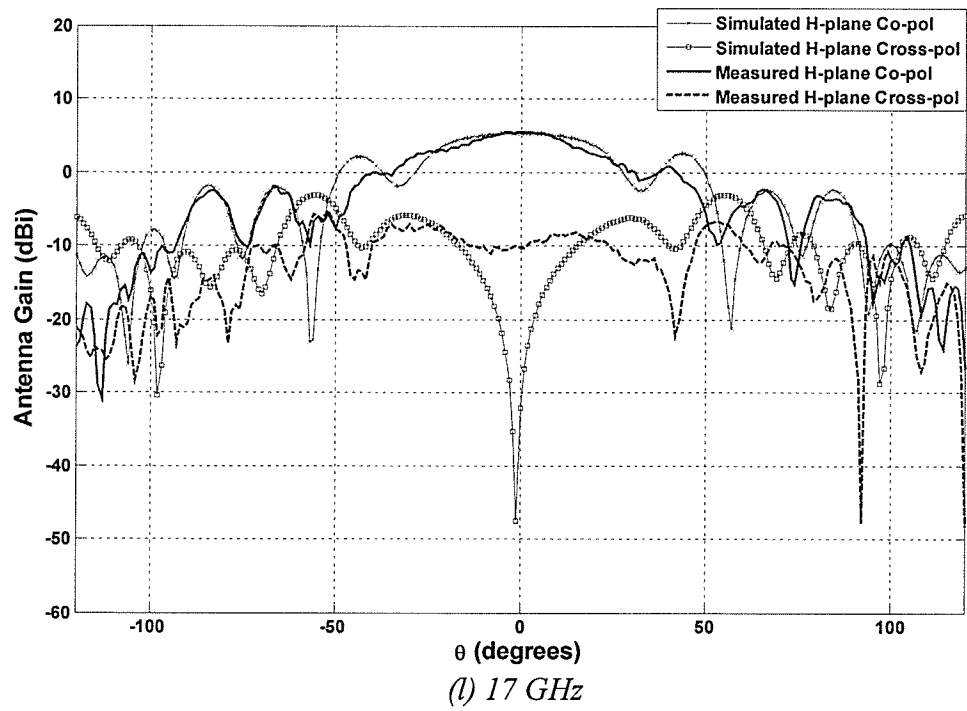
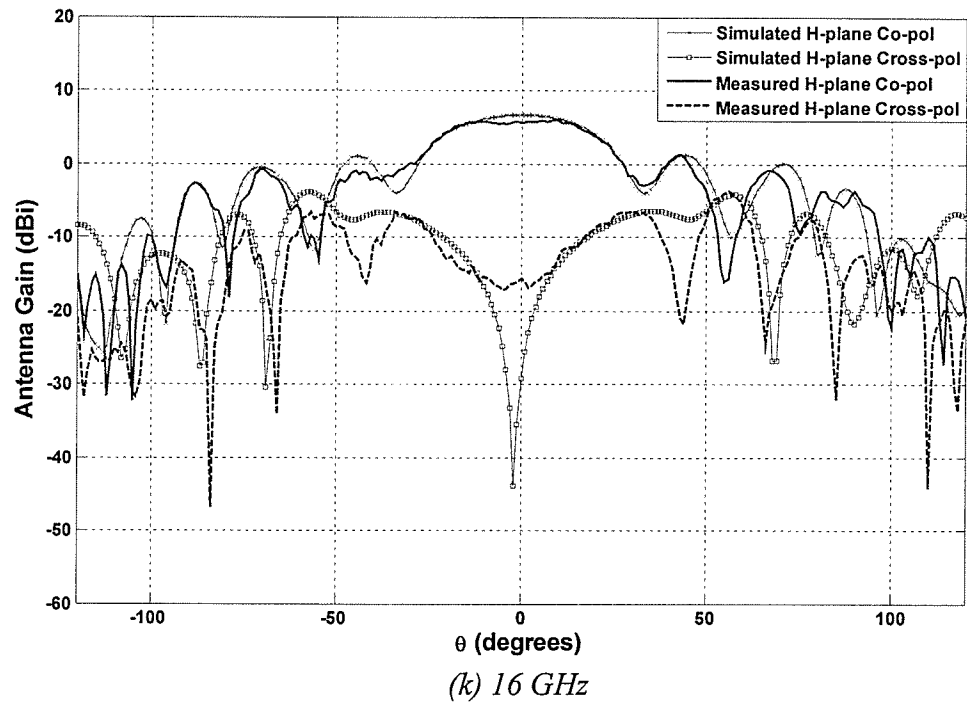


Fig. 6.7 (k), (l)

Fig. 6.7 contd.

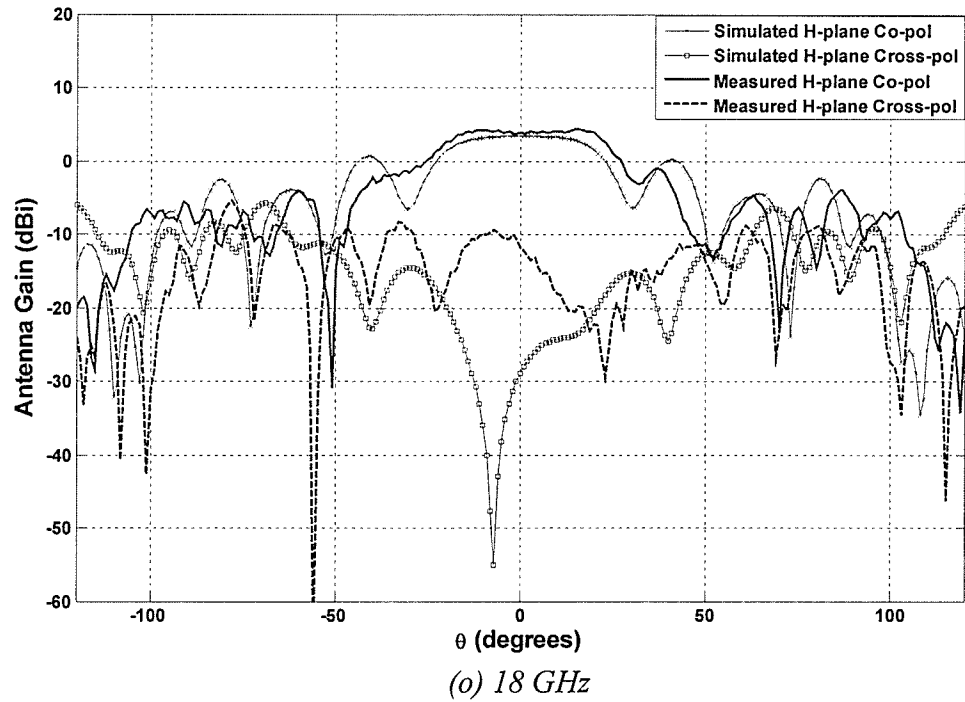


Fig. 6.7 Simulated and measured H-plane ($\phi=0^\circ$ plane) radiation patterns of the balanced antipodal Vivaldi given in Fig. 5.10 and Fig. 6.1 respectively with $\epsilon_r = 2.5$, $h = 1.5$ mm, $\tan\delta = 0.001$. Other parameters are given in Fig. 6.1

A comparison of the important simulated and measured H-plane co-pol and cross-pol characteristics are summarized in Tables 6.3 and 6.4.

Frequency (GHz)	Boresight Gain (dBi)		Peak Gain (dBi)		Position of Peak Gain		3 dB BW		10 dB BW	
	Sim	Meas	Sim	Meas	Sim	Meas	Sim	Meas	Sim	Meas
6	9.218	9.852	9.218	9.871	0°	3°	70°	62°	106°	99°
7	9.608	7.158	9.608	7.467	0°	5°	52°	52°	98°	95°
8	10.319	9.545	10.319	9.545	0°	0°	50°	48°	80°	75°
9	10.757	11.533	10.757	11.562	0°	1°	46°	41°	78°	71°
10	10.707	10.626	10.707	10.649	0°	1°	42°	43°	74°	84°
11	9.967	9.324	9.967	9.347	0°	-1°	38°	31°	131°	128°
12	9.988	9.785	9.988	9.809	0°	1°	38°	36°	100°	92°
13	9.165	6.431	9.165	6.524	0°	-3°	35°	38°	123°	117°
14	8.409	6.226	8.410	6.349	1°	-4°	37°	41°	118°	119°
15	7.069	6.573	7.069	6.731	0°	5°	35°	38°	112°	101°
16	6.686	5.580	6.686	5.997	0°	9°	43°	49°	64°	102°
17	5.340	5.439	5.340	5.474	0°	1°	47°	48°	106°	90°
18	5.111	3.855	3.414	4.352	0°	16°	44°	50°	60°	89°

Table 6.3 Summary of the simulated and measured H-plane co-pol pattern characteristics of the balanced antipodal Vivaldi given in Fig. 5.10 and Fig. 6.1 respectively

Frequency (GHz)	Boresight Cross-pol (dBi)		Peak Cross-pol (dBi)		Position of Peak Cross-pol	
	Sim	Meas	Sim	Meas	Sim	Meas
6	-43.733	-26.428	-10.297	-10.158	-124°	-67°
7	-44.174	-23.484	-10.056	-13.907	-73°	-70°
8	-49.150	-20.891	-9.470	-7.911	61°	57°
9	-35.500	-13.038	-6.481	-3.464	50°	-47°
10	-52.190	-14.366	-5.880	-7.047	-47°	-40°
11	-42.672	-35.015	-4.662	-6.078	40°	-34°
12	-40.015	-16.304	-7.788	-3.222	108°	36°
13	-27.705	-15.307	-2.343	-8.123	-149°	-24°
14	-30.537	-13.501	-6.172	-5.094	-28°	60°
15	-29.008	-7.585	-5.628	-5.427	152°	78°
16	-29.227	-15.679	-3.931	-3.730	-58°	56°
17	-32.137	-10.287	-3.079	-5.273	55°	-52°
18	-26.194	-11.889	-4.656	-5.442	158°	-78°

Table 6.4 Summary of the simulated and measured H-plane cross-pol pattern characteristics of the balanced antipodal Vivaldi given in Fig. 5.10 and Fig. 6.1 respectively

From Fig. 6.6 and 6.7 it can be seen that the measured co-pol patterns in both principle planes are in close agreement to the simulated ones. The asymmetrical nature of the E-plane co-pol patterns observed in the simulation results are observed in the measured results as well. From Tables 6.1 and 6.3 it can be observed that the measured boresight and peak gain levels are in close agreement to the simulated ones. However, the measured cross-pol levels in both principle planes, as seen in Tables 6.2 and 6.4, are higher than the simulated ones. This may be due to a misalignment of the etched flares on either side of the substrate or a misalignment of the flares on either substrate when they were fastened together with the help of screws. Another factor that may have caused higher measured cross-pol levels is the fastening screws themselves, which may have interfered with the performance of the fabricated antenna.

6.4 Study of Phase Centre

A study of the location of the phase centre could be carried out for the fabricated Vivaldi in the H-plane (xz plane, i.e. $\phi=0^\circ$ plane) only, for the frequency range of 9 to 12 GHz (with a one GHz step). The measured H-plane phase centre was determined by taking phase patterns for an angle off main beam axis θ ranging from -30 to 30° while pivoting the antenna about different points along the length of the slot; the phase centre being located at the pivot point that gave greatest degree of flatness over the mentioned angle off main beam axis range [15]. The H-plane phase centre location for the fabricated Vivaldi was found to lie over a portion of the antenna axis rather than existing at a single point, as was found in the case of the simulated phase centre results of chapter five. The maximum tolerable phase difference $\Delta\phi$ was found to be 35° at this location.

A study of the H-plane phase centre for the simulated results with its appropriate maximum phase difference tolerability $\Delta\phi$ of 15° was also carried out in the 9 to 12 GHz range in order to compare with the measured results. The measured phase centre location was found to lie within the antenna axis portion of the simulated results. A comparison of the measured and simulated phase center locations is given in Fig. 6.8.

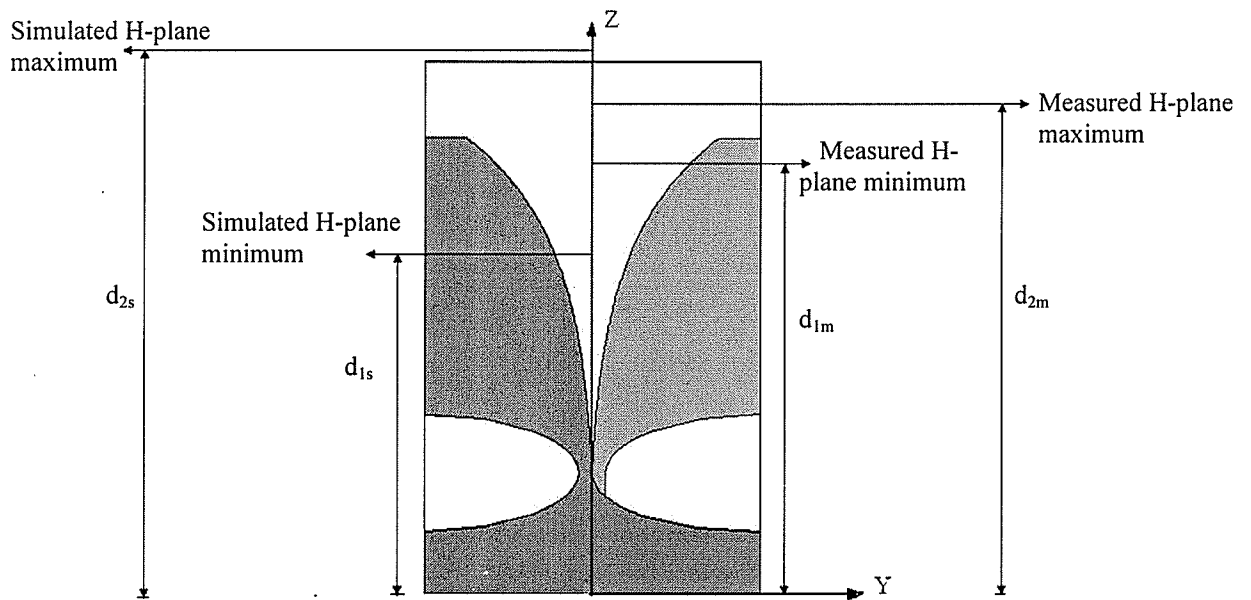


Fig. 6.8 Geometry of the balanced antipodal Vivaldi with substrate elongation of 12.80 mm indicating the portion of antenna axis where the simulated ($\Delta\phi = 15^\circ$) and measured ($\Delta\phi = 35^\circ$) H-plane phase centres lie; $d_{1m} = 74.22\text{mm}$, $d_{2m} = 80.75\text{mm}$, $d_{1s} = 57\text{mm}$, $d_{2s} = 90\text{mm}$. Dimensions of the antenna are given in Fig. 5.10

6.5 Summary

In this chapter, an experimental verification of one of the balanced antipodal Vivaldi models of chapter five was presented. The simulated and measured return loss and radiation patterns were given and it was seen that the results were in close agreement with each other. The H-plane phase centre location of the fabricated antenna for the frequency range of 9 to 12 GHz was found and it was compared to the corresponding simulated results.

CHAPTER 7

CONCLUSION

7.1 Summary

In this thesis, two different types of Vivaldi antennas were investigated. A single sided Vivaldi fed by a microstrip feed line given in [9] (Model 1) was simulated using a finite element method design and analysis package Ansoft HFSS v 10.1 and its far-field radiation patterns were studied in the 6 to 20 GHz range. A null at boresight in the simulated E-plane co-pol patterns with increase in frequency of operation was observed. The location of the E and H-plane phase centre on the antenna axis was investigated, and it was found that it does not confine itself to a single point on the axis, but rather lies on portion of the axis for a specified maximum tolerable phase difference $\Delta\phi$. Next, the effect of taper length on the performance of the antenna was studied. The slotline length was first increased (Model 2) and it was found that this elongation slightly improved the simulated return loss and gain of the antenna. However, null at boresight in the E-plane co-pol patterns still appeared. The phase centre of this model was again found to be situated on a portion of the antenna axis. The slotline length of the original model (Model 1) was then truncated (Model 3) and it was found that this truncation deteriorated the simulated return loss and gain of the antenna. The phase centre location on the antenna axis was also studied for this model.

After studying the effect of length of taper on the antenna performance, the effect of rate of taper and width of the antenna was studied. The rate of taper of Model 1 was increased (Model 4) and it was found that this increase in rate slightly improved the gain

of the antenna. However, it did not help in minimizing the phase variation of the co-pol radiation at the phase centre location. The rate of taper of Model 1 was then decreased (Model 5) and it was found that this led to a significant deterioration of the simulated return loss performance of the antenna. The antenna gain was also slightly affected by this decrease in rate of taper. The phase centre location was also studied. Finally, the last study that was carried out on the single sided Vivaldi was the effect of width truncation on the antenna performance. Interestingly, this truncation (Model 6) led to a significant increase simulated antenna gain and also to a disappearance of null at boresight in the E-plane co-pol patterns. Also, the phase variation of the co-pol radiation at the phase centre location of this model was found to be the smallest out of all six single sided Vivaldi models presented. The Average E and H-plane phase centres were also found to be the most stable through out the entire considered frequency range compared to all the other single sided models that were studied here. Not only did Model 6 exhibit a performance superior to that of the remaining five models, but also, it possessed the attractive feature of being extremely compact in size. Hence this model was concluded to be the optimum design out of all single sided Vivaldi antenna models studied in this thesis.

The second type of Vivaldi antenna that was investigated was the balanced antipodal Vivaldi. As Model 6 of chapter four was seen to have the best performance out of the six single sided Vivaldi antennas studied, its dimensions were chosen to design a balanced antipodal Vivaldi antenna. The simulations were again carried out with Ansoft HFSS v. 10.1. This balanced antipodal Vivaldi was also found to have a very good performance regarding radiation patterns and phase centre location. However, it could not overcome the broadband limitations that were observed in the single sided Vivaldi

models. In order to achieve a much larger bandwidth, a balanced antipodal Vivaldi with a wider aperture than the former was designed. The effect of substrate elongation on the gain of this antenna was studied, and it was observed that with increase in length of the substrate, there was an increase in gain. The location of phase centre for the antenna model with substrate elongation of 12.80 mm was studied and it was found that it did not have as stable a phase centre behavior as that of Model 6 of chapter four. The effect of substrate shaping was also investigated and it was found that it played a significant role in increasing the gain of the antenna at higher frequencies of operation. From an overall inspection, it was concluded that an elongated as well as shaped substrate was the best design for the balanced antipodal Vivaldi antenna to achieve an optimum gain performance.

In order to confirm the analysis, the balanced antipodal Vivaldi antenna of chapter five with a substrate elongation of 12.80 mm was fabricated and tested in the Antenna Laboratory at the University of Manitoba. It was chosen not only for its noteworthy performance, but also due to practical issues. The measured return loss and far-field radiation patterns were in close agreement with the simulated results. The H-plane phase centre for the fabricated antenna was studied for the 9 to 12 GHz range and its location was in close agreement to that of the simulated results for the same frequency range.

To summarize, a thorough parametric study of a single sided Vivaldi antenna was carried out through which, a compact model was developed, whose performance (with regard to radiation patterns and phase centre location) was superior to the existing design. A better understanding of the types of Vivaldi antennas was obtained by conducting a study of two different balanced antipodal Vivaldi models. From this study, it was

concluded that a balanced antipodal Vivaldi antenna with a wide aperture and an elongated as well as shaped substrate was the best design to achieve an optimum bandwidth and gain performance.

7.2 Future Work

A few future research topics arising from this work are listed below:

- More detailed parametric study of the single sided and balanced antipodal Vivaldi antennas.
- Use of these antennas as elements of a phased array system and studying the array performance as well as each individual element's behavior.
- Investigating the location of the E and H-plane phase centre over the entire antenna surface as opposed to only along its axis and hence making it a 2-D problem.
- Finding suitable techniques to reduce the cross-pol levels of these antennas

REFERENCES

- [1] P.J. Gibson, "The Vivaldi aerial," in *Proc. 9th Eur. Microwave Conf.*, pp. 101-105, 1979.
- [2] E. Gazit, "Improved design of the Vivaldi antenna," *IEE Proc. H*, vol. 135, No. 2, pp. 89-92, April 1988.
- [3] D. H. Schaubert, "Endfire tapered slot antenna characteristics," in *Sixth International Conf. on Antennas and Propagation 1989*, vol. 1, pp. 432-436, April 1989.
- [4] S. G. Mao and S. L. Chen, "Time-domain characteristics of ultra-wideband tapered loop antennas," *Electronics Letters*, vol. 42, No. 22, pp. 1262-1263, October 2006.
- [5] A. H. Mohammadian, A. Rajkotia, and S. S. Soliman, "Characterization of UWB transmit-receive antenna system," in *IEEE Conference on Ultra Wideband Systems and Technologies 2003*, pp. 157-161, November 2003.
- [6] K. S. Yngvesson *et. al*, "Endfire tapered slot antennas on dielectric substrates," *IEEE Trans. On Antennas and Propagation*, vol. 33, No. 12, pp. 1392-1400, December 1985.
- [7] L. R. Lewis, M. Fassett, and J. Hunt, "A broadband stripline array element," in *IEEE Antennas and Propagation Society International Symposium 1974*, vol. 12, pp. 335-337, June 1974.
- [8] R. Janaswamy, "An accurate Moment Method model for the tapered slot antenna," *IEEE Trans. On Antennas and Propagation*, vol. 37, No. 12, pp. 1523-1592, December 1989.

- [9] E. Thiele and A. Taflove, "FD-TD analysis of Vivaldi flared Horn antennas and arrays," *IEEE Trans. On Antennas and Propagation*, vol. 42, No. 5, pp. 633-641, May 1994.
- [10] J. Shin and D. H. Schaubert, "A parameter study of stripline-fed Vivaldi notch-antenna arrays," *IEEE Trans. On Antennas and Propagation*, vol. 47, No. 5, pp. 879-886, May 1999.
- [11] D. H. Schaubert and T.H. Chio, "Wideband Vivaldi arrays for large aperture antennas," in *Proc. of the Conf. on Perspectives on Radio Astronomy: Technologies for Large Antenna Arrays 1999*, pp. 49-57, April 1999.
- [12] J. D. S. Langley, P. S. Hall, and P. Newham, "Novel ultrawide-bandwidth Vivaldi antenna with low crosspolarisation," *Electronics Letters*, vol. 29, No. 23, pp. 2004-2005, November 1993.
- [13] Q. Wu, B. Jin, L. Bin, Y. Wu, and L. Li, "An approach to the determination of the phase center of Vivaldi-based UWB antenna," in *IEEE Antennas and Propagation Society International Symposium 2006*, pp. 563-566, July 2006.
- [14] A. Elsherbini, C. Zhang, S. Lin, M. Kuhn, A. Kamel, A. E. Fathy, and H. Elhennawy, "UWB antipodal Vivaldi antennas with protruded dielectric rods for higher gain, symmetric patterns and minimal phase center variations," in *IEEE Antennas and Propagation Society International Symposium 2007*, pp. 1973-1976, June 2007.
- [15] J. W. Bowen, "Astigmatism in tapered slot antennas," *International Journal of Infrared and Millimeter Waves*, vol. 16, No. 10, 1995.

- [16] R. Janaswamy and D. H. Schaubert, "Analysis of the tapered slot antenna," *IEEE Trans. On Antennas and Propagation*, vol. AP-35, No. 9, pp. 1058-1064, September 1987.
- [17] S. N. Prasad and S. Mahapatra, "A new MIC slot-line aerial," *IEEE Trans. On Antennas and Propagation*, vol. AP-31, No. 3, pp. 525-527, May 1983.
- [18] K. S. Yngvesson *et. al*, "The tapered slot antenna- A new integrated element for millimeter-wave applications," *IEEE Trans. On Microwave Theory and Techniques*, vol. 37, No. 2, pp. 365-374, February 1989.
- [19] R. E. Collin and F. J. Zucker, *Antenna Theory Part 2, Inter-University Series, Vol 7*. McGraw-Hill Inc., 1969.
- [20] J. D. S. Langley, P. S. Hall, and P. Newham, "Balanced antipodal Vivaldi antenna for wide bandwidth phased arrays," *IEE Proc. On Microwaves, Antennas and Propagation*, vol. 143, No. 2, pp. 97-102, April 1996.
- [21] L. Tianming, R. Yuping, and N. Zhongxia, "Analysis and design of UWB Vivaldi antenna," *IEEE 2007 International Symposium on Microwave, Antenna, Propagation, and EMC Technologies for Wireless Communications*, pp. 579-581, August 2007.
- [22] J. P. Weem, Z. Popovic, and B. M. Notaros, "Vivaldi antenna arrays for SKA," *IEEE Antennas and Propagation Society International Symposium 2000*, vol. 1, pp. 174-177.
- [23] K. C. Gupta, R. Garg, and I. J. Bahl, *Microstrip Lines and Slotlines*. Artech House Inc., 1979.

- [24] D. H. Schaubert, "Wide-Band phased arrays of Vivaldi notch antennas," in *10th International Conference on Antennas and Propagation*, No. 436, pp. 1.6-1.12, April 1997.
- [25] B. Schuppert, "Microstrip/slotline transitions: modeling and experimental investigation," *IEEE Trans. On Microwave Theory and Techniques*, vol. 36, No. 8, pp. 1272-1282, August 1988.
- [26] IEEE Std. 145-1993, *IEEE Standard Definition of Terms of Antennas*.
- [27] N. Fourkis, N. Lioutas, and N. V. Shuley, "Parametric study of the co- and crosspolarisation characteristics of tapered planar and antipodal slotline antennas," *IEE Proc. H*, vol. 140, No. 1, pp. 17-22, February 1993.
- [28] R. Q. Lee, "Notch antennas," Tech. rep., Glenn Research Centre, July 2004.